

Dissertation

Martin Roland Steinel

A dual species optical atomic clock

ISSN 2941-1297
ISBN 978-3-944659-58-9

DOI 10.7795/110.20260204

Genauigkeit | Objektivität | Leidenschaft

www.ptb.de

Martin Roland Steinel

A dual species optical atomic clock

Dissertation

PTB-Diss-26

Braunschweig, 03. Februar 2026

ISSN 2751-6598

ISBN 978-3-944659-58-9

DOI 10.7795/110.20260204

Empfohlene Zitierweise/recommended citation

Steinel, M.R., 2026. *A dual species optical atomic clock*.
Dissertation, Gottfried Wilhelm Leibniz Universität Hannover.
Braunschweig: Physikalisch-Technische Bundesanstalt.
PTB-Bericht Diss-26. ISBN 978-3-944659-58-9.
Verfügbar unter: <https://doi.org/10.7795/110.20260204>

Herausgeber:

Physikalisch-Technische Bundesanstalt
ISNI: 0000 0001 2186 1887

Presse und Öffentlichkeitsarbeit

Bundesallee 100
38116 Braunschweig

Telefon: (05 31) 592-93 21
Telefax: (05 31) 592-92 92
www.ptb.de

A dual species optical atomic clock



Von der Fakultät für Mathematik und Physik
der Gottfried Wilhelm Leibniz Universität Hannover
zur Erlangung des Grades

Doktor der Naturwissenschaften Dr. rer. nat.

genehmigte Dissertation von

M.Sc. Martin Roland STEINEL

2026

Referent: PD. Dr. Ekkehard PEIK
Korreferentin: Prof. Dr. Tanja E. MEHLSTÄUBLER
Korreferent: Prof. Dr. Jürgen ESCHNER
Tag der Promotion: 16.12.2025

Abstract

Frequency standards based on optical transitions between electronic states of trapped ions have reached uncertainties below 10^{-18} ¹. The Stark shift caused by room-temperature blackbody radiation (BBR) causes the largest correction for most high-performance optical clock. The systematic uncertainty of $^{171}\text{Yb}^+$ clocks based on the $^2S_{1/2}(F=0) \rightarrow ^2D_{3/2}(F=2)$ electric quadrupole (E2) and $^2S_{1/2}(F=0) \rightarrow ^2F_{7/2}(F=3)$ electric octupole (E3) transitions is currently limited to 28×10^{-18} and 1.5×10^{-18} , respectively, by the fractional accuracy of the differential polarizability $\Delta\alpha_{\text{dc}}$ of approximately 2% ².

In the scope of this thesis, a dual species clock based on $^{171}\text{Yb}^+$ and $^{88}\text{Sr}^+$ ions was set up, operated and evaluated, to overcome this barrier. Since $\Delta\alpha_{\text{dc}}$ is known with a smaller fractional uncertainty of 0.04% for the $^2S_{1/2} \rightarrow ^2D_{5/2}$ E2 transition of $^{88}\text{Sr}^+$ ³, this allows for a transfer of $\Delta\alpha_{\text{dc}}$ from $^{88}\text{Sr}^+$ to $^{171}\text{Yb}^+$ following a method proposed in ⁴. The optical intensity of a laser is calibrated with the Stark shift it causes on the $^{88}\text{Sr}^+$ clock transition, allowing for the determination of $\Delta\alpha_{\text{dc}}$ of the $^{171}\text{Yb}^+$ clock transitions. This allows for a reduction of the fractional uncertainty of $\Delta\alpha_{\text{dc}}$ for both $^{171}\text{Yb}^+$ clock transitions below 0.4% and clock operation on the E2 and E3 transition with a fractional BBR shift uncertainty of 0.84×10^{-18} and 0.24×10^{-18} is enabled, respectively.

However the value of $\Delta\alpha_{\text{dc}}$ determined in this thesis does not agree with ², a fractional offset of approximately 14% is observed. To investigate this discrepancy further, $\Delta\alpha_{\text{dc}}$ is measured in the same manner as in ² for the $^{88}\text{Sr}^+$ clock transition. The same offset of approximately 14% is found, calling the accuracy of at least one of these methods into question.

Finally, the first optical frequency ratio \mathcal{R} between the $^{88}\text{Sr}^+$ clock transition and the $^{171}\text{Yb}^+$ E3 transition is measured. The fractional uncertainty of \mathcal{R} is 23×10^{-18} . \mathcal{R} in combination with the absolute frequency of the E3 transition allows for the determination of the $^{88}\text{Sr}^+$ absolute frequency ν_{Sr^+} with an uncertainty limited by the caesium references. The value of ν_{Sr^+} falls outside of the recommended range, but is corroborated by measurements of the same quantity by other institutes ^{5 6}.

¹M. Marshall et al., Phys. Rev. Lett. 135, 033201 (2025)

²N. Huntemann et al., Phys. Rev. Lett. 116, 063001 (2016)

³T. Lindvall et al., Phys. Rev. Lett. 135, 043402 (2025)

⁴M. D. Barrett et al., Phys. Rev. A 100, 043418 (2019)

⁵C. Marceau et al., Metrologia 62.4, 045001 (2025)

⁶T. Lindvall et al., Phys. Rev. Appl. 24, 044082 (2025)

Keywords: Optical clocks, Multi-species clocks, Differential polarizability

Schlagworte: Optische Uhren, Multi-Spezies-Uhren, Differentielle Polarisierbarkeit

Acknowledgements

During my time at PTB and before, many different people have supported me in a variety of ways on my journey towards this thesis. Every person relies on others, be it via technical support, discussions regarding scientific results or social connections and I would not have been able to finish the work presented here without my colleagues and friends. For this reason, I want to thank these people here to acknowledge their contributions to this work.

First and foremost I thank Nils Huntemann, the group leader of *Optical clocks with trapped ions* at Physikalisch Technische Bundesanstalt (PTB), for supporting me in my scientific work presented here from the very beginning in every regard. From organizing funding, providing the lab infrastructure and all necessary devices over discussions about the scientific goals, experimental techniques and relevant physics to reviewing abstracts for conferences, public presentations and scientific publications, you always provided more than what was required to successfully do cutting-edge research. I am certain that your group will continue to produce highly relevant research on optical clocks, fundamental physics and whatever else comes up in the coming decades. Also the discussions with you about topics outside of physics were always fascinating and showed me perspectives I rarely encounter otherwise. All in all, thank you for the support in finishing this thesis.

I also want to thank my thesis advisor and head of the department Time and Frequency at PTB, Ekkehard Peik. While not present in the laboratory day to day, your overall guidance regarding the research project and which questions might prove interesting is always appreciated. In addition, your knowledge of atomic physics and its historical development provided me with many new insights into long-term research. In addition, I thank you for refereeing this thesis.

I give thanks to Hu Shao, the postdoc who started setting up the YbSr1 system before I arrived at PTB. While we only worked together for 6 months, before you left for your home country, the foundation you provided regarding laser systems, the ion trap and the vacuum system allowed me to hit the ground running at the start of my PhD. Also I learned the fundamentals in operating the system itself from you, while we worked on it together in the beginning.

I thank Burghard Lipphardt, the now retired head of the electronics division and the frequency combs of the group, for his continued support regarding both electronics and optical frequency measurements. Your expertise will be hard to replace and your ability to explain the details of the frequency stabilization and

measurement techniques employed in this thesis is greatly appreciated.

I want to thank Melina Filzinger, the PhD student who joined shortly after my start in the group. Your different areas of expertise, especially regarding vacuum systems, were very helpful during my time at PTB. I also enjoyed the many experimental problems we solved together on your and my experiment, this always provided a breath of fresh air. Also the conversations we had about academic life, the group and many other things were always great and showed me additional perspectives.

I also thank Nele Wendt, the physics technician who joined us for her training and was an employee afterwards. Your skills in setting up laser systems took a large load off our shoulders and also your perspective from outside academia was always welcome. In addition, I also enjoyed your baking a lot, be it cakes you prepared on your own or the group bake events you organized.

I give thanks to Martin Menzel, Andreas Hoppmann and Michael Kazda for your amazing mechanical and electrical work for the group. Not only is your support invaluable for the operation of any system in our group, I also learned many things about mechanical and electrical design, the mechanical workshop and electrical components from you and hope to further my knowledge in these fields more and more.

I want to thank Richard Lange, Jian Jiang and Saaswath Jeyalathaa Karthikeyan as other PhD students and postdocs during my time in the group. Richard, your guidance regarding the optical clocks in this group allowed for a quick start in working with systems other than YbSr1. Your thesis is by now a reference provided to most students and interns here and your achievements are a guiding point for everyone. Jian and Saaswath, your projects also provide valuable insight into the performance of single ion clocks and discussions with you are always fruitful, be it about my work or atomic physics in general.

I thank Niklas Kuhrmeyer, Thilo Schmidt, Mirko Wytopil and Marius Jathe for support in many different ways as members of the group during my thesis work. Being a part of your projects allowed for a broad investigation of topics and I am happy to profit from the results these provided. Also I enjoyed our conversations about physics as well as about topics other than physics during this time.

I thank Stefan Weyers, Johannes Rahm and Maksim Okhapkin for your explanations regarding and operation of the caesium and thorium clocks, respectively. Caesium clocks as the primary standard are still a vital component of frequency metrology and the nuclear clock, now that the thorium transition is found, represents the future of this field. Working at the intersection of all these devices has provided me with important experiences.

I want to thank Tanja Mehlstäubler, Jonas Keller, Elena Jordan, Tabea Nordmann and Malte Brinkmann, members of the research group focussing on multi-ion clocks at PTB, for your ion trap without which none of this work would have

been possible. Also details on multi-ion operation and ion control sequences in your setup were helpful to get started in the beginning of my work. I hope that future collaborations between your and our group will continue to be fruitful and produce high-value scientific research. In particular I thank Tanja Mehlstäubler for refereeing the thesis as well.

I give thanks to Martina Bäumlner and Birgit Römer, the secretaries of the department Time and Frequency. Without your valuable administrative work, I would not have been able to focus so much on research. In general, I extend these thanks to the whole administrative department of PTB that has to deal with sudden requests regarding purchases, mail deliveries and printing scientific posters on a regular basis.

I thank Erik Benkler, Thomas Legero and Uwe Sterr for providing the ultrastable laser which is the phase reference for all our clock lasers as well as a central part of the frequency comb infrastructure. Without it, my work would be much more difficult and not allow for easy comparisons of the different clocks operated at PTB with each other.

I want to thank Christian Lisdat, my second advisor in the PTB PhD program, with whom I discussed my research from a new perspective. Additionally, I thank his group members Sören Dörscher, Kilian Stahl and Joshua Klose for support both with hardware components such as a temperature stabilized chiller and discussions about the work discussed in this thesis.

I thank Piet Schmidt and his group, especially the subgroup of Fabian Wolf, Maximilian Zawierucha and Till Rehmert, where I spent two weeks for a laboratory exchange during my PhD. Your molecular spectroscopy experiment gave me the opportunity to gain some experience with more complex atomic systems and it was in general a great way to compare and contrast our different approaches to high-precision spectroscopy.

I thank Marco Antonio Lopez Ordonez and Holger Lecher for providing the calibration of the infrared power meter and discussions regarding the observed polarizability discrepancy. Without this support, the polarizability measurements would not have been possible.

I want to thank Andrey Surzhykov and Anton Peshkov for support regarding theoretical physics in the polarizability measurements. It was very helpful to have someone familiar with the topic from the theoretician's side for correctly relating optical intensities, electric fields and the polarizability value with each other.

I give thanks to Thomas Lindvall and Anders Wallin. Your experience with $^{88}\text{Sr}^+$ clocks was invaluable in getting the details of the uncertainty budget right and where the limiting factors of our system might come from. I especially enjoyed my two week visit to your laboratory, where I learned many things about your laser locking techniques and alternative approach to a $^{88}\text{Sr}^+$ clock.

I thank Jürgen Eschner for refereeing this thesis and for providing the education during my Bachelor and Master at Saarland University, which prepared me to a great extent for the work at PTB.

I want to thank my close family for the continued support on my way through life, school, university and to this thesis. Without you, Helga and Forest Edsall, Andrea Schulz, Thomas, Nicole, Lara and Lilly Steinel, Tina, Kel and Roman Boyer, Knut and Edith Schneider, Susanna and Andreas Hertel, Kassandra and Tanis Schwärzel, Silke Schneider, Wolfgang Thiel, Nora and Dio Schneider, Ullrich, Andrea, Philipp, Richard and Viktor Schneider, I would not have made it this far and I hope that we continue to enjoy our time together for a long while.

In a similar manner, I thank my closest friends Denise Hell, Judith Huwig, Max Junk and Aline Jochem for your open minds and ears ever since we attended school together. Even when complaining about problems with clock lasers, ion cooling or laser power measurements, you stayed interested in my work and life. Your perspectives outside of my physics bubble are always valuable to me and I want to stay connected with you as much as our lives allow for.

I want to thank my fellow students at Saarland University that supported me in my studies and in starting the PhD at PTB. Sascha Thieltges, without you by my side, the advanced physics laboratories courses and university life in general would have been much more dull and less insightful. Kevin Kaub, Hubert Lam, I always value your perspectives on physics research, life in academia and especially remember the trip to Berlin to the national meetup of the physics student councils fondly. Marco und Kordula Schellnhuber, Wiebke Buhrow, Andreas Keller and Nils König, I thank you for the many nights we spent away from work, be it in the student council room or online once the pandemic hit and we scattered throughout Germany afterwards. Also, I want to thank Lena Wagner for the time we spent together before I moved to Braunschweig and the support you gave me in deciding to start my PhD at PTB.

Finally, I give my deepest thanks to my parents Cathrin and Arthur Steinel. Your support throughout my whole life was tremendous and prepared me for the academic and personal challenges I faced over the years. Without you, I would not be standing where I am today.

Contents

List of Figures	xi
List of Tables	xiii
Acronyms and abbreviations	xv
1. Introduction to optical atomic clocks and this thesis	3
1.1. Figures of merit: Stability and accuracy	7
1.2. Multi-species, multi-ion optical clocks	11
1.3. Key results and structure of the thesis	13
2. Optical clocks based on trapped ions	17
2.1. Trapping a charged particle with electromagnetic fields	17
2.2. Cooling the ion to the Doppler limit	24
2.3. Coherent interaction between cold ions and electromagnetic radiation	29
2.4. Properties of clock transitions of $^{171}\text{Yb}^+$ and $^{88}\text{Sr}^+$	37
2.5. Resolved sideband cooling of the $^{88}\text{Sr}^+$ and $^{171}\text{Yb}^+$ ions and heating rate measurements	44
3. Experimental setup for the multi-species, multi-ion clock YbSr1	49
3.1. Chip-based multi-ion trap for YbSr1	49
3.2. Doppler cooling lasers	55
3.3. Optical setup around the ion trap	61
3.4. Ion loading procedure	63
3.5. Magnetic field control and measurements	64
3.6. Background pressure measurement	69
3.7. Clock laser setup, frequency measurement and stabilization	72
4. Frequency shifts due to electric fields	79
4.1. The dynamical polarizability model	82
4.2. Magic wavelength measurement for $^{88}\text{Sr}^+$	88
4.3. Polarizability measurements with infrared laser radiation	91
5. Polarizability ratio measurements between $^{88}\text{Sr}^+$ and $^{171}\text{Yb}^+$	101
5.1. Common experimental setup for polarizability ratio measurements	102
5.2. Tensorial polarizability of $^{88}\text{Sr}^+$	106
5.3. Polarizability ratio measurements for $^{171}\text{Yb}^+$	109

Contents

5.4. Polarizability ratio of $^{88}\text{Sr}^+$ and $^{171}\text{Yb}^+$ clock transitions	113
6. $^{88}\text{Sr}^+ / ^{171}\text{Yb}^+$ E3 frequency ratio measurement	121
6.1. Clock transition interrogation sequence	121
6.2. Systematic frequency shifts and their uncertainty	126
6.3. Frequency instability and multi-ion operation	136
6.4. Frequency ratio measurement and absolute frequency determination	138
7. Summary and outlook	143
7.1. Polarizability ratio measurement and BBR shift uncertainty reduction	143
7.2. Comparison between polarizability measurement methods	145
7.3. Measurement of the $^{88}\text{Sr}^+ / ^{171}\text{Yb}^+$ E3 optical frequency ratio	146
Appendices	149
A. Legend for optical elements	151
Bibliography	153

List of Figures

1.1.	Unit relations in the new SI	4
1.2.	Overview over the elements of an optical clock	6
1.3.	Comparison of the Allan deviation for different noise sources	8
2.1.	Mathieu stability diagram	20
2.2.	Motional spectrum of a trapped ion at small and large q	22
2.3.	Level structure of $^{171}\text{Yb}^+$ and $^{88}\text{Sr}^+$ relevant for Doppler cooling	26
2.4.	Thermal Rabi oscillations	32
2.5.	Carrier sideband excitation probability comparison	34
2.6.	Motional energy contained within Fock states with large n	35
2.7.	Level structure of $^{171}\text{Yb}^+$ and $^{88}\text{Sr}^+$ relevant for clock operation	38
2.8.	Coupling strength for an E2 transition	40
2.9.	Coupling strength for an E3 transition	40
2.10.	Clock pumping for $^{88}\text{Sr}^+$	43
2.11.	Heating rate measurement for axial and radial motion	47
3.1.	Images of the ion trap	50
3.2.	Sketch of the trap electrodes and their function	51
3.3.	Sketch of the ion transfer sequence	54
3.4.	Sketch of the Doppler cooling laser stabilization setup	55
3.5.	Sketch of the repump laser stabilization setup	58
3.6.	Sketch of the 370 nm laser board	59
3.7.	Sketch of the 422 nm laser board	60
3.8.	Optical setup around the ion trap	61
3.9.	Measurement of the magnetic field decay	66
3.10.	Autler-Townes splitting schematic	68
3.11.	Autler-Townes splitting measurement results	69
3.12.	Histogram of the crystal stability	72
3.13.	Clock laser distribution and stabilization to traps and frequency combs	73
3.14.	Sketch of the optical setup and stabilization of the Sr master laser	74
3.15.	Sketch of the optical setup of the Sr clock laser distribution	78
4.1.	Polarizability model for $^{171}\text{Yb}^+$ E2	85
4.2.	Polarizability model for $^{171}\text{Yb}^+$ E3	86
4.3.	Polarizability model for $^{88}\text{Sr}^+$ E2	86
4.4.	Magic wavelength measurement	90

List of Figures

4.5.	Beam profile of the QCL laser at the ion position	95
4.6.	Comparison of differential polarizability values for $^{88}\text{Sr}^+$	98
5.1.	Spectrum of the QCL laser	104
5.2.	Fractional offsets of the $^{171}\text{Yb}^+$ polarizability ratios	112
5.3.	Polarizability ratio of the $^{171}\text{Yb}^+$ E2 and $^{88}\text{Sr}^+$ clock transitions .	117
5.4.	Fractional offsets of the $^{171}\text{Yb}^+$ polarizability values	119
6.1.	Experimental pulse sequence for the $^{88}\text{Sr}^+$ clock	125
6.2.	BBR shift estimate due to trap heating	130
6.3.	Allan deviation of Sr/E3 frequency ratio	138
6.4.	Frequency ratio measurement	139
6.5.	Absolute frequency of the $^{88}\text{Sr}^+$ clock transition	140
A.1.	Legend of optical elements	151

List of Tables

4.1. Lightshift-based polarizability values for the $^{88}\text{Sr}^+$ clock transition	97
5.1. Variation of the clock transition polarizabilities	105
5.2. Fractional correction of the polarizability due to laser spectral intensity distributions	105
5.3. M1/E1 polarizability ratio values	105
5.4. Polarizability ratios of the $^{171}\text{Yb}^+$ clock transitions	111
5.5. Polarizability scale factors for $^{171}\text{Yb}^+$ in the MIR range	111
5.6. Absolute polarizabilities of the $^{171}\text{Yb}^+$ clock transitions	118
6.1. Systematic uncertainty budget	127

Acronyms and abbreviations

- 3D** Three Dimensions 64, 66, 70, 72, 138
- AC** Alternating Current 14, 51, 67, 69, 70, 72, 84, 133, 136, 142
- AOM** Acousto-Optic Modulator 6, 58, 61–63, 65, 76–81, 133, 141, 142
- AR** Anti-Reflection 65, 97
- ARTIQ** Advanced Real-Time Infrastructure for Quantum physics 54, 58, 65, 67
- BBR** Black Body Radiation 11–15, 86–92, 101–103, 105, 106, 116, 118, 123–125, 133–135, 142, 144, 147, 149–152
- BIPM** Bureau International des Poids et Mesures 4, 152
- CCTF** Consultative Committee for Time and Frequency 147, 153
- CEO** Carrier Envelope Offset 5, 6, 78
- DAC** Digital-to-Analog Converter 54, 67
- DC** Direct Current 13, 20, 23, 51–54, 67, 73, 86, 97, 101, 102, 104, 105, 108, 114, 119, 140
- DDS** Direct Digital Synthesis 53, 58, 65, 79
- DFB** Distributed Feedback 58, 60
- DSUB** D Subminiature 54
- E1** Electric Dipole 28–30, 34, 42, 44, 46, 49, 58, 86–88, 90, 91, 109
- E2** Electric Quadrupole 11, 13–15, 29, 37, 40–43, 45, 64, 65, 70, 75, 76, 87, 89, 90, 98, 100, 103–105, 108–110, 112–114, 116–124, 127, 149, 150
- E3** Electric Octupole 11–15, 29, 37, 40–43, 45, 51, 57, 58, 60, 64, 70, 75–78, 87, 89, 90, 93, 100, 104–110, 113, 114, 116–118, 122–124, 127, 135, 136, 142, 144, 146, 147, 149–153
- ECDL** External Cavity Diode Laser 51, 58, 60, 77, 78, 93
- EDFA** Erbium-Doped Fiber Amplifier 93
- EOM** Electrooptic Modulator 59, 61, 63, 64, 77, 78

Acronyms and abbreviations

- FEM** Finite Element Modelling 134
- FSR** Free Spectral Range 58
- GNSS** Global Navigation Satellite System 145, 146
- HWP** Half Waveplate 57, 58, 60–62
- M1** Magnetic Dipole 29, 42, 69, 70, 87, 107–109, 142
- M2** Magnetic Quadrupole 29
- MIR** Mid Infrared 11–14, 63, 65, 83, 89, 95, 98, 99, 102, 103, 105–109, 116, 118, 124, 151
- NA** Numerical Aperture 64, 65
- NIR** Near Infrared 11, 14, 25, 75, 76, 87, 93, 95, 100–102, 114
- NIST** National Institute of Science and Technology 3, 87
- NMI** National Metrology Institute 3, 127
- NPL** National Physics Laboratory 3, 101, 102, 114, 123, 146, 147
- NRC** National Research Council Canada 13, 15, 92, 102, 146, 147
- OPS** Optical Phase Stabilizer 80
- PBS** Polarizing Beam Splitter 57, 58, 60–62, 93, 94
- PCB** Printed Circuit Board 51, 52
- PDH** Pound-Drever-Hall 51, 77, 78
- PI** Proportional Integral 58, 78
- PID** Proportional Integral Derivative 78
- PM** Polarization Maintaining 57, 58, 60–62
- PMT** Photon Multiplier Tube 63, 64, 66, 120, 143
- PTB** Physikalisch Technische Bundesanstalt vii, 3, 10, 11, 13, 14, 51, 54, 58, 67, 75, 80, 93, 97, 101, 102, 114, 145, 146, 149
- QCL** Quantum Cascade Laser 97, 99, 100, 106–109, 116–118, 123
- QPN** Quantum Projection Noise 7, 8, 11, 142–144
- QUEST** Centre for Quantum Engineering and Space-Time Research 51
- QWP** Quarter Waveplate 58, 61, 62

- RAM** Residual Amplitude Modulation 78
- RF** Radio Frequency 13, 14, 23, 28, 52–54, 69–72, 78, 79, 83, 91, 101–105, 119, 123, 125, 129, 133–137, 139–141, 144, 145, 150–152
- RMS** Root Mean Square 9, 96, 100, 106, 112, 137, 138, 140
- SI** Système International d’Unités 3–6, 9
- SNR** Signal-to-Noise Ratio 7, 80
- TA** Tapered Amplifier 51, 79, 81
- TAI** Temps Atomique International 146, 147
- UHV** Ultra High Vacuum 51
- ULE** Ultra Low Expansion glass 75
- VCO** Voltage Controlled Oscillator 80
- VTT** VTT Technical Research Centre of Finland 13, 92, 102, 145–147

1. Introduction to optical atomic clocks and this thesis

Time is one of the most fundamental parts of the physical description of our universe. While Albert Einstein has revealed within the framework of special and general relativity that space and time are emergent phenomena of one malleable spacetime [Ein05; Ein16], in day to day life we experience the progress of time as proceeding at a constant rate everywhere. For this reason, our unit of time, the *second*, is at the center of the *Système International d'Unités* (SI) [BIP19] and enters into the calculation of most other units in it as is shown in Fig. 1.1. It is defined by fixing *the unperturbed ground state hyperfine transition frequency of the caesium 133 atom* $\Delta\nu_{Cs}$ to [BIP19]

$$\Delta\nu_{Cs} = 9\,192\,631\,770/\text{s} = 9\,192\,631\,770\text{ Hz}, \quad (1.1)$$

where the unit Hz is defined as the reciprocal second. Since this number defines the unit, it has no uncertainty. Every frequency or time measured with an instrument needs to refer back to this number in some way, to be consistent with the SI. For this reason, National Metrology Institute (NMI)s around the world such as PTB in Germany [Bau05; Wey+18], National Institute of Science and Technology (NIST) in the United States of America [Hot+23] and National Physics Laboratory (NPL) in the United Kingdom [Szy+16] operate caesium clocks, so called *primary standards*, that realize the SI second.

Even though the definition of the second is free of uncertainty, its realizations are not. For example, electromagnetic fields at the position of the caesium atoms change the energy difference of the hyperfine states, causing the observed transition frequency to differ from the unperturbed reference $\Delta\nu_{Cs}$. The magnitude of these perturbations has to be quantified, which is only possible with finite accuracy, limiting the overall uncertainty of the primary frequency standard. The best-performing caesium clocks [Szy+16; Wey+18; Hot+23; Bea+25] reach a fractional uncertainty of around 1×10^{-16} , which corresponds to a frequency uncertainty of 1 μHz .

On the other hand, optical frequency standards already reach below a fractional uncertainty of 1×10^{-18} [Bre+19; Aep+24; Mar+25b], primarily because they operate at a higher frequency of 100-1000 THz, making them more insensitive to any frequency shifts not proportional to the optical frequency itself. They are based

1. Introduction to optical atomic clocks and this thesis

on transitions from the atomic ground state to a long-lived excited state that are driven with laser radiation. For this reason, a change of the definition of the second in the SI is proposed, to refer the second to one or multiple optical transitions [Dim+24]. This would allow for absolute frequency measurements with significantly smaller uncertainty, but requires reproducible and reliable operation of optical frequency standards [Dim+24]. Nevertheless, already today a selection of optical transitions are recognized as *secondary* realizations of the second with frequency values determined from previous measurements against Cs clocks and frequency ratio measurements between optical standards [Mar+24]. These *recommended values of standard frequencies* are reviewed and updated on a regular basis by the Bureau International des Poids et Mesures (BIPM), the last update at time of writing was performed in 2021 [Mar+24].

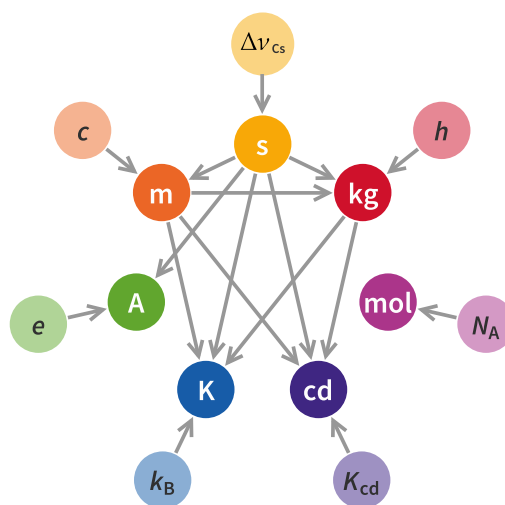


Figure 1.1.: *Unit relations in the new SI. The base units of the SI are the second (s), kilogram (kg), mole (mol), Candela (cd), Kelvin (K), Ampere (A) and meter (m). They are defined by fixing the values of various constants in nature, the caesium hyperfine frequency ($\Delta\nu_{Cs}$), Planck constant (h), Avogadro constant (N_A), luminous efficacy of a defined visible radiation (K_{cd}), Boltzmann constant (k_B), elementary charge (e) and speed of light in vacuum (c), respectively [BIP19]. The arrows indicate whether a unit is used to define another unit in the system in combination with the defining constant. Out of all of these, only the second and the mole are purely dependent on their defining constants and the second is a part of every other unit in the system, except for the mole. Image source: [Pis20]*

From a top level view, an optical frequency standard consists of the following elements, which are sketched in Fig. 1.2:

1. Local oscillator: A laser with high short-term (< 10 s) frequency stability provided by an ultrastable resonator [Mat+17]. It can be adjusted in its

frequency with electronic and optical elements and is sent to the atomic reference and frequency comb.

2. Atomic reference: The atom which contains the optical reference transition, that is used as the basis for the optical frequency standard. The local oscillator frequency is compared with the reference and adjusted such that it is on resonance with the atomic transition. This stabilizes the local oscillator long-term (> 100 s) to a natural constant, the atomic transition frequency.
3. Frequency comb: The frequency of the local oscillator is measured at the frequency comb [YC05; FB19]. It consists of a fs-pulsed laser with an actively stabilized repetition rate and Carrier Envelope Offset (CEO). By employing supercontinuum generation in optical fibers [BWR00], a spectrum spanning at least one frequency octave ($\nu_{\max} \geq 2\nu_{\min}$) in the optical range is produced, consisting of narrow peaks spaced by the repetition rate. Since the repetition rate and CEO are referenced to the SI second via a caesium fountain clock, this allows for absolute measurements of the local oscillator frequency and consequently atomic transition frequency.

An optical *clock* is strictly speaking a continuously operating optical frequency standard counting cycles from a set initialization time onwards [MS21]. The optical frequency standard discussed in this thesis was not operated in this fashion. In practice, the terminology is used more or less interchangeably, so many optical frequency standards are called optical clocks even though they provide no time signal.

1. Introduction to optical atomic clocks and this thesis

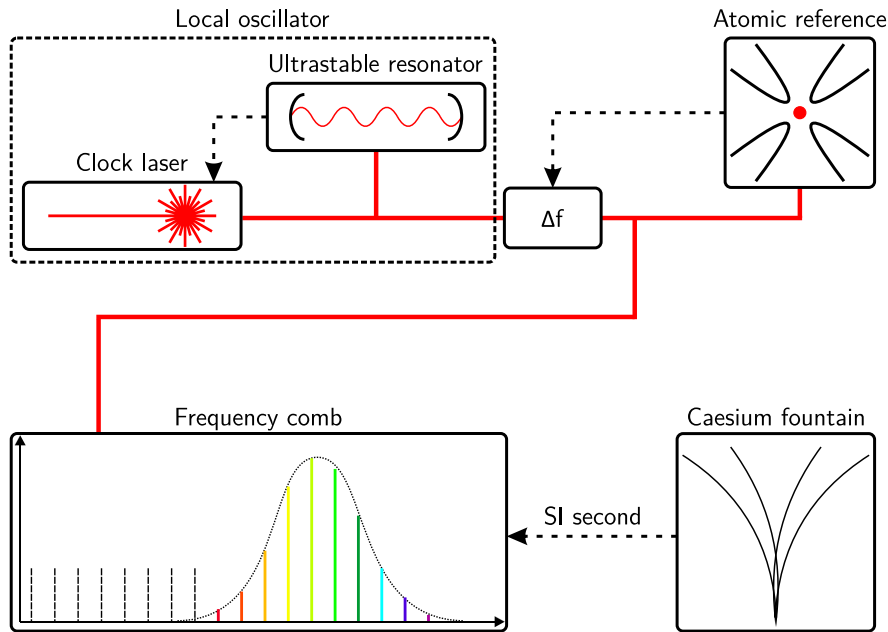


Figure 1.2.: Overview over the elements of an optical clock. An optical clock combines several elements in order to allow for frequency comparisons with the current primary realization of the SI second. A clock laser with adjustable frequency emits radiation shown in red that is sent to an ultrastable resonator or cavity [Mat+17]. This pair of mirrors is spaced apart at a distance that changes very slowly and transmits light in a narrow frequency range repeating every free spectral range. By measuring the reflection of the laser from the resonator, the frequency of the clock laser is stabilized to the cavity length, indicated by the dashed arrow. This produces a laser with high frequency stability on short (<10 s) time scales [Mat+17], called the local oscillator. The light passes through an optical element that can change the oscillator frequency by Δf , such as an Acousto-Optic Modulator (AOM), and is distributed to two elements: The laser light is sent to 1. the atomic reference, where its frequency deviation from the atomic transition is determined. The frequency offset Δf is adjusted repeatedly such that the oscillator is on resonance with the atomic reference transition, 2. to a frequency comb [YC05; FB19]. This fs-pulsed laser is referenced in its properties (the repetition rate f_{rep} and CEO f_{ceo}) to the SI second, which is provided by a Caesium fountain clock [Wey+18; Hot+23; Szy+16; Bea+25]. By measuring f_{rep} and f_{ceo} as well as determining the frequency offset of the laser from the m -th comb tooth Δf , the absolute frequency $\nu = m \cdot f_{\text{rep}} + f_{\text{ceo}} + \Delta f$ of the local oscillator stabilized to the atomic reference is measured with the comb. Frequency comb image source (modified): [Har06]

1.1. Figures of merit: Stability and accuracy

Two figures of merit are central to the performance of an optical clock: the *instability* and the *accuracy* of the frequency output. On an abstract level, the instability quantifies what the noise properties of the clock are, how the clock frequency $\nu(t)$ varies over time. The accuracy is equal to the uncertainty of the overall clock frequency offset from the unperturbed reference quantity.

Stability The frequency of an optical clock varies because of fundamental effects such as Quantum Projection Noise (QPN) or the uncontrolled changes of experimental conditions. To compare clocks at different frequencies on equal footing, the *fractional deviation from the mean* $y(t) = \nu(t)/\bar{\nu} - 1$ is computed. Then the *Allan deviation* $\sigma_y(\tau)$ [All66; RH08] of M time-averaged frequency samples $y_j(\tau) = \langle y(t) \rangle_{\tau, j}$, $1 \leq j \leq M$ with averaging time τ is defined as

$$\sigma_y(\tau) = \sqrt{\sigma_y^2(\tau)} = \sqrt{\frac{1}{2(M-1)} \sum_{j=1}^{M-1} (y_{j+1}(\tau) - y_j(\tau))^2} \quad (1.2)$$

and quantifies the instability for a given averaging time. The intuitive meaning of the Allan deviation is that the frequency output $\nu(t)$ averaged over the time τ varies within $\sigma_y(\tau)$. The statistical uncertainty of the mean frequency $\bar{\nu}$ of a measurement lasting a time T is $\sigma_y(T)$. The advantage of the Allan deviation over e.g. the standard error of the mean $\bar{\sigma}$ is that $\sigma_y(\tau)$ is properly defined and converges for a broad variety of noise spectra, for which $\bar{\sigma}$ diverges [All66; RH08]. The effect of noise sources with different spectral content on the Allan deviation is depicted in Fig. 1.3.

A fundamental type of noise relevant for optical clocks is QPN. As is described in Section 2.4 in more detail, the measurement involved with the operation of the clock projects the quantum state $|\psi\rangle = a|g\rangle + b|e\rangle$ into either the ground state $|g\rangle$ or excited state $|e\rangle$. This projection introduces white noise to the frequency signal with a magnitude related to the linewidth of the transition $\delta\nu$ and cycle time t_C until the clock transition is interrogated again [PST05]. This results in the Allan deviation of a clock purely limited by QPN of [PST05]

$$\sigma_y(\tau) = C_0 \frac{\delta\nu}{\bar{\nu}} \sqrt{\frac{t_C}{\tau}}, \quad (1.3)$$

where C_0 encapsulates the Signal-to-Noise Ratio (SNR) of the measurement and depends on the precise interrogation scheme of the clock [PST05]. This shows that narrow linewidths and short cycle times (up to the Fourier limit relating linewidth and interrogation time) are necessary to minimize QPN and reduce the

1. Introduction to optical atomic clocks and this thesis

measurement time τ to reach a given uncertainty of the clock frequency. For the clock discussed in this thesis, QPN is the dominant contribution to the total noise, but clocks can also be limited by their cycle time (resulting in *Dick* noise [Lud+15]) or show more complex noise components such as frequency drifts or flicker noise. One important caveat is that the instability of a clock cannot be measured without a reference oscillator. So, the instability of a frequency ratio $\mathcal{R} = \nu_1/\nu_2$ between two clocks with frequencies ν_1 and ν_2 is measured, instead. The Allan deviation of \mathcal{R} is then dominated by the more unstable clock or minimally a factor of $\sqrt{2}$ higher than the single clock instability, if both of them contribute equally to σ_y . Since the Allan deviation of white frequency noise decreases with larger averaging times, the instability is commonly reported as $\sigma_y(1\text{ s})$. The current record instability is around $\sigma_y(1\text{ s}) = 50 \times 10^{-18}$ [Oel+19; Sch+20] for optical clocks, while comparisons between systems sharing the same clock lasers reach $\sigma_y(1\text{ s}) = 1.5 \times 10^{-18}$ nowadays [Kim+25].

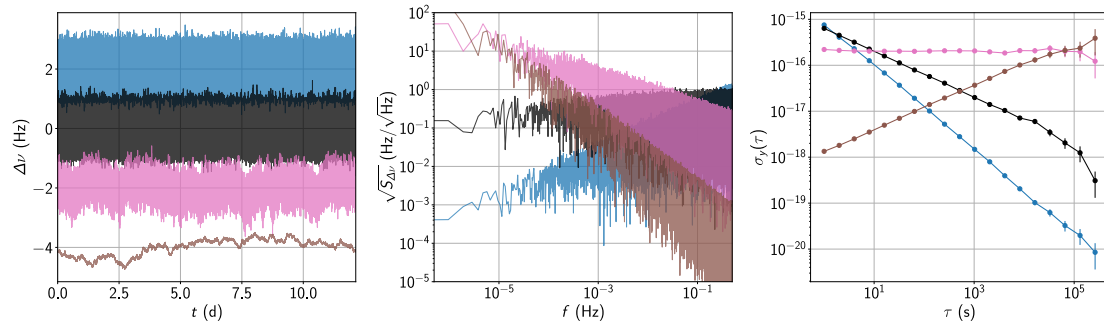


Figure 1.3.: Comparison of the Allan deviation for different noise sources. Flicker phase noise (blue), white frequency noise (black), flicker frequency noise (pink) and random walk frequency noise (brown) lead to different behaviour of the Allan deviation $\sigma_y(\tau)$ with respect to the averaging time τ . This is shown here for computer-generated noise with an amplitude of 1 Hz on an optical standard with a mean frequency of 500 THz. The sampled data on the left is offset from the mean by a multiple of 2 Hz for each noise type to compare them more easily. The figure in the middle shows the spectral density amplitude $\sqrt{S_{\Delta\nu}}$ of the noise, which shows particular slopes for each noise type. White frequency has the same amplitude at each frequency f , blue noise has a lower amplitude at lower frequencies. Pink and brown noise show the opposite behaviour, their amplitude increases at smaller f . The right figure shows the Allan deviation for several averaging times of the individual noise samples. The Allan deviation of white and blue noise decrease for larger τ , allowing for more precise determinations of the mean frequency by increasing the measurement time. Pink and brown noise on the other hand do not decrease and ultimately correspond to a variation of the center frequency, which limits the overall uncertainty for long measurement times. For a real frequency standard, a weighted combination of all these noise types is observed.

Accuracy The goal of an optical frequency standard is to reproduce an unperturbed atomic transition frequency ν_0 . This is a constant of nature determined from fundamental parameters such as the fine-structure constant. Various effects cause the observed frequency to differ from the unperturbed case, e.g. electromagnetic fields, the Doppler effect caused by movement of the atom and collisions of the clock atom with other atoms [Lud+15]. All of these effects are measured or calculated and an appropriate correction $\Delta\nu$ is applied to the clock frequency to produce the unperturbed value. The uncertainty $u(\Delta\nu)$ with which $\Delta\nu$ can be determined limits the overall uncertainty $u(\nu_0)$ of the unperturbed frequency. It is usually called the *systematic uncertainty* and reported as the fractional value $u(\Delta\nu)/\nu_0$. The lowest reported systematic uncertainty to date is 5.5×10^{-19} [Mar+25b]. One important systematic uncertainty is that of the best caesium fountain clocks of around 1×10^{-16} [Wey+18; Hot+23; Szy+16; Bea+25]. Since the SI unit Hz is defined with reference to the Cs transition, this is also the systematic uncertainty limit of all absolute frequency measurements, unless measurements are performed against a large ensemble of independent Cs clocks. In that case, uncorrelated systematic frequency shifts can be assumed to be independent and normally distributed, which allows for a reduction of the systematic uncertainty below the limit of any particular clock.

Frequency measurements always have to be performed with respect to another clock that provides the reference. This means that one measures a frequency ratio $\mathcal{R} = \nu_1/\nu_2$ with the frequencies ν_1 and ν_2 of clocks 1 and 2 respectively. An absolute frequency measurement refers to the special case that one of the clocks is a caesium clock. This means that the total fractional uncertainty u_{tot} of an optical frequency ratio measurement is the Root Mean Square (RMS) of the individual fractional clock uncertainties u_1 and u_2

$$u_{\text{tot}} = \frac{u(\mathcal{R})}{\mathcal{R}} = \sqrt{u_1^2 + u_2^2} = \sqrt{\left(\frac{u(\nu_1)}{\nu_1}\right)^2 + \left(\frac{u(\nu_2)}{\nu_2}\right)^2}. \quad (1.4)$$

The individual uncertainties u_j are the RMS of the fractional statistical uncertainty $u_{\text{stat},j}$ and the fractional systematic uncertainty $u_{\text{sys},j}$ of each individual clock

$$u_j = \frac{u(\bar{\nu}_j)}{\nu_{0,j}} = \sqrt{u_{\text{stat},j}^2 + u_{\text{sys},j}^2}. \quad (1.5)$$

Consequently, the uncertainty of \mathcal{R} is limited by the combined systematic uncertainty of both clocks and requires sufficiently large averaging times to reduce the statistical uncertainty of both clocks below the systematic limit. This informs the different types of optical clocks, their advantages, disadvantages and specific properties.

Types of optical clocks At PTB multiple optical frequency standards have been and are in operation [SPT05; Fal+11; Hun+16; San+19; Han+19b; Sch+20; Stu+21; Lan21; Ste+23; Hau+25; Nos+25]. They can be divided in roughly three categories, all of which have their advantages and disadvantages in terms of stability and accuracy:

1. Neutral atom clocks [Fal+11; Sch+20; Nos+25]: The atoms, which possess the optical reference transition, remain uncharged and are trapped with high-intensity laser radiation. This results in a large number of atoms being interrogated at once and consequently a high stability of the output frequency [Kat+03]. But the atoms are experiencing a large electromagnetic field which may shift the unperturbed frequency significantly. To minimize this effect, a trapping laser wavelength is chosen that shifts the energy of both the ground and excited state by the same amount, causing a differential frequency shift of 0 Hz [Kat+03]. These optical clocks are not covered further in this thesis, a review on them is contained in [Lud+15].
2. Single ion clocks [SPT05; Hun+16; San+19; Han+19b; Stu+21; Lan21; Ste+23]: A single charged atom, an ion, is interrogated in a trap of oscillating electromagnetic fields, a Paul trap [Pau90]. The ion resides in a largely field-free environment, causing only small frequency shifts. On the other hand, only a single ion is interrogated repeatedly, which results in a comparatively high instability [PST05]. Compared to neutral clocks, this results in long averaging times to reach a given frequency uncertainty.
3. Multi ion clocks [Ste+23; Hau+25]: Similiar to single ion clocks, the same trapping mechanism is used. But multiple ions are trapped within the same potential and interrogated simultaneously [Pre+92]. This reduces the averaging time proportional to the number of ions to reach a given statistical uncertainty, but care needs to be taken that all ions are affected by electric and magnetic fields sufficiently homogeneously. The idea of a microwave multi-ion clock using a linear ion trap was first proposed in 1992 [Pre+92]. Multi-ion clocks using optical transitions started to be developed from 2012 onwards [Her+12] and are currently starting to be employed in frequency ratio measurements [Kel+19; Ste+23; Hau+25]. They operate in a middle ground between neutral atom and single ion clocks, the stability is significantly better compared to single ion systems even for a moderate (around 10) amount of ions and the ions are still trapped without any large electromagnetic fields.

Specifically in the group *Optical clocks with trapped ions* at PTB, where I did the work for this thesis, three generations of single-ion $^{171}\text{Yb}^+$ clocks *Yb1* [SPT05; Hun+16], *Yb2* [San+19] and *Yb3* [Lan21] have been developed and operated. They were employed in absolute frequency measurements of the $^{171}\text{Yb}^+$ clock transitions [Tam+09; Hun+12; Lan+21a], optical frequency comparisons between $^{171}\text{Yb}^+$ clock transitions in the same and different experiments [San+19; Lan+21a], international

clock comparison campaigns [Lin+25c], Lorentz symmetry tests [San+19], investigation of the variation of fundamental constants [Lan+21a; Fil+23] and searches for dark matter [Fil+23]. Also, novel schemes to determine the excited state lifetime of the $^{171}\text{Yb}^+$ Electric Octupole (E3) transition [Lan+21b], compensate tensorial [Lan+20] and clock-laser induced [San+18] frequency shifts as well as differential polarizability measurements [Hun+16] were developed and implemented in these systems. Additionally, a collaborative project with partners from industry led to the development of *Opticlock*, a single-ion, compact, transportable $^{171}\text{Yb}^+$ clock [Stu+21]. All of these systems only trap and interrogate a single ion of a single species, but there are some key advantages to a multi-ion, multi-species optical clock.

The limiting systematic uncertainty for these single ion clocks operating at room temperature is the knowledge of the differential polarizability $\Delta\alpha$ [San+18; Lan21; Tof+24]. This quantity is the proportionality constant between the Black Body Radiation (BBR) temperature and the frequency shift induced by thermal electromagnetic fields. It is known with a fractional uncertainty of approximately 2% [Hun+16; Bay+20] from measurements with intensity-calibrated Near Infrared (NIR) and Mid Infrared (MIR) lasers. This limits the BBR shift uncertainty to a fractional value of 28×10^{-18} and 1.5×10^{-18} for the Electric Quadrupole (E2) and E3 transition, respectively and precludes the optical clocks based on $^{171}\text{Yb}^+$ from reaching the 10^{-19} uncertainty regime. Overcoming this limitation is one of the primary objectives of the multi-species clock discussed in this thesis.

1.2. Multi-species, multi-ion optical clocks

This thesis focuses on the first multi-species, multi-ion optical frequency standard in group *Optical clocks with trapped ions* at PTB called *YbSr1*. In this system, single or multiple $^{171}\text{Yb}^+$ and $^{88}\text{Sr}^+$ ions can be used as the reference for single-ion or multi-ion optical clocks. This provides the following advantages over a single-ion, single-species system.

Stability improvement with multi-ion clocks As mentioned in the previous section, interrogating multiple ions of the same type simultaneously reduces the instability of the optical clock. QPN is independent for each ion, so the average over all N ions reduces the instability by a factor of \sqrt{N} compared to the single ion stability $\sigma_{y,1}(\tau)$ [Rie06]

$$\sigma_{y,N}(\tau) = \frac{\sigma_{y,1}(\tau)}{\sqrt{N}} \quad (1.6)$$

under the assumption that each ion contributes equally to the mean clock frequency.

1. Introduction to optical atomic clocks and this thesis

Since the Allan deviation reduces with $\sqrt{\tau}$, if it is dominated by white noise, the time T to reach a given statistical uncertainty u_{stat} scales with N

$$T = \frac{1}{N} \frac{\sigma_{y,1}^2(1\text{ s})}{u_{\text{stat}}^2} \text{s}, \quad (1.7)$$

so 10 ions reduce the averaging time by an order of magnitude. For single-ion clocks based on the E3 transition of $^{171}\text{Yb}^+$, instabilities of $\sigma_y(1\text{ s}) = 1 \times 10^{-15}$ are typical [Dör+21]. To reach a statistical uncertainty of 0.1×10^{-18} requires $10^8\text{s} \approx 3\text{ yr}$ of averaging time, so reducing the measurement time to months in a multi-ion clock is a significant improvement. For this reason, I built up the first multi-ion optical clock in the group *Optical clocks based on trapped ions* to gain knowledge with multi-ion traps, interrogation sequences for multiple ions and perform first measurements with ion chains. These results inform and support the next-generation system *YbSr2* focused on multi-ion clock operation.

Sensitivity to new physics Optical clocks are used to investigate fundamental physics, such as variations of fundamental constants over time [Pei+04; God+14; Hun+14; Lan+21a; Fil+23; She+23], dark matter [Col+21; Fil+23; She+23] and Lorentz invariance [San+19]. These measurements typically rely on the fact that different clock transitions have different frequency sensitivities with respect to parameters such as the fine-structure constant α [God+14; Lan+21a; Fil+23] or orientation of the excited state wavefunction in space [San+19]. While these measurements can be and are performed between separate optical clocks, this requires that any non-fundamental effects, such as temperature and magnetic field variations, are sufficiently well under control to not mask the quantity being investigated. In a multi-species system, these perturbing effects are mostly common to both clocks, since their distance from each other is typically on the μm scale. This heavily relaxes the requirement on control of external perturbations and allows for more accurate investigations of new physics effects.

Sensitivity to external perturbations Multi-species clocks have an advantage over single species clocks with respect to their accuracy. Often, the frequency shift induced by external perturbations has to be measured, relying on specific properties of the ion species interrogated. For example, the differential polarizability $\Delta\alpha$ of the clock transition is known with significantly different fractional uncertainty for $^{88}\text{Sr}^+$ (0.04% [Dub+14; Lin+25b]) and $^{171}\text{Yb}^+$ (2% [Hun+16; Bay+20]). This allows for calibration of MIR laser intensities with $^{88}\text{Sr}^+$ and the reduction of the uncertainty of $\Delta\alpha$ for $^{171}\text{Yb}^+$ using the calibrated intensity. This has the potential to reduce the fractional BBR frequency shift uncertainty at room temperature below 10^{-19} for the $^{171}\text{Yb}^+$ E3 clock transition.

1.3. Key results and structure of the thesis

The thesis concerns the setup and operation of the optical clock *YbSr1* in the group *Optical clocks with trapped ions* at PTB. Key results of this work are

- a measurement of the $^{88}\text{Sr}^+ / ^{171}\text{Yb}^+$, E3 optical frequency ratio with a fractional uncertainty of 23×10^{-18} and a direct determination of the trap-induced BBR shift. This allows for calculation of the $^{88}\text{Sr}^+$ absolute frequency limited by the systematic uncertainty of Cs clocks [Wey+18; Lan+21a] and a value inconsistent with the recommended frequency as a secondary representation of the second [Mar+24] is found. This result is corroborated by recent determinations of the same quantity by National Research Council Canada (NRC) [Mar+25a] and VTT Technical Research Centre of Finland (VTT) [Lin+25a], supporting an adjustment of the recommended frequency of the $^{88}\text{Sr}^+$ clock transition [Mar+24].
- the first direct observation of the instability reduction due to multi-ion operation of an optical clock. Three $^{88}\text{Sr}^+$ ions show a significantly reduced instability, limited by the spatially non-resolved state detection mechanism, and the resulting frequency agrees with the single-ion result.
- a measurement of the magic wavelength of the $^{88}\text{Sr}^+$ clock transition differential polarizability around 1550 nm, which is consistent with theory. This allows for a more accurate determination of the dynamic correction of the BBR shift and in general interpolation of the differential polarizability between the magic wavelength and the Direct Current (DC) value [Dub+14; Lin+25b].
- a direct optical intensity-based measurements of the $^{88}\text{Sr}^+$ differential polarizability at a perturbing wavelength of 10.6 μm and 8.5 μm , relevant for the BBR shift at room temperature. These measurements show a consistent offset of the same quantity from the measurements using the trap Radio Frequency (RF) field [Dub+14; Lin+25b]. This persists across different perturbing wavelengths as well as experimental implementations and agrees with the corresponding values of the $^{171}\text{Yb}^+$ clock transitions.
- a polarizability transfer measurement employing MIR lasers to reduce the differential polarizability uncertainty and consequently the BBR shift uncertainty for the $^{171}\text{Yb}^+$ clock transitions. With the currently acquired data, this allows for a fractional BBR shift uncertainty of 0.84×10^{-18} on the E2 transition and 0.24×10^{-18} for the E3 transition, but changes the magnitude of the BBR shift by 4σ and more than 5σ , respectively. This is due to the discrepancy observed between the differential polarizability of $^{88}\text{Sr}^+$ for optical and RF fields mentioned in the previous bullet point. Nonetheless, this result allows for the operation of $^{171}\text{Yb}^+$ clocks with an overall uncertainty below 10^{-18} , if the discrepancy is resolved and the uncertainty of the $^{88}\text{Sr}^+$

polarizability does not increase significantly.

The thesis is structured as follows:

1. Chapter 1 (this chapter) contains an overview of optical clocks, their general operation, key figures of merit and scientific achievements. In particular, the previous work in the group *Optical clocks with trapped ions* at PTB and the advantages of multi-species, multi-ion clocks are summarized, as they serve as the background on which this work rests.
2. Chapter 2 contains an overview of the theoretical background on ion trapping, cooling and clock spectroscopy. Also the electronic structure of $^{88}\text{Sr}^+$ and $^{171}\text{Yb}^+$ and the coupling between electromagnetic radiation and the ion states relevant for this thesis are discussed. A greater emphasis is given to state initialization for both species, the effect of ion motion on spectroscopy and sub-Doppler cooling as well as heating rate measurements.
3. Chapter 3 contains the experimental setup of the ion trap, cooling lasers, clock lasers and detection optics. The magnetic field perturbing the ions is investigated in more detail. On the one hand, the decay of the magnetic field applied during cooling of $^{171}\text{Yb}^+$ is measured to estimate its effect on other results in this thesis. On the other hand, the Alternating Current (AC) magnetic field induced by the trap RF drive is measured using the Autler-Townes method discussed in [Gan+18] to determine its contribution to the overall clock uncertainties.
4. Chapter 4 contains the theoretical background on the quadratic Stark shift of the clock transitions and direct measurements of the differential polarizability with NIR and MIR lasers. The effect of BBR and its parametrization is discussed in greater detail to correctly infer the BBR shift from single-wavelength polarizability measurements. The magic wavelength measurement of $^{88}\text{Sr}^+$ in the NIR is presented, which allows for a smaller uncertainty of the dynamic correction of the BBR shift and interpolation of polarizability values in the MIR region. Also, direct measurements of the polarizability using MIR lasers are shown and reveal a consistent discrepancy compared with the RF-based values from [Dub+14; Lin+25b]. The source of this discrepancy needs to be investigated further to determine which value is correct for the evaluation of the BBR shift.
5. Chapter 5 contains the polarizability ratio measurements for the scalar and tensorial polarizabilities of the $^{88}\text{Sr}^+$ and $^{171}\text{Yb}^+$ clock transitions. These ratios are in agreement with previous determinations [SPT05; Hun14; Hun+16; Bay+20] of the same quantities of the $^{171}\text{Yb}^+$ transitions at a significantly reduced uncertainty. The transfer measurement between $^{88}\text{Sr}^+$ and $^{171}\text{Yb}^+$ allows for a reduction of the BBR shift uncertainty at room temperature to 0.84×10^{-18} and 0.24×10^{-18} for the E2 and E3 transition, respectively. But due to the discrepancy found in chapter 4, the BBR shift changes by 4σ

for the E2 transition and more than 5σ for the E3 transition.

6. Chapter 6 contains the measurement of the optical frequency ratio between the $^{88}\text{Sr}^+$ and $^{171}\text{Yb}^+$, E3 clocks with a fractional uncertainty of 23×10^{-18} . Of particular note are the method to determine the trap-induced BBR shift and operation of the system as a multi-ion clock. The optical frequency ratio in combination with the absolute E3 frequency in [Lan+21a] allow for a determination of the $^{88}\text{Sr}^+$ clock frequency with a fractional uncertainty of 1.3×10^{-16} , limited by the uncertainty of the Cs fountain clock [Wey+18]. This absolute frequency supports a discrepancy of the clock frequency from the recommended value [Mar+24] already observed at NRC [Jia+22]. The content of this chapter is largely published in [Ste+23].
7. Chapter 7 contains the summary of the thesis and an outlook on future measurements regarding multi-ion clocks and polarizability measurements.

2. Optical clocks based on trapped ions

To repeatedly interrogate clock transitions found in ions, it is necessary to confine them in a region in space (*trap* the ions) and to remove the motional energy they gain from interactions with the environment (*cool* the ions). For both purposes, understanding the motional dynamics of a single or multiple ions in oscillating electric fields, a *Paul trap*, is required. Once the ions are trapped and cooled, coherent interaction between laser radiation close to resonance with the clock transition is possible. The electronic structure of $^{88}\text{Sr}^+$ and $^{171}\text{Yb}^+$, effects of ion motion on coherent spectroscopy, state initialization and sub-Doppler cooling are discussed.

2.1. Trapping a charged particle with electromagnetic fields

In classical physics, a particle possessing a charge q and rest mass m , travelling with the velocity \vec{v} , experiences a force \vec{F}_L caused by electric fields \vec{E} and magnetic fields \vec{B} according to the *Lorentz force law* [Lor02]

$$m\vec{a} = \vec{F}_L = \frac{d\vec{p}}{dt} = q(\vec{E} + \vec{v} \times \vec{B}), \quad (2.1)$$

where \vec{a} is the acceleration of the charged particle and \vec{p} is its classical momentum $\vec{p} = m\vec{v}$. In relativistic physics, the classical momentum \vec{p} is replaced by the relativistic momentum $\vec{p}_R = \gamma(|\vec{v}|)\vec{p}$ [KK73, p. 492] and the coordinate time dt is related to the proper time $d\tau = \gamma(|\vec{v}|) dt$ by the Lorentz factor [KK73, p. 500]

$$\gamma(|\vec{v}|) = \frac{1}{\sqrt{1 - (|\vec{v}|/c)^2}}. \quad (2.2)$$

Confining a particle in a finite region of space is equivalent to realizing a field configuration with a stable minimum of the corresponding electromagnetic potential (φ, \vec{A}) , where the potentials and fields are related via [Dem12, p. 137]

2. Optical clocks based on trapped ions

$$\vec{E} = -\vec{\nabla}\varphi - \frac{\partial}{\partial t}\vec{A}, \quad \vec{B} = \vec{\nabla} \times \vec{A}. \quad (2.3)$$

It is shown in [Ear39] that a static electric field \vec{E} on its own cannot fulfill this stability condition, which is known as *Earnshaw's theorem*. For this reason, either a time-varying field $\vec{E}(t)$ or an additional static magnetic field \vec{B} is necessary to realize a stable configuration. Devices that use the latter approach are called *Penning traps* and are employed in a variety of fundamental experiments in physics [Sai+22; And+23; Sas+23].

In this thesis, I employ on the first approach: generating a time-varying electric field $\vec{E}(t)$ (and corresponding induced magnetic field $\vec{B}(t)$) to produce a time-averaged, effective potential $(\varphi_{\text{eff}}, \vec{A}_{\text{eff}})$ that features a stable minimum for the charged particle. Devices operating on this principle are called *Paul traps* [Pau90] and are a versatile technology used in fundamental research [Cai+17; Pat+20], quantum information applications [Boc+18; Fig+19; Nad+22] and public outreach [MH22].

The following derivations are based on the review on particle motion in Paul traps [Lei+03]. For the sake of specificity, let us consider the case of a single atomic ion with charge q and mass m residing in a harmonic electric potential

$$\begin{aligned} \varphi(x, y, z, t) &= \varphi_{\text{dc}}(x, y, z) + \varphi_{\text{rf}}(x, y, z, t) & (2.4) \\ &= \frac{1}{2}U_{\text{dc}}(k_x x^2 + k_y y^2 + k_z z^2) + \frac{1}{2}U_{\text{rf}} \cos(\Omega_{\text{rf}} t)(c_x x^2 + c_y y^2 + c_z z^2) & (2.5) \end{aligned}$$

where U_{dc} is the amplitude of the static potential φ_{dc} , U_{rf} is the amplitude of the time-varying (or dynamic) potential φ_{rf} and Ω_{rf} is the angular frequency of the dynamic potential. The factors $k_{x,y,z}$ and $c_{x,y,z}$ specify the geometry with respect to the spatial coordinates (x, y, z) of the static and dynamic potential respectively. The Laplace equation

$$\nabla^2 \varphi(x, y, z, t) = \left(\frac{\partial^2}{\partial x^2} + \frac{\partial^2}{\partial y^2} + \frac{\partial^2}{\partial z^2} \right) \varphi(x, y, z, t) = 0 \quad \forall x, y, z, t, \quad (2.6)$$

which is derived from Maxwell's equations for electromagnetic fields in free space, imposes restrictions on the geometric factors, which represents a specific case of Earnshaw's theorem

$$k_x + k_y + k_z = 0 \quad (2.7)$$

$$c_x + c_y + c_z = 0 \quad (2.8)$$

2.1. Trapping a charged particle with electromagnetic fields

and shows explicitly that pure static confinement ($k_x, k_y, k_z > 0$, $c_x = c_y = c_z = 0$) is impossible.

While it is possible to trap ions purely with dynamic fields, corresponding to the case $U_{\text{dc}} \equiv 0$, the relevant case for the work in this thesis is static confinement along one axis (arbitrarily chosen as z) and dynamical confinement across the remaining two axes (arbitrarily chosen as x and y). This leads to the following relations for the geometric factors

$$k_z = -(k_x + k_y) > 0 \quad (2.9)$$

$$c_z = 0 \quad (2.10)$$

$$c_x = -c_y \quad (2.11)$$

to achieve a stable equilibrium for the motion of a positively charged ion. To derive the equations of motion for the ion, the electric field $\vec{E}(x, y, z, t)$ is calculated from Eq. (2.3) and Eq. (2.6) to be

$$\vec{E}(x, y, z, t) = -U_{\text{dc}} \begin{pmatrix} k_x x \\ k_y y \\ k_z z \end{pmatrix} - U_{\text{rf}} \cos(\Omega_{\text{rf}} t) \begin{pmatrix} c_x x \\ c_y y \\ c_z z \end{pmatrix}. \quad (2.12)$$

The set of differential equations describing the ion motion follows from the application of Eq. (2.1) to Eq. (2.12)

$$\frac{d^2}{dt^2} \begin{pmatrix} x \\ y \\ z \end{pmatrix} = -\frac{q}{m} U_{\text{dc}} \begin{pmatrix} k_x x \\ k_y y \\ k_z z \end{pmatrix} - \frac{q}{m} U_{\text{rf}} \cos(\Omega_{\text{rf}} t) \begin{pmatrix} c_x x \\ c_y y \\ c_z z \end{pmatrix} \quad (2.13)$$

and are three independent differential equations of second order with explicit time dependence. For this reason, the solution can be studied for an arbitrary direction of motion r_j and the constraints Eq. (2.9) to Eq. (2.11) are applied later on.

With the substitutions

$$\xi = \frac{1}{2} \Omega_{\text{rf}} t, \quad a_j = \frac{4qU_{\text{dc}}}{m\Omega_{\text{rf}}^2} k_j, \quad q_j = -\frac{2qU_{\text{rf}}}{m\Omega_{\text{rf}}^2} c_j \quad (2.14)$$

Eq. (2.13) takes the shape of a *Mathieu equation* [Mat68]

$$\frac{d^2}{d\xi^2} r_j + (a_j - 2q_j \cos(2\xi)) r_j = 0, \quad (2.15)$$

2. Optical clocks based on trapped ions

which is a well-studied differential equation with known non-analytic solutions [KRM18]. Of particular interest are the regions in the parameter space of a_j and q_j , where stable orbits are found, i. e. solutions for which the coordinate r_j stays bounded for all generalized times ξ . These are precisely the parameters that produce a potential φ along this axis that traps the ion and are illustrated in Fig. 2.1. The boundaries of the stability regions correspond to periodic solutions

$$r_j(\xi) = c_0(a_j, q_j)ce_0(\xi, q_j) + \sum_{n=1}^{\infty} \left(c_n(a_j, q_j)ce_n(\xi, q_j) + s_n(a_j, q_j)se_n(\xi, q_j) \right), \quad (2.16)$$

with the *integer* Mathieu functions $ce_n(\xi, q_j)$ and $se_n(\xi, q_j)$, where the coefficients $c_n(a_j, q_j)$ and $s_n(a_j, q_j)$ are calculated iteratively to the required precision of the solution [KRM18; Olv+].

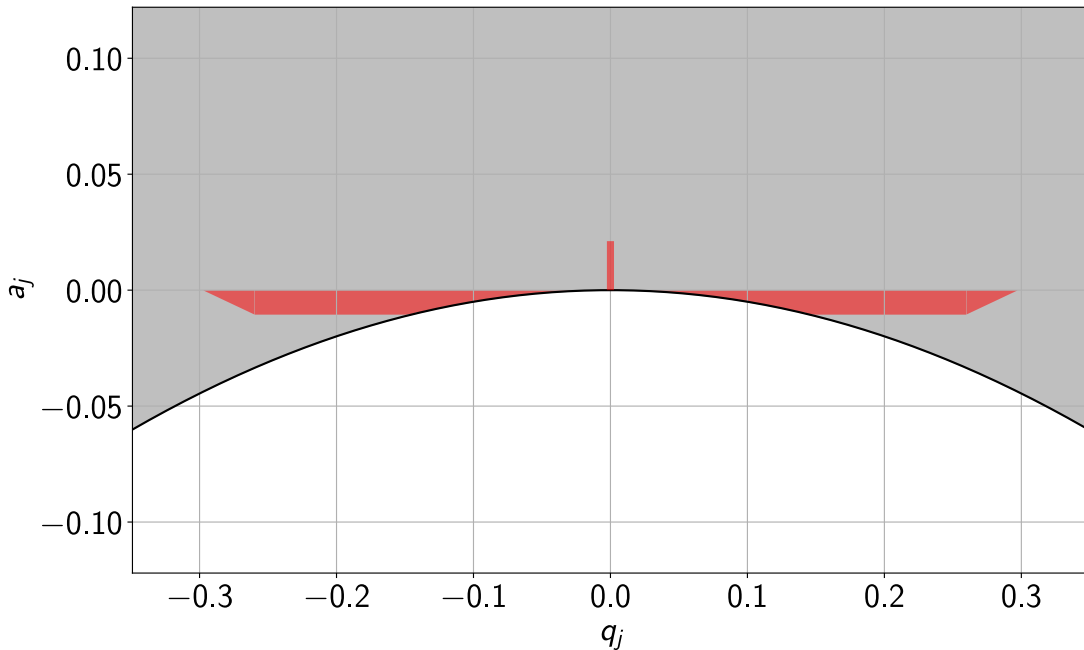


Figure 2.1.: *Mathieu stability diagram. The parameters of the Mathieu equation Eq. (2.15) which feature stable solutions, where the ion is confined within the trap, are shaded in grey. The white region contains unstable solutions, where the ion coordinate grows without bound. The thick line separates the regions, a numerical expressions for it is found in [KRM18]. The red shading shows the parameter region where the ion trap in this thesis is operated. The DC confinement along the trap axis corresponds to a positive value of a_z at $q_z=0$. This causes $a_{x,y} = -a_z/2$ to satisfy the boundary condition Eq. (2.9) and limits the maximum axial confinement for a given value of $q_{x,y}$. Since both $|a_j|$ and $|q_j|$ are significantly smaller than 1, the ion motion is well described by the approximate solution Eq. (2.19).*

2.1. Trapping a charged particle with electromagnetic fields

The solutions for parameters on the interior of the stability regions are not periodic in time, but physically accessible. In this case, the eigenfunctions of the solutions are *fractional* Mathieu functions $\text{me}_\nu(\xi, q_j)$ and can be expanded into the full solution

$$r_j(\xi) = \sum_{n=-\infty}^{\infty} m_n(a_j, q_j) \text{me}_{\nu+2n}(\xi, q_j), \quad (2.17)$$

with similarly calculated coefficients $m_n(a_j, q_j)$ [Olv+].

Secular motion and micromotion While it is possible to confine ions in any of the stability regions, the ion trap discussed in this thesis operates in the center region where both $|q_j|$ and $|a_j|$ are smaller than 1. The Mathieu equation can be solved numerically to investigate the motion of the ion in this trapping region. In addition, an approximate analytic solution $r_j^a(\xi)$ can be formulated for $|a_j|, |q_j|^2 \ll 1$. For the initial conditions

$$r_j^a(\xi = 0) = r_0, \quad \left. \frac{d}{d\xi} r_j^a \right|_{\xi=0} = v_0 \quad (2.18)$$

the approximate solution is equal to

$$r_j^a(\xi) = \frac{r_0}{1 - q_j/2} \cos(\beta_j \xi) \left(1 - \frac{q_j}{2} \cos(2\xi) \right) + \frac{v_0}{\beta_j} \sin(\beta_j \xi) \left(1 - \frac{q_j}{2} \sin(2\xi) \right), \quad (2.19)$$

with $\beta_j = \sqrt{a_j + q_j^2/2}$. Equation (2.19) shows that there are three frequency components to the motion of the ion. The *secular* motion with an angular frequency $\omega_{\text{sec}} = \beta_j \Omega_{\text{rf}}/2$ and the *intrinsic micromotion* with angular frequencies $\Omega_{\text{rf}} \pm \omega_{\text{sec}}$. The spectral density amplitude of the displacement of an $^{88}\text{Sr}^+$ ion from the trap center for $\Omega_{\text{rf}} = 2\pi \times 14.404$ MHz, $a = 0$, $q = 0.25$, $r_0 = 0$ m, $v_0 = 0.18$ m/s is shown in Fig. 2.2 on the left-hand side. The numerical solution is obtained with the `scipy` [Vir+20] python package using the implicit solver *Radau* [HW91] after transforming the second-order differential equation Eq. (2.15) into a system of two first order differential equations. One can see that the approximate solution correctly identifies the frequencies of secular motion ($\omega_{\text{sec}} = 2\pi \times 1250$ kHz) and intrinsic micromotion.

For large q , the approximate solution does not accurately reproduce all dominant frequencies of motion anymore. The right hand side of Fig. 2.2 shows the spectral density amplitude for the same parameters except that $q = 0.75$, which results in an expected secular frequency of 3800 kHz. Due to the large confinement of

2. Optical clocks based on trapped ions

the ion, the secular frequency is shifted from the expected value and additional components at high frequencies appear. The maximum confinement at which the ion trap is operated in this thesis corresponds to $q \approx 0.3$, so the approximate solution Eq. (2.19) is sufficient to investigate the ion motion.

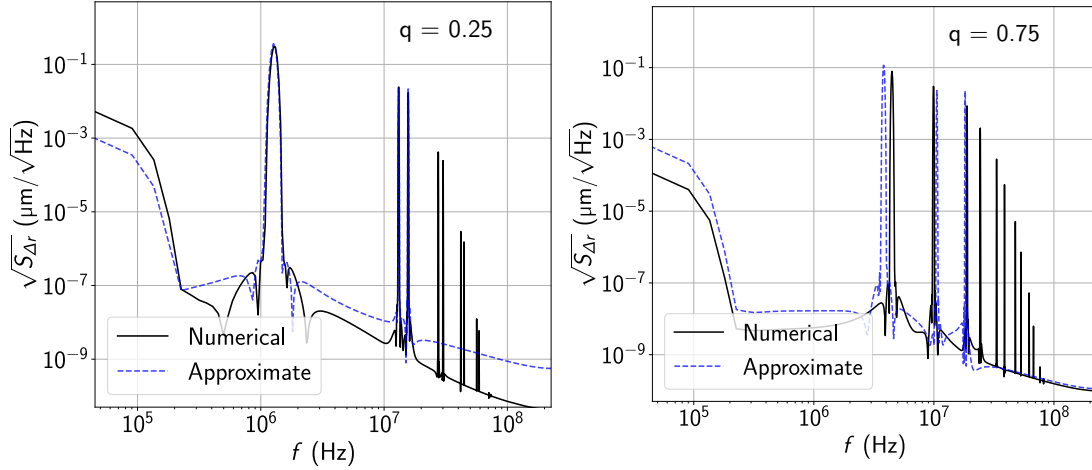


Figure 2.2.: Motional spectrum of a trapped ion at small and large q . The spectral density amplitude $\sqrt{S_{\Delta r}}$ of the displacement Δr from the mean position of a trapped ion for $q=0.25$ is shown on the left, determined by the numerical solution of the Mathieu equation (black solid line) and the approximate solution for small q (blue dashed line). The corresponding $\sqrt{S_{\Delta r}}$ for $q=0.75$ is shown on the right. A Kaiser window ($\alpha=14$) [HRS02] is applied to the data before calculating the spectral density amplitude. While the approximate solution correctly identifies the secular motion at the angular frequency ω_{sec} and dominant intrinsic micromotion components at the angular frequencies $\Omega_{rf} \pm \omega_{sec}$, for small q , at large q additional motional frequencies become relevant that are not included in Eq. (2.19). Additionally, the secular frequency is shifted to a higher value than expected from Eq. (2.19).

Equation (2.13) and the corresponding solutions assume that no electric field interacts with the ion that is not generated by the trap itself. In practice, this assumption is often wrong, since surface charges on the trap geometry cause a significant field at the position of the ion. A static external electric field $\vec{E}_{ext} = (E_x, E_y, E_z)_{ext}$ displaces the ion from the trap center and causes *excess micromotion*. This modifies Eq. (2.15) to

$$\frac{d^2}{d\xi^2} r_j + (a_j - 2q_j \cos(2\xi)) r_j = r_{ext,j}, \quad (2.20)$$

where $j = (x, y, z)$, $r_{ext,j} = 4qE_{ext,j}/(m\Omega_{rf}^2)$. The effect of the offset field can be more easily seen in the approximate solution Eq. (2.19) with the initial conditions Eq. (2.18)

$$r_j^a(\xi) = \left(r_{\text{ext},j} + \left(\frac{r_0 - r_{\text{ext},j}}{1 - q_j/2} - r_{\text{ext},j} \right) \cos(\beta_j \xi) \right) \left(1 - \frac{q_j}{2} \cos(2\xi) \right) \quad (2.21)$$

$$+ \left(r_{\text{ext},j} + \frac{v_0 + q_j r_{\text{ext},j}}{\beta_j} \sin(\beta_j \xi) \right) \left(1 - \frac{q_j}{2} \sin(2\xi) \right), \quad (2.22)$$

which includes an additional oscillation of the ion proportional to the amplitude of the external field at the frequency of the RF trap drive Ω_{rf} , the excess micromotion. It can substantially affect the coherence of ion-light interaction and causes frequency shifts [Ber+98; Kel+15]. For this reason, it needs to be minimized as much as possible by applying a field opposite to \vec{E}_{ext} with electrodes placed in the vicinity of the ion. The magnitude of excess micromotion can be measured in a variety of ways [Kel+15]. The *photon-correlation method* [Kel+15] is discussed in Section 2.2, since this method is used in this thesis.

Motion of ion crystals Since a multi-ion system is considered in this thesis, the equations of motion for multiple ions in the same potential are of interest. In general, the other ions are point charges that produce an electric field according to Coulomb's law. For this reason, the equations of motion for the position \vec{r}_a of each ion a are

$$\frac{d^2}{dt^2} \vec{r}_a = -\frac{q_a}{m_a} \left(U_{\text{dc}} \begin{pmatrix} k_x x_a \\ k_y y_a \\ k_z z_a \end{pmatrix} + U_{\text{rf}} \cos(\Omega_{\text{rf}} t) \begin{pmatrix} c_x x_a \\ c_y y_a \\ c_z z_a \end{pmatrix} - \frac{1}{4\pi\epsilon_0} \sum_{b \neq a} q_b \frac{\vec{r}_a - \vec{r}_b}{|\vec{r}_a - \vec{r}_b|^3} \right), \quad (2.23)$$

with the mass of the ion m_a , the charge q_a , the static field $U_{\text{dc}} \vec{k}$, the rf field $U_{\text{rf}} \cos(\Omega_{\text{rf}} t) \vec{c}$ and the dielectric constant ϵ_0 . Usually, all ions have positive charge ($q > 0$), so they repel each other and may form stable configurations called *ion crystals* [Dre+98]. These crystals exhibit transitions between different spatial configurations and have been investigated by a variety of groups [Blü+88; BKW92; Blo+00; Par+13]. Equation (2.23) can also be numerically solved to investigate the behaviour of large crystals with significant expansion along all three trapping axes [Pre+91].

For the purposes of this work it is sufficient to approximate Eq. (2.23) for the case of a so-called *linear chain*, where the ions are comparatively strongly confined along the radial RF trapping directions (x, y) and weakly confined along the axial DC trapping direction (z). In this case, the ions orient themselves along the z -axis and do not significantly spread along the x - and y -axes. This allows for ion

2. Optical clocks based on trapped ions

trapping along the whole chain at low and constant micromotion, a necessity for high-precision spectroscopy [Rai+92]. The time-dependence of the potential is usually discarded for analysis of ion strings and the static harmonic approximation used instead to derive laws for the different phases of the ion crystal [MW01; MF04]. The transition between a linear chain of N ions and the so-called *zig-zag mode* occurs once the ratio between the axial secular frequency and average radial secular frequency reaches [MF04]

$$\frac{\omega_{\text{ax}}}{\omega_{\text{rad}}} \approx \frac{4}{3} \frac{\sqrt{\ln N}}{N}, \quad (2.24)$$

so the ion traps for multi-ion-spectroscopy are usually operated below this critical ratio. In this case, the ion motion can be decomposed into components along the axial and radial directions, which do not couple with each other [Rai+92; MW01]. The potential can be well approximated with a Taylor expansion around the equilibrium positions of the individual ions, which results in an eigenvalue problem to determine the crystal dynamics [MW01]. This eigenvalue problem can be solved to determine the secular frequencies and participation of each ion to the motion at the respective secular frequency for a given crystal configuration [MW01]. Determining the kinetic energy of each ion in the chain is necessary for high-accuracy operation of a multi-ion optical clock and discussed in detail in [Vyb+23]. All in all, a linear ion chain can be investigated with well-established numerical and experimental techniques, developed to enable high-precision spectroscopy and quantum state control.

2.2. Cooling the ion to the Doppler limit

Using the techniques described in Section 2.1 ions are confined to a region of space, but still possess all initial kinetic energy they entered the trap with. When loading $^{171}\text{Yb}^+$ ions from thermally evaporated atoms emitted by a 500 °C oven [Wod+21], they possess an average kinetic energy of 85 meV. Due to additional energy imparted by the ionization process, the kinetic energy is substantially higher than this value. Still, the ion can be confined within the eV deep ion trap, but has to be *cooled* to enable coherent interaction with laser radiation with a wavelength shorter than 1 μm .

Even if coherent spectroscopy is not a possibility, laser radiation can still interact with the trapped ion. The ions used in this work possess an electronic level structure with many states which are well described by alkali-like wavefunctions. This is because Sr and Yb are elements with completely filled inner electronic shells and a filled outer s-shell. When one electron is removed via ionization, a single outer electron remains, which experiences the nuclear core and inner electron shell approximately as a central positive charge. The ground state electronic configu-

ration for $^{171}\text{Yb}^+$ and $^{88}\text{Sr}^+$ are $[\text{Xe}]4f^{14}6s^1$ and $[\text{Kr}]5s^1$, respectively. Simplified level structures with all states relevant to the initial ion cooling are depicted in Fig. 2.3. Transitions between the electronic states are driven with electromagnetic radiation in the visible and NIR region.

To describe the interaction of electromagnetic radiation at an angular frequency offset δ from the transition between two electronic states $|g\rangle$ and $|e\rangle$ with finite lifetime τ (and corresponding natural linewidth Γ) of the excited state, the *optical Bloch equations* can be employed [MS99]. In this model, the two states couple with the electric field $\vec{E}(\vec{r}, t) = 1/2(\vec{E}_0 e^{-i\omega t} + \vec{E}_0^* e^{i\omega t})$ via the transition electric dipole moment \vec{d} , resulting in the *Rabi frequency* $\Omega = \vec{d} \cdot \vec{E}_0 / \hbar$ with which the population is oscillating between $|g\rangle$ and $|e\rangle$. For long interaction times with respect to $1/\Omega$ or τ the excited state population saturates at a fixed value where the excitation rate and spontaneous decay rate balance with each other. Since τ is shorter than $1\ \mu\text{s}$ for the optical transitions in Fig. 2.3, only the steady state excitation probability $p_e(t \gg \tau)$ is observable. Each spontaneous decay from $|e\rangle$ emits a photon, which can be collected with some probability determined by the imaging system of the ion trap. This way the excited state population for different frequency detunings of the cooling laser from resonance is measured via the rate of collected photons. If $\Omega \ll \gamma$ the observed linewidth of the transition is given by the spontaneous decay rate $1/\tau$. Once Ω reaches and surpasses γ , the transition broadens significantly above the natural linewidth and starts to saturate towards $p_e = 0.5$, the theoretical maximum.

2. Optical clocks based on trapped ions

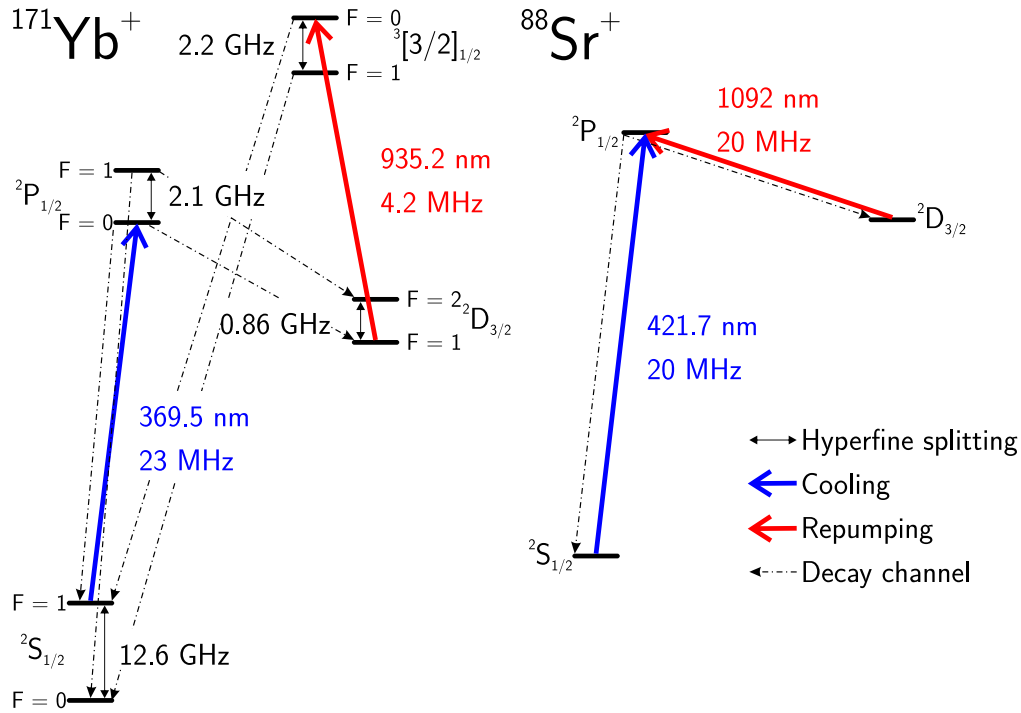


Figure 2.3.: Level structure of $^{171}\text{Yb}^+$ and $^{88}\text{Sr}^+$ relevant for Doppler cooling. The simplified level structure (not to scale) of $^{171}\text{Yb}^+$ [Sem+18] and $^{88}\text{Sr}^+$ [Dub+10] relevant for Doppler cooling. All electronic states are labeled as $^{2S+1}L_J$, where L is the orbital angular momentum, S is the electronic spin and J the total electronic angular momentum. One exception is the bracket state $^3[3/2]_{1/2}$, which is a result of JK pair coupling in contrast to the other states which are well described by LS coupling [Cow81, p. 128]. Since the $^{171}\text{Yb}^+$ nucleus possesses a nuclear spin of $I=1/2$, each electronic state also splits into two hyperfine levels with angular momentum $F=I \pm J$. The Zeeman sublevels for each state are not shown. For each optical transition the center wavelength and natural linewidth are given. The main decay channels from the excited states are shown to indicate the cooling cycle and state preparation for $^{171}\text{Yb}^+$.

With this interaction between the trapped ion and a laser it is possible to cool the ion, when the laser is detuned below resonance ($\delta < 0$). In this case, momentum of the ion is reduced by the absorption of a counterpropagating photon, while the spontaneous emission direction is random and consequently adds no kinetic energy on average [Dem13, p. 395]. The linewidth of the transition, natural or broadened, limits the lowest temperature of the ion because of the balance of photon emissions and absorptions with different energies. The so-called *Doppler limited* temperature T_D for a transition with linewidth Γ at detuning $\Gamma/2$ is

$$T_D = \frac{\hbar\Gamma}{2k_B} = 0.024 \text{ mK/MHz} \times \frac{\Gamma}{2\pi}, \quad (2.25)$$

which results in a temperature of 0.48 mK for a transition with a linewidth of 20 MHz. The actual ion temperature may be higher, if additional heating sources due to electrical noise are present or because of decay to other states not connected to the Doppler cooling transition and can be determined with measurements that are discussed in Section 2.3. To reach the Doppler temperature, a laser with a linewidth significantly smaller than the natural linewidth of the transition is necessary and its intensity needs to be well below the saturation limit of the cooling transition.

In practice, addressing purely the transition ${}^2S_{1/2} \leftrightarrow {}^2P_{1/2}$ is not sufficient to cool the ion to the Doppler temperature. This is due to decay into the ${}^2D_{3/2}$ state which has a natural lifetime of 55 ms for Yb^+ [Sha+23] and 430 ms for Sr^+ [Sah+06]. The probability for decay into this state after excitation by the cooling laser is given by the *branching ratio* b , which is 0.5% for the decay ${}^2P_{1/2} \rightarrow {}^2D_{3/2}$ in Yb^+ [Olm+07] and 5.5% for the same transition in Sr^+ [Zha+16]. If the ion is in this state, it does not couple to the cooling light anymore and starts to gain kinetic energy for the lifetime of the excited state. Since this is much longer than the lifetime $\tau_{\text{cool}} \approx 1/\Gamma/b \ll 100 \mu\text{s}$ in the ${}^2S_{1/2} \leftrightarrow {}^2P_{1/2}$ system, the ion is not actually cooled for the majority of the time it is trapped. For this reason, an additional laser is necessary, that couples the long-lived ${}^2D_{3/2}$ state to a short-lived excited state that decays back into the ground state. This laser is often called a *repump* or *quench* laser. The repump transitions for ${}^{171}\text{Yb}^+$ and ${}^{88}\text{Sr}^+$ are shown in Fig. 2.3.

So far, the discussion of the cooling mechanism and decay assumes that the electronic structure does not possess a hyperfine component. For ${}^{88}\text{Sr}^+$ this is correct, because the nuclear spin I is equal to zero. ${}^{171}\text{Yb}^+$ on the other hand has a nucleus with $I=1/2$, which results in a hyperfine splitting of each electronic state with angular momentum J into two states with total angular momentum $F=J \pm I=J \pm 1/2$. The splitting between these states is between approximately 1-10 GHz, so they are significantly further apart than the natural linewidth of the optical transitions of approximately 20 MHz. This means, that they cannot be addressed with a single unmodulated laser simultaneously without introducing a large amount of saturation broadening. This issue is overcome by modulating additional sidebands on the cooling and repumper lasers, that correspond to the additional transitions between the hyperfine states. But even with all necessary frequencies of the cooling lasers, an additional problem rears its head, *coherent population trapping*.

Since the state $|S_{1/2}, F=1\rangle$ has a higher multiplicity than the higher lying energy state $|P_{1/2}, F=0\rangle$, coherent population trapping can arise at small magnetic fields [BB02; ETH10]. In that case, a superposition of Zeeman states in the ground and excited state can always be found, that does not couple to the electric field and forms a so-called *dark state* [BB02; Ejt10]. The ion is then pumped into this dark state and its fluorescence is heavily reduced. This problem is mitigated by applying a sufficiently strong ($\approx 300 \mu\text{T}$) magnetic field to clearly define the quantization axis

2. Optical clocks based on trapped ions

[BB02; Ejt10] or by modulating the cooling and repump laser polarization [BB02]. Dark states generally can also be employed for optical pumping, for example by irradiating the ion with σ_+ -polarized light [Coh75]. A more detailed review on this topic is found in [BB02; ETH10; Ejt10], where the dependence of the fluorescence on magnetic field strength, laser polarization and intensity is described theoretically as well as investigated theoretically and experimentally.

Micromotion detection with photon-correlation The Electric Dipole (E1) transitions used for Doppler cooling can also be employed to measure excess micromotion of the ion due to displacement from the trap center. A variety of methods are discussed in [Ber+98; Kel+15], the one in use in this thesis is the *photon correlation method*. The Doppler shift due to ion motion in the direction of the cooling laser modulates the fluorescence signal [Höf+97; Ber+98]. The photon scattering rate γ is dependent on the frequency detuning Δ from the atomic resonance as discussed in section 2.2 and the relationship between γ and Δ is approximately linear if the laser is set to the half-maximum detuning $\Delta = -\Gamma/2$. In the reference frame of the ion, Δ changes due to the Doppler shift $\delta_D(\Omega_{\text{rf}}, x_\mu)$ dependent on the rf trap drive frequency Ω_{rf} and micromotion amplitude x_μ . This results in the photon scattering rate varying with a fixed phase relation with respect to Ω_{rf} [Ber+98; Kel+15]

$$S(t) = S_0 + \Delta S(x_\mu, \Omega_{\text{rf}}) \cos(\Omega_{\text{rf}}t - \varphi), \quad (2.26)$$

with the mean fluorescence S_0 , fluorescence modulation amplitude ΔS and modulation phase φ . By measuring the arrival times of photons with respect to the RF phase, the parameters S_0 , ΔS and φ are measured. This requires a time-resolved fluorescence signal detection with time resolution better than at least twice the inverse trap frequency [Sha49]. Equation (2.26) is only approximately true, a derivation of the accurate fluorescence modulation signal is found in [Kel+15]. Specifically, to determine the micromotion amplitude x_μ or correspondingly the RF field amplitude E_{rf} , the relationship between the modulation parameter $\beta = kq/m/\Omega_{\text{rf}}^2 E_{\text{rf}}$ and $\Delta S/S_0$ needs to be accurately calculated. A quadratic model

$$E_{\text{rf}} = A \frac{\Delta S}{S_0} + B \left(\frac{\Delta S}{S_0} \right)^2 \quad (2.27)$$

is usually sufficient to determine E_{rf} in the amplitude and frequency range relevant for optical clocks [Kel+15] and employed in this thesis. It is important to mention that these relations only hold, if the modulation signal does not contain a significant component with frequencies $n\Omega_{\text{rf}}$, $n > 1$. This is the case, if the micromotion is very large, which causes substantial frequency shifts. If micromotion cannot be compensated completely, as is the case in linear ion traps with a significant axial

micromotion component, this may limit the trap depth at which the ion trap can be operated.

2.3. Coherent interaction between cold ions and electromagnetic radiation

The overall goal of an optical clock is to determine the unperturbed center frequency of an optical transition with small uncertainty. If the natural linewidth of a transition is large, long averaging times are required, so E1 transitions are not suitable for optical clocks with low uncertainty. For this reason, *forbidden* transitions are employed, for which the matrix element $\langle g|\hat{d}_\alpha|e\rangle$ involving the E1 operator \hat{d} is equal to zero. Instead, the higher orders of the electromagnetic multipole are relevant for the transition moment T_{ge} , such as Magnetic Dipole (M1) (\hat{m}), E2 (\hat{Q}), Magnetic Quadrupole (M2) (\hat{M}) and E3 (\hat{O}) contributions [BAJ12]

$$T_{ge} = -i\frac{\Delta E}{\hbar} \sum_{\alpha} \mathcal{E}_{\alpha} \langle g|\hat{d}_{\alpha}|e\rangle \quad (2.28)$$

$$+ic \sum_{\alpha} \left(\vec{k} \times \vec{\mathcal{E}}\right)_{\alpha} \langle g|\hat{m}_{\alpha}|e\rangle + \frac{1}{2} \frac{\Delta E}{\hbar} \sum_{\alpha\beta} k_{\alpha} \mathcal{E}_{\beta} \langle g|\hat{Q}_{\alpha\beta}|e\rangle \quad (2.29)$$

$$-\frac{1}{2} c \sum_{\alpha\beta} \left(\vec{k} \times \vec{\mathcal{E}}\right)_{\alpha} k_{\beta} \langle g|\hat{M}_{\alpha\beta}|e\rangle + i\frac{1}{6} \frac{\Delta E}{\hbar} \sum_{\alpha\beta\gamma} k_{\alpha} k_{\beta} \mathcal{E}_{\gamma} \langle g|\hat{O}_{\alpha\beta\gamma}|e\rangle, \quad (2.30)$$

with the polarization vector $\vec{\mathcal{E}}$ and the propagation vector \vec{k} . This description does not include other physical processes such as state mixing that allow the coupling between states without any expected transition matrix element [TMK17]. The indices α, β, γ run over the three spatial directions x, y, z . This shows that transitions between $|g\rangle$ and $|e\rangle$ are still allowed if $\langle g|\hat{d}_{\alpha}|e\rangle = 0$, albeit at coupling strengths proportional to approximately $(a_0/\lambda)^2$ for an E2 transition and $(a_0/\lambda)^4$ for an E3 transition, where a_0 is the Bohr radius and $\lambda = 2\pi/|\vec{k}|$. Consequently, if no further decay path exists for the excited state than back to the ground state, it is long-lived with lifetimes greater than 50 ms [Sha+23; Sah+06; Lan+21b]. This results in natural linewidths of several Hz and below, significantly narrower than the dipole allowed transitions. For this reason, these transitions are used as references for optical clocks.

When employing these forbidden transitions, the interaction between electromagnetic radiation and a trapped Doppler-cooled ion has to be investigated more carefully. Since the natural linewidth Γ of a few Hz is significantly smaller than the secular frequency ω_{sec} of a few hundred kHz, the ion-light interaction may be

2. Optical clocks based on trapped ions

within the *Lamb-Dicke* regime [Lei+03]. It is defined for a particle confined in a box with length a , interacting with radiation with a wavelength λ as

$$a < \lambda. \quad (2.31)$$

For a trapped ion with mass m at a temperature T and angle between the laser k -vector and ion velocity direction θ , this corresponds to [Lei+03]

$$\sqrt{\frac{k_B T}{2\hbar\omega_{\text{sec}}}}\eta = \sqrt{\frac{k_B T}{2\hbar\omega_{\text{sec}}}} \frac{2\pi}{\lambda} \sqrt{\frac{\hbar}{2m\omega_{\text{sec}}}} \cos\theta \ll 1, \quad (2.32)$$

where η is called the *Lamb-Dicke parameter*. Intuitively this condition means that the oscillation amplitude along the k -vector within the trapping potential is significantly smaller than the wavelength of the laser radiation interacting with the ion. This is a necessary condition for coherent spectroscopy, since the ion samples multiple phases of the electromagnetic wave otherwise. For a $^{171}\text{Yb}^+$ ion Doppler-cooled to 0.55 mK (the Doppler limit for the E1 cooling transition), interacting with radiation at 435 nm, a secular frequency ω_{sec} of about 500 kHz is necessary to be well within the Lamb-Dicke regime if the ion velocity and laser direction are collinear.

Up until the discussion of the Lamb-Dicke regime, the ion motion is considered classical. But for an accurate description of the light-matter interaction for two electronic states of a trapped ion that possesses some velocity, the motion also has to be included in a quantized way. For this purpose it is practical to approximate the potential as harmonic with frequency ω_{sec} , resulting in the following Hamilton operator for the complete system [Lei+03]

$$\hat{H} = \hat{H}_{\text{ion}} + \hat{H}_{\text{motion}} + \hat{H}_{\text{interaction}} \quad (2.33)$$

$$= -\frac{\hbar\omega_0}{2}|g\rangle\langle g| + \frac{\hbar\omega_0}{2}|e\rangle\langle e| + \hbar\omega_{\text{sec}}\left(\hat{a}^\dagger\hat{a} + \frac{1}{2}\right) \quad (2.34)$$

$$+ \frac{\hbar\Omega_0}{2} \exp\left(i\eta\left(\hat{a}e^{-i\omega_{\text{sec}}t} + \hat{a}^\dagger e^{i\omega_{\text{sec}}t}\right)\right) e^{i(\Phi-\delta)t}|e\rangle\langle g| \quad (2.35)$$

$$+ \frac{\hbar\Omega_0}{2} \exp\left(-i\eta\left(\hat{a}^\dagger e^{i\omega_{\text{sec}}t} + \hat{a}e^{-i\omega_{\text{sec}}t}\right)\right) e^{-i(\Phi-\delta)t}|g\rangle\langle e|, \quad (2.36)$$

with the resonant angular frequency difference between the ground state $|g\rangle$ and excited state $|e\rangle$ ω_0 , the angular frequency detuning of the incident radiation from resonance δ , the Rabi frequency Ω_0 and the raising (lowering) operators \hat{a}^\dagger (\hat{a}) of the harmonic oscillator describing the ion motion. This Hamiltonian is valid under the rotating wave approximation and the assumption that the ion is confined within the lowest-order region of the stability chart Fig. 2.1 [Lei+03]. For this

2.3. Coherent interaction between cold ions and electromagnetic radiation

Hamiltonian, states are well described in the product basis of the internal state ($|g\rangle, |e\rangle$) and the quanta of motion ($|n\rangle$) [SM00]. A generic state is then described by the density operator [SM00]

$$\hat{\rho} = \sum_{n=0}^{\infty} a_n |g, n\rangle\langle g, n| + b_n |e, n\rangle\langle e, n| \quad (2.37)$$

where the complex coefficients a_n and b_n depend on the internal and motional state of the trapped ion.

If the ion is cooled and confined sufficiently to be within the Lamb-Dicke regime, the exponent in the interaction part of the Hamiltonian can be approximated to first order in η [Lei+03]

$$\hat{H} = \hat{H}_{\text{ion}} + \hat{H}_{\text{motion}} + \hat{H}_{\text{interaction}} \quad (2.38)$$

$$= -\frac{\hbar\omega_0}{2} |g\rangle\langle g| + \frac{\hbar\omega_0}{2} |e\rangle\langle e| + \hbar\omega_{\text{sec}} \left(\hat{a}^\dagger \hat{a} + \frac{1}{2} \right) \quad (2.39)$$

$$+ \frac{\hbar\Omega_0}{2} \left(1 + i\eta \left(\hat{a} e^{-i\omega_{\text{sec}} t} + \hat{a}^\dagger e^{i\omega_{\text{sec}} t} \right) \right) e^{i(\Phi - \delta t)} |e\rangle\langle g| \quad (2.40)$$

$$+ \frac{\hbar\Omega_0}{2} \left(1 - i\eta \left(\hat{a}^\dagger e^{i\omega_{\text{sec}} t} + \hat{a} e^{-i\omega_{\text{sec}} t} \right) \right) e^{-i(\Phi - \delta t)} |g\rangle\langle e|, \quad (2.41)$$

which reveals the three different types of transitions that can be driven. If the laser frequency equals the center frequency of the transition ($\delta=0$), the motional state $|n\rangle$ is unchanged and the ion cycles between the ground and excited state ($|g\rangle|n\rangle \leftrightarrow |e\rangle|n\rangle$). This is called the *carrier* transition and is the one excited to determine the unperturbed center frequency during clock operation. If the laser frequency is offset from the center by the secular frequency of the ion ($\delta = \pm\omega_{\text{sec}}$), a motional sideband is driven, that changes both the internal and motional state ($|g\rangle|n\rangle \leftrightarrow |e\rangle|n \pm 1\rangle$). Consequently, the transition is called a *blue/red sideband* transition and has applications from resolved sideband cooling [Die+89] to quantum logic spectroscopy [Sch+05]. It is also possible to drive transitions at detunings that are integer-multiples of the secular frequency ($\delta = \pm k\omega_{\text{sec}}, k \in \mathbb{N}$), which change the motional state by the appropriate amount of quanta ($|g\rangle|n\rangle \leftrightarrow |e\rangle|n \pm k\rangle$). These transitions are then called *first, second, third, ... order sideband* transitions.

To investigate the effect of the ion motion on the coherent light-matter interaction between the laser of the ion, it is useful to assume initially that $\delta=0$, the excited state lifetime is much longer than the interrogation time and that the ion is in a thermal motional state with mean occupation number $\bar{n} = 1 / \left(\exp(\hbar\omega_{\text{sec}}/k_B T) - 1 \right) \approx k_B T / (\hbar\omega_{\text{sec}})$, where the temperature T is given by the Doppler limit Eq. (2.25), if no additional heating sources are present. In this case the probability p_n for the ion to be found in the motional state $|n\rangle$ is [Lou00, p. 14]

2. Optical clocks based on trapped ions

$$p_n(\bar{n}) = \frac{1}{1 + \bar{n}} \left(\frac{1}{1 + 1/\bar{n}} \right)^n, \quad (2.42)$$

which results in the excited state population $P_e(t)$ [Roo00]

$$P_e(t) = \frac{1}{2} \left(1 - \sum_{n=0}^{\infty} p_n(\bar{n}) \cos(\Omega_{n,n}t) \right), \quad (2.43)$$

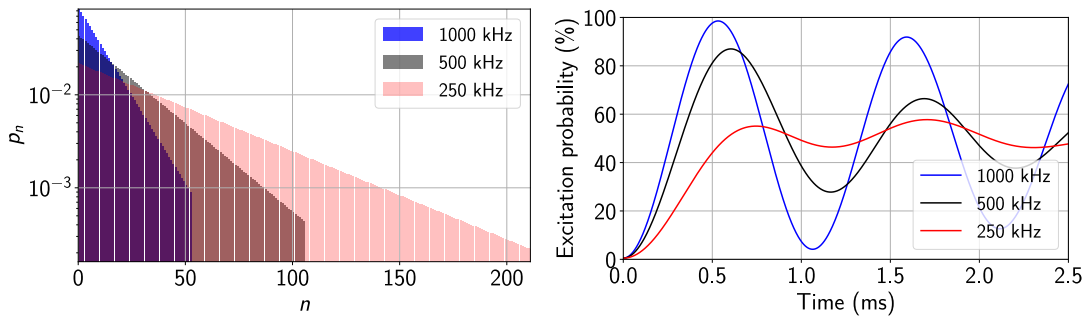


Figure 2.4.: *Thermal Rabi oscillations.* The thermal distribution p_n (left-hand side, Eq. (2.42)) and excitation probability $P_e(t)$ (right-hand side, Eq. (2.43)) for the 435 nm transition of $^{171}\text{Yb}^+$ at the Doppler temperature of 0.55 mK for various confinement strengths. The states included are cut off once 99 % of the total population is accounted for. The thermal distribution shows the expected exponential decay and it can be seen that many states need to be included at low confinement to accurately describe the Rabi oscillation. At low confinement, the maximum excitation probability is significantly less than 100 %, which shows the need for a high secular frequency to operate the clock with low instability.

with the effective Rabi frequency $\Omega_{n,n} = \Omega_0 e^{-\eta^2/2} L_n(\eta^2)$, where Ω_0 is the Rabi frequency in Eq. (2.41) and $L_n(\eta^2) = 1 - n\eta^2 + n(n-1)\eta^4/4 + O(\eta^6)$ is the Laguerre polynomial [AS72, p. 775]. The distribution and excited state population for various confinement strengths is shown in Fig. 2.4. While each Rabi oscillation for a given n is perfectly coherent, the weighted average due to the thermal distribution Eq. (2.43) shows a contrast loss and a saturation of the excitation probability at 50 % for long interaction times. Since the instability of an optical clock increases, when the maximum excitation probability is reduced, it is generally advisable to reduce the mean occupation number as much as possible. This is primarily achieved via operating at high ω_{sec} , but additional cooling below the Doppler limit also improves the overall contrast. Resolved sideband cooling may result in a non-thermal distribution, though, which results in the need for a more detailed measurement of p_n to determine frequency deviations due to the ion motion.

2.3. Coherent interaction between cold ions and electromagnetic radiation

This is possible by measuring the relative excitation strength between the carrier and sideband transitions at a fixed laser intensity. The Rabi frequency of the m -th sideband transition $\Omega_{n,n+m}$, with positive m describing blue sidebands and negative m describing red sidebands, is changed from the carrier $\Omega_{n,n}$ proportional to the Lamb-Dicke factor η [Lei+03]

$$\Omega_{n,n+m} = \Omega_0 e^{-\eta^2/2} \eta^{|m|} \sqrt{\frac{n_{<}!}{n_{>}!}} L_{n_{<}}^{|m|}(\eta^2), \quad (2.44)$$

where $n_{<}(n_{>})$ is $\min(n, n+m)$ ($\max(n, n+m)$) and $L_n^\alpha(x)$ is the generalized or associated Laguerre polynomial. These Rabi frequencies substitute Ω_n in Eq. (2.43) when calculating the excitation of the ion when driving the secular sideband frequencies. This coherent interaction is not only useful for temperature measurements, but can also be employed in quantum logic spectroscopy, if the ion is sufficiently cooled to the motional ground state [Sch+05]. A comparison of the scaling of the excitation probability for times $t \ll 1/\Omega_0$ shows that the ratio of $P_e(t)$ of the 1st red sideband and carrier is proportional to the mean population of a thermal state \bar{n} [Roo00]

$$\frac{P_e^{\text{1st red}}(t)}{P_e^{\text{carrier}}(t)} \approx \sum_{n=0}^{\infty} p_n(\bar{n}) \frac{\eta^2 n \Omega_0^2}{\Omega_0^2} = \eta^2 \sum_{n=0}^{\infty} p_n(\bar{n}) n = \eta^2 \bar{n}, \quad t \ll 1/\Omega_0. \quad (2.45)$$

To determine how good this approximation is, one can solve Eq. (2.43) for the 1st red sideband and the carrier numerically given a fixed \bar{n} and η . The result is shown in Fig. 2.5 together with the relative excitation strength of the blue sideband. The approximation is valid within 10% for interrogation times below approximately $2\pi/(4\Omega_0)$. If a more accurate determination is necessary, the difference between the approximation and numerical solution can be applied to any collected data. This is particularly important if \bar{n} is used to determine frequency shifts of the optical clock with sufficient precision.

An alternative method to determine \bar{n} , independent of the Lamb-Dicke factor η , is comparing the relative excitation probability of the first red and blue sideband transition at constant laser intensity [Lei+03]. If the excitation probabilities are p_r and p_b , respectively, then \bar{n} is equal to [Lei+03]

$$\bar{n} = \frac{1}{p_b/p_r - 1}. \quad (2.46)$$

While Eq. (2.46) in principle is valid even at high temperatures ($T \approx 1$ mK), the difference in the excitation probability becomes smaller as T increases. This produces a comparatively high uncertainty in \bar{n} [Roo00], so it is primarily applicable to ground-state cooled ions.

2. Optical clocks based on trapped ions

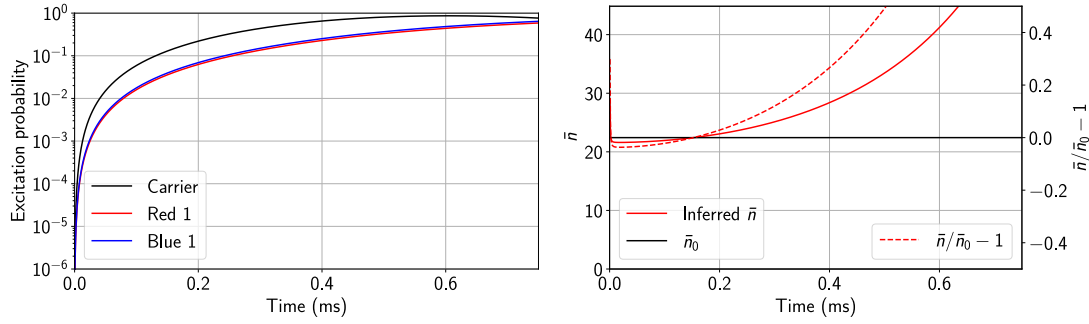


Figure 2.5.: *Carrier sideband excitation probability comparison.* The figure on the left shows the excitation strength of the carrier and sideband transitions of the same ion in a thermal motional state as in Fig. 2.4 ($\Omega_0 = 2\pi/1$ ms, $\lambda = 435$ nm, $m = 171$ u, $T_D = 0.55$ mK, $\omega_{sec} = 2\pi \times 500$ kHz, $\bar{n} \approx 22.4$, $\eta \approx 0.111$). The states of the thermal distribution are included up to a missing population of 1×10^{-6} to accurately model the relative excitation probability for short times as well. At short times, the excitation probability is roughly an order of magnitude smaller for the first sidebands and the blue sidebands always has a larger coupling strength than the red sideband. The figure on the right shows the inferred thermal average population \bar{n} from comparison of the 1st red sideband and carrier excitation strength at various pulse times. The residual error from the true value \bar{n}_0 is shown as a dashed line and shows that the fractional error of \bar{n} is less than 10% for $t < 0.25$ ms. The rise of \bar{n} at very short times is due to the finite population included in the numerical calculation of the excitation probability and not physical. Since the difference between \bar{n} and \bar{n}_0 can be calculated for a given Lamb-Dicke parameter and pulse length, \bar{n}_0 can be determined from the inferred population \bar{n} with smaller uncertainty, if necessary.

Driving the red sidebands also allows for cooling below the Doppler-limit of the E1 cooling transition of the ion due to the narrow linewidth of the clock transition. Every excitation on a red sideband transition of order m removes m quanta of motion from the ion. Since the ion is confined within the Lamb-Dicke regime, any decay from the excited state (be it natural or facilitated with a repumper) occurs preferably on the carrier transition, i.e. no quanta of motion are gained or lost [Lei+03]. Effectively, this removes motional energy from the ion until a state with minimum energy is reached once the cooling process is balanced by heating processes. States with an average occupation number \bar{n} well below 0.1 have been observed [Lei+03].

Care has to be taken though, if the confinement of the ion is not sufficiently high enough to be well in the Lamb-Dicke regime. In that case, there is a significant amount of the total motional energy $E_{tot} = \sum_{n=0}^{\infty} E_n p_n(\bar{n})$, $E_n = \hbar\omega(n + 1/2)$ contained in Fock states with high n . As shown in Fig. 2.6, the coupling strength of the 1st red sideband can have its first minimum at a point n_{min} where a significant fraction of E_{tot} is contained in states with $n > n_{min}$. This means that driving the

2.3. Coherent interaction between cold ions and electromagnetic radiation

1st red sideband only couples weakly to a superposition of states around n_{\min} , causing reduced cooling performance. This discrepancy is not easily observable with temperature measurements on the 1st red sideband, so the 2nd order transition has to be employed instead. Not accounting for the remaining motional energy causes an incorrect frequency shift estimate.

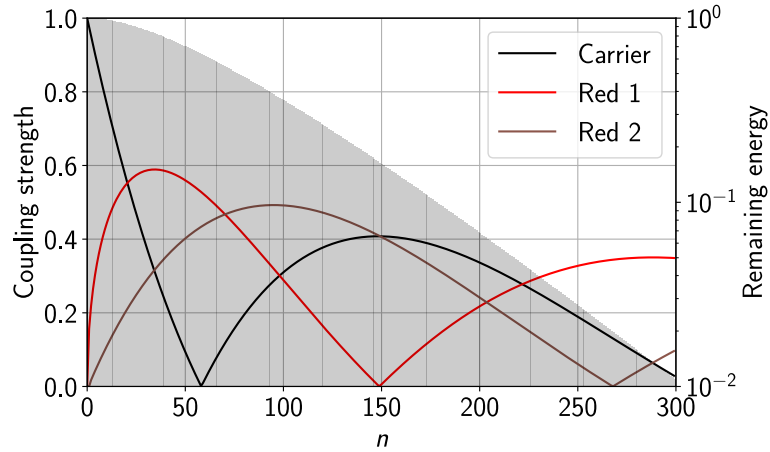


Figure 2.6.: *Motional energy contained within Fock states with large n . The relative coupling strength $|\Omega_{n,n+m}/\Omega_{0,0}|$ of the carrier ($m=0$), 1st red sideband ($m=-1$) and 2nd red sideband ($m=-2$) transitions for an ion in the same thermal motional state as in Fig. 2.4 ($\lambda = 435$ nm, $m = 171$ u, $T_D = 0.55$ mK, $\omega_{sec} = 2\pi \times 250$ kHz, $\bar{n} \approx 45.3$, $\eta \approx 0.157$) has several minima. The shaded histogram shows the remaining energy $E(m > n)$ in all states m larger than n relative to the total energy E_{tot} . This shows that around 16 % of the motional energy lie beyond the first zero crossing of the 1st red sideband. When cooling the ion on this transition, the kinetic energy will not be removed efficiently for a superposition of states around $n = 149$. If all energy contained within states with $n < 149$ is cooled to $n = 0$ and all energy in $n \geq 149$ is cooled to $n = 149$, a bimodal distribution with an average occupation number $\bar{n} \approx 24.3$ is realized, even though the excitation probability of the red sideband transition is significantly reduced. Interleaved cooling on the 2nd and 1st order sideband resolves this issue, such that only a small amount of motion cannot be cooled.*

Rabi spectroscopy Equation (2.43) assumes that the clock transition is excited on resonance, which means that the clock laser frequency ν_L is equal to the atomic center frequency ν_0 . In general, this is not true, there is some frequency detuning $\Delta\omega/(2\pi) = \Delta\nu = \nu_L - \nu_0$ of the laser from the atomic resonance. This changes $P_e(t)$ on the carrier transition to [Sha+18]

2. Optical clocks based on trapped ions

$$P_e(t, \Delta\omega, \Omega_0) = \frac{1}{2} \frac{1}{1 + \left(\frac{\Delta\omega}{\Omega_0}\right)^2} \left(1 - \sum_{n=0}^{\infty} p_n(\bar{n}) \cos \left(\sqrt{1 + \left(\frac{\Delta\omega}{\Omega_0}\right)^2} \Omega_{n,nt} \right) \right), \quad (2.47)$$

if the laser detuning is far away from the sideband transition at detuning ω_{sec} compared to the Rabi frequency Ω_0 ($|\Delta\omega - \omega_{\text{sec}}|/\Omega_0 \gg 1$). A few special cases can be more easily compared, if the ion is in its motional ground state ($\bar{n}=0$). In that case, Eq. (2.47) reduces to

$$P_e(t, \Delta\omega, \Omega_0) = \frac{1}{2} \frac{1}{1 + \left(\frac{\Delta\omega}{\Omega_0}\right)^2} \left(1 - \cos \left(\sqrt{1 + \left(\frac{\Delta\omega}{\Omega_0}\right)^2} \Omega_0 e^{-\eta^2/2t} \right) \right) \quad (2.48)$$

$$\approx \frac{1}{2} \frac{1}{1 + \left(\frac{\Delta\omega}{\Omega_0}\right)^2} \left(1 - \cos \left(\sqrt{1 + \left(\frac{\Delta\omega}{\Omega_0}\right)^2} \Omega_0 t \right) \right), \quad \eta \ll 1 \quad (2.49)$$

where the approximation in the last step is generally valid in the Lamb-Dicke regime. Two special cases are of interest in this thesis:

1. $t = \pi/\Omega_0, \Delta\omega = 0 \Rightarrow P_e(t, \Delta\omega, \Omega_0) = 1$: A *Rabi π -pulse* on resonance, that transfers the complete population of the ground state $|g\rangle$ into the excited state $|e\rangle$. It is useful to determine the maximum excitation probability which may be limited due to e.g. motional decoherence, insufficient ground state initialization or the natural lifetime of the excited state.
2. $t = \pi/\Omega_0, \Delta\omega \approx \pm 0.76\Omega_0 \Rightarrow P_e(t, \Delta\omega, \Omega_0) \approx 0.54$, $\frac{\partial}{\partial \Delta\omega} P_e(t, \Delta\omega, \Omega_0)$ is at an extremum: A pulse for which the laser is detuned from the resonance by the detuning $\Delta\omega$ where $P_e(t, \Delta\omega, \Omega_0)$ is maximally sensitive to variations of the laser frequency. At these points, the frequency information can be obtained most precisely with each clock pulse, which make them the optimal points to operate an optical clock. Conventionally, $\Delta\omega \approx \pm 0.8\Omega_0$ is chosen as the interrogation detuning instead, which corresponds to $P_e(t, \Delta\omega, \Omega_0) \approx 0.50$. The fractional reduction of $\frac{\partial}{\partial \Delta\omega} P_e(t, \Delta\omega, \Omega_0)$ is approximately 0.3% if this detuning is chosen compared to the optimum.

Finally, the natural lifetime of the excited state τ_e is related to the optimum interrogation time of an optical clock transition. Incorporating it into Eq. (2.49) changes the excited state population of a Rabi interrogation on resonance to ($\Gamma = 1/\tau_e$) [LL06]

$$P_e(t, 0, \Omega_0) = \frac{1}{2} \frac{e^{-\frac{\Gamma t}{2}}}{1 - \left(\frac{\Gamma}{4\Omega_0}\right)^2} \left(1 - \cos \left(\sqrt{1 - \left(\frac{\Gamma}{4\Omega_0}\right)^2} \Omega_0 t \right) \right) \quad (2.50)$$

in the limit where $\Omega_0 > \Gamma/4$. A general formula for P_e is derived in [LL06] without this assumption. The interrogation time that results in the smallest frequency instability of an optical clock is approximately equal to $1.88\tau_e$ [PST05], at which point the reduced linewidth and contrast loss balance with each other.

2.4. Properties of clock transitions of $^{171}\text{Yb}^+$ and $^{88}\text{Sr}^+$

The discussion of ion-light interaction in Section 2.3 is generally applicable to a variety of transitions with narrow linewidths. Three specific clock transitions are employed in this work, the $^2S_{1/2} \rightarrow ^2D_{5/2}$ E2 transition in $^{88}\text{Sr}^+$ as well as the $^2S_{1/2}(F=0) \rightarrow ^2D_{3/2}(F=2)$ E2 and $^2S_{1/2}(F=0) \rightarrow ^2F_{7/2}(F=3)$ E3 transition in $^{171}\text{Yb}^+$, which are depicted in Fig. 2.7. All ground and excited states apart from $^2F_{7/2}$ feature a closed inner electronic shell and a single outer electron. The $^2F_{7/2}$ state on the other hand is well described by the configuration $[\text{Xe}] 4f^{13} 6s^2$, a hole in the f-shell surrounded by a closed outer s-shell. All of these transitions have been employed as references for optical clocks in the past and are listed as secondary representations of the second [BIP19]. All states split into $2J + 1$ or $2F + 1$ substates in a weak magnetic field due to the Zeeman effect [Zee97]. Since a magnetic field is necessary to define a quantization axis for coherent ion-light interaction, the interrogated transitions are between a Zeeman substate in the ground and excited state, respectively.

Since the energy offset of each Zeeman state from the mean value is proportional to m_J or m_F , the transition frequency also varies proportional to the magnetic field if the magnetic quantum number of either the ground or excited state is not equal to zero or the Zeeman shift for both states is equal. So, the hyperfine structure resulting in $m_F=0$ Zeeman states in the ground and excited state in $^{171}\text{Yb}^+$ produces a transition frequency first-order insensitive to magnetic field variations. This reduces the amount of magnetic shielding necessary for long coherent interrogation heavily and is a large advantage of $^{171}\text{Yb}^+$ over $^{88}\text{Sr}^+$ as a clock. For the $^{88}\text{Sr}^+$ clock transition, every individual transition between Zeeman states is linearly sensitive to magnetic field variations. On the other hand, efficient cooling of $^{171}\text{Yb}^+$ requires a large magnetic field as discussed in section 2.2, which is inconvenient for high-precision clock operation. For this reason, the field needs to be switched between small and large amplitudes, resulting in a higher frequency instability due to the additional waiting time until the magnetic field magnitude

2. Optical clocks based on trapped ions

has reduced to a sufficiently small value. This is not necessary for $^{88}\text{Sr}^+$, where a constant small magnetic field is sufficient for efficient cooling and spectroscopy.

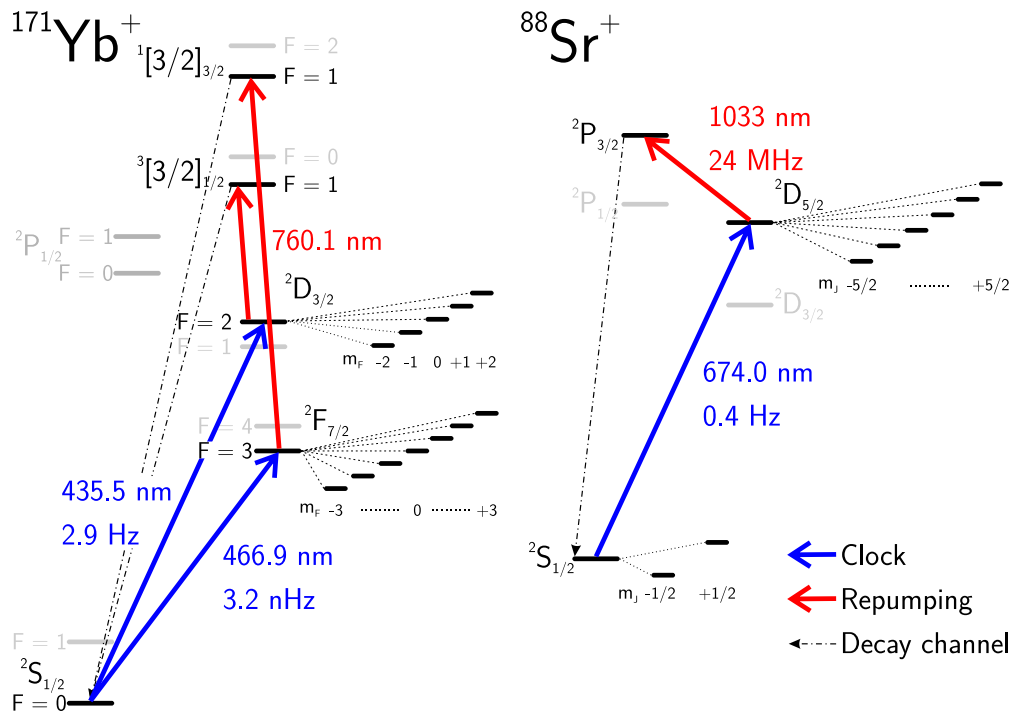


Figure 2.7.: Level structure of $^{171}\text{Yb}^+$ and $^{88}\text{Sr}^+$ relevant for clock operation. The simplified level structure of $^{171}\text{Yb}^+$ and $^{88}\text{Sr}^+$ relevant for clock operation. Other states relevant for Doppler cooling or additional hyperfine levels are depicted in a faint grey. All electronic states are labeled as $^{2S+1}L_J$, where L is the electronic angular momentum, S is the electronic spin and J the total electronic angular momentum. Exceptions are the bracket states $^3[3/2]_{1/2}$ and $^3[3/2]_{3/2}$, which are a result of JK pair coupling [Cow81, p. 128]. Since the $^{171}\text{Yb}^+$ nucleus possesses a nuclear spin of $I=1/2$, each electronic state splits into two hyperfine levels with angular momentum $F=J \pm 1/2$. For each optical transition (except for the $D_{3/2} \rightarrow ^3[3/2]_{1/2}$ transition described in Fig. 2.3) the center wavelength and natural linewidth are given, if known. The main decay channels from the excited states are shown, too. In a weak magnetic field the states split into a fixed number of sub-states due to the Zeeman effect with a shift from the mean value proportional to their magnetic quantum number m_J or m_F .

The magnetic field vector also determines the coupling strength of laser radiation with a given polarization to the different transitions between Zeeman substates. Given a magnetic field direction \vec{e}_B , laser propagation direction \vec{e}_k and linear laser polarization direction \vec{e}_p , two angles can be defined, which parametrize the coupling strength. One is the angle θ_k between \vec{e}_k and \vec{e}_B . The other is the angle φ_p , which is the angle between \vec{e}_p and \vec{e}_B in the plane spanned by \vec{e}_k and \vec{e}_B , if \vec{e}_k and \vec{e}_B

are not collinear. If they are collinear, the polarization has no influence on the coupling strength. The algebraic expressions for these angles are

$$\cos \theta_k = \vec{e}_B \cdot \vec{e}_k, \quad \sin \varphi_p = (\vec{e}_B \times \vec{e}_k) \cdot \vec{e}_p. \quad (2.51)$$

The relative coupling strength $c(\theta_k, \varphi_p) = \Omega_0(\theta_k, \varphi_p) / \max(\Omega_0(\theta_k, \varphi_p))$ for an E2 and E3 transition depends on the difference in the magnetic quantum number between the ground and excited state. For an E2 transition $|\Delta m| \leq 2$ and for an E3 transition $|\Delta m| \leq 3$ are possible, all higher $|\Delta m|$ have a coupling strength that is identically zero. For an E2 transition $c(\theta_k, \varphi_p)$ is [Tay96, p. 96]

$$c(\theta_k, \varphi_p) = \begin{cases} 4 \sin^2 \theta_k \cos^2 \theta_k \cos^2 \varphi_p & \text{if } |\Delta m| = 0 \\ (\cos^2 \theta_k - \sin^2 \theta_k)^2 \cos^2 \varphi_p + \cos^2 \theta_k \sin^2 \varphi_p & \text{if } |\Delta m| = 1 \\ \sin^2 \theta_k (\cos^2 \theta_k \cos^2 \varphi_p + \sin^2 \varphi_p) & \text{if } |\Delta m| = 2 \end{cases} \quad (2.52)$$

and is depicted in Fig. 2.8. For an E3 transition $c(\theta_k, \varphi_p)$ is [Tay96, p. 132]

$$c(\theta_k, \varphi_p) = \begin{cases} \frac{4}{N} \sin^2 \theta_k \cos^2 \varphi_p (1 - 5 \cos^2 \theta_k)^2 & \text{if } |\Delta m| = 0 \\ \frac{1}{16} \left(\cos^2 \theta_k \cos^2 \varphi_p (11 - 15 \cos^2 \theta_k)^2 + \sin^2 \varphi_p (1 - 5 \cos^2 \theta_k)^2 \right) & \text{if } |\Delta m| = 1 \\ \sin^2 \theta_k \cos^2 \varphi_p (1 - 3 \cos^2 \theta_k)^2 + 4 \sin^2 \theta_k \cos^2 \theta_k \sin^2 \varphi_p & \text{if } |\Delta m| = 2 \\ \sin^4 \theta_k (\cos^2 \theta_k \cos^2 \varphi_p + \sin^2 \varphi_p) & \text{if } |\Delta m| = 3, \end{cases} \quad (2.53)$$

where the normalization constant $N = \left(3 + 5 \cos \left(4 \arctan \left(\sqrt{13/2 - \sqrt{165}/2} \right) \right) \right)^2 + \sin^2 \left(2 \arctan \left(\sqrt{13/2 - \sqrt{165}/2} \right) \right) \approx 7.585$ is determined with Wolfram Mathematica and $c(\theta_k, \varphi_p)$ is depicted in Fig. 2.9.

2. Optical clocks based on trapped ions

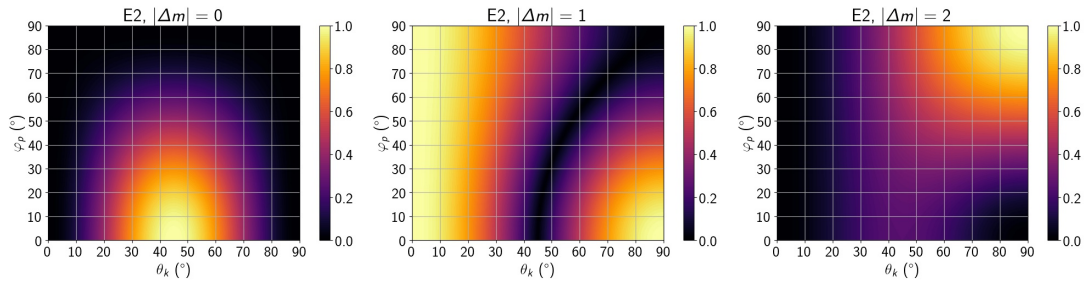


Figure 2.8.: *Coupling strength for an E2 transition. The relative coupling strength $c(\theta_k, \varphi_p) = \Omega_0(\theta_k, \varphi_p) / \max(\Omega_0(\theta_k, \varphi_p))$ of an E2 transition depends on the angles θ_k (angle between the magnetic field \vec{e}_B and laser propagation direction \vec{e}_k) and φ_p (angle between \vec{e}_B and the polarization direction \vec{e}_P in the plane spanned by \vec{e}_B and \vec{e}_k). $c(\theta_k, \varphi_p) = c(\pm\theta_k, \pm\varphi_p)$ and depends on the difference in the magnetic quantum number between the ground and excited state Δm . The three figures show $c(\theta_k, \varphi_p)$ for linear laser polarization and $|\Delta m| \leq 2$, higher differences cannot be coupled on an E2 transition.*

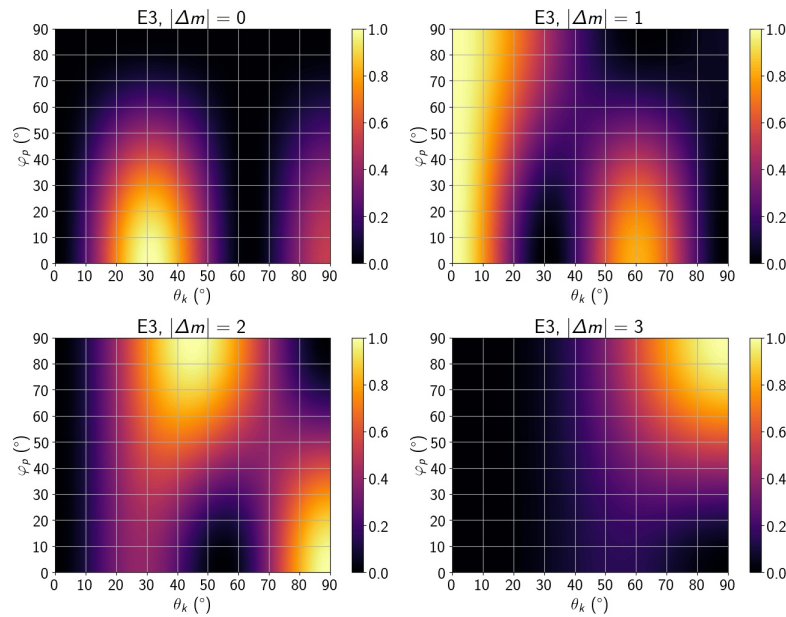


Figure 2.9.: *Coupling strength for an E3 transition. The relative coupling strength $c(\theta_k, \varphi_p) = \Omega_0(\theta_k, \varphi_p) / \max(\Omega_0(\theta_k, \varphi_p))$ of an E3 transition depends on the angles θ_k (angle between the magnetic field \vec{e}_B and laser propagation direction \vec{e}_k) and φ_p (angle between \vec{e}_B and the polarization direction \vec{e}_P in the plane spanned by \vec{e}_B and \vec{e}_k). $c(\theta_k, \varphi_p) = c(\pm\theta_k, \pm\varphi_p)$ and depends on the difference in the magnetic quantum number between the ground and excited state Δm . The four figures show $c(\theta_k, \varphi_p)$ for linear laser polarization and $|\Delta m| \leq 3$, higher differences cannot be coupled on an E3 transition.*

State detection For the clock transitions discussed here, when the ion is in the excited state $|e\rangle$, it leaves the Doppler cooling cycle, since it does not couple to the relevant lasers anymore. This fact can be exploited to measure the excitation probability P_e with fluorescence detection. If the ion is in the ground state $|g\rangle$, it couples to the Doppler cooling lasers and will fluoresce in the same way as during Doppler cooling. This is called a *bright* state and corresponds to the case that the clock transition was not excited. On the other hand, if the ion was excited, it is in $|e\rangle$, there will be no fluorescence and a *dark* state will be detected. This directly corresponds to a projective measurement in $|g\rangle$ or $|e\rangle$, respectively. P_e can be approximately determined by interrogating the transition with the same parameters N times and detecting k dark states. Then $P_e \approx k/N$, with a statistical uncertainty limited by N .

Repump transitions While the ion returns to $|g\rangle$ through direct decay after approximately the excited state lifetime, this introduces a comparatively long time the clock is not in operation and increases its frequency instability. In principle it is possible to drive the clock transition in reverse $|e\rangle \rightarrow |g\rangle$, but often an additional transition is used that couples $|e\rangle$ to another state with short lifetime that preferably decays back into $|g\rangle$. The Rabi frequency on the *repump*, *clear-out* or *quench* transition is significantly larger than the Rabi frequency of the clock transition. This way, the ion can be returned to the Doppler cooling cycle quickly and consistently with a laser that does not need to fulfill the same strict frequency stability criteria as the clock laser.

For the $^2D_{5/2}$ state in $^{88}\text{Sr}^+$, the $^2D_{5/2} \rightarrow ^2P_{3/2}$ E1 transition at 1033 nm is used for this purpose. For the $D_{3/2}(F=2)$ state in $^{171}\text{Yb}^+$, resonant with the $^2D_{3/2}(F=2) \rightarrow ^3[3/2]_{1/2}(F=1)$ transition, the situation is more complicated, since the Doppler cooling repumper already couples to the $^2D_{3/2}(F=1)$ state. The frequency difference between the cooling repumping transition and clock repumping transition is only approximately 3.1 GHz, which means that the Doppler cooling process necessary for state detection can clear out the $D_{3/2}(F=2)$ state, causing bright detections, even though the clock transition was successfully excited. This limits the 935 nm intensity during the detection process and maximum detectable excitation probability. The repump transition for the E3 transition is $^2F_{7/2}(F=3) \rightarrow ^1[3/2]_{3/2}(F=1)$ at 760 nm and is itself an E2 transition due to the angular momentum difference and parity conservation between the states. This means that a comparatively high laser intensity is necessary to drive the transition quickly enough and the laser needs to be frequency stabilized sufficiently well. Another clear-out scheme only employing an M1 transition at 638 nm also exists [Für+20], but requires also a repumper from the $^2D_{5/2}$ state at 1650 nm.

State initialization One requirement for a high clock excitation probability is that the ion is initially in a single ground state $|g\rangle$. If the ground state of the

2. Optical clocks based on trapped ions

Doppler cooling cycle possesses multiple sublevels, the population is spread over a subset of these levels, instead. Population in the excited states ${}^2P_{1/2}$ and ${}^2D_{3/2}$ after cooling is stopped can be disregarded, since their lifetime is short either naturally or due to the repump lasers. Generally, the Doppler cooling lasers have to be turned off before driving the clock transition and by slightly ($\approx 100 \mu\text{s}$) delaying the shut-off of the repump laser compared to the cooling lasers, it can be ensured that the ion is in one of the sub-states of the ${}^2S_{1/2}$ manifold.

In the case of ${}^{171}\text{Yb}^+$, the ion should be initialized in the ${}^2S_{1/2}(F=0)$ hyperfine state, which does not possess any Zeeman sub-states apart from the single $m_F=0$ state. For this reason, it is sufficient to implement a process that transfers population from the ${}^2S_{1/2}(F=1)$ states into the ${}^2S_{1/2}(F=0)$ state. This is achieved by driving the ${}^2S_{1/2}(F=1) \rightarrow {}^2P_{1/2}(F=1)$ transition at a frequency offset of 2.1 GHz from the main Doppler cooling transition, since the ${}^2P_{1/2}(F=1)$ state preferably decays into the ${}^2S_{1/2}(F=0)$ state. After 1 ms, more than 90% of the population are pumped into ${}^2S_{1/2}(F=0)$, finishing state initialization for the ${}^{171}\text{Yb}^+$ E2 and E3 transition.

Due to the missing hyperfine structure, the process is more complicated for ${}^{88}\text{Sr}^+$, since the ground state ${}^2S_{1/2}$ is split in two Zeeman substates with $m_J = \pm 1/2$. At the magnetic field strength used in this thesis, the frequency splitting between the two states is less than 20 MHz, the natural linewidth of the Doppler cooling transition. For this reason, the states are approximately equally populated and it is not possible to address only one m_J state using frequency offsets as for the hyperfine states in ${}^{171}\text{Yb}^+$. One popular option for state initialization is to use a circularly polarized Doppler cooling laser and align the magnetic field with the propagation direction of this laser [HAP72]. This initialization procedure works well, if the magnetic field can be set to coincide well with the laser propagation vector and only one of the m_J states is needed for the experimental sequence. If both m_J states are required, either the laser polarization needs to be switched on the fly, e.g. with a Pockels cell, or the magnetic field direction needs to be changed, introducing magnetic field transients.

Another option not requiring additional optical devices or boundary conditions on the magnetic field is to use the ${}^2S_{1/2} \rightarrow {}^2D_{5/2}$ clock and ${}^2D_{5/2} \rightarrow {}^2P_{3/2}$ repump transition already in use for clock operation. This method is employed in some ion trap quantum processors as well to achieve initial states with high purity [Pog+21; Pji22]. The procedure is shown in Fig. 2.10 and works as follows after Doppler cooling:

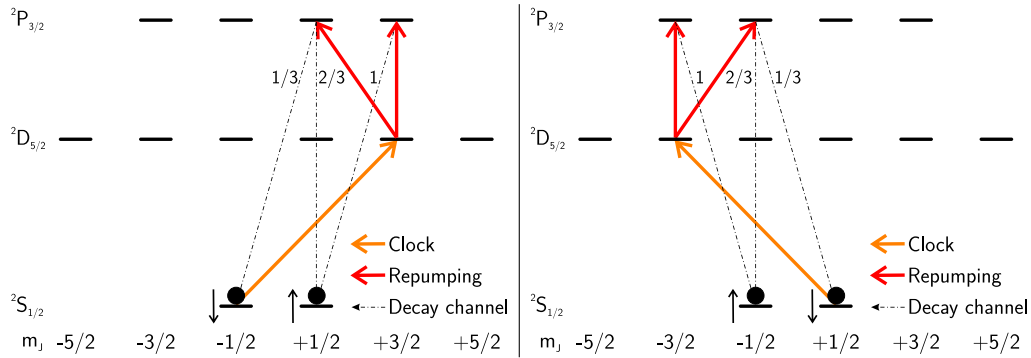


Figure 2.10.: Clock pumping for $^{88}\text{Sr}^+$. The figures illustrate the state initialization process for $^{88}\text{Sr}^+$ in either $^2S_{1/2}(m_J=+1/2)$ on the left hand side or $^2S_{1/2}(m_J=-1/2)$ on the right hand side. After Doppler cooling, both states are roughly equally populated. The clock laser addresses the outermost possible transition $^2S_{1/2}(m_J=\pm 1/2) \rightarrow ^2D_{5/2}(m_J=\mp 3/2)$ and completes a π pulse, such that the maximum amount of population is transferred into the corresponding excited state. Then it is repumped into the $^2P_{3/2}$ state where it decays back into the ground state within ns. The repump laser is polarization modulated to excite both the $\Delta m=0$ and $\Delta m=\pm 1$ transitions. Due to Clebsch-Gordan coefficients for the $^2D_{5/2} \rightarrow ^2P_{3/2}$ transition and the selection rules of the decay into $^2S_{1/2}$, most of the population decays into the opposite Zeeman ground state compared to where the initial clock pulse started. The squared Clebsch-Gordan coefficients of the decay channels are shown next to the corresponding arrows. By repeating this procedure multiple times, the population in this state grows and the population in the other state shrinks, both indicated by arrows next to the corresponding state.

1. Drive a π -pulse on the $^2S_{1/2}(m_J=\pm 1/2) \rightarrow ^2D_{5/2}(m_J=\mp 3/2)$ transition, which transfers the maximum amount of population into the excited state. This is the maximum possible Δm transition from the state which is to be depleted.
2. Turn on the 1033 nm repump laser for $\approx 10 \mu\text{s}$ to quench the excited state. While this laser does not selectively drive transitions between Zeeman sub-states due to the broad linewidth, it is an E1 transition nonetheless. This means that it can only change the magnetic quantum number m_J between the $D_{5/2}$ and $^2P_{3/2}$ states by a magnitude of 0 or 1. For this reason, only the states $^2P_{3/2}(m_J=\mp 3/2)$ and $^2P_{3/2}(m_J=\mp 1/2)$ are reached, respectively.
3. After a few ns the $^2P_{3/2}$ state decays into the $^2S_{1/2}$ state on an E1 transition. While this decay can reach both Zeeman sub-states, it preferably decays into the $^2S_{1/2}(m_J=\mp 1/2)$ state, which does not couple to the initial clock pulse. Consequently, there is now a population imbalance between the $^2S_{1/2}(m_J=+1/2)$ and $^2S_{1/2}(m_J=-1/2)$ state.
4. Repeat this process until the desired state initialization purity is reached. This process is limited by off-resonant excitations of other transitions by

2. Optical clocks based on trapped ions

the initial clock laser pulse, depending on the Rabi frequency, magnetic field and secular frequencies of the ion. Purities of 95 % are reached within 1 ms, limited by the Rabi frequency of the clock laser and separation of the adjacent transitions in a magnetic field of approximately 4 μT , and are sufficient for clock spectroscopy.

Since this process is largely independent of the magnetic field direction, as long as the $|\Delta m=2|$ transition has a sufficiently large Rabi frequency, and can easily switch between initialization in either ground state by changing the clock laser frequency, it is suitable for the experiments in this thesis. Usually, 1-5 ms are spent on state initialization, similar to the time for Doppler cooling. The process described here is the pulsed variant, but it is also possible to continuously pump with both the 674 nm clock laser and 1033 nm repump laser. The only care that has to be taken is that the 1033 nm laser can cause a significant Stark shift of the clock transition, changing the frequency where pumping is most effective. This can be mitigated by setting the frequency of the 1033 nm on resonance, where the Stark shift is zero. In practice, scanning the repump laser frequency and measuring the initialization purity is a quick and reliable way to determine the optimum setting.

2.5. Resolved sideband cooling of the $^{88}\text{Sr}^+$ and $^{171}\text{Yb}^+$ ions and heating rate measurements

Both the $^{171}\text{Yb}^+$ E2 and $^{88}\text{Sr}^+$ E2 transition are good options to implement resolved sideband cooling on, but it is easier on the $^{88}\text{Sr}^+$ transition. The differences between $^{171}\text{Yb}^+$ and $^{88}\text{Sr}^+$ come from how the decay into the ground state limits the number of cooling pulses before the ion needs to be reinitialized. While this is in principle possible on the $^{171}\text{Yb}^+$ E3 transition as well, the small coupling strength would necessitate very large laser intensities without a significant advantage over the $^{171}\text{Yb}^+$ E2 transition. The general idea is to excite the red motional sidebands at detuning ω_{sec} from their respective carrier transitions and decay back to the ground state on a carrier transition due to the Lamb-Dicke regime as described in Section 2.3.

For $^{88}\text{Sr}^+$, the sideband cooling sequence is as follows:

1. The ion is pumped into the $m_J = -1/2$ ground state with the procedure described in Section 2.4.
2. The red sideband of the $^2S_{1/2}(m_J = -1/2) \rightarrow ^2D_{5/2}(m_J = -5/2)$ transition is excited with a π -pulse.
3. The 1033 nm repump transition is driven for $\approx 10 \mu\text{s}$, causing the population to reach the $^2P_{3/2}(m_J = -3/2)$ state. Other states cannot be reached since

this is an E1 transition.

4. From the branching ratios in the $^2P_{3/2}$ state [Zha+16], 94.1% of all decays reach the $^2S_{1/2}(m_J = -1/2)$ state, the initial state before the sideband cooling pulse. Because of this, the $^2S_{1/2}(m_J = -1/2) \rightarrow ^2D_{5/2}(m_J = -5/2) \rightarrow ^2P_{3/2}(m_J = -3/2) \rightarrow ^2S_{1/2}(m_J = -1/2)$ set is called a *cycling* transition, since no reinitialization of the state is necessary after sideband cooling most of the time. On average, 12 such cycles can be performed, before it is more likely that at least one decay did not immediately reach the $^2S_{1/2}$ state, which can, but does not have to, interrupt the cooling cycle.
5. The next most likely decay 5.3% of the time is back into the $^2D_{5/2}$ state. By using Clebsch-Gordon coefficients it is possible to determine the branching ratio of the decay into $^2D_{5/2}(m_J = 5/2, -3/2, -1/2)$. 2/3 of all decays reach the state $^2D_{5/2}(m_J = -5/2)$, so they do not leave the cycling transition by being excited into the $^2P_{3/2}$ state again. The other states on the other hand now enable decays into the $^2S_{1/2}(m_J = +1/2)$ state, leaving the cooling cycle. This limits the amount of cooling cycles to approximately 25 before the ion state has to be reinitialized. This is done without heating up the ion using the standard procedure described in Section 2.4. So the sequence 2-3-4 is interrupted by step 1 every 25 cooling pulses.

The last possible decay from the $^2P_{3/2}$ state is into the $^2D_{3/2}$ state with a probability of 0.6%. If the 1092 nm laser is turned off, the ion is trapped there for the lifetime of 430 ms [Sah+06]. This happens after approximately 120 cycles, so is only an issue if a lot of cooling is necessary. By turning on the 1092 nm repump laser, the ion can be returned to the $^2S_{1/2}$ state and reinitialized for further cooling. The natural decay from the $^2D_{5/2}$ state does not significantly influence the cooling performance, since usually the cycling time is much shorter than the excited state lifetime.

Due to the cycling nature of the resolved sideband cooling of $^{88}\text{Sr}^+$, the clock and 1033 nm laser can also be turned on simultaneously for a cooling time t , interleaved with reinitialization of the $^2S_{1/2}$ state. The same caveat regarding the light shift of the 1033 nm laser on the clock transition as for the state initialization in Section 2.4 applies here as well.

For $^{171}\text{Yb}^+$ the sideband cooling sequence is different due to the different method of state initialization:

1. Initialize the ion in the $^2S_{1/2}(F=0)$ state with the 370 nm cooling transition.
2. Excite the red sideband of the $^2S_{1/2}(F=0, m_F=0) \rightarrow ^2D_{3/2}(F=2, m_F=0)$ transition with a π -pulse.
3. Turn on the 935 nm repump laser to drive the $^2D_{3/2}(F=2) \rightarrow ^3[3/2]_{1/2}(F=1)$ transition, which decays primarily into the $^2S_{1/2}(F=0)$ state. This also forms a cycling transition and allows for many cooling pulses before the ion

2. Optical clocks based on trapped ions

has to be reinitialized.

4. A decay into the ${}^2S_{1/2}(F=1)$ state is also possible with smaller probability, which requires reinitialization with the 370 nm laser. This needs to be done as shortly as possible, since the broad linewidth of the cooling transition causes heating of the ion up to the Doppler limit. A reinitialization time of 10 μs after each cooling pulse proves effective and allows for cooling below $\bar{n}=1$.
5. Repeat step 2-3-4 as long as necessary.

Due to the heating of the 370 nm laser, continuous cooling is more challenging on ${}^{171}\text{Yb}^+$ and not employed in this thesis.

Heating rate measurements Resolved sideband cooling is used to determine the heating rate of the axial motional mode of the trapped ion. Specifically, a single ${}^{88}\text{Sr}^+$ ion is confined with an angular axial secular frequency of $\omega_{\text{ax}}=2\pi \times 374$ kHz and continuously sideband-cooled on the red sideband of the $|S, m_S=-1/2\rangle \rightarrow |D, m_D=-5/2\rangle$ carrier transition for 20 ms. Then, the excitation probability of the red and blue motional sidebands of the same carrier transition is determined at the same laser intensity and probe time. This allows for a measurement of \bar{n} according to Eq. (2.46) which is converted into a temperature with $T_{\text{axial}}=\hbar\omega_{\text{ax}}\bar{n}/k_B$. This "classical" temperature disregards the zero-point energy and corresponding modified relationship between temperature and the average population of the quantum harmonic oscillator. For the minimum observed average occupation number is $\bar{n}_{\text{axial}}=0.220(6)$, which corresponds to a population of the motional ground state with 82 % probability [Die+89], the classical temperature equals $T_{\text{axial}}=3.9(1)$ μK . After ground state cooling, a variable amount of time t_{settle} passes without sideband or Doppler cooling before the temperature of the ion is determined. This allows for measurement of the axial heating rate $\Delta\bar{n}_{\text{axial}}/\Delta t=40(2)/\text{s}$ or $\Delta T_{\text{axial}}/\Delta t=0.72(3)$ mK/s, which is an important parameter for determining the thermal motional shift of ion clocks.

A similar measurement is performed to measure the heating rate of the radial motional modes. Due to the higher temperature of the radial modes after sideband cooling, the excitation probability ratio between the red sidebands and carrier transition is employed to measure \bar{n} instead. Since η is a parameter in this measurement, both the secular frequency and projection of the motion onto the clock laser need to be accounted for. The projection of the radial modes on the interrogating beam is determined by measuring the excitation strength of each sideband with two beams orthogonal to each other. As a result, the direction of radial motion of the mode with a higher secular frequency encloses an angle of $57(8)^\circ$ with the plane in which the Doppler cooling lasers propagate and the other mode encloses an angle of $33(8)^\circ$ at $\omega_x=2\pi \times 1347$ kHz and $\omega_y=2\pi \times 1324$ kHz. By varying t_{settle} and using Eq. (2.45) to determine the radial temperature along the x-axis and

2.5. Resolved sideband cooling of the $^{88}\text{Sr}^+$ and $^{171}\text{Yb}^+$ ions and heating rate measurements

y-axis $T_{x,y}$, a heating rate of $\Delta\bar{n}_x/\Delta t = 190(23)/\text{s}$ or $\Delta T_x/\Delta t = 12.3(1.5) \text{ mK/s}$ and $\Delta\bar{n}_y/\Delta t = 195(19)/\text{s}$ or $\Delta T_y/\Delta t = 12.4(1.2) \text{ mK/s}$ is found. Later measurements show a significantly larger value of $18.1(2.2) \text{ mK/s}$ for the average radial heating rate at a similar trap depth, which is used for the correction of the thermal frequency shift in Section 6.2. It is assumed that the large radial heating rate is the result of electric field gradients connected to uncompensable axial micromotion [Kal+21], but. Both the measurements of the axial and radial heating rates are shown in Fig. 2.11.

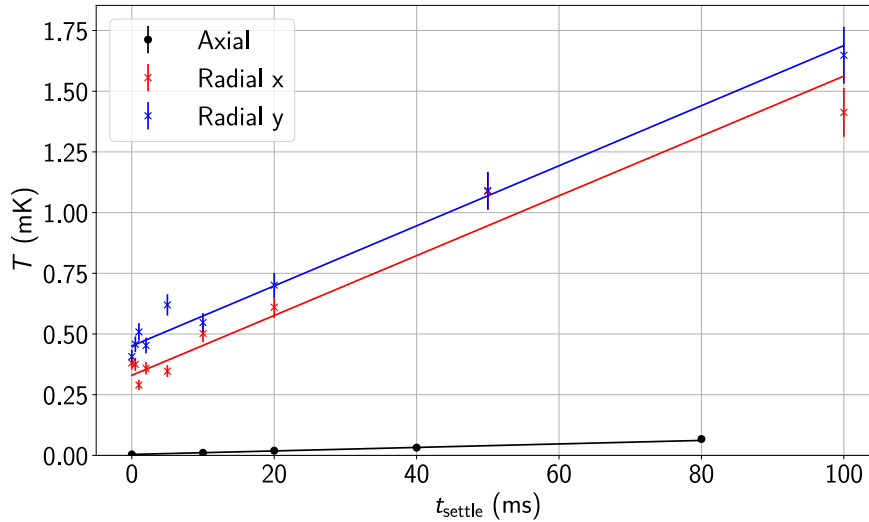


Figure 2.11.: *Heating rate measurement for axial and radial motion. The temperature of the axial and radial directions of motion is determined via resolved-sideband spectroscopy on the $^{88}\text{Sr}^+$ clock transition. The axial mode is cooled close to the motional ground state, while the radial modes are cooled below the Doppler limit of the E1 cooling transition, but do not reach below $\bar{n}=1$. The ion is not cooled for the time t_{settle} and then the average population \bar{n} of the motional mode is measured. A heating rate of $0.72(3) \text{ mK/s}$ is observed for the axial motion as well as $12.3(1.5) \text{ mK/s}$ and $12.4(1.2) \text{ mK/s}$ for the radial motion along the x-axis and y-axis, respectively.*

3. Experimental setup for the multi-species, multi-ion clock YbSr1

This chapter describes the experimental apparatus employed for the measurements reported in this thesis. Specifically, the multi-segment, multi-ion linear trap in which the ions are stored for the measurements is discussed. The optical setup around the trap including cooling lasers, repumping lasers, clock lasers and the imaging system is described along with the cooling laser stabilization and distribution setups. The DC and AC magnetic fields are measured using the clock transitions directly to correct for any systematic effects in the measurements presented. The background pressure in the Ultra High Vacuum (UHV) environment is determined from reordering of an ion crystal to estimate the pressure frequency shift for the optical clock. Finally, the $^{88}\text{Sr}^+$ clock laser setup consisting of an External Cavity Diode Laser (ECDL) that is Pound-Drever-Hall (PDH)-locked to a filter cavity, amplification of the cavity transmission with an injection diode and Tapered Amplifier (TA) as well as stabilization of the laser to the E3 clock laser via a frequency comb is presented.

3.1. Chip-based multi-ion trap for YbSr1

The ion trap used for YbSr1 is based on a design from and built by the research group *Quantum clocks and Complex Systems* headed by Prof. Dr. Tanja Mehlstäubler in the research institute Centre for Quantum Engineering and Space-Time Research (QUEST) located on PTB campus [Kel+19; Hau+25; Jor+25]. In particular, Malte Brinkmann published a Master thesis partially on building the specific trap in operation in YbSr1 [Bri20, ch. 3]. For this reason, I will only summarize the key points of the design and focus on the specifics relevant for the measurements discussed in the thesis. Photographs of the trap are shown in Fig. 3.1.

The body of the trap consists of four Printed Circuit Board (PCB) chips stacked on top of each other with a gap in the middle. The chip material is Rogers 4350B [Cor22] and all conducting paths on them are coated with gold. The whole trap is situated in UHV with a pressure below 1×10^{-10} mbar = 10 nPa for

3. Experimental setup for the multi-species, multi-ion clock YbSr1

experiments carried out between June 2020 and June 2023 and a pressure below 1×10^{-9} mbar = 100 nPa since then. The ions are confined in the middle of the gap with RF and DC voltages delivered to individual electrode segments etched into the trap chips. Eight such segments in addition to two so-called *endcap* electrodes on the outer edges of the gap exist on each of the four boards. The RF voltage providing the radial confinement, is common to all segments and delivered to the trap via copper strips. These connect directly to a carrier board on which the trap is glued with metal posts and mounted to the vacuum flange.

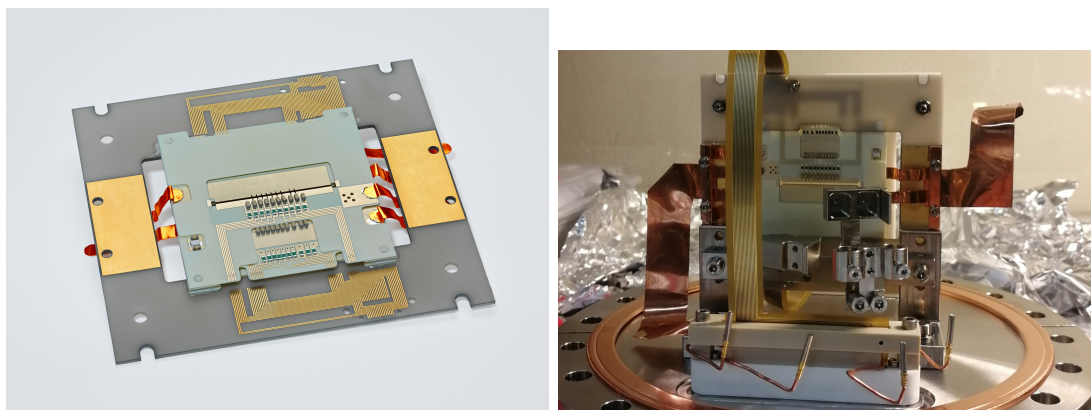


Figure 3.1.: *Photographs of the ion trap used in YbSr1. The image on the left shows the front side facing the imaging system, the image on the right shows the back side facing the samples of Yb and Sr. The trap consists of a stack of four PCB boards hand-assembled to form a linear trap for ions in the gap in the middle. Several resistors and capacitors are soldered on the chips to filter voltage noise with frequencies above 135 Hz on the trap electrodes. The DC signals are carried via a flexible PCB ribbon shown on the left, the RF voltage is delivered via copper strips.*

The DC voltages on the other hand are individually supplied to each of the 40 electrodes via tracks on the chips, with intermediate electric low-pass filters with a cut-off frequency of 135 Hz. These are necessary to minimize the electric field noise the ions experience at their secular frequency > 100 kHz, which leads to heating of the ion. When building the trap into the vacuum system, some of the filter capacitors fell off the trap body, exposing the electrodes to all external noise. To mitigate this problem, external filters are added to the DC supply, which will be discussed later in this section. Axial confinement of the ions is provided by applying a positive voltage on electrodes on either side of the trap segment, approximating a harmonic potential in its center. Additionally, voltage gradients can be applied to both the electrodes on the inner chips as well as the outer chips to move the ion position relative to the trapping geometry. This is necessary to compensate stray electric fields, thereby minimizing micromotion in the radial direction. A sketch of the electrodes and their positioning is shown in Fig. 3.2. The DC voltages as well as the connections to two Pt100 temperature sensors are delivered to the

chips from the carrier board via a flexible cable printed with conducting tracks. Due to the low thermal conductivity of Rogers 4350B, the temperature readings deviate from the temperature of electrodes in the close vicinity of the ion. Both the RF and DC signals are supplied to the carrier board by vacuum-feedthroughs, connected to the RF resonator and DC supply, respectively.

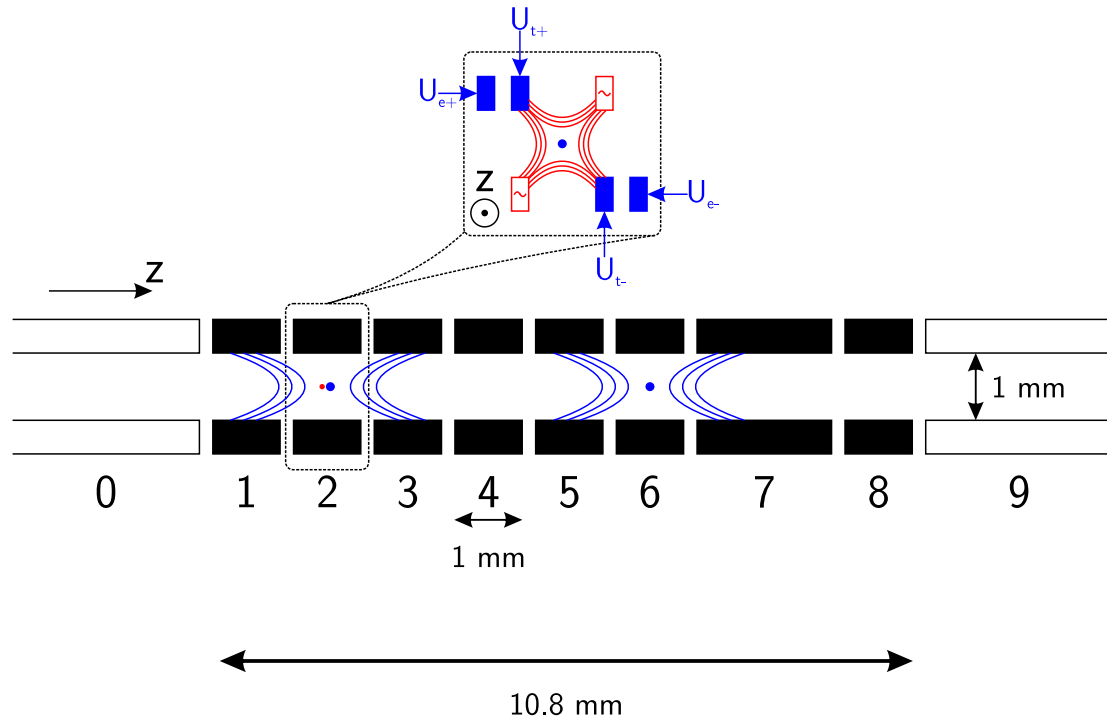


Figure 3.2.: *Sketch of the trap electrodes and their function. This sketch shows the region in the center of the trap chips where the ions are confined. It is divided along the z -axis into 10 segments, for which the applied DC voltage can be controlled individually. All segments apart from segment 7 have the same length, width and height of 1 mm. Segment 7 is twice as long to reduce edge effects for long ion strings, but was not used for spectroscopy in this thesis. The ions are interrogated in segment 2 and can be stored for further use in any other segment (such as segment 6 depicted here). Axial confinement (represented as blue arcs) is provided with an applied DC voltage on neighbouring segments and radial confinement (represented as red arcs) with a RF voltage common to all segments. The inset shows the view along the trap axis of one segment, revealing the individual electrodes to which DC (blue) and RF voltages are applied. Voltage gradients between U_{t+} , U_{t-} , U_{e+} and U_{e-} allow positioning the ion radially in the center, minimizing excess micromotion.*

The RF voltage is supplied by a Direct Digital Synthesis (DDS) controlled with

3. Experimental setup for the multi-species, multi-ion clock YbSr1

an Advanced Real-Time Infrastructure for Quantum physics (ARTIQ) system, producing up to $10 \text{ dBm} = 10 \text{ mW}$ of output power at 13-14 MHz. This is amplified by 25 dB with a broadband external amplifier and fed into a tunable RF resonator. Radial secular frequencies of up to 870 kHz have been observed on $^{171}\text{Yb}^+$ with this setup. The resonator is connected to the ion trap with a vacuum feed-through. While connected to the ion trap, the resonance frequency of the resonator can be adjusted from 12.8 MHz to 13.7 MHz with a variable capacitance connected between the RF coil and the grounded housing. The quality factor of the resonator and trap together is $Q = \Omega_0 / \Delta\Omega = 425$, filtering out a large amount of electric field noise at the secular frequencies of the ion. A pick-off of the RF voltage allows to monitor the trap depth with a power detector that converts the RF signal into a DC voltage. Under normal operating conditions the power varies by less than 0.02 dB, which corresponds to an instability of the radial secular frequencies of 2%.

The supply of the DC voltage has varied over the lifetime of the experimental setup. The trap electrodes are connected to two 40-pin D Subminiature (DSUB) vacuum feed-throughs, exposing the pins to the outside of the vacuum chamber. Initially, a DSUB cable was directly connected to a Digital-to-Analog Converter (DAC) controlled via ARTIQ, allowing to apply voltages from -10 V to 10 V to the electrodes. Since some of the U_e electrodes are missing the capacitors of their intravacuum electric lowpass filters, these were replaced with external lowpass filters with a cutoff frequency of 160 Hz. While this setup allows for the trapping and cooling of ions, coherent spectroscopy is limited after Doppler cooling due to the comparatively low axial secular frequency of 270 kHz for $^{171}\text{Yb}^+$.

For this reason, two different kinds of voltage amplifiers were added over time. Their inputs are still controlled by the same DAC, but translate the input voltages to larger voltages while retaining the ability to apply gradients with sufficient accuracy. The first amplifier consisted of four operational amplifiers manually connected to the electrodes U_{t+} and U_{t-} in segment 1 and 3. They are supplied with 32 V and -3 V and amplify the input voltage to allow for output voltages in the range -1.7 -29 V, sufficient for micromotion compensation and allowing for secular frequencies up to 460 kHz for $^{171}\text{Yb}^+$.

This amplifier was eventually replaced by a device designed and built by an electronic workshop at PTB with operational amplifiers supplied by voltages of 90 V and -15 V . This amplifier connects to all electrodes and provides different gain for the U_t and U_e electrodes, allowing for gradients sufficient for micromotion compensation as well as voltages above 50 V, the rating limit of the filter capacitors on the ion trap. The relation between the input and output voltages is determined semi-automatically by setting voltages with the DAC and measuring the output with a digital multimeter, finally fitting a linear model including cross-talk between the voltages applied to the electrodes of a segment. This allows for straight-forward and precise control of large confinement voltages as well as voltage gradients created

via the electrodes of all trap segments.

Due to individual control over all segments, ions can also be transferred between the trapping regions. This is useful to store ions in other segments while loading or during certain parts of spectroscopic sequences involving multiple ions. The sequence to split an ion crystal and transfer it to another segment is depicted in Fig. 3.3 and consists of the following steps:

1. Add an additional confinement voltage on one side of the trapping region.
2. Lower the confinement voltage of the trapping region towards the next segment to produce a potential well that stretches over two segments.
3. Increase the confinement voltage of the middle segment to split the ion crystal into two separate trapping regions, sharing a common endcap.
4. Repeat this sequence once more to completely separate the ions from each other.

Merging two ions with an adjacent endcap voltage works the same way, but in reverse. All of these sequences (split, transfer, merge) are reliable with no failure after 100 repetitions and are combined for automatic loading of ions and in certain spectroscopic sequences.

3. Experimental setup for the multi-species, multi-ion clock YbSr1

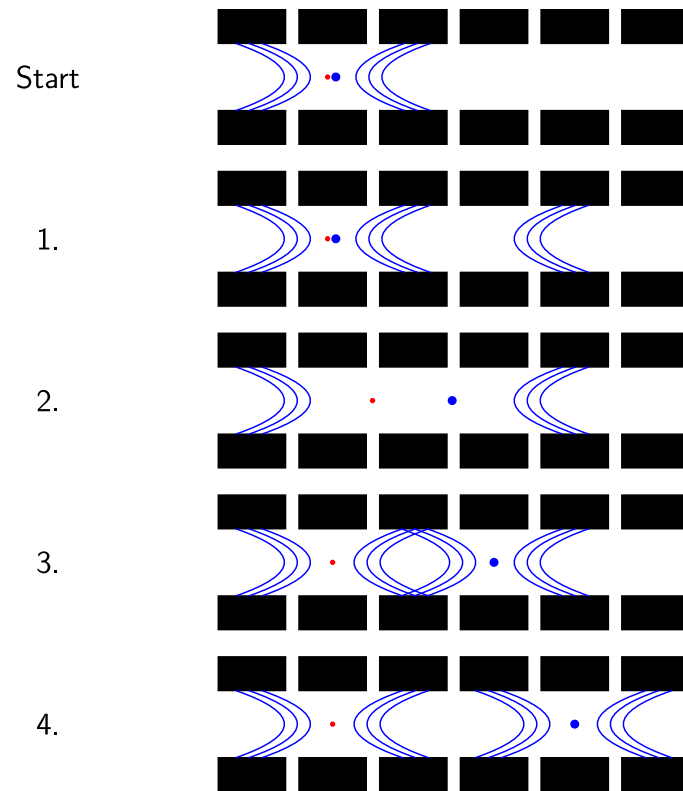


Figure 3.3.: *Sketch of the ion transfer sequence. The sequence to separate ions in a crystal and split them to two independent segments is depicted in this figure. It starts with an ion crystal aligned along the trap axis (Start). Then, a new confinement voltage is added and the previous confinement removed (1, 2). This produces a very shallow potential spread over multiple segments (2). By increasing the confinement voltage in the middle of the crystal, they are split and share a common endcap electrode (3). By repeating this sequence, they can be separated completely (4).*

3.2. Doppler cooling lasers

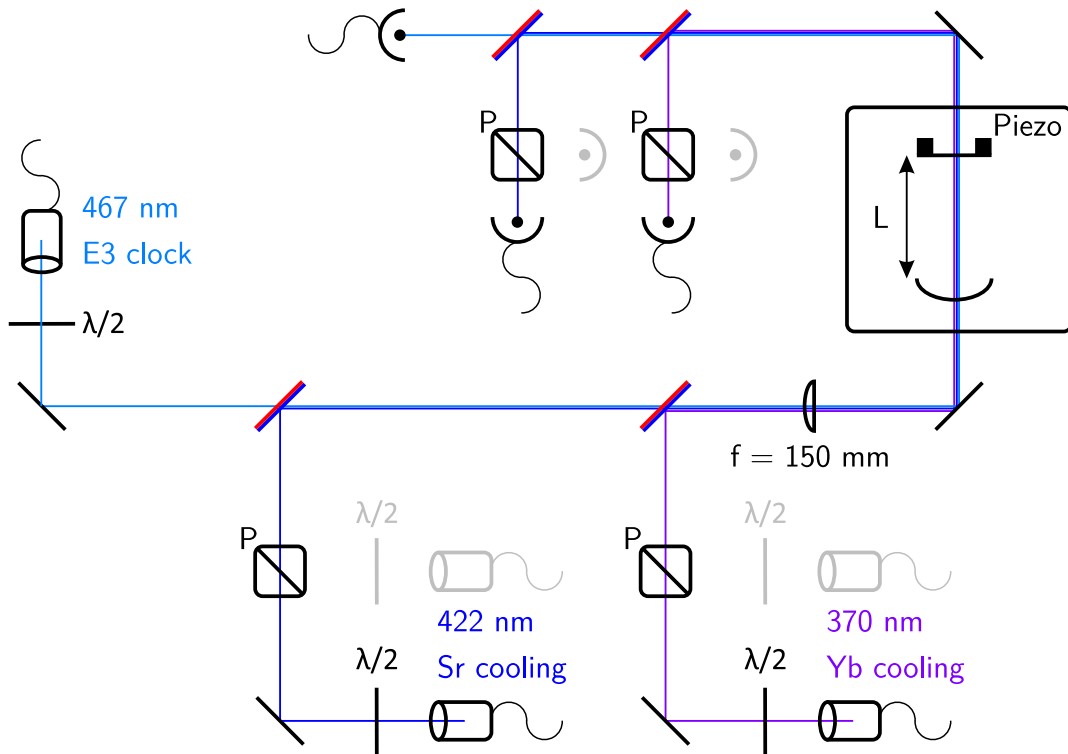


Figure 3.4.: Sketch of the Doppler cooling laser stabilization setup. The lasers to Doppler cool $^{171}\text{Yb}^+$ and $^{88}\text{Sr}^+$ are stabilized to the E3 clock laser via an optical resonator. All lasers are delivered to the setup with Polarization Maintaining (PM) fibers. The resonator length L is continuously scanned with the piezoelectric actuator mounted on one side of the outcoupling mirror such that all lasers are transmitted at some point during the scan. Lasers at different wavelengths are overlaid with each other at dichroic mirrors. Lasers at the same wavelength, but originating from different setups, such as the ones shown in gray, are overlaid via their polarization with Polarizing Beam Splitter (PBS). The polarization is adjusted with a Half Waveplate (HWP) to have maximum transmission or reflection at the PBS. The collimated laser beams are matched to the incoupling mode of the resonator with a lens with a focal length of 150 mm. The overlaid lasers are separated after the resonator with dichroic mirrors and PBS, their intensity is measured with photodiodes. The photodiode signal of the E3 laser is used to reference the offset of the resonator length scan to the clock laser. The photodiode signals of the other lasers are used to adjust their current such that their frequency offset from the E3 laser is constant.

Various laser systems are needed for Doppler cooling and clear-out of the excited states of the clock transitions. These each consist of a commercial or home-built

3. Experimental setup for the multi-species, multi-ion clock YbSr1

laser and optics for distributing light, as well as changing its polarization and frequency. Two important characteristics of the lasers are their linewidth and long-term frequency drift, which should be below the natural linewidth of the transitions they address, if possible. For the transitions relevant in this section, their natural linewidth is above 1 MHz with the exception of the E3 repump laser at 760 nm. While the ECDL and Distributed Feedback (DFB) lasers themselves already have linewidths below 1 MHz, their center frequency drifts significantly over time due to temperature variations and stress changes of the laser resonator. To keep the center frequency stable and controllable, all Doppler cooling and repump lasers are stabilized to the length of a scannable optical resonator with a Free Spectral Range (FSR) of ≈ 500 MHz and finesse of $\mathcal{F} > 1000$. The resonators are placed within a vacuum housing that has been flooded with air. The valve connecting the inside and outside of the vacuum housing is closed to minimize the influence of pressure differentials between these two points. Sketches of the setups are shown in Fig. 3.4 for the blue lasers with a wavelength $\lambda < 500$ nm and Fig. 3.5 for the red lasers with a wavelength $\lambda > 700$ nm.

The resonator length can be changed with an piezoelectric actuator and is continuously scanned over the FSR of the shortest wavelength laser stabilized to the resonator. When the laser is on resonance with the cavity, light is transmitted through it and detected on a photodiode. The laser frequency is actively stabilized by adjusting the laser current or piezo voltage such that the resonator length where the transmission is at a maximum stays fixed. The length scan and Proportional Integral (PI) stabilization are implemented with a digital controller developed and manufactured at PTB that can control up to 8 lasers. To fix the reference point of the resonator scan, a clock laser with small frequency drift is also sent to the resonator. The controller changes the length scan range such that the position of the clock laser within the scan also does not change. In this way, the Doppler cooling laser center frequency is stabilized to the clock laser, which only exhibits small frequency variations compared to the E1 transition linewidths.

With the lasers stabilized sufficiently for Doppler cooling and repumping, they are distributed to the ion trap. The sketches of the distribution setup for the 370 nm and 422 nm laser are shown in Fig. 3.6 and Fig. 3.7, respectively. Generally, the laser itself is an ECDL from Toptica coupled directly into a PM fiber. Various PBS allow for flexible distribution of laser power to the wavemeter for monitoring the laser wavelength, the transfer cavity for active stabilization as discussed previously and three different ports at the ion trap. The path to the trap is mechanically blocked with a shutter during clock interrogation. An AOM is added to each path to modify the laser frequency along that path by a few MHz and to act as a fast switch independent of the shutter. Each AOM is supplied by the ARTIQ DDS amplified by 30 dB. A combination of a HWP and a Quarter Waveplate (QWP) in front of the fiber couplers allows to match the laser polarization with the fast or slow axis of the PM fiber, minimizing polarization fluctuations of the light while travelling in the fiber. At one port, the Doppler cooling laser is overlaid with the

ionization lasers with dichroic mirrors. The ionization lasers can be mechanically blocked separately from the cooling laser. Specific to the 370 nm laser are two Electrooptic Modulator (EOM)s that phase-modulate the cooling laser light at a frequency of 14.748 GHz and 2.105 GHz. These are necessary for bridging the gap between the hyperfine states of $^{171}\text{Yb}^+$ for Doppler cooling and state initialization, respectively. They are supplied with amplified synthesizers which are switched on and off during the experimental sequence.

The corresponding setups for the repump and ionization lasers are not shown, since they are significantly less complicated. The lasers are either Toptica ECDL (399 nm, 405 nm, 461 nm), home-built ECDL (399 nm, 1033 nm, 1092 nm) or home-built DFB (760 nm, 935 nm) systems. They are distributed to a wavemeter, all but the ionization lasers are distributed to a transfer cavity setup as well as the ion trap setup. The ionization lasers are not frequency stabilized with the transfer cavities and are combined with the Doppler cooling beams as shown in Fig. 3.6 and Fig. 3.7. For some measurements, the $^{88}\text{Sr}^+$ ionization lasers were stabilized to the wavemeter. The 1033 nm and 1092 nm laser are overlapped with a dichroic mirror before being sent to the ion trap setup. The 760 nm and 935 nm lasers are phase modulated with EOMs at frequencies of 5.3 GHz and 3.07 GHz, respectively, to address the hyperfine structure of $^{171}\text{Yb}^+$ discussed in Section 2.2 and Section 2.4.

3. Experimental setup for the multi-species, multi-ion clock YbSr1

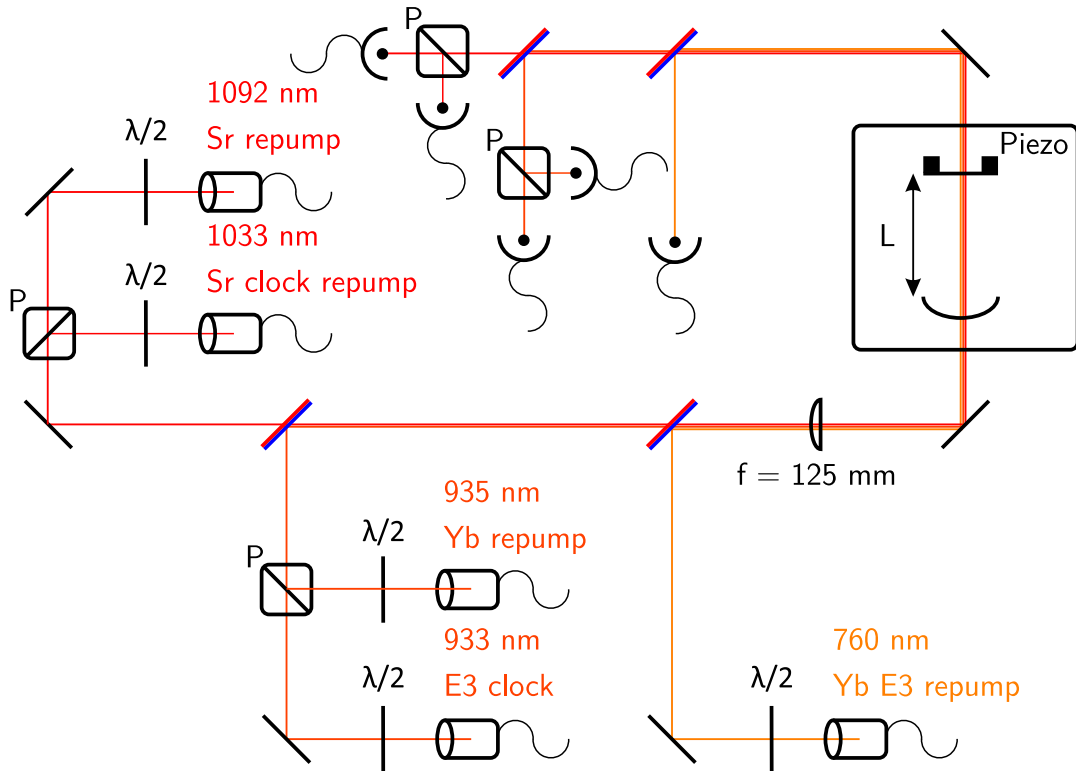


Figure 3.5.: Sketch of the repump laser stabilization setup. The lasers to repump $^{171}\text{Yb}^+$ and $^{88}\text{Sr}^+$ are stabilized to the infrared fundamental of the E3 clock laser via an optical resonator. All lasers are delivered to the setup with PM fibers. The resonator length L is continuously scanned with the piezoelectric actuators mounted on one side of the outcoupling mirror such that all lasers are transmitted at some point during the scan. Lasers at different wavelengths are overlaid with each other at dichroic mirrors. Lasers too close in wavelength to separate them with a dichroic mirror are overlaid with each other using PBS. The polarization is adjusted with a HWP to have maximum transmission or reflection at the PBS. The collimated laser beams are matched to the incoupling mode of the resonator with a lens with a focal length of 125 mm. The overlaid lasers are separated after the resonator with dichroic mirrors and PBS and their intensity measured with photodiodes. The photodiode signal of the E3 laser is used to reference the offset of the resonator length scan to the clock laser. The photodiode signals of the other lasers are used to adjust their current such that their frequency offset from the E3 laser is constant.

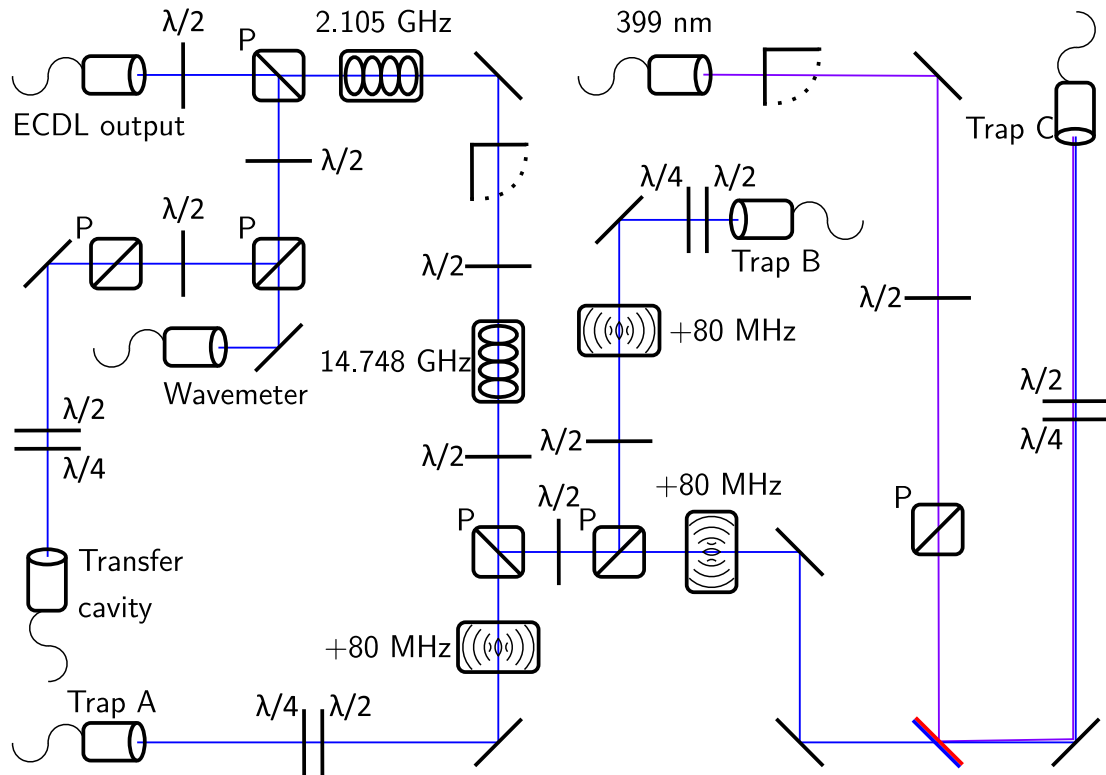


Figure 3.6.: Sketch of the 370 nm laser board. The light is split into various paths with PBS and polarization matched to PM fibers using a QWP and HWP. A mechanical shutter blocks the light in the path towards the trap during clock interrogation. The laser is phase modulated with two EOMs to address the hyperfine structure of $^{171}\text{Yb}^+$. AOMs allow for separate frequency detunings and optical switching of the three individual paths towards the trap. The ionization laser is overlaid with the cooling laser using a dichroic mirror and sent to port C of the ion trap setup.

3.3. Optical setup around the ion trap

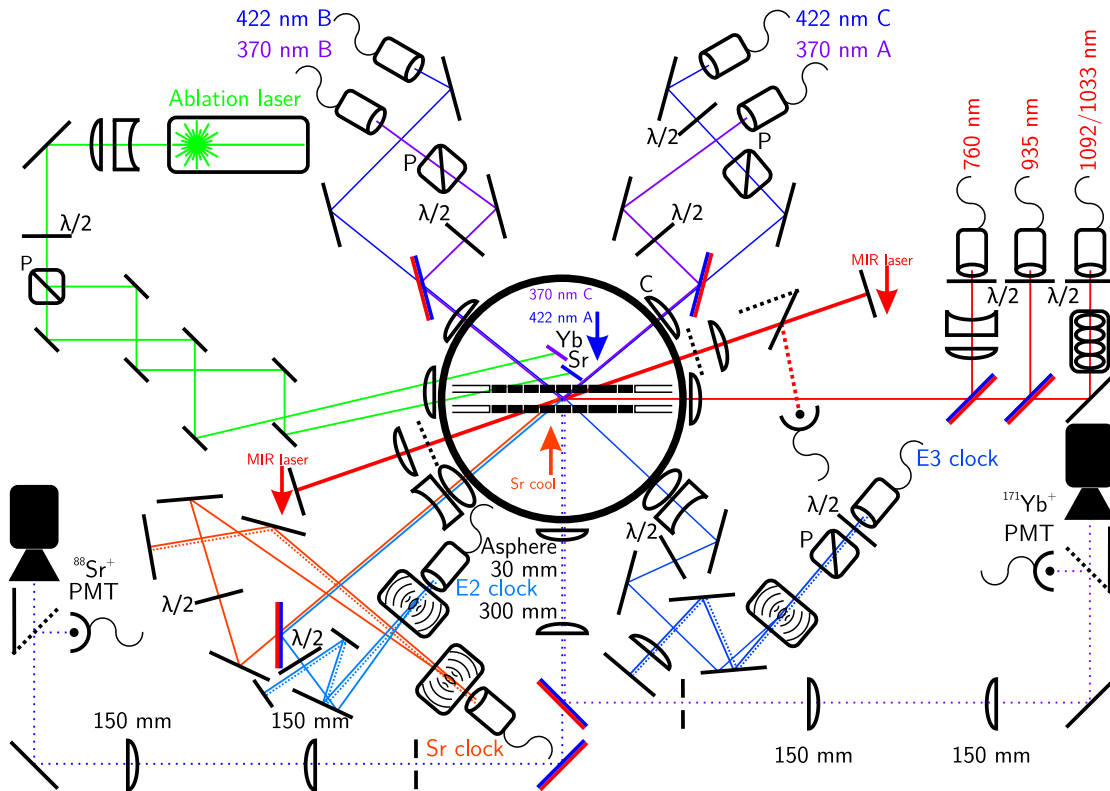


Figure 3.8.: *Optical setup around the ion trap.* The figure shows the top view of the optical setup surrounding the vacuum chamber in which the ion trap is situated. Within the vacuum chamber, two ablation targets are placed next to the trap, one for Yb and one for Sr atoms. The ablation laser path is chosen by adjusting the laser polarization. All laser beams apart from the ablation beam are focused onto the ions with convex 1" lenses. The cooling lasers shown here enclose an angle of 30° with the trap axis and approximately 45° with either radial direction of motion. Additionally, cooling and ionization lasers enter the vacuum chamber from the top, indicated by the arrow in the center. The $^{171}\text{Yb}^+$ and $^{88}\text{Sr}^+$ cooling and repump beams are overlaid with each other using dichroic mirrors. The 760 nm beam is expanded before being focused on the ions. The $^{88}\text{Sr}^+$ repump beams are polarization modulated at a frequency of 10 MHz with an EOM. The clock laser beams are built up on the opposite sides of the cooling beams. All three are frequency shifted with an AOM to match the laser frequency with the atomic resonance. The undiffracted beam is reflected back into the optical fiber to stabilize the optical path length. An additional laser beam for $^{88}\text{Sr}^+$ state initialization enters the ion trap vertically, indicated by the arrow in the center. The MIR lasers for polarizability measurements enclose an angle of 15° with the trap axis and can enter the ion chamber from either side. They also enter the figure plane vertically. The fluorescence emitted by the two ion species is collected with a common aspheric lens, split with a dichroic mirror and focused on separate Photon Multiplier Tube (PMT)s or cameras.

3. Experimental setup for the multi-species, multi-ion clock $\text{YbSr}1$

The optics surrounding the vacuum chamber of the ion trap are depicted in Fig. 3.8. There are in total three sets of Doppler cooling lasers, one orthogonal to the trap axis entering from the top and two with an angle of 30° relative to the trap axis. The latter two paths enclose an angle of 120° and all three beams are at an angle of approximately 45° with respect to the radial directions of motion of the ion. This setup enables cooling of all ion motion with either of the latter cooling ports and determination of ion micromotion in Three Dimensions (3D). Port B is focused on the ions more strongly to minimize scattered light during state detection, the other two cooling ports are focused with cylindric lenses only orthogonal to the trap axis. While this necessitates higher laser power for laser cooling, the intensity gradient along a linear crystal is heavily reduced.

The repump lasers are all aligned with the trap axis and overlaid with each other using dichroic mirrors. The 760 nm laser is enlarged to a beam diameter of approximately 10 mm at the focussing lens for a sufficiently high intensity at the ion position to repump the excited state of the E3 clock transition. The $^{88}\text{Sr}^+$ repump beams are polarization modulated with a frequency of 10 MHz using an EOM to couple to all Zeeman states for efficient state clear-out and Doppler cooling.

The fluorescence emitted by the ions during Doppler cooling is collected with an asphere with a Numerical Aperture (NA) of 0.38 after being transmitted through a re-entrant viewport. To magnify the image, the collimated fluorescence is focused with a lens with $f=300$ mm and then split with a dichroic mirror into the $^{171}\text{Yb}^+$ or $^{88}\text{Sr}^+$ detection path. In each of these paths, an aperture is placed at the focal point of the 300 mm lens and then captured with a 150 mm 1:1 telescope to refocus the light at a spot further along the imaging system. The focus of the image is placed on either a camera sensor or PMT, resulting in a total magnification of the ion image of approximately 10, where the NA of the whole imaging system is approximately 0.3 as determined from the spot size of a single trapped ion of $5.9\ \mu\text{m}$. The camera pixel size is $2.4\ \mu\text{m} \times 2.4\ \mu\text{m}$, allowing for two ions to be distinguished, if they are a distance of approximately $1\ \mu\text{m}$ apart from each other. The first two lenses of the imaging system can be moved independently from the rest with micrometer screws to capture the image of different segments. The area visible on the camera sensor encloses around 2 full trap segments.

Ionization lasers follow the same path as the vertical beams, which results in largely Doppler free interaction with the evaporated atoms during loading. Two targets are placed in the vacuum chamber next to the ion trap, one with Yb atoms and one with Sr atoms. An ablation laser is focused via two separate paths on both targets, allowing to choose which element should be loaded.

Two ports are used for the clock lasers, both enclose an angle of 30° with the trap axis. The E2 and Sr clock lasers share a port and are overlapped with a dichroic mirror. All clock lasers are enlarged to a beam diameter of 5-20 mm at the focussing lens to reach light intensities sufficient for Rabi frequencies of 0.02-10 kHz. The small Rabi frequency corresponds to the E3 transition, which

requires a significantly higher intensity for the same Ω than the E2 transition due to its small coupling strength. The frequency offsets of the clock lasers are adjusted with AOM supplied by ARTIQ AD9914 DDS to interrogate different transitions and stabilize the laser to the atomic resonance. The undiffracted beam of each clock laser is reflected back into the fiber to stabilize the path length of the laser.

Additionally, a higher-intensity $^{88}\text{Sr}^+$ clock laser beam is transmitted vertically, orthogonal to the trap axis. With that beam, Rabi frequencies up to 100 kHz are reached, but it is not path length stabilized. Its primary function is to state initialize $^{88}\text{Sr}^+$ quickly before clock interrogation and sub-Doppler cool the radial sidebands.

For the polarizability measurements in Chapter 4 and Chapter 5, MIR lasers are focused onto the ions at an angle of 15° with respect to the trap axis. Due to their wavelength of $> 8\ \mu\text{m}$ and the low NA of the viewport, the minimum achievable beam diameter is limited to approximately $400\ \mu\text{m}$. A transmitting Anti-Reflection (AR)-coated window is placed between the focusing lens and viewport to displace the beam for the measurements in Section 4.3. The lasers itself are situated further away from the trap and are sent via free space to above the experiment. They enter the optical setup around the ion trap by being reflected downward into the plane shown in Fig. 3.8.

3.4. Ion loading procedure

The Yb atoms are emitted from their metallic sample of natural isotopic composition with two different methods. The sample can be heated up resistively with an oven by passing a current of approximately 800 mA at a voltage of approximately 4 V through it. After roughly 45 s the sample is at a sufficiently high temperature to emit a stream of atoms that intersects with the cooling and ionization lasers at the trap center.

Alternatively, it is also possible to generate an atomic cloud by irradiating the sample with a high intensity laser pulse. This heats up a local spot on the target significantly and evaporates the metal into an expanding atomic cloud. A small solid angle of this cloud travels towards the ion trap. This method is called *ablation loading* and is employed in variety of ion trap experiments for a large number of elements [Lei+07; Whi+22; Li+24]. The ablation laser in use for the experiment has a wavelength of 532 nm, maximum average power of 1.5 W and pulse length of 2 ns at a maximum repetition rate of 10 kHz. This results in a maximum peak intensity of $0.8\ \text{GW}/\text{mm}^2$ after the ablation laser is focused to a beam diameter of approximately $15\ \mu\text{m}$ on the target. Laser ablation is possible for both Yb and Sr metal targets, for the latter species this is the only option for loading in the setup presented here. Before the polarizability measurements were started, 50 - 100 subsequent pulses were sufficient to reliably load ions of both elements

3. Experimental setup for the multi-species, multi-ion clock YbSr1

into the trap. After the automatic reloading measurements in Chapter 5, where several thousand loading cycles were executed on the Sr target within a couple of hours, ablation loading became much less reliable. Hundreds of attempts with 1000 ablation pulses were necessary to load a single ion in the time following these measurements, which is mitigated by moving the laser to a different spot on the ablation target. Still, the loading efficiency fluctuates much more over time than before the automatic reloading measurements and readjustments of the ablation laser every few months is necessary now.

For both species, a two-stage ionization procedure is employed for isotope selective loading. Neutral Yb is excited to the intermediate 1P_1 state with a laser at a wavelength of 399 nm. The atom is then ionized with the 370 nm Doppler cooling light. For neutral Sr, two dedicated ionization lasers are in use. The 461 nm laser excites the atom to the 1P_1 state and the 405 nm laser ionizes it. As discussed in section 3.3, the propagation vectors of all of these beams are orthogonal to the velocity of the atomic beam to minimize the Doppler shift of the transition frequencies with respect to the lasers.

Loading Sr ions is automated for the measurements in Chapter 5. All ionization lasers are unblocked, the cooling lasers are red-detuned by approximately 500 MHz, the ablation laser is pulsed, the ionization lasers are blocked, the cooling lasers are locked to their Doppler cooling frequency and the amount of ions is determined from the PMT signal. If a single ion is loaded, the procedure is finished, otherwise it repeats. Ionization laser frequencies are stabilized to a wavemeter to compensate for drifts over time. This allows for reliable loading of single ions over hundreds of subsequent cycles after optimizing the ionization wavelengths and position of the ablation laser on the target.

3.5. Magnetic field control and measurements

Since the energy difference between each Zeeman component of the $^{88}\text{Sr}^+$ clock transition is linearly sensitive to magnetic fields, the trap has to be shielded from magnetic field noise as much as possible. This is primarily achieved with two layers of Mu-metal, a ferromagnetic alloy that blocks low-frequency magnetic field fluctuations [Cor21]. The Mu-metal encloses most of the vacuum chamber with holes cut out for optical access and electric connections, reducing the magnetic field variation over 200 ms to approximately 0.5 nT. This is determined from the maximum achievable coherence time of the $^{88}\text{Sr}^+$ clock transition limited by magnetic field noise.

Four pairs of coils are installed to control the magnitude and direction of the magnetic field during clock spectroscopy and Doppler cooling. They are mounted on 3D-printed holders inside the Mu-metal shielding and supplied with current from external sources.

The *large* coil pair is turned on during Doppler cooling of $^{171}\text{Yb}^+$ to produce a magnetic field of $180\ \mu\text{T}$ along the direction of the imaging system. The current is supplied by a laboratory power supply and switched with a solid state relay controlled via ARTIQ that blocks the DC flow through the coils, but allows AC components with a frequency above $500\ \text{kHz}$ to pass through. When the relay is open, no current flows through the coils and the magnetic field produced by the large coils decays with a magnitude variation of $75\ \text{nT}$ between waiting times of $30\ \text{ms}$ and $150\ \text{ms}$ as is depicted in Fig. 3.9. From a waiting time of $145\ \text{ms}$ onwards, the residual change of the magnetic field magnitude due to the decay is smaller than the long-term observed instability of $0.5\ \text{nT}$. After the clock pulse is applied to the ion, the solid state relay is closed again to turn on the large field for state detection.

Three *small* coil pairs are oriented along the trap axis, imaging system and vertical direction to produce magnetic fields up to approximately $30\ \mu\text{T}$ along any chosen direction during clock spectroscopy. Their current is supplied with a driver built by PTB controlled with the ARTIQ DAC to change the direction and magnitude of the field during spectroscopic sequences. The linear relationship between the coil currents and magnetic field vector is calibrated with the $^{171}\text{Yb}^+$ ion directly by determining the center frequency the $^2S_{1/2}(F=0, m_F=0) \rightarrow ^2D_{3/2}(F=2, m_F=-1)$ and $^2S_{1/2}(F=0, m_F=0) \rightarrow ^2D_{3/2}(F=2, m_F=-2)$ clock transitions at 13 different magnetic field directions and magnitudes.

The total magnetic field $\vec{B}(t) = \vec{B}_0 + \Delta\vec{B}(t)$ consists of the static offset \vec{B}_0 and the time-varying component $\Delta\vec{B}(t)$. Slow variations with respect to the probe time of the clock transition are directly observed via the frequency offset of transitions $|S, m_S\rangle \rightarrow |D, m_D\rangle$ where at least one of m_S and m_D is not equal to zero. This is due to the linear Zeeman shift averaged over the probe time T

$$\Delta\nu_{Z1} = \frac{\mu_B}{h} \langle \vec{B} | \rangle_T (g_D m_D - g_S m_S), \quad (3.1)$$

with the Bohr magneton μ_B , Planck constant h and ground (excited) state Landé factor g_S (g_D).

3. Experimental setup for the multi-species, multi-ion clock YbSr1

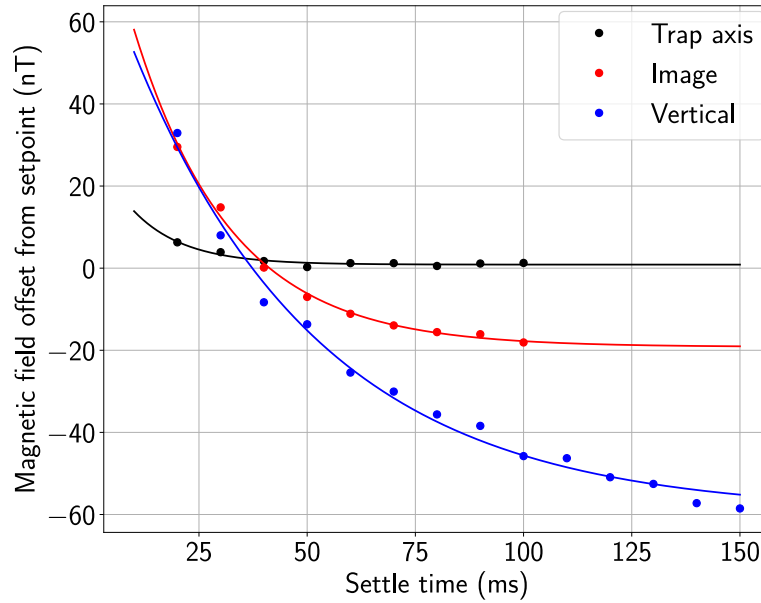


Figure 3.9.: *Measurement of the magnetic field decay. A magnetic field of $2.4 \mu T$ is set with the small coils along the trap axis, the imaging system and the mutually orthogonal vertical direction. The center frequency of the $^{171}\text{Yb}^+ S_{1/2}(F=0, m_F=0) \rightarrow D_{3/2}(F=2, m_F=-2)$ transition is measured for various settle times after the current for the large magnetic field, supplying $180 \mu T$, is switched off. The magnetic field offset from the setpoint $\Delta B(t)$ follows an exponential decay with a lifetime of $12(3) \text{ ms}$, $22(2) \text{ ms}$ and $45(4) \text{ ms}$ for the trap axis, imaging and vertical direction, respectively.*

AC magnetic field measurement If on the other hand the variation of $\Delta \vec{B}(t)$ is significantly faster than the probe time, so that a sinusoidal oscillation of $\Delta \vec{B}(t)$

$$\Delta \vec{B}(t) = \vec{A} \sin(\omega t), \quad (3.2)$$

with amplitude \vec{A} and angular frequency $\omega \gg 2\pi/T$, then $\Delta \vec{B}(t)$ cannot be directly observed in this way. A potentially large magnetic field with high frequency results from induced currents in the generation of the RF trapping field as discussed in [Gan+18; Arn+20]. This AC magnetic field causes a frequency shift in optical clocks of up to several 10^{-17} [Gan+18], which means that \vec{A} needs to be determined with sufficient accuracy to correct for the offset.

One method to measure the AC magnetic field relies on *Autler-Townes-splitting* in a strongly coupled multi-level system [AT55; Gan+18]. For example, the ground state $S_{1/2}$ of the $^{88}\text{Sr}^+$ clock transition splits into two substates due to the Zeeman effect with a frequency difference of

$$\Delta\nu_{S_{1/2}} = \frac{\mu_B}{\hbar} g_S |\vec{B}|. \quad (3.3)$$

The transition $|S, m_S = -1/2\rangle \leftrightarrow |S, m_S = +1/2\rangle$ is an M1 transition and couples to RF magnetic fields of the appropriate frequency. This means that the induced RF magnetic field due to the trap drive with an angular frequency Ω_{RF} is resonant with this transition when

$$|\vec{B}| = \frac{\hbar\Omega_{\text{RF}}}{g_S\mu_B}, \quad (3.4)$$

which results in $|\vec{B}| = 475 \mu\text{T}$ for $g_S = 2.002$ and $\Omega_{\text{RF}} = 2\pi \times 13.3 \text{ MHz}$. At this magnetic field strength, the two Zeeman states couple strongly to each other due to the transverse magnetic field B_{\perp} with respect to the direction of \vec{B}_0

$$B_{\perp} = \sqrt{|\vec{B}|^2 - \left(\frac{\vec{B} \cdot \vec{B}_0}{|\vec{B}_0|}\right)^2}, \quad (3.5)$$

that drives the M1 transition with a Rabi frequency of [Gan+18; Jos+24]

$$\Omega_0 = \frac{1}{2} \mu_B g_S \sqrt{J(J+1) - m_J(m_J \pm 1)} B_{\perp}, \quad (3.6)$$

where J is the total angular momentum and the sign in the bracket depends on the direction of the spin-flip transition. Now, if one excites e.g. the $|S, +1/2\rangle \rightarrow |D, +5/2\rangle$ transition, two resonances are observed instead of the usual one resonance at the transition center frequency. The frequency difference, the Autler-Townes splitting, between the left (L) and right (R) resonance is

$$|\nu_R - \nu_L| = \frac{1}{2\pi} \sqrt{\Omega_0^2 + \left(\frac{\mu_B}{\hbar} g_S |\vec{B}| - \Omega_{\text{RF}}\right)^2}, \quad (3.7)$$

which means that B_{\perp} can be determined by measuring the splitting on resonance. A schematic of the level structure and coupling strength resulting in Autler-Townes splitting is shown in Fig. 3.10. The full 3D magnitude \vec{A} of the AC field is determined by measuring the frequency splitting $|\nu_R - \nu_L|$ for different orientations of the offset field \vec{B}_0 .

The result of an Autler-Townes measurement using the $^{88}\text{Sr}^+ |S, +1/2\rangle \rightarrow |D, +5/2\rangle$ transition at different trap RF powers and along three different directions is shown in Fig. 3.11. The magnetic field is primarily generated with around 1.04 A of current in the large coils oriented along the imaging direction, supplied by a 6-digit

3. Experimental setup for the multi-species, multi-ion clock YbSr1

precision current source. A comparison of the observed splitting at three different trap RF power settings shows the expected scaling between the RF power and B_{\perp} up to a residual offset of 0.3 dB between the lowest and highest setting. The small coils are used to tilt \vec{B}_0 by 5° towards the trap axis or vertical direction to determine the full AC field. This results in the following AC magnetic field at the +6 dB power setting (at which the average radial secular frequency of a $^{88}\text{Sr}^+$ ion is approximately 1200 kHz)

$$\Delta\vec{B}(t) = 1.047(48) \mu\text{T} \begin{pmatrix} 0.839(38) \\ 0.106(26) \\ 0.5336(60) \end{pmatrix} \sin(\Omega_{\text{RF}}t) \quad (3.8)$$

where the x-axis is oriented along the imaging direction, the y-axis is vertically oriented and the z-axis coincides with the trap axis. This field magnitude results in a fractional frequency shift of $53.7(4.9) \times 10^{-18}$ and $3.84(35) \times 10^{-18}$ for the $^{171}\text{Yb}^+$ E2 and E3 transition, respectively [Gan+18]. The shift on the $^{88}\text{Sr}^+$ clock transition of $7.67(70) \times 10^{-21}$ is significantly smaller, since it does not possess any hyperfine structure, so the closest M1 transition affected by the RF field is the fine-structure transition $|D_{5/2}\rangle \leftrightarrow |D_{3/2}\rangle$ at a frequency of 8.4 THz.

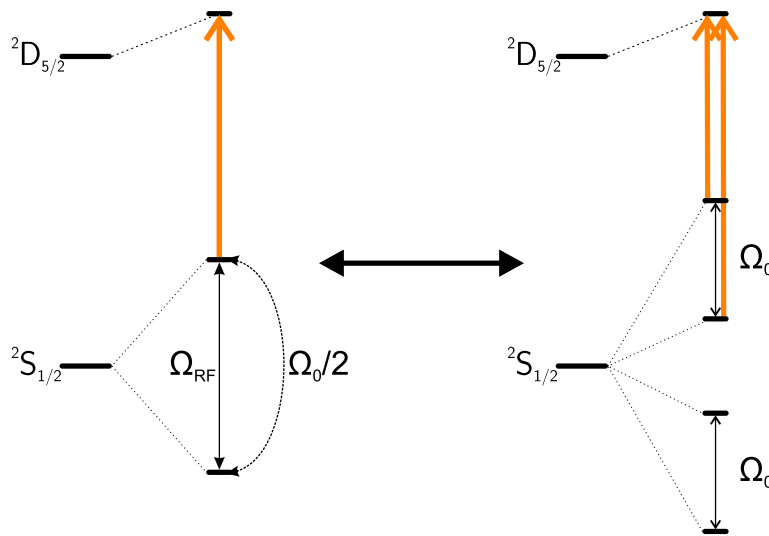


Figure 3.10.: *Autler-Townes splitting schematic. The reduced level structure of the $^{88}\text{Sr}^+$ clock transition relevant for the Autler-Townes measurement is depicted on the left-hand side. The splitting of the Zeeman states in the ground state is set equal to the trap RF drive angular frequency Ω_{RF} , which couples the states with a Rabi frequency Ω_0 . This is equivalent to an additional splitting of each Zeeman state in the S manifold into two states spaced by Ω_0 as depicted on the right-hand side. When the clock laser frequency is scanned over the corresponding frequency range, this produces two resonances which are offset from each other by Ω_0 .*

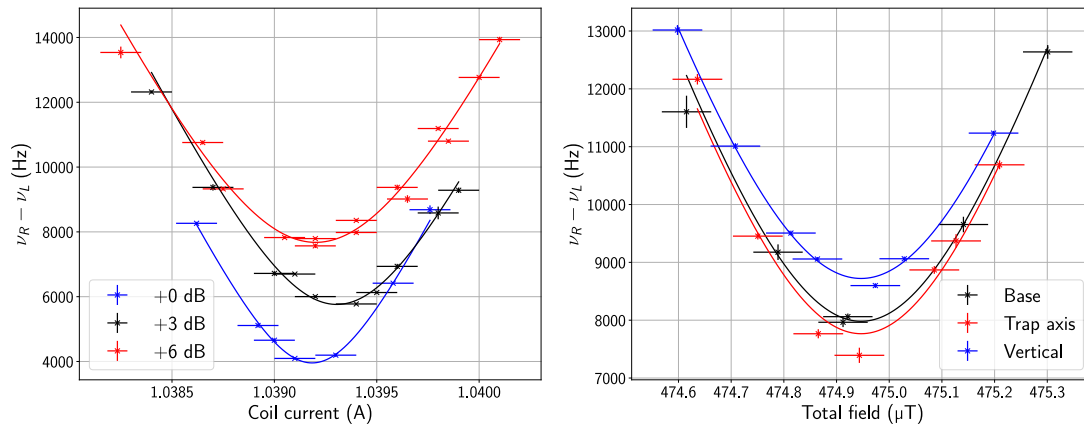


Figure 3.11.: *Autler-Townes splitting measurement results. The figures show the frequency difference between the two resonances of the three-level system at different magnetic field strengths. The magnetic field is supplied by a coil oriented along the imaging direction with around 1.04 A of current flowing through it and a set of smaller coils that allow for the tilting of the magnetic field vector. On the left hand side the minimum splitting shows the expected linear dependence on the trap drive power up to a deviation of 0.3 dB between the smallest and highest RF power setting. On the right hand side the magnetic field is tilted by 5° from the initial direction (Base) towards the trap axis and the vertical direction. This allows for a determination of the full 3D AC magnetic field amplitude at the trap drive frequency.*

3.6. Background pressure measurement

Collisions of background gas atoms with the trapped ions cause frequency shifts and may melt the crystal if the collision energy is sufficiently high. The residual pressure in the vacuum chamber cannot easily be determined from the ion pump current, since it is below the pump resolution limit of 1 nA for pressures below 1×10^{-10} mbar. Additionally, the pressure at the ion position may be substantially different from the pressure at the ion pump location. Instead, the trapped ions themselves are employed as a pressure sensor, a method developed in [Han+19a]. To determine the uncertainty of the clocks due to background gas collisions, it is important to determine the background gas pressure p_{BG} more accurately than is possible using the ion pump.

With a linear ion trap it is possible to determine p_{BG} from the reordering of the ion crystal after a collision with a background gas atom. The rate at which the ions switch positions Γ within the linear chain is proportional to the collision rate γ , which is proportional to p_{BG} . Under the assumption that all collisions are *Langevin collisions* the collision rate and pressure are related via [Für+19, p. 84]

3. Experimental setup for the multi-species, multi-ion clock YbSr1

$$\gamma = \frac{2\pi}{k_B T} \sqrt{\frac{C_4}{\mu_{BG}}} p_{BG}, \quad (3.9)$$

with the temperature T , reduced mass of the trapped ion and background gas μ_{BG} and C_4 parameter C_4 determined from the static polarizability α_0 of the background gas

$$C_4 = \frac{e^2}{8\pi\epsilon_0} \alpha_0, \quad (3.10)$$

which is $C_4 = 91 \times 10^{-60} \text{ Jm}^4$ for molecular hydrogen, the expected dominant background gas component.

When all ions in the crystal are illuminated with Doppler cooling light, different species or different isotopes need to be trapped in the same chain to detect reorderings by changes of the position of bright and dark ions. Importantly, even for a 2 ion crystal, half of the collision are missed, since no change is detected when the ions return to their initial positions after the interaction with the background gas. For a crystal with N ions of which M are bright, the collision rate per ion Γ_{ion} corrected by this effect is

$$\Gamma_{\text{ion}} = \frac{1}{N \left(1 - \frac{M!(N-M)!}{N!} \right)} \Gamma, \quad (3.11)$$

derived from combinatorics involving the multiplication table of factorial numbers read by antidiagonals (OEIS A098361). This correction is only valid, if all orderings are equally likely to occur.

Another correction is from the potential barrier E_{reorder} the collision has to overcome for a reordering to potentially occur. It is dependent on the ratio ξ between axial (ω_{ax}) and radial (ω_{rad}) secular frequencies [Han+19a] and is

$$\xi = \sqrt{\left(\frac{\omega_{\text{rad}}}{\omega_{\text{ax}}} \right)^2 + \frac{1}{2}} \quad (3.12)$$

$$E_{\text{reorder}} = \frac{3}{4} \left(\frac{\sqrt{m} \omega_{\text{ax}} e^2}{2\pi\epsilon_0} \right)^{2/3} \left(\left(\frac{2(\xi^2 + 1/2)(\xi^2 + \mu/2)}{\xi^2(\mu + 1) + \mu} \right)^{1/3} - 1 \right), \quad (3.13)$$

with the single ion mass m and reduced mass of the ions in the crystal μ . This simplification of the relation in [Han+19a] is valid if the radial asymmetry of the trap due to DC confinement is small compared to the radial secular frequency ($\alpha=0.5$ in their notation). Under the assumption that collisions with energy below

E_{reorder} do not cause a reordering of the crystal and that the energy distribution is given by the Maxwell-Boltzmann distribution at temperature T , the fraction λ of all collisions that surpass the barrier is

$$\lambda = \frac{2}{\sqrt{\pi}} \int_{\frac{E_{\text{reorder}}}{\eta k_B T}}^{\infty} du \sqrt{u} e^{-u}, \quad (3.14)$$

where η quantifies the average fraction of the background gas kinetic energy transferred to the ion upon a collision [Han+19a]

$$\eta = \frac{2\rho}{(1+\rho)^2}, \quad \rho = \frac{m_{\text{bg}}}{m_{\text{ion}}}. \quad (3.15)$$

Putting it all together, the background pressure p_{BG} is then given by

$$p_{\text{BG}} = \frac{k_B T}{2\pi} \sqrt{\frac{\mu_{\text{BG}}}{C_4}} \frac{\Gamma_{\text{ion}}}{\lambda}. \quad (3.16)$$

A crystal consisting of 2 $^{171}\text{Yb}^+$ and 1 $^{174}\text{Yb}^+$ is employed for the background pressure measurement. $^{171}\text{Yb}^+$ is fluorescing and $^{174}\text{Yb}^+$ provides the dark partner. The measurement lasts approximately 2 days in total. After 43 hours the $^{174}\text{Yb}^+$ ion is lost, but the $^{171}\text{Yb}^+$ ions spends some time in the $^2F_{7/2}$ state, extending the measurement time. The ion fluorescence is recorded with the camera and the ion center position is automatically determined in post-processing to detect reorder events. The mean time interval between the reorderings τ is the inverse of the mean reorder rate Γ . The histogram of τ is shown in Figure 3.12 together with a fitted exponential decay that results in $\Gamma = 0.115(6)/\text{min}$. From Eq. (3.16) it follows that $\eta \approx 0.023$, $\lambda \approx 0.627$ and $p_{\text{BG}} = 6.2(4) \text{ nPa} = 6.2(4) \times 10^{-11} \text{ mbar}$. After the exchange of a vacuum window in 2023 the pressure rose by about an order of magnitude, determined in the same way with a few hours of measurement time.

3. Experimental setup for the multi-species, multi-ion clock YbSr1

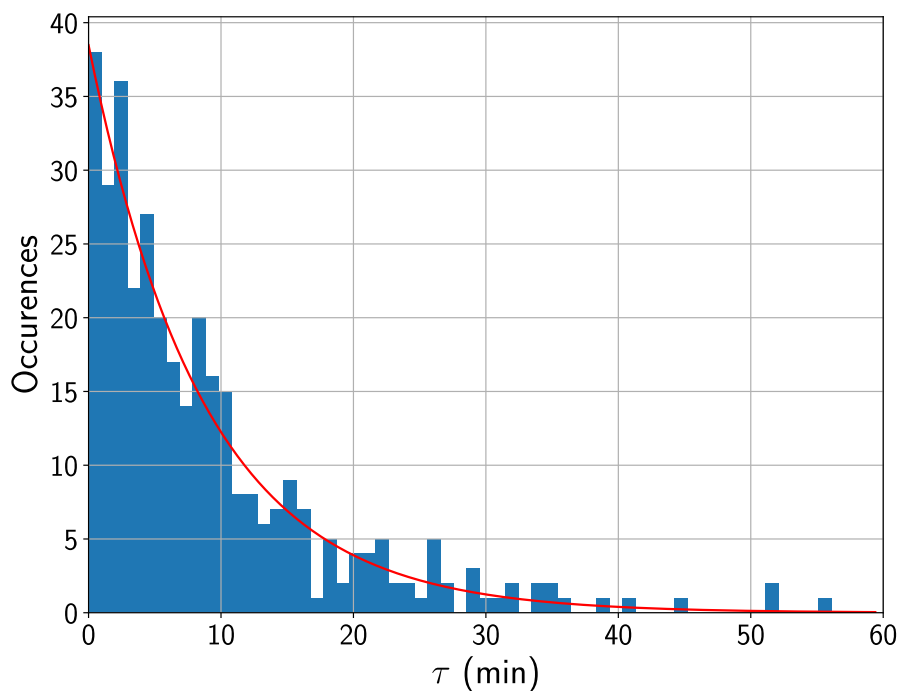


Figure 3.12.: *Histogram of the crystal stability. The histogram of the lifetime τ of the crystal before a reordering is detected shows an exponential decay depicted in red with a mean lifetime of 8.7(5) min. This is expected due to the random occurrence of collisions over time and corresponding exponential distribution of the lifetime.*

3.7. Clock laser setup, frequency measurement and stabilization

Three different clock lasers are in use for this experiment. The E2 laser at 435 nm and E3 laser at 467 nm for $^{171}\text{Yb}^+$ spectroscopy use additional ports of existing systems that are in use for the single ion clocks at PTB [Hun+16; Lan+21a]. The E3 laser is stabilized to an Ultra Low Expansion glass (ULE) cavity in the laboratory and a NIR laser referenced to a cryogenic silicon resonator at PTB which features a fractional frequency drift of around $5 \times 10^{-19}/\text{s}$ with a flicker floor of 4×10^{-17} [Mat+17]. This allows for coherent spectroscopy of optical transitions with interrogation times exceeding 3 s on the $^{171}\text{Yb}^+$ clock transition, if all other contributions to laser-ion decoherence are sufficiently small. The E2 laser is phase-stabilized to the E3 laser by fixing the optical frequency ratio between the clock lasers at a frequency comb in the laboratory. The E2 and E3 laser stabilization setups relevant for this thesis are shown in Fig. 3.13.

3.7. Clock laser setup, frequency measurement and stabilization

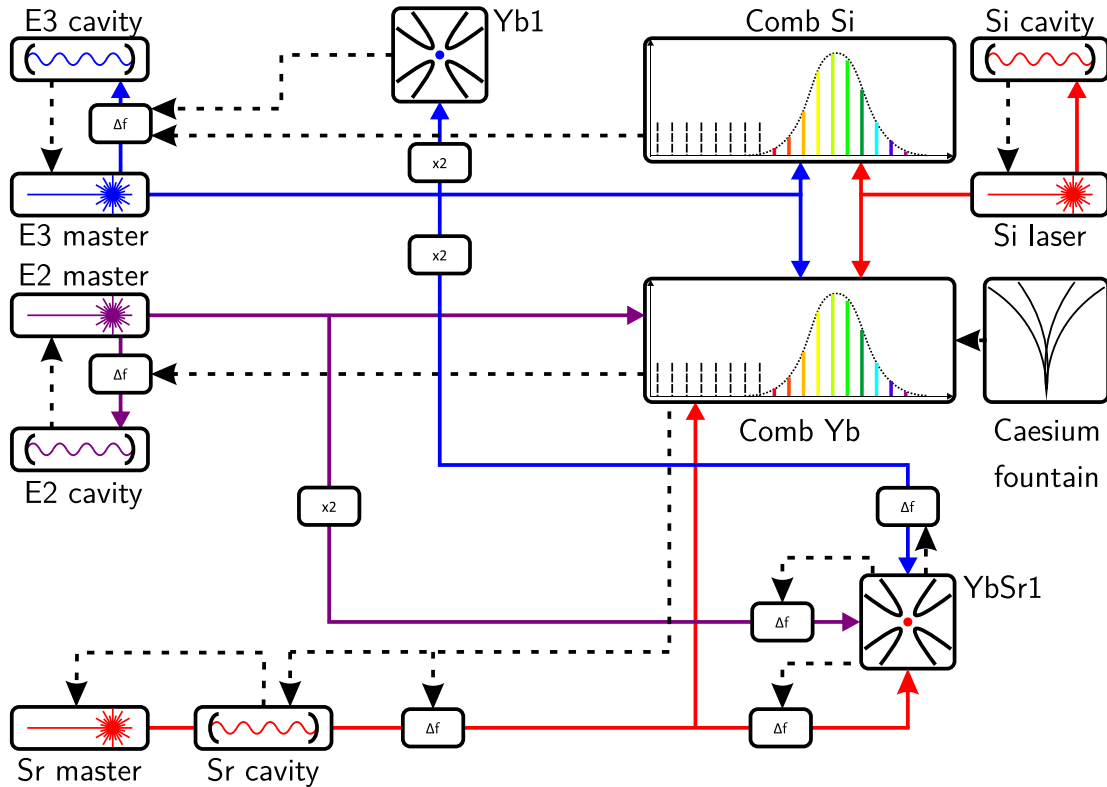


Figure 3.13.: Clock laser distribution and stabilization to traps and frequency combs. This figure shows the different clock lasers, their distribution to the traps and combs relevant to the work in this thesis and the control paths to stabilize the clock laser frequency. The E3 laser is short-term stabilized to a NIR laser referenced to the ultra-stable silicon cavity [Mat+17]. For times longer than 100 s, the clock laser frequency is stabilized to the corresponding optical transition in $^{171}\text{Yb}^+$, produced by the optical clock Yb1. The E2 laser is stabilized to the E3 laser at a frequency comb in the laboratory that also receives the silicon laser to compensate for any phase errors between the combs [Ben+19]. Both the E3 and E2 laser are frequency-doubled from their NIR fundamental to reach the resonant frequency of the optical transition. The laboratory comb is additionally referenced to a Cs fountain clock. The Sr clock laser is locked to the E3 laser at the same comb with an AOM for fast feedback and by adjusting the length of the filter cavity to correct for frequency drifts. All three lasers arrive at YbSr1, which produces a feedback signal to an AOM for each clock to determine the center frequency of the optical transitions. Frequency comb image source (modified): [Har06]

3. Experimental setup for the multi-species, multi-ion clock YbSr1

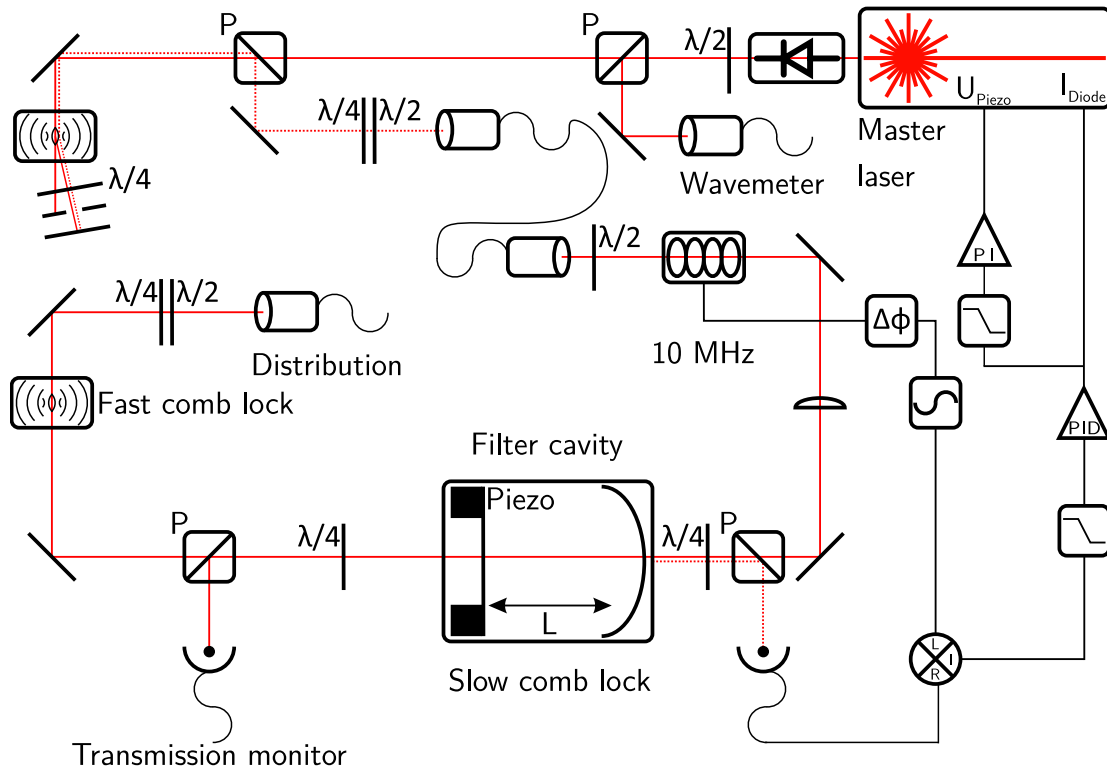


Figure 3.14.: Sketch of the optical setup and stabilization of the Sr master laser. This figure shows the stabilization setup of the $^{88}\text{Sr}^+$ clock laser to the filter cavity, producing approximately $20\ \mu\text{W}$ of optical power coupled into the distribution fiber with a linewidth of approximately 5 Hz. The output of an ECDL is phase-modulated with an EOM at a frequency of 10 MHz and coupled into a scannable optical resonator with finesse $\mathcal{F} \approx 34000$. The laser is stabilized using the PDH technique [Dre+83] and steers the diode current as well as piezo voltage of the master laser. The transmission through the cavity is frequency-offset with an AOM and coupled into a fiber connected to the distribution board in Fig. 3.15. The cavity length and AOM offset frequency are adjusted such that the frequency ratio between the $^{88}\text{Sr}^+$ and E3 clock laser is fixed to a defined number at the frequency comb. This way, the $^{88}\text{Sr}^+$ laser inherits the frequency stability of the E3 laser.

The clock laser for the $^2S_{1/2} \rightarrow ^2D_{5/2}$ transition of $^{88}\text{Sr}^+$ is a separate device that was built up specifically for the YbSr1 system and is used by the YbSr2 system now, too. Since the E3 laser already features a narrow linewidth and small frequency drift, the $^{88}\text{Sr}^+$ clock laser is designed to be referenced to it via a frequency comb. As shown in Fig. 3.14 the basis of the clock laser is a home-built ECDL at 674 nm. An optical isolator with 57 dB isolation protects the laser diode from optical feedback. It is detuned with a double pass AOM and coupled into a fiber connected to a separate bread board on which an optical resonator with a finesse $\mathcal{F} \approx 34000$ is placed. The double pass AOM is installed to actively stabilize the

power sent to the cavity to minimize Residual Amplitude Modulation (RAM) induced by the PDH EOM, but is currently operated with a fixed RF amplitude and frequency. The light is phase-modulated with an EOM at a frequency of approximately 10 MHz to implement a PDH stabilization scheme [Dre+83]. The laser is matched to the input mode of the resonator with a lens and the reflection of the light on the resonator is detected on a photo diode. The photodiode signal is low-pass filtered to remove the component at twice the modulation frequency and mixed with the modulation signal at a phase offset of 115° to the EOM input signal which produces a voltage proportional to the frequency offset of the laser from the cavity resonance. The phase is not 45° due to phase delays, e.g. due to cable length differences between the two signal paths. The full error signal is used as the input for a Proportional Integral Derivative (PID) stabilization that modifies the current of the laser diode with a locking bandwidth of 500 kHz. The output signal of the PID controller is low-pass filtered and modifies the piezo voltage of the ECDL with a PI control loop to follow drifts of the resonator length with the laser.

Due to the quality factor of the cavity and locking bandwidth of the PDH stabilization, the output is spectrally filtered with a bandwidth smaller than 35 kHz, heavily reducing the noise at the secular frequencies of the ion. The filtered light is monitored on a photo diode and frequency offset by an AOM before being coupled into a fiber connected to the distribution board. The length of the filter cavity and frequency of the AOM and in turn the laser source are controlled to generate a fixed optical ratio with the E3 clock laser that is already stabilized to the silicon resonator. Both the Sr clock laser and E3 clock laser fundamental (at 934 nm) are measured at the same comb with repetition rate f_{rep} and CEO f_{ceo} . If the laser is at an optical frequency ν_x , it produces a beat at frequency f_x according to the comb formula

$$\nu_x = m_x f_{\text{rep}} + f_{\text{ceo}} + f_x \quad (3.17)$$

where $m_x \in \mathbb{N}$ is the number of the comb tooth closest to ν_x . By dividing both sides of the equation by ν_x , the relation connecting m_x and f_x for two lasers measured at the same frequency comb is

$$\frac{m_{\text{E3}} f_{\text{rep}} + f_{\text{ceo}} + f_{\text{E3}}}{\nu_{\text{E3}}} = \frac{m_{\text{Sr}} f_{\text{rep}} + f_{\text{ceo}} + f_{\text{Sr}}}{\nu_{\text{Sr}}}, \quad (3.18)$$

which is rearranged to

$$\left(\frac{\nu_{\text{Sr}}}{\nu_{\text{E3}}} m_{\text{E3}} - m_{\text{Sr}} \right) f_{\text{rep}} + \left(\frac{\nu_{\text{Sr}}}{\nu_{\text{E3}}} (f_{\text{ceo}} + f_{\text{E3}}) - (f_{\text{ceo}} + f_{\text{Sr}}) \right) = 0. \quad (3.19)$$

To stabilize the Sr clock laser frequency to the E3 clock laser, it is sufficient to investigate the term in the second bracket. The first bracket only involves integer

3. Experimental setup for the multi-species, multi-ion clock YbSr1

numbers, the optical frequency ratio and the common repetition rate, all of which are fixed numbers and do not allow for control of f_{Sr} . At the correct lock point $m_{\text{E3}}\nu_{\text{Sr}}/\nu_{\text{E3}} - m_{\text{Sr}} = 0$ and can be disregarded. To realize a specific optical frequency ratio $\nu_{\text{Sr}}/\nu_{\text{E3}}$, the term in the second bracket is set to zero, which results in the following expression for the offset f_{Sr} :

$$f_{\text{Sr}} = \left(\frac{\nu_{\text{Sr}}}{\nu_{\text{E3}}} - 1 \right) f_{\text{ceo}} + \frac{\nu_{\text{Sr}}}{\nu_{\text{E3}}} f_{\text{E3}} \quad (3.20)$$

Importantly, Eq. (3.20) assumes that the beat signal with the correct comb tooth is employed for both lasers, otherwise the frequency ratio $\nu_{\text{Sr}}/\nu_{\text{E3}}$ will be different from the target value. The calculation Eq. (3.20) is performed with RF components such as mixers, frequency dividers and DDS, which allows for the generation of f_{Sr} with a bandwidth of several MHz and reduced noise compared to a direct measurement at the comb. By mixing f_{Sr} with a fixed reference frequency provided with a DDS, an error signal is generated that controls the filter cavity length and AOM such that $\nu_{\text{Sr}}/\nu_{\text{E3}}$ is a fixed number. The control path of the $^{88}\text{Sr}^+$ clock laser in comparison to the existing clock lasers is shown in Fig. 3.13.

The transmission of the filter cavity is sent to a separate bread board shown in Fig. 3.15 which amplifies the laser power and distributes it to the frequency comb and ion trap. The power of the frequency stable light on this board is around 10 μW and coupled into a temperature stabilized laser diode. The free-running emission of this diode is broad band and not suitable for coherent spectroscopy. By seeding the diode with the frequency stable light for *injection locking*, it obtains the spectral characteristics of the input laser and narrows its emission spectrum at an output power of roughly 2 mW. This is sufficient to seed a TA which amplifies the laser to an output power of approximately 50 mW, enough to supply two ion traps and the frequency comb with clock laser light.

Since the light is distributed to the comb and trap with optical fibers over several meters, path length fluctuations are an issue that has to be addressed. Temperature, pressure and humidity variations cause variations of the optical index of refraction n or Doppler shifts due to changes of the fiber length L [Ben+19]. The largest contributors are often the temperature induced variation of n and L , which typically results in a fractional frequency change of [Ben+19]

$$\frac{\Delta\nu}{\nu} = \frac{nL}{c} \left(\frac{1}{n} \frac{\partial n}{\partial T} + \frac{1}{L} \frac{\partial L}{\partial T} \right) \frac{\partial T}{\partial t} \approx \frac{1.4 \times 10 \text{ m}}{0.3 \text{ m/ns}} \times \frac{10^{-5}}{\text{K}} \times \frac{0.5 \text{ K}}{10 \text{ h}} = 7 \times 10^{-18}, \quad (3.21)$$

which means that temperature variations of 0.5 K/10 h cause fractional frequency fluctuations of the light transmitted through optical fibers on the 10^{-17} scale. To deliver frequency stable light to the comb and ion trap, active path length stabilization is employed in the clock laser setup. Light sent to the frequency

3.7. Clock laser setup, frequency measurement and stabilization

sensitive ports of the trap and comb is frequency adjusted with an AOM before the fiber and reflected back through the same fiber, accumulating approximately twice the frequency error. On the distribution board, it is overlaid with clock laser light that was not sent through the fiber and did not accumulate this frequency error. By measuring the beat signal between the stable local oscillator and light transmitted through the fiber, the phase offset between the two beams is determined. A frequency offset to correct for the phase error is applied to the AOM via a Voltage Controlled Oscillator (VCO) or Optical Phase Stabilizer (OPS) with a locking bandwidth between 50 kHz and 200 kHz, often limited by the SNR of the interference signal. The latter device was developed and constructed at PTB and provides detection of the beat signal, correction of the AOM frequency and logging of various performance parameters of the path length stabilization [Kuh21]. Observation of the fiber length stabilization beat signal with an OPS or frequency counter is critical, since frequency errors can occur that are not adequately corrected. In this case, data points just before and after the error occurred are discarded.

One port on the distribution board is not path length stabilized, which is employed for resolved sideband cooling and state initialization. Since both of these procedures only require a frequency resolution of 10 Hz at most, due to the high Rabi frequencies of more than 1 kHz employed, the mHz fluctuations due to temperature variations are negligible. Instead, the light is frequency offset with a double pass AOM to enable frequency detunings of MHz without significant reduction of the coupling efficiency into the trap port. This is particularly useful for sideband cooling of radial modes at a secular frequency of more than 1 MHz.

3. Experimental setup for the multi-species, multi-ion clock YbSr1

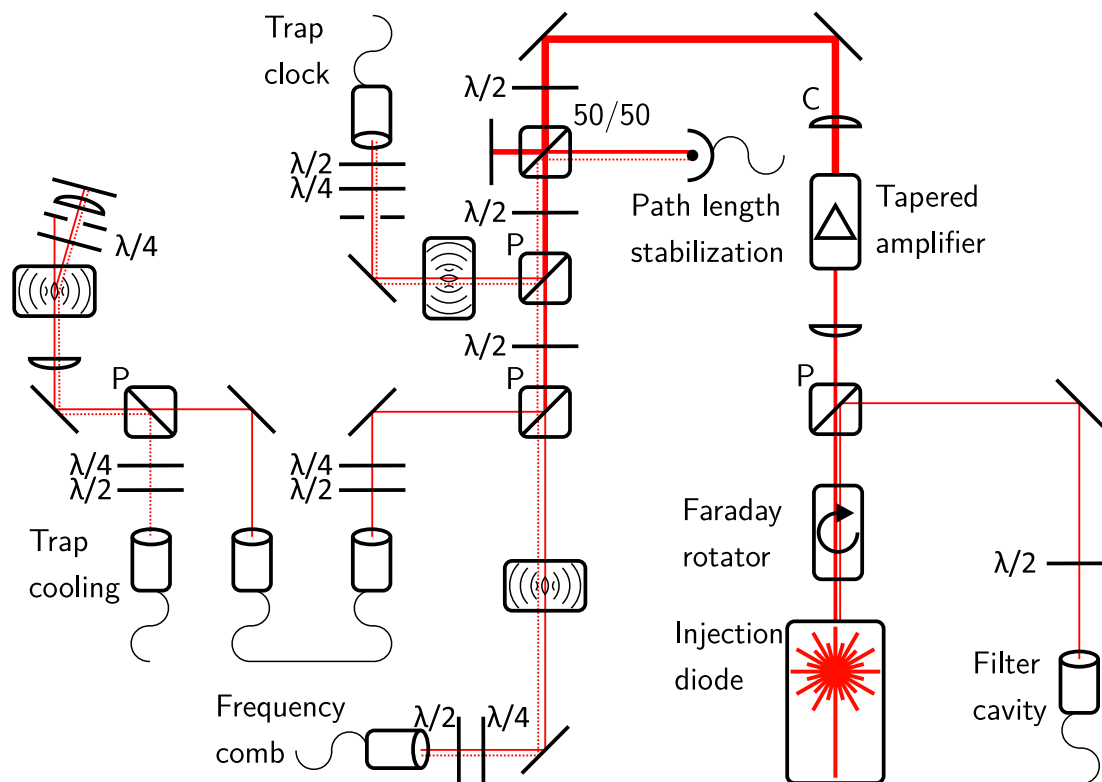


Figure 3.15.: Sketch of the optical setup of the Sr clock laser distribution. The filtered laser light from the master laser in Fig. 3.14 is the seed for an injection locked diode, providing approximately 2 mW of output power with the same spectral characteristics as the stable seed. It is further amplified with a TA to approximately 50 mW and distributed to the optical clock, the cooling and state initialization port as well as the frequency comb. The light coupled into the clock port and comb port is reflected back to measure any phase fluctuations with reference to the unperturbed light on the distribution board. The frequency of the laser in these paths is modified with AOMs to correct for these phase errors. The cooling light is not stabilized, but diffracted with a double-pass AOM to cover a larger detuning range than the other ports without significant coupling loss in the fiber towards the ion trap.

4. Frequency shifts due to electric fields

A major improvement of $^{171}\text{Yb}^+$ clocks would result from a more accurate determination of the sensitivity of the reference transitions to room-temperature black body radiation, which consists of electromagnetic fields peaking in the MIR wavelength region. For this reason, it is necessary to discuss the effect of electric fields on the clock transitions in $^{171}\text{Yb}^+$ and $^{88}\text{Sr}^+$. Electric fields interact with the electronic wavefunction of a state $|\psi\rangle$ of the trapped ion and change its energy E_ψ due to the *Stark effect*. States with defined parity do not possess a permanent electric dipole moment, so the linear contribution of the Stark effect is zero [Dem16, p. 349]. Even if no permanent dipole moment is present, the electric field induces an electric dipole moment, which in turn interacts with \vec{E} to change E_ψ . This is the quadratic Stark effect and causes an energy shift ΔE_ψ of

$$\Delta E_\psi = -\frac{1}{2}\alpha_\psi |\vec{E}|^2, \quad (4.1)$$

with the (induced) polarizability α_ψ . Higher order contributions exist, but are significantly smaller and will be neglected in the following discussion. In an optical clock, the energy difference between two states $|g\rangle$ and $|e\rangle$ is determined, and both states are affected by \vec{E} . This results in the *differential* quadratic Stark shift $\Delta\nu_{\text{Stark}}$

$$h\Delta\nu_{\text{Stark}} = -\frac{1}{2}(\alpha_e - \alpha_g) |\vec{E}|^2 = -\frac{1}{2}\Delta\alpha |\vec{E}|^2, \quad (4.2)$$

with the *differential polarizability* $\Delta\alpha$. Both α and consequently $\Delta\alpha$ vary with the angular frequency of the perturbing electric field as discussed in Section 4.1.

For an electromagnetic wave with angular frequency ω , the electric field magnitude varies with time, so the Stark shift varies with time at the angular frequency ω as well. If the clock interrogation time t is short with respect to $1/\omega$, the variation of $|\vec{E}|^2$ can be followed and manifests as a time-varying offset of the clock frequency, called the *DC Stark shift*. If on the other hand t is long compared to $1/\omega$, as is usually the case for optical and RF fields, the clock frequency varies during the interrogation and produces an offset from the unperturbed frequency proportional

4. Frequency shifts due to electric fields

to the time-average of $|\vec{E}(t)|^2$

$$h\Delta\nu_{\text{Stark, AC}} = h\langle\Delta\nu_{\text{Stark}}\rangle = -\frac{1}{2}\Delta\alpha\left\langle|\vec{E}(t)|^2\right\rangle, \quad (4.3)$$

called the *AC Stark shift*. If $\vec{E}(t)$ varies sinusoidally with amplitude \vec{E}_0 , the time average can be rewritten to be

$$h\Delta\nu_{\text{Stark, AC}} = -\frac{1}{4}\Delta\alpha|\vec{E}_0|^2. \quad (4.4)$$

The magnetic component of the optical electromagnetic field causes a second-order AC Zeeman shift, since the first-order Zeeman shift averages to zero over many periods of the wave. The AC Zeeman shift is usually significantly smaller than the quadratic Stark shift [Gan+18], unless resonant enhancement plays a role.

So far, only an electric field interacts with the ion. In practice, one usually has to define a quantization axis with a magnetic field \vec{B} to separate the Zeeman sub-states of the ground state and excited state as discussed in Section 2.4. This causes the electronic wavefunctions with orbital angular momentum ($L > 0$, i.e. not S states [AS68, p. 132]) to orient themselves with respect to \vec{B} which has an influence on the induced electric dipole moment causing the quadratic Stark shift. If the magnetic field splitting is large with respect to the Stark shift, the basis $|J, m_J\rangle$ remains good and the quadratic Stark shift is a small perturbation which can be split into the *scalar* part independent of \vec{B} as well as the *vectorial* and *tensorial* parts which depend on the relationship between \vec{E} and \vec{B} and the magnetic quantum number m_J [LSR13]. The electromagnetic field propagation direction is given by \vec{k} and the polarization is described with the complex vector $\vec{\epsilon}$ [SSA16]

$$\vec{\epsilon} = e^{i\sigma}(\cos(\phi)\vec{\epsilon}_{\text{maj}} + i\sin(\phi)\vec{\epsilon}_{\text{min}}), \quad (4.5)$$

where ϕ corresponds to the angle of polarization, σ is an arbitrary global phase and $\vec{\epsilon}_{\text{maj/min}}$ are the directions of the major and minor axis of the polarization ellipse. In that case, the quadratic Stark shift in a magnetic field \vec{B} , which encloses the angles $\theta_k, \theta_{\text{maj}}$ and θ_{min} with $\vec{k}, \vec{\epsilon}_{\text{maj}}$ and $\vec{\epsilon}_{\text{min}}$, respectively is [SSA16]

$$h\Delta\nu_{\text{Stark}} = -\frac{1}{2}|\vec{E}|^2\left((\alpha_{e,S} - \alpha_{g,S}), \text{ Scalar}\right) \quad (4.6)$$

$$+ \sin(2\phi)\cos(\theta_k)\frac{m_J}{2J}(\alpha_{e,V} - \alpha_{g,V}), \text{ Vectorial} \quad (4.7)$$

$$+ \frac{3\cos^2(\theta_p) - 1}{2}\frac{3m_J^2 - J(J+1)}{J(2J-1)}(\alpha_{e,T} - \alpha_{g,T}), \text{ Tensorial}, \quad (4.8)$$

where $\cos^2(\theta_p) = \cos^2(\phi) \cos^2(\theta_{\text{maj}}) + \sin^2(\phi) \cos^2(\theta_{\text{min}})$. With the differential polarizabilities $\Delta\alpha_j = \alpha_{e,j} - \alpha_{g,j}$, Eq. (4.8) can be rewritten as

$$h\Delta\nu_{\text{Stark}} = -\frac{1}{2}|\vec{E}|^2 \left(\Delta\alpha_S + \sin(2\phi) \cos(\theta_k) \frac{m_J}{2J} \Delta\alpha_V \right) \quad (4.9)$$

$$+ \frac{3 \cos^2(\theta_p) - 1}{2} \frac{3m_J^2 - J(J+1)}{J(2J-1)} \Delta\alpha_T. \quad (4.10)$$

If the laser polarization is linear, $\phi=0$ and $\vec{\epsilon}_{\text{maj}}$ is the polarization direction. In this case, Eq. (4.10) reduces to

$$h\Delta\nu_{\text{Stark}} = -\frac{1}{2}|\vec{E}|^2 \left(\Delta\alpha_S + \frac{3 \cos^2(\theta_p) - 1}{2} \frac{3m_J^2 - J(J+1)}{J(2J-1)} \Delta\alpha_T \right). \quad (4.11)$$

A further simplification results from the fact that the ground states of the clock transition investigated in this work possess no orbital angular momentum $L=0$. This means that their tensorial shift is equal to 0 and consequently $\Delta\alpha_T = \alpha_{e,T}$.

The tensorial shift can be completely disregarded at the *magic angle* θ_m where

$$\frac{3 \cos^2(\theta_m) - 1}{2} = 0 \Rightarrow \theta_m = \arccos\left(\frac{1}{\sqrt{3}}\right) \approx 54.7^\circ, \quad (4.12)$$

and also when the field is isotropic, like inside a black body. The fine-structure angular momentum J and its projection m_J are replaced with the hyperfine-structure angular momentum F and its projection m_F in Eq. (4.8) to describe the Stark shift between two hyperfine states. For Eq. (4.11) to remain correct in the case of nonzero nuclear spin, the polarizabilities of hyperfine-states with total angular momentum F , electronic angular momentum J , and nuclear angular momentum I are written as [AS68, p. 131]

$$\alpha_S(F) = \alpha_S(J) \quad (4.13)$$

$$\alpha_T(F) = (-1)^{I+J+F} \sqrt{\frac{F(2F-1)(2J+3)(2J+1)(J+1)}{(2F+3)(F+1)(2J-1)J}} \begin{Bmatrix} F & J & I \\ J & F & 2 \end{Bmatrix} \alpha_T(J), \quad (4.14)$$

where the term in angular brackets is a Wigner $6j$ symbol.

4.1. The dynamical polarizability model

In the previous section it is assumed that the polarizability α is constant for a given electric field with amplitude \vec{E}_0 oscillating at an angular frequency ω . While this description covers simple cases like static electric fields (where α is the DC polarizability) or monochromatic laser radiation (where α is the polarizability at the angular frequency ω of the radiation), other sources exist with a broad emission spectrum, such as BBR. For this reason, constructing a model $\alpha(\omega)$ is required over the frequency range relevant for room-temperature BBR. Additionally, a model of $\alpha(\omega)$ is useful to predict the polarizability for sources at various frequencies from a set of measured values.

A common model for the dynamical polarizability $\alpha(\omega)$ of an electronic state $|\psi\rangle$ with total angular momentum J_0 is derived from perturbation theory and based on E1 transitions from $|\psi\rangle$ to a set of other states $\{|\phi_j\rangle\}$ at energy differences ΔE_{0j} from $|\psi\rangle$, with transition matrix elements M_{0j} and total angular momentum J_j [PD06; SSC16]. In that case, the scalar polarizability $\alpha_S(\omega)$ for an electric field oscillating at the frequency ω is [SSC16; Hua+24]

$$\alpha_S(\omega) = \frac{2}{3(2J_0 + 1)} \sum_j \frac{\Delta E_{0j}}{\hbar^2 \omega^2 - \Delta E_{0j}^2} |M_{0j}|^2, \quad (4.15)$$

the vector polarizability $\alpha_V(\omega)$ is [Hua+24]

$$\alpha_V(\omega) = \sqrt{\frac{24J_0}{(J_0 + 1)(2J_0 + 1)}} \quad (4.16)$$

$$\sum_j (-1)^{J_0+J_j+1} \begin{Bmatrix} J_0 & 1 & J_0 \\ 1 & J_j & 1 \end{Bmatrix} \frac{\Delta E_{0j}}{\hbar^2 \omega^2 - \Delta E_{0j}^2} |M_{0j}|^2, \quad (4.17)$$

and the tensor polarizability $\alpha_T(\omega)$ is [SSC16; Hua+24]

$$\alpha_T(\omega) = \sqrt{\frac{40J_0(2J_0 - 1)}{3(J_0 + 1)(2J_0 + 3)(2J_0 + 1)}} \quad (4.18)$$

$$\sum_j (-1)^{J_0+J_j} \begin{Bmatrix} J_0 & 2 & J_0 \\ 1 & J_j & 1 \end{Bmatrix} \frac{\Delta E_{0j}}{\hbar^2 \omega^2 - \Delta E_{0j}^2} |M_{0j}|^2, \quad (4.19)$$

under the assumption that the perturbing field is detuned from resonance of any E1 transition by at least several linewidths [SSC16].

This disregards higher-order transitions such as M1 and E2, since they are significantly weaker than the E1 transitions considered. Additionally, only transitions of the valence electron are considered, but the core consisting of all non-valence electrons and feedback of the valence electron to the core also need to be taken into account [SSC16]. Usually they are estimated as fixed polarizabilities α_{core} and α_{vc} , respectively. Since α_{core} is the same for all states that only differ by the electronic state of the valence electron, it does not have any effect on the differential polarizability $\Delta\alpha(\omega)$.

The free parameters in this model are the energy differences ΔE_{0j} and matrix elements M_{0j} for each transition considered. The energy differences are usually sufficiently well known from spectroscopic data (e.g. the NIST atomic spectra database [Kra+24]) but the matrix elements are often not available experimentally. They are computed numerically [SSC16; LSR13; SSA16] and supplanted by specific measurements, if they are available. These can be direct determinations of matrix elements [Het+15], excited state lifetimes [Sha+23], branching ratios [Zha+16] or differential polarizabilities at specific frequencies [Hua+24]. Matrix elements for many alkaline and alkaline earth atoms and ions as well as a few highly charged ions are found in [Bar+22].

An additional method developed in [BA25] is based on the extrapolation of direct polarizability measurements to other wavelengths. This is useful for the E3 transition, because measurements over the NIR wavelength range of both the scalar and tensorial polarizability are available in [Hun14; Hun+16]. Additionally, a zero crossing of $\Delta\alpha_S^{\text{E3}}$ is observed in [Lan21] and is also used as input data. $\Delta\alpha_S(\lambda)$ and $\Delta\alpha_T(\lambda)$ are shown in Fig. 4.1, Fig. 4.2 and Fig. 4.3 for the $^{171}\text{Yb}^+$ E2, E3 and $^{88}\text{Sr}^+$ clock transitions respectively.

The polarizability α_{dc} for static or low-frequency fields, where ω is significantly smaller than the resonance frequency of the transition with smallest frequency in the model, is the special case $\alpha_{\text{dc}} = \alpha_S(0)$. It is particularly important for optical clocks, since α_{dc} is used in the determination of the BBR shift at room temperature [PD06]. A black body with temperature T emits electromagnetic radiation with a spectral energy density $\partial u_\omega(\omega, T)/\partial\omega$ according to *Planck's law* [Pla01]

$$\frac{\partial u_\omega(\omega, T)}{\partial\omega} = \frac{\hbar}{\pi^2 c^3} \frac{\omega^3}{e^{\frac{\hbar\omega}{k_B T}} - 1}, \quad (4.20)$$

which is related to the time-averaged squared spectral electric field density it generates by

$$\frac{\partial \langle E^2 \rangle}{\partial\omega}(\omega, T) = \frac{1}{\epsilon_0} \frac{\partial u_\omega(\omega, T)}{\partial\omega} \quad (4.21)$$

for BBR at temperature T in vacuum.

4. Frequency shifts due to electric fields

The Stark shift for a transition perturbed by an electric field with a spectral distribution $\langle E^2 \rangle(\omega)$ is calculated as [PD06]

$$\Delta\nu_{\text{Stark}} = \int_0^\infty d\omega \frac{d\Delta\nu_{\text{Stark}}}{d\omega} \quad (4.22)$$

$$= -\frac{1}{2\hbar} \int_0^\infty d\omega \Delta\alpha(\omega) \frac{\partial \langle E^2 \rangle(\omega)}{\partial \omega}. \quad (4.23)$$

By combining Eq. (4.21) and Eq. (4.23), the quadratic Stark shift $\Delta\nu_{\text{BBR}}(T)$ of the clock transition frequency due to BBR at temperature T is calculated numerically to be

$$\Delta\nu_{\text{BBR}}(T) = -\frac{1}{4\pi^3 \varepsilon_0 c^3} \int_0^\infty d\omega \Delta\alpha_S(\omega) \frac{\omega^3}{e^{\frac{\hbar\omega}{k_B T}} - 1}. \quad (4.24)$$

Only the scalar polarizability is relevant for BBR due to its isotropy. Since the spectral overlap of BBR with the lowest-frequency E1 resonance is usually small, the static polarizability $\Delta\alpha_{\text{dc}} := \Delta\alpha_S(0)$ and *dynamic correction* η are used to parametrize $\Delta\nu_{\text{BBR}}(T)$ at room temperature for different optical clocks [Jia+09]

$$\Delta\nu_{\text{BBR}}(T) = -\frac{2\sigma}{h\varepsilon_0 c} T^4 \Delta\alpha_{\text{dc}} \left(1 + \frac{15}{\pi^4} \int_0^\infty du \left(\frac{\Delta\alpha_S(\omega)}{\Delta\alpha_{\text{dc}}} - 1 \right) \frac{u^3}{e^u - 1} \right), \quad u = \frac{\hbar\omega}{k_B T} \quad (4.25)$$

$$= -\frac{\langle E^2(T^4) \rangle}{2h} \Delta\alpha_{\text{dc}} (1 + \eta) \quad (4.26)$$

$$\approx -52.227\,75 \text{ mHz} \left(\frac{T}{300 \text{ K}} \right)^4 \frac{\Delta\alpha_{\text{dc}}}{10^{-40} \text{ Jm}^2/\text{V}^2} (1 + \eta), \quad (4.27)$$

with the Stefan-Boltzmann constant σ . η corrects for the dynamic behaviour of $\Delta\alpha$ over the BBR spectrum at a temperature of approximately 300 K.

If the differential polarizability at a different frequency ω_0 is known with small uncertainty, it is useful to parametrize $\Delta\nu_{\text{BBR}}(T)$ as

$$\Delta\nu_{\text{BBR}}(T) = -\frac{2\sigma}{h\varepsilon_0 c} T^4 \Delta\alpha_S(\omega_0) (1 + \xi(\omega_0, T)), \quad (4.28)$$

where $\xi(\omega_0, T)$ is

$$\xi(\omega_0, T) = \frac{15}{\pi^4} \int_0^\infty du \left(\frac{\Delta\alpha_S(\omega)}{\Delta\alpha_S(\omega_0)} - 1 \right) \frac{u^3}{e^u - 1}, \quad u = \frac{\hbar\omega}{k_B T}. \quad (4.29)$$

Since BBR at a temperature of 300 K has a maximum spectral energy density at a wavelength $\lambda=9.7\ \mu\text{m}$, determining $\Delta\alpha_S$ in this MIR frequency range provides a better approximation of $\Delta\nu_{\text{BBR}}$ using Eq. (4.28), compared to $\Delta\alpha_{\text{dc}}$. Figure 4.1, Fig. 4.2 and Fig. 4.3 show the spectral energy density at various temperatures around 300 K and η and $\xi(10.6\ \mu\text{m})$ for the $^{171}\text{Yb}^+$ E2, E3 and $^{88}\text{Sr}^+$ clock transitions, respectively.

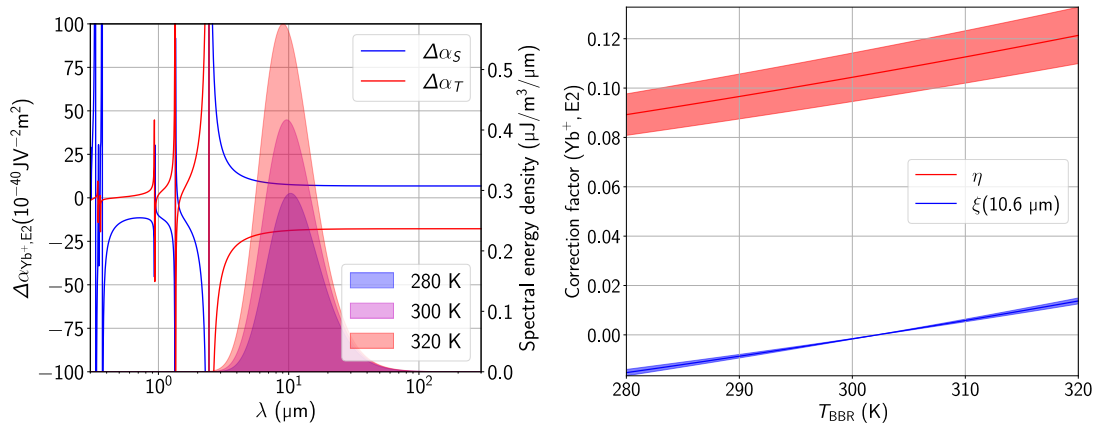


Figure 4.1.: Polarizability model for $^{171}\text{Yb}^+$ E2. The figure on the left hand side shows scalar and tensorial differential polarizability $\Delta\alpha_{S/T}$ for the E2 transition of $^{171}\text{Yb}^+$ at various wavelengths λ according to the E1 resonance model [Bié+98]. The BBR energy density at around room-temperature is shown as well. Due to the significant curvature of $\Delta\alpha_S$ in the region around $\lambda \approx 10\ \mu\text{m}$, the dynamic correction η shown on the right is around 10% at room temperature. $\xi(10.6\ \mu\text{m})$ on the other hand is close to zero and can be determined with smaller uncertainty.

4. Frequency shifts due to electric fields

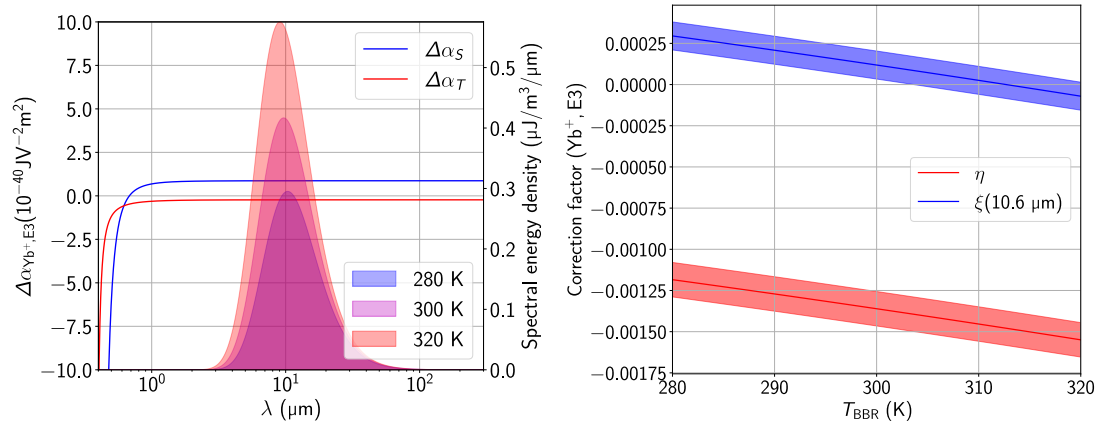


Figure 4.2.: Polarizability model for $^{171}\text{Yb}^+$ E3. The figure on the left hand side shows scalar and tensorial differential polarizability $\Delta\alpha_{S/T}$ for the E3 clock transition of $^{171}\text{Yb}^+$ at various wavelengths λ according to the extrapolation model [BA25] supplied with measurements from [Hun14; Hun+16; Lan21], which results in a dynamic polarizability consistent with all data points within their uncertainty. Mind that the scale of the vertical axis is reduced by a factor 10 compared to Fig. 4.1 and Fig. 4.3. The BBR energy density at around room-temperature is shown as well. Since the resonances do not have significant overlap with the BBR spectral energy density, the dynamic correction η shown on the right in the same temperature range is less than 1 % at room temperature and stays small within the temperature range shown.

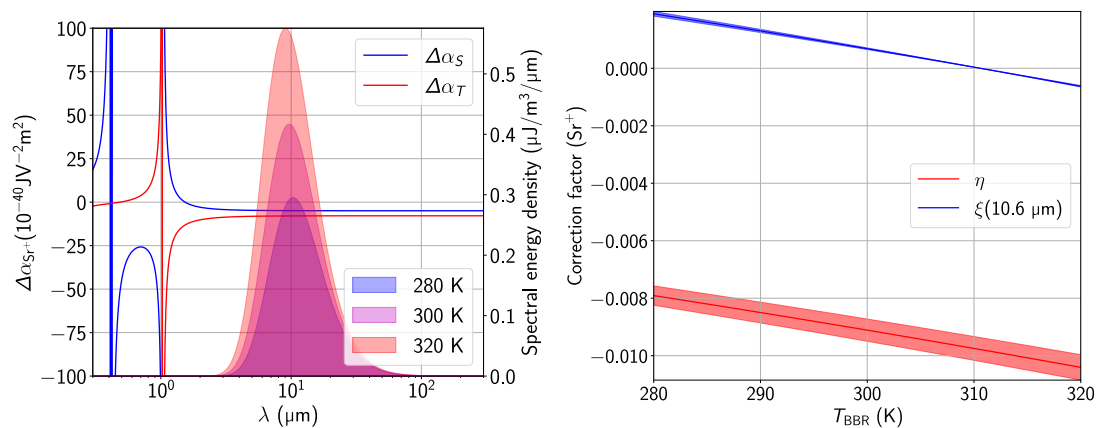


Figure 4.3.: Polarizability model for $^{88}\text{Sr}^+$ E2. The figure on the left hand side shows scalar and tensorial differential polarizability $\Delta\alpha$ for the clock transition of $^{88}\text{Sr}^+$ at various wavelengths λ according to the E1 resonance model [Bar+22]. The BBR energy density at around room-temperature is shown as well. Since the resonances do not have significant overlap with the BBR radiation density, the dynamic correction η shown on the right in the same temperature range is around 1 % at room temperature and stays small within the temperature range shown.

Figure 4.3 shows that $\Delta\alpha_S < 0$ for $\lambda \rightarrow \infty$ for the $^{88}\text{Sr}^+$ clock transition, which causes a positive BBR shift. This enables a measurement method to determine $\Delta\alpha_S (10^7 \mu\text{m}) \approx \Delta\alpha_{\text{dc}}$ based on excess micromotion [Ber+98]. As discussed in Section 2.1, displacement of the trapped ion from the RF center by electric fields causes driven motion at the angular frequency of the trap Ω_{rf} . If the clock transition of the ion is interrogated by a laser, two frequency shifts have to be taken into account due to micromotion. The velocity v of the ion causes a 2nd-order Doppler shift $\Delta\nu_D$

$$\frac{\Delta\nu_D}{\nu_0} = -\frac{v^2}{2c^2}, \quad (4.30)$$

and the electric field E of the trap causes a quadratic Stark shift $\Delta\nu_S$ equal to

$$\frac{\Delta\nu_S}{\nu_0} = -\Delta\alpha_S \frac{E^2}{2h\nu_0}, \quad (4.31)$$

where c is the speed of light, h is the Planck constant and ν_0 is the optical transition frequency. Since both shifts vary in time with the trap drive at a frequency of approximately 5-50 MHz and the interrogation time of ms averages over many periods of this oscillation, only the time-averaged frequency shifts are observable. From the equations of motion in Section 2.1, the sum of the time averaged squared Doppler and Stark Shift are approximately

$$\frac{\langle\Delta\nu_D\rangle + \langle\Delta\nu_S\rangle}{\nu_0} = -\left(\frac{r_0\Omega}{2c}\right)^2 \left(1 + \frac{\Delta\alpha_S}{h\nu_0} \left(\frac{mc\Omega}{e}\right)^2\right), \quad (4.32)$$

with the micromotion amplitude r_0 , ion mass m , speed of light c and ion charge e . If $\Delta\alpha_S < 0$, there exists a trap drive angular frequency Ω_0 where $\langle\Delta\nu_D\rangle + \langle\Delta\nu_S\rangle = 0$, which means that no frequency shift is observed even though the ion experiences micromotion [Ber+98; Dub+14]. The differential polarizability is then given by [Ber+98; Dub+14]

$$\Delta\alpha_S = -h\nu_0 \left(\frac{e}{mc\Omega_0}\right)^2, \quad (4.33)$$

so it only depends on the *magic trap drive frequency* Ω_0

$$\Omega_0 = \frac{e}{mc} \sqrt{-\frac{h\nu_0}{\Delta\alpha_S}} \quad (4.34)$$

at which no micromotion shift is observed. This can be measured with an uncertainty below 1 %, at which point higher order effects have to be considered [Dub+14;

4. Frequency shifts due to electric fields

Lin+25b]. For the clock transition of $^{88}\text{Sr}^+$ $\Delta\alpha_S(\Omega_0) = -4.7938(71) \times 10^{-40} \text{ Jm}^2/\text{V}^2$ [Dub+14] as measured by NRC, which corresponds to $\Omega_0 = 2\pi \times 14.404(10) \text{ MHz}$. A more recent measurement by VTT of the same quantity found $\Delta\alpha_S(\Omega_0) = -4.8314(20) \times 10^{-40} \text{ Jm}^2/\text{V}^2$ [Lin+25b], reducing the fractional uncertainty to 0.04%. But the two measurements show a fractional offset of 0.78(15)%, corresponding to a discrepancy of 5σ . As mentioned in [Lin+25b], it is currently unclear what the source of this disagreement is, but the authors suspect an unrecognized frequency offset between the two clocks involved in the NRC measurement [Dub+14].

4.2. Magic wavelength measurement for $^{88}\text{Sr}^+$

Another feature of $\Delta\alpha_S(^{88}\text{Sr}^+)$ visible in Fig. 4.3 is its zero crossing at a wavelength of approximately 1550 nm. A laser with time-averaged intensity $\langle I \rangle$ and the *magic wavelength* λ_0 where $\Delta\alpha_S(\lambda_0) = 0$ does not cause any scalar frequency shift. The vectorial $\Delta\alpha_V$ and tensorial $\Delta\alpha_T$ polarizability are not necessarily equal to 0 at this wavelength, so individual transitions between Zeeman states may still be frequency shifted. Since the light shift is equal to zero for any intensity I , λ_0 can be measured with small uncertainty compared to values of $\Delta\alpha_S$ that depend on accurate knowledge of I .

The knowledge of $\Delta\alpha_S$ over the room-temperature BBR spectrum and consequently the dynamic correction uncertainty can be deduced from the theoretical estimate by measuring the magic wavelength for the $^{88}\text{Sr}^+$ clock transition around 1550 nm. The theoretical prediction of λ_0 is 1532(15) nm using the atomic structure data from [Bar+22] as well as measured transition rates from [Zha+16].

To measure λ_0 , a single $^{88}\text{Sr}^+$ ion is trapped and irradiated with NIR laser radiation via the view port of the vacuum enclosure depicted in Fig. 3.8 that ordinarily is employed for the E3 clock laser. The laser light is produced by an ECDL with an output power of approximately 5 mW and amplified with a broadband Erbium-Doped Fiber Amplifier (EDFA) to 40 mW in front of the vacuum window. Its approximate beam diameter at the ion position is 70 μm . The laser is polarization-filtered with a PBS and the transmitted power is monitored continuously with a photodiode. The laser wavelength is changed by adjusting the laser grating angle and spans 1520-1570 nm. The center wavelength is measured with a calibrated wavemeter that has an uncertainty of 30 MHz, provided to me by department 4.3 at PTB. Both the wavemeter uncertainty and laser linewidth of less than 1 MHz are significantly smaller than the minimum distance between two measurement points of approximately 1 nm. Changes in the laser power at different wavelengths are compensated with the EDFA to always measure at approximately equal power.

To separate the scalar and tensorial light shift, four individual transitions between Zeeman states of the ground and excited state are interrogated. These are the

$|S, m_S = \pm 1/2\rangle \rightarrow |D, m_D = \pm 3/2\rangle$ and $|S, m_S = \pm 1/2\rangle \rightarrow |D, m_D = \pm 5/2\rangle$ transitions at frequencies $\nu_{\pm 1/2}^{\pm 3/2}$ and $\nu_{\pm 1/2}^{\pm 5/2}$, respectively. All frequencies are measured as ratios with respect to the $^{171}\text{Yb}^+$, E3 clock Yb1 which features a systematic uncertainty of 2.7×10^{-18} [San+19]. A reference measurement without the NIR radiation shifting the $^{88}\text{Sr}^+$ frequency is performed separately and reaches an uncertainty of 4×10^{-17} , an order of magnitude smaller than the smallest uncertainty of the ratios determined with the laser radiation. The frequencies of transition pairs with opposite magnetic quantum number are averaged to

$$\nu^{3/2} = \frac{\nu_{+1/2}^{+3/2} + \nu_{-1/2}^{-3/2}}{2}, \quad \nu^{5/2} = \frac{\nu_{+1/2}^{+5/2} + \nu_{-1/2}^{-5/2}}{2}, \quad (4.35)$$

which are free of the first-order Zeeman shift. Additionally, any vector light shifts are also canceled, since they are proportional to the quantum number m_J as seen in Eq. (4.10). The scalar $\Delta\nu_S$ and tensorial shift $\Delta\nu_T$ remain and are extracted with the following weighted averages [Dub+13]

$$\Delta\nu_S(\lambda) = -\Delta\alpha_S(\lambda) \frac{\langle I \rangle}{2h\varepsilon_0 c} = \frac{1}{6}\nu^{5/2} + \frac{5}{6}\nu^{3/2} \quad (4.36)$$

$$\Delta\nu_T(\lambda) = -\Delta\alpha_T(\lambda) \frac{\langle I \rangle}{2h\varepsilon_0 c} \frac{3\cos^2\theta_p - 1}{2} = \frac{5}{6}(\nu^{5/2} - \nu^{3/2}). \quad (4.37)$$

The measured scalar sensitivity $\Delta\nu_S(\lambda)/P$ and scalar to tensor polarizability ratio $\Delta\alpha_S(\lambda)/\Delta\alpha_T(\lambda)$ are shown in Fig. 4.4.

A quadratic polynomial $\Delta\nu_S(\lambda)/P = a(\lambda - \lambda_0) - b(\lambda - \lambda_0)^2$ is a sufficient model for $\Delta\alpha_S(\lambda)$ in the measured wavelength range to extract λ_0 with a fractional error of less than 10^{-7} . The magic wavelength $\lambda_0 = 1538.75(10)$ nm is consistent with the theoretical prediction and reduces the uncertainty by a factor 150. This provides confidence in the differential polarizability model itself as well as the dynamic correction η and allows for a more precise determination of matrix elements in the model to match λ_0 between theory and experiment.

4. Frequency shifts due to electric fields

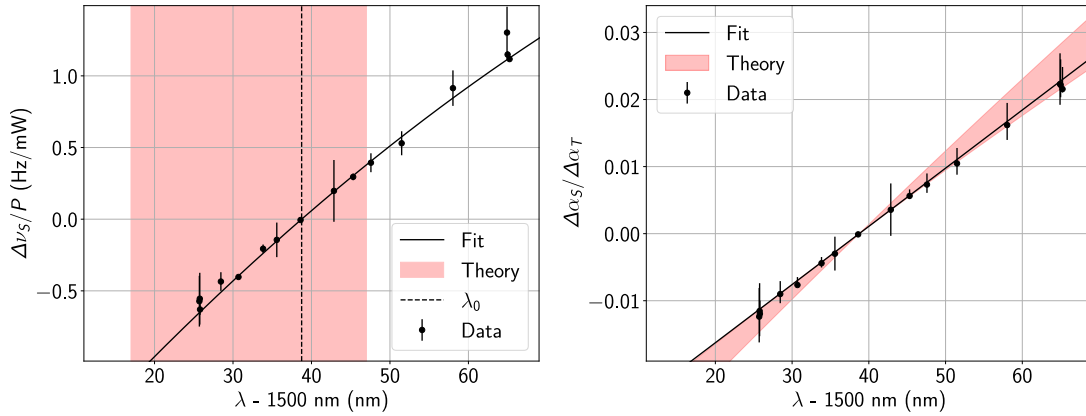


Figure 4.4.: *Magic wavelength measurement.* The figure on the left shows the measured scalar sensitivity of the $^{88}\text{Sr}^+$ clock transition to laser radiation at various wavelengths λ . At $\lambda = \lambda_0 = 1538.75(10)$ nm, the sensitivity is equal to zero, corresponding to the magic wavelength. The solid line is a fit to the data using a quadratic polynomial $\Delta\nu_S(\lambda)/P = 47.55(87) \text{ mHz}/(\text{mW nm})(\lambda - \lambda_0) - 0.385(75) \text{ mHz}/(\text{mW nm}^2)(\lambda - \lambda_0)^2$, which approximates of the differential polarizability in this wavelength range sufficiently well to extract the magic wavelength from the data. The figure on the right shows the ratio between the tensor and scalar polarizability using the same data as well as the corresponding fit using a linear polynomial $\Delta\alpha_S/\Delta\alpha_T(\lambda) = 0.868(31) \times 10^{-3}/\text{nm}(\lambda - \lambda_0)$. The theoretical predictions are shown as shaded red areas for both figures. The measured magic wavelength and scalar-tensor ratio agree well with the theoretical prediction.

To extract $\Delta\alpha_T(\lambda)$ from $\Delta\nu_T(\lambda)$, it is necessary to know the angle θ_p between the quantization axis \vec{b} and polarization direction \vec{e} as evident in Eq. (4.11). The magnetic field direction is set with the three small pairs of Helmholtz coils to maximize the tensor shift, which is done with a fractional uncertainty of 10%. While the laser radiation is linearly polarized parallel to the optical table with a PBS with an extinction ratio greater than 1000:1, it also passes a vacuum window before irradiating the ion. The mechanical stresses on the window induce a birefringence, which rotates the polarization and introduces a circular component. The latter is not problematic, since this only leads to a vector light shift, which is canceled by interrogating pairs of transitions between opposite Zeeman states. The maximum rotation of the polarization is assumed to be 6° , the amount observed in [Ste+13] for a standard vacuum viewport, and taken as the full uncertainty. This results in $\cos\theta_p = 1.00^{+0.00}_{-0.05}$ for the cosine of the angle between \vec{b} and \vec{e} and is already included in the uncertainty of the data shown in Fig. 4.4.

To summarize, a magic wavelength of the $^{88}\text{Sr}^+$ $S_{1/2} \rightarrow D_{5/2}$ clock transition is determined to be $\lambda_0 = 1538.75(10)$ nm, consistent with the theoretical prediction of the polarizability model based on matrix elements in [Bar+22] and measurements in [Zha+16]. The ratio between the scalar and tensorial polarizability also

matches expectation. This supports the expected curvature of $\Delta\alpha_S(\lambda)$ in the MIR wavelength range and allows for an accurate interpolation of polarizability values between $\Delta\alpha_{\text{dc}}$ and $\Delta\alpha_S(\lambda_0)$.

4.3. Polarizability measurements with infrared laser radiation

The differential polarizability $\Delta\alpha_S$ of the $^{88}\text{Sr}^+$ clock transition had not been investigated using MIR radiation so far. Measurements of $\Delta\alpha_S(\lambda)$ for clock transitions of other ion species in the MIR and NIR wavelength region have been performed, but these do not possess a magic frequency Ω_0 which allows for an accurate determination of $\Delta\alpha_{\text{dc}}$ [Ros+06; Hun+16; Arn+18; Bay+20]. To check the consistency between the two measurement approaches, I measure $\Delta\alpha_S(10.6\ \mu\text{m})$ and $\Delta\alpha_S(8.5\ \mu\text{m})$ with MIR laser radiation and compare the result with $\Delta\alpha_{\text{dc}}$ and the expected ratio $\Delta\alpha_S(10.6\ \mu\text{m})/\Delta\alpha_{\text{dc}}$ or $\Delta\alpha_S(8.5\ \mu\text{m})/\Delta\alpha_{\text{dc}}$, which is known with small uncertainty from the theoretical model and the magic wavelength measurement in Section 4.2.

The quadratic Stark shift $\Delta\nu_{\text{Stark}}$ due to a laser beam is proportional to the differential polarizability $\Delta\alpha$ and local time-averaged laser intensity $\langle I \rangle(x, y)$

$$\langle \Delta\nu_{\text{Stark}} \rangle(x, y) = -\frac{1}{2h\varepsilon_0 c} \Delta\alpha \times \langle I \rangle(x, y). \quad (4.38)$$

Since the total power P of the beam is equal to the integrated intensity, the integrated quadratic Stark shift is proportional to the differential polarizability [Hun+16; Bay+20]

$$\int_{-\infty}^{\infty} dx \int_{-\infty}^{\infty} dy \langle \Delta\nu_{\text{Stark}} \rangle(x, y) = -\frac{1}{2h\varepsilon_0 c} \Delta\alpha \int_{-\infty}^{\infty} dx \int_{-\infty}^{\infty} dy \langle I \rangle(x, y) \quad (4.39)$$

$$= -\frac{1}{2h\varepsilon_0 c} \Delta\alpha \times P. \quad (4.40)$$

This means that by measuring the power P of the laser at the ion position and integrating the light shift over the complete beam profile, the differential polarizability can be determined as

$$\Delta\alpha = -\frac{2h\varepsilon_0 c}{P} \int_{-\infty}^{\infty} dx \int_{-\infty}^{\infty} dy \langle \Delta\nu_{\text{Stark}} \rangle(x, y). \quad (4.41)$$

Importantly, the power has to be measured with a calibrated photo detector and any optical losses between the location of the power measurement and the ion have to be characterized to determine P .

4. Frequency shifts due to electric fields

In principle, ion movement during the interrogation (e.g. due to secular motion or micromotion) causes the observed Stark shift to be modified, because the ion samples different parts of the intensity profile over time. If the center position of the ion is (x_0, y_0) and it oscillates around the center position with a RMS amplitude (σ_x, σ_y) at a frequency significantly higher than the inverse interrogation time, the Stark shift is

$$\langle \Delta\nu_{\text{Stark}} \rangle_{t, \sigma_x, \sigma_y}(x_0, y_0) = -\frac{1}{2h\varepsilon_0 c} \Delta\alpha \times \langle I \rangle_{\sigma_x, \sigma_y}(x_0, y_0). \quad (4.42)$$

For an elliptical gaussian beam in the focus with beam radii (w_a, w_b) at an angle θ with respect to the coordinate system (x, y) and a beam center (x_0, y_0) , the time-averaged intensity $\langle I \rangle(x, y)$ is

$$\langle I \rangle(x, y) = \frac{2P}{\pi w_a w_b} \exp(-2(g_{aa} + g_{bb} - g_{ab})) \quad (4.43)$$

$$g_{aa} = \left(\left(\frac{x - x_0}{w_a} \right)^2 + \left(\frac{y - y_0}{w_b} \right)^2 \right) \cos^2 \theta \quad (4.44)$$

$$g_{bb} = \left(\left(\frac{x - x_0}{w_b} \right)^2 + \left(\frac{y - y_0}{w_a} \right)^2 \right) \sin^2 \theta \quad (4.45)$$

$$g_{ab} = 2(x - x_0)(y - y_0)(1/w_a^2 - 1/w_b^2) \cos \theta \sin \theta, \quad (4.46)$$

which reduces to the standard circular gaussian intensity profile for a centered beam $(x_0=0, y_0=0)$ and $w_a=w_b=w_0$ as well as $\theta=0$

$$\langle I \rangle(x, y) = \frac{2P}{\pi w_0^2} \exp\left(-2\frac{x^2 + y^2}{w_0^2}\right). \quad (4.47)$$

The largest spatial gradient of this intensity distribution occurs at $r = \sqrt{x^2 + y^2} = \pm w_0/2$. Oscillatory ion motion with an RMS amplitude σ causes the largest deviation $\delta\nu_{\text{Stark}}$ from the fixed point approximation of the Stark shift at these points. It is equal to

$$\frac{\delta\nu_{\text{Stark}}}{\langle \Delta\nu_{\text{Stark}} \rangle(r = \pm w_0/2)} = -2\frac{\sigma}{w_0} + O\left(\left(\frac{\sigma}{w_0}\right)^2\right). \quad (4.48)$$

The integral in Eq. (4.40) can be approximated experimentally by determining the light shift at various equidistant points of the beam profile and numeric integration. If the beam profile is sufficiently well approximated by a gaussian distribution, Eq. (4.46) in combination with Eq. (4.38) also allows for determination of $\Delta\alpha$

without sampling the whole beam profile. In that case, the gaussian profile is fit to the observed light shift at various points not necessarily sampled in an equidistant manner. Deviations from the gaussian profile cause an error, but can be estimated by the residuals of the observed intensity pattern from the gaussian ideal.

Experimental setup Two laser sources are used for this measurement, a 10.60(3) μm CO_2 laser with up to 10 W of output power and a 8.568(1) μm Quantum Cascade Laser (QCL) with up to 400 mW of output power. While the CO_2 laser is comparatively spectrally narrow with a linewidth of significantly less than the specified center wavelength uncertainty of 0.03 μm , the QCL has a specified broader linewidth of 0.21 μm . Since the fractional slope $\frac{\partial\Delta\alpha_S}{\partial\lambda}/\Delta\alpha_S(^{88}\text{Sr}^+, 8.568 \mu\text{m})$ of the scalar polarizability is $3.65(11) \times 10^{-3}/\mu\text{m}$, the fractional uncertainty due to the laser wavelength is 0.77×10^{-3} . A more careful investigation of the effect of the spectral intensity distribution of this laser on the measured differential polarizability is found in Section 5.1, but is not required here due to the significantly larger uncertainty from optical losses. The fractional slope at 10.6 μm is even smaller with $\frac{\partial\Delta\alpha_S}{\partial\lambda}/\Delta\alpha_S(^{88}\text{Sr}^+, 10.6 \mu\text{m}) = 1.889(57) \times 10^{-3}/\mu\text{m}$, causing a negligible maximum fractional error of 0.057×10^{-3} due to the uncertainty of the laser wavelength.

The lasers are set up next to the ion trap and supplied with electrical power as well as temperature stabilized cooling water. The electrical supply for the CO_2 laser is a DC voltage source while the QCL is supplied with a laser diode current controller. A maximum fractional power drift of 1.5%/h is observed with the CO_2 laser and less than 0.05%/h with the QCL after stabilizing the cooling water temperature to better than 0.1 K.

The laser power is determined with a thermopile power meter capable of measuring up to 30 W of power, which is calibrated by PTB at a wavelength of 10.6 μm with a fractional uncertainty of 0.5%. The optical power of the beam is measured just before the last lens focussing the beam onto the ion as depicted in Fig. 3.8. Losses due to the lens, displacement window and vacuum windows are determined by comparing the transmitted power to the incoming power when the beam is centered on the ion. The transmission of a single ZnSe vacuum window AR coated from 8 μm to 12 μm is 94.6(3.4)%, which is determined from the total transmission through both windows of 90.3(5)% and direct measurements with two separate windows not used in the experimental setup. The reflectivity of the windows not installed in the setup is 1.1%, so the rest of the optical power is dissipated as losses in the window material. The uncertainty of the vacuum window transmission does not allow for a determination of $\Delta\alpha_S$ with a fractional uncertainty below 3.4%.

Since the MIR laser beams have to be significantly expanded before focussing to reach a sufficiently small beam waist at the ion position, diffraction effects due to the lens aperture radius $a = 12.7$ mm have to be taken into account. Pure broadening of the beam while retaining its gaussian intensity distribution does not

4. Frequency shifts due to electric fields

cause a systematic shift of the inferred polarizability, but ringing of the intensity distribution similar to an Airy disk reduces the optical power P_{central} enclosed in the central spot compared to the total power P . This causes a systematic shift of the inferred polarizability when it is related to the optical power measurement, which determines P and not the relevant P_{central} . For the maximum beam radius $w = 9.4(1.9)$ mm of the CO₂ beam at the beam expander telescope lens before directing the laser beam towards the optical setup around the ion chamber in Fig. 3.8, $P_{\text{central}}/P = 0.974(16)$ [Li07]. The polarizability values for ⁸⁸Sr⁺ and the E2 transition are determined with this correction applied to the data.

After the last focussing lens with a focal length of 300 mm, where the diameter of the collimated laser beam is approximately 7 mm, the beam is transmitted through a 5.0(3) mm thick ZnSe (refractive index $n = 2.403$) window mounted on a mirror mount with micrometer screws that displaces the beam laterally upon inducing a tilt. The relationship between the beam displacement Δx and the tilt angle $\Delta\varphi$ is derived from geometric optics as

$$\Delta x = d \left[\sin(\varphi_0 + \Delta\varphi) \left(1 - \sqrt{\frac{1 - \sin^2(\varphi_0 + \Delta\varphi)}{n^2 - \sin^2(\varphi_0 + \Delta\varphi)}} \right) \right. \quad (4.49)$$

$$\left. - \sin(\varphi_0) \left(1 - \sqrt{\frac{1 - \sin^2(\varphi_0)}{n^2 - \sin^2(\varphi_0)}} \right) \right]. \quad (4.50)$$

The angle $\Delta\varphi$ is measured by reflecting a visible laser on the surface of the window and observing the displacement of the reflected beam after it travels a distance of 2005 mm. This allows for a determination of $\Delta\alpha$ with negligible uncertainty compared to the power calibration uncertainty. The initial angle φ_0 of the window with respect to the beam propagation is measured with a triangle ruler.

Equation (4.50) is derived from geometric optics for a single beam with a tilt angle $\Delta\varphi$, which does not capture the full behaviour of the gaussian beam. Since it is focused with a lens before the window, each part of the beam has a different angle with respect to the window due to the beam curvature. This modifies the displacement Δx by a constant fractional offset κ with respect to the approximation Eq. (4.50). κ is determined by individually calculating the displacement for 200 sampled rings at different radii from the center and comparing the displacement between this beam and the displacement from Eq. (4.50). κ varies between 1% and 2% in this setup, dependent on the wavelength λ and beam waist w_0 of each beam. The following data are corrected for κ .

The Stark shift due to the perturbing MIR laser field is measured at several displacements Δx . The laser power is measured with the calibrated power meter after each individual determination. Since the displacement is done by hand and the whole beam area cannot be covered due to the limited displacement range,

4.3. Polarizability measurements with infrared laser radiation

a direct integration of the light shift is not easily possible. Instead, an elliptical Gaussian beam Eq. (4.46) is fitted to the observed intensity profile to determine the beam waist and peak light shift.

Since the quantity of interest is the scalar polarizability $\Delta\alpha_S$ and I did not operate at the magic angle for this measurement, the scalar and tensorial Stark shift have to be separated. The vectorial light shift is averaged out by interrogating pairs of $|S_{1/2}, \pm 1/2\rangle \rightarrow |D_{5/2}, \pm m_D\rangle$ transitions, similar to the averaging of linear Zeeman shifts. The dependence of the tensorial Stark shift $\Delta\nu_T$ on the magnetic quantum number m_D of the excited state allows for the following averaging to extract the scalar shift $\Delta\nu_S$ from the light shift $\Delta\nu_{m_S}^{m_D}$ of the transition $|S_{1/2}, m_S\rangle \rightarrow |D_{5/2}, m_D\rangle$ in the same way as in Eq. (4.36) [Dub+13].

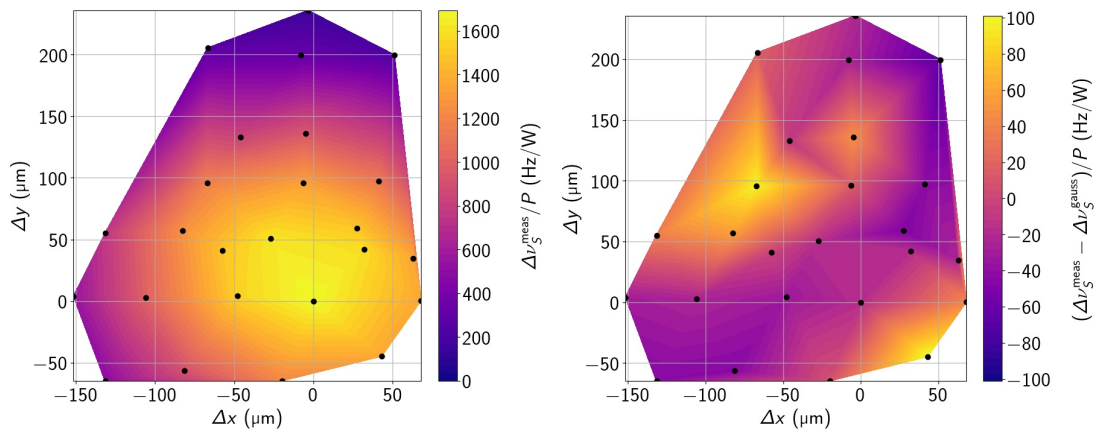


Figure 4.5.: *Beam profile of the QCL laser at the ion position. The scalar light shift sensitivity $\Delta\nu_S^{\text{meas}}/P$ is determined at various displacements of the QCL laser beam with respect to the $^{88}\text{Sr}^+$ ion. The measurement points in the figure on the left are indicated by black dots, which are interpolated to produce the contour plot. An elliptical gaussian profile $\Delta\nu_S^{\text{gauss}}/P$ is fit to the data to extract the beam waist and peak light shift sensitivity. The residuum between the data and gaussian profile is shown on the right. No pattern indicating significant non-gaussian contributions to the light intensity is visible.*

Results The beam radii of the CO_2 laser are $(w_a, w_b) = (286(11) \mu\text{m}, 225.4(6.8) \mu\text{m})$ and of the QCL they are $(w_a, w_b) = (227.0(7.8) \mu\text{m}, 208.5(6.9) \mu\text{m})$. This means that the maximum fractional light shift error introduced by ion motion with an RMS amplitude of $0.2 \mu\text{m}$ as a worst-case approximation is less than 0.2% , significantly smaller than the other uncertainty contributions. Neither profile has a significant tilt of its major and minor axis with respect to the coordinate system in which they are measured ($\theta = 0$). The differential polarizability of the $^{88}\text{Sr}^+$ clock transition extracted from these measurements is

4. Frequency shifts due to electric fields

$$\Delta\alpha_S^{\text{Sr}}(10.6\ \mu\text{m}) = -4.05(26) \times 10^{-40}\ \text{Jm}^2/\text{V}^2 \quad (4.51)$$

$$\Delta\alpha_S^{\text{Sr}}(8.5\ \mu\text{m}) = -4.03(25) \times 10^{-40}\ \text{Jm}^2/\text{V}^2. \quad (4.52)$$

In addition, I repeat the measurement of $\Delta\alpha_S^{\text{Sr}}(8.5\ \mu\text{m})$ with the beam entering from the opposite side of the vacuum chamber to estimate the asymmetry of the vacuum window absorption and find

$$\Delta\alpha_S^{\text{Sr}}(8.5\ \mu\text{m}) = -3.92(18) \times 10^{-40}\ \text{Jm}^2/\text{V}^2. \quad (4.53)$$

The beam profile of this measurement with $(w_a, w_b) = (198.5(5.3)\ \mu\text{m}, 199.8(4.1)\ \mu\text{m})$ is shown as an example in Fig. 4.5. No pattern indicating significant non-gaussian contributions to the light intensity are visible in the residuum between the model and the data.

All of the values are consistent with each other when taking into account the polarizability ratio $\Delta\alpha_S^{\text{Sr}}(10.6\ \mu\text{m})/\Delta\alpha_S^{\text{Sr}}(8.5\ \mu\text{m}) = 1.005\ 38(23)$, but significantly different from the value determined from the magic frequency measurement $\Delta\alpha_{\text{dc}}^{\text{Sr}} = -4.7938(71) \times 10^{-40}\ \text{Jm}^2/\text{V}^2$ [Dub+14] extrapolated to $10.6\ \mu\text{m}$ with the ratio $\Delta\alpha_S^{\text{Sr}}(10.6\ \mu\text{m})/\Delta\alpha_{\text{dc}}^{\text{Sr}} = 0.990\ 21(42)$. Similiar results are obtained when comparing to the result $\Delta\alpha_{\text{dc}}^{\text{Sr}} = -4.8314(20) \times 10^{-40}\ \text{Jm}^2/\text{V}^2$ from [Lin+25b], instead.

With the polarizability ratio measurement between the $^{88}\text{Sr}^+$ clock transition and the E2 and E3 transition of $^{171}\text{Yb}^+$ discussed in Chapter 5, values for $\Delta\alpha_S^{\text{E2}}$ and $\Delta\alpha_S^{\text{E3}}$ can be converted into $\Delta\alpha_S^{\text{Sr}}$ without adding significantly to the uncertainty. These are available at a wavelength of $7.17\ \mu\text{m}$ for the E2 and E3 transition [Bay+20] and in the NIR range for the E3 transition [Hun+16]. In the latter work these measurements are used to extrapolate $\Delta\alpha_{\text{dc}}^{\text{E3}}$, which is almost equal to $\Delta\alpha_S^{\text{E3}}(10.6\ \mu\text{m})$ due to the small dynamic correction of the E3 transition. The same holds true for the conversion between $\Delta\alpha_S^{\text{E3}}(7.17\ \mu\text{m})$ and $\Delta\alpha_S^{\text{E3}}(10.6\ \mu\text{m})$. For the E2 transition, the correction $\Delta\alpha_S^{\text{E2}}(10.6\ \mu\text{m})/\Delta\alpha_S^{\text{E2}}(7.17\ \mu\text{m}) = 0.895(4)$ is significant, though. A measurement of $\Delta\alpha_S^{\text{E2}}(10.6\ \mu\text{m})$ performed in this work is consistent with the value obtained in [Bay+20]. With the polarizability ratio measurement discussed in Chapter 5, the $^{171}\text{Yb}^+$ values for $\Delta\alpha_S$ can be converted to $\Delta\alpha_S^{\text{Sr}}$. They are listed in Table 4.1 together with the direct measurements discussed previously.

4.3. Polarizability measurements with infrared laser radiation

Transition	λ	$\Delta\alpha_S^{\text{Sr}}(10.6 \mu\text{m})(10^{-40} \text{Jm}^2/\text{V}^2)$
$^{88}\text{Sr}^+$	10.6 μm	-4.05(26)
$^{88}\text{Sr}^+$	8.568 μm	-4.05(25)
$^{88}\text{Sr}^+$ (backward)	8.568 μm	-3.96(18)
$^{171}\text{Yb}^+$ E2	10.6 μm	-4.16(19)
$^{171}\text{Yb}^+$ E2 (NPL) [Bay+20]	7.17 μm	-4.17(11)
$^{171}\text{Yb}^+$ E3 (NPL) [Bay+20]	7.17 μm	-4.072(87)
$^{171}\text{Yb}^+$ E3 (PTB) [Hun+16]	DC (from NIR)	-4.236(77)
Weighted average		-4.144(71)

Table 4.1.: *Lightshift-based polarizability values for the $^{88}\text{Sr}^+$ clock transition at 10.6 μm determined with radiation at different wavelengths and in different experimental setups. All values not supplied with a citation are measured in the scope of this thesis with the method discussed in this chapter. The values from NPL and PTB are measured in a similar way with different photo-detectors and beam-displacement setups. The polarizabilities of $^{171}\text{Yb}^+$ clock transitions are converted into their corresponding $^{88}\text{Sr}^+$ value with the polarizability ratio $\Delta\alpha_S^{\text{Sr}}/\Delta\alpha_S^{\text{Yb}}$ from Chapter 5. All values are consistent with a single weighted mean of $-4.144(71) \times 10^{-40} \text{Jm}^2/\text{V}^2$, where the uncertainty takes correlations between measurements into account.*

To determine $\Delta\alpha_S^{\text{Sr}}(10.6 \mu\text{m})$ using all light-shift based results, the weighted average of all data in Table 4.1 is computed, using inverse variance weighting. Care has to be taken to include correlations between the measurements using the same optical power meter and having common optical losses, which increases the uncertainty of the mean value. The weighted mean of the measurements of $\Delta\alpha_S^{\text{Sr}}(10.6 \mu\text{m})$ is equal to

$$\Delta\alpha_S^{\text{Sr}}(10.6 \mu\text{m}) = -4.144(71) \times 10^{-40} \text{Jm}^2/\text{V}^2, \quad (4.54)$$

with a reduced χ^2 of 0.6 when disregarding correlations. The non-zero correlation coefficients generally range from 0.3 to 0.6 and a single value of 0.8 for the correlation between the NPL polarizabilities. The values for $\Delta\alpha_S^{\text{Sr}}(10.6 \mu\text{m})$ are shown in Fig. 4.6 together with the magic RF-method based value and the theoretical prediction from the matrix elements and polarizability model. The mean lightshift-based polarizability value is inconsistent by more than 5σ with the magic-frequency based reference value used for BBR shift correction so far and shows that the discrepancy persists across clock transitions, laboratories, experiments and laser as well as detector sources. Also no undiscovered resonance appears to influence the measurement, since the polarizabilities at different wavelengths are consistent with each other according to the polarizability model.

4. Frequency shifts due to electric fields

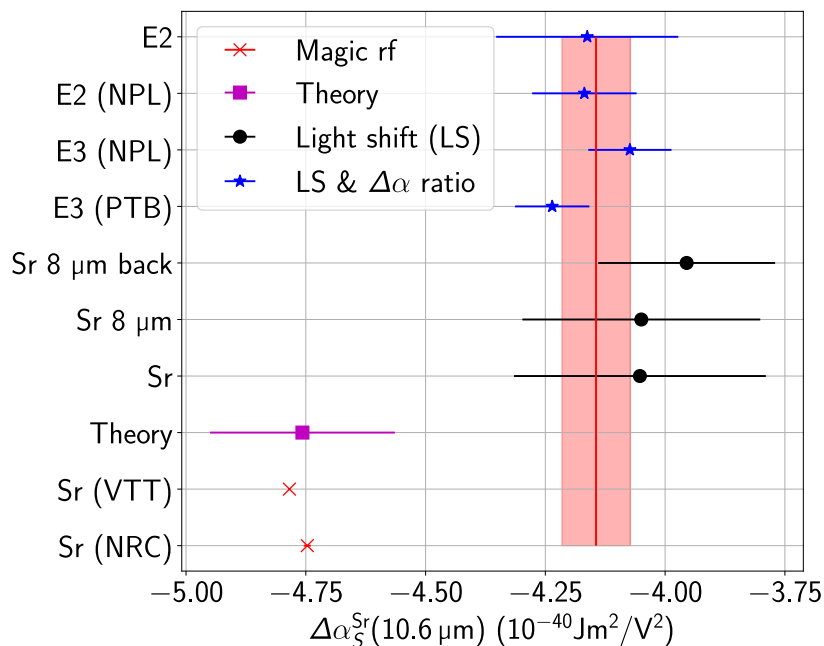


Figure 4.6.: Comparison of differential polarizability values for $^{88}\text{Sr}^+$. The differential polarizability $\Delta\alpha_{\text{S}}^{\text{Sr}}(10.6\mu\text{m})$ is shown based on different measurements with different methods from this chapter and Chapter 5. Values that are not determined at a perturbing wavelength of $10.6\mu\text{m}$ are adjusted based on the polarizability model. The magic RF value from NRC [Dub+14] is used for the BBR shift so far and determined for extremely long wavelengths $\lambda \approx 10^7\mu\text{m}$. An additional recent measurement by VTT is offset from the NRC value by $0.78(15)\%$. The theoretical prediction is the value determined from the polarizability model [Bar+22] and agrees well with the magic RF values. All measurements based on light shifts caused by NIR and MIR radiation on the other hand show a significant discrepancy of about 13% to the reference value. These include direct measurements on the $^{88}\text{Sr}^+$ clock transition as well as $^{171}\text{Yb}^+$ polarizabilities transferred to the $^{88}\text{Sr}^+$ value with the polarizability ratio measurement in Chapter 5. The E3 measurement at PTB is an extrapolation of NIR measurements to DC [Hun+16]. The NPL measurements were performed with a $7.17\mu\text{m}$ laser [Bay+20]. In this thesis, the polarizability is measured with $10.6\mu\text{m}$ and $8.5\mu\text{m}$ laser radiation. In addition, the beam path is also reversed to estimate absorption asymmetries in the vacuum windows, shown as the back measurement. All these measurements are consistent with a single mean value of $-4.144(71) \times 10^{-40} \text{ Jm}^2/\text{V}^2$ shown as a red line with the uncertainty shaded in red. This uncertainty considers correlations between the measurements.

Conclusion The measurement of the differential polarizability of the $^{88}\text{Sr}^+$ clock transition using MIR radiation directly reveals a disagreement between two currently well-established methods to determine $\Delta\alpha_{\text{S}}$. On the one hand, the

4.3. Polarizability measurements with infrared laser radiation

current reference value for $\Delta\alpha_{\text{dc}}$ determined from a magic-frequency measurement using perturbing fields in the RF frequency range agrees between two independent determinations up to a fractional offset of 0.78(15) % and also is supported by the prediction from the polarizability model. On the other hand, measurements of $\Delta\alpha_S$ with MIR laser radiation relying on calibrated optical power detectors and geometric optics cluster around a value that disagrees with this reference value by 13.7(1.6) %. These include measurements using laser sources at different wavelengths, separate setups of the optical path and also independent values of $\Delta\alpha_S$ for the $^{171}\text{Yb}^+$ clock transitions. The latter measurements are converted into polarizability values for $^{88}\text{Sr}^+$ with the polarizability ratio measurement in Chapter 5. This discrepancy corresponds to a change of the fractional BBR shift at 300 K of the $^{88}\text{Sr}^+$ clock transition frequency ν_0 by

$$\frac{\Delta\nu_{\text{BBR}}(\text{MIR}) - \Delta\nu_{\text{BBR}}(\text{RF})}{\nu_0} = -71.0(8.3) \times 10^{-18}, \quad (4.55)$$

if the optical intensity measurements produce the correct polarizability. While this does not significantly affect the absolute frequency value of the clock transition, it is an important contribution to optical frequency ratio measurements. It is currently unclear, which method of the two suffers from an unrecognized systematic error, so other measurements are required. For example, by changing the temperature of the trap environment, the change in BBR shift can be measured directly and compared with the differential polarizability values discussed here. Such a measurement has the potential to resolve the observed tension, unless it results in a separate value for $\Delta\alpha_S$. A measurement of this nature was performed between a room-temperature and cryogenic Ca^+ clock in [Hua+24], which shows agreement between the RF-based polarizability value and the observed frequency difference between the clocks.

Another consistency check could be performed by measuring the combined scalar and tensorial magic frequency of the $^{171}\text{Yb}^+$ E2 clock transition. It does not possess scalar polarizabilities $\Delta\alpha_S(10^7\mu\text{m})$ smaller than 0, so the Doppler and scalar Stark shifts have the same sign. On the other hand, the tensorial polarizability $\Delta\alpha_T(10^7\mu\text{m})$ modifies the total shift due to excess micromotion to

$$\begin{aligned} \frac{\langle\Delta\nu_D\rangle + \langle\Delta\nu_S\rangle}{\nu_0} &= -\left(\frac{r_0\Omega}{2c}\right)^2 \left(1 + \frac{\Delta\alpha_S}{h\nu_0} \left(\frac{mc\Omega}{e}\right)^2\right) \\ &\times \left(1 + \frac{3\cos^2(\theta) - 1}{2} \frac{3m_F^2 - F(F+1)}{F(2F-1)} \Delta\alpha_T/\Delta\alpha_S\right), \end{aligned} \quad (4.56)$$

$$(4.57)$$

which can feature a zero crossing, if $1 + \frac{3\cos^2(\theta)-1}{2} \frac{3m_F^2-F(F+1)}{F(2F-1)} \Delta\alpha_T/\Delta\alpha_S < 0$. Here, θ is the angle between the quantization axis and the electric field direction, F is

4. Frequency shifts due to electric fields

the total angular momentum of the excited state of the clock transition and m_F is its projection on the quantization axis. This is the case for the E2 transition, if $m_F = 2$ and $\theta = 0$, which results in the expected magic frequency $\tilde{\Omega}_0 = 2\pi \times 8.886(18)$ MHz when using the measured polarizability values at $10.6 \mu\text{m}$ from Chapter 5 extrapolated to DC. This is not possible for the E3 transition, because the magnitude of $\Delta\alpha_T(10^7 \mu\text{m})$ is too small compared to $\Delta\alpha_S(10^7 \mu\text{m})$. By determining the combined tensorial and scalar magic frequency $\tilde{\Omega}_0$, the scalar polarizability $\Delta\alpha_S(10^7 \mu\text{m})$ of the E2 transition can be measured with RF fields with higher accuracy than in [SPT05]. This method requires that the angle θ between the magnetic field direction and perturbing electric field due to micromotion is measured with sufficiently high accuracy and that all other tensorial shifts, e.g. due to electric field gradients, are known with lower uncertainty than the micromotion shift as well.

5. Polarizability ratio measurements between $^{88}\text{Sr}^+$ and $^{171}\text{Yb}^+$

$^{171}\text{Yb}^+$ clocks operating at room temperature are currently limited in their systematic uncertainty by the BBR shift $\Delta\nu_{\text{BBR}}$. Specifically, $\Delta\alpha_{\text{dc}}$, discussed in detail in Chapter 4, is known with a fractional uncertainty of 2-3 % from measurements relying on calibrated laser intensities [Hun+16; Bay+20]. This limits the overall fractional systematic uncertainty of $^{171}\text{Yb}^+$ E2 clocks to 28×10^{-18} and of E3 clocks to 1.5×10^{-18} at a temperature of 300 K.

For $^{88}\text{Sr}^+$, on the other hand, $\Delta\alpha_{\text{dc}}$ is known with a fractional uncertainty of 0.04 % [Lin+25b]. The reduced uncertainty is due to a different measurement principle based on the magic RF frequency that is independent of optical power calibrations. It is discussed in more detail in Section 4.1.

It follows that the uncertainty of $\Delta\alpha_{S,E3}$ and $\Delta\alpha_{S,E2}$ can be reduced by determining the scalar differential polarizability ratio $\rho_{S,E3/\text{Sr}}(\lambda) = \Delta\alpha_{S,E3}(\lambda)/\Delta\alpha_{S,\text{Sr}}(\lambda)$ (and the corresponding ratio for the E2 transition) at a wavelength λ by measuring the light shift ratio for these clock transitions when perturbed by a laser operating at the wavelength λ . This method was first proposed in [BAS19], and has been employed for a polarizability transfer measurement from $^{40}\text{Ca}^+$ to $^{27}\text{Al}^+$ at a perturbing wavelength of 1068 nm [Wei+24]. The fractional uncertainty for $\Delta\alpha_{\text{dc}}$ in [Wei+24] is 2.9 % due to the extrapolation of the $^{40}\text{Ca}^+$ polarizability from 1068 nm to long ($\lambda \gg 100 \mu\text{m}$) wavelengths.

In contrast, in this thesis, the measurement was performed with perturbing radiation in the MIR wavelength range and the extrapolation of $\Delta\alpha_{\text{dc}}^{\text{Sr}}$ to 10.6 μm is possible with small uncertainty from the polarizability model and magic wavelength measurement in Chapter 4. From such a measurement $\Delta\alpha_{S,E3}(\lambda)$ is given by

$$\Delta\alpha_{S,E3}(\lambda) = \rho_{S,E3/\text{Sr}}(\lambda)\Delta\alpha_{S,\text{Sr}}(\lambda) = \rho_{S,E3/\text{Sr}}(\lambda)(1 + \varepsilon(\lambda))\Delta\alpha_{\text{dc},\text{Sr}}, \quad (5.1)$$

where $\varepsilon(\lambda)$ is the correction factor to extrapolate the $^{88}\text{Sr}^+$ polarizability from the DC value to the wavelength λ . By measuring the magic wavelength of the $^{88}\text{Sr}^+$ clock transition to be 1538.75(10) nm as presented in Section 4.2, $\varepsilon(10.6 \mu\text{m})$ and $\varepsilon(8.568 \mu\text{m})$ are determined to be $-0.00979(42)$ and $-0.01508(64)$, respectively.

This allows for a reduction of the fractional $^{171}\text{Yb}^+$ E3 BBR shift uncertainty below 10^{-19} , if sufficiently precise measurements of the BBR temperature T are available [Dol+15; Nor+20] and the ratio is measured to that level.

5.1. Common experimental setup for polarizability ratio measurements

In the following measurements, a single ion, either $^{171}\text{Yb}^+$ or $^{88}\text{Sr}^+$, is trapped and the respective clock transitions are interrogated to determine the frequency offset of the atomic transitions from their corresponding clock lasers stabilized to an independent optical clock Yb1 [San+19]. The setup of the clock laser stabilization is shown in Fig. 3.13. The center frequency is shifted by a CO_2 laser with a wavelength of $10.60(3)\ \mu\text{m}$, a power of 10 W and an approximate beam diameter of $400\ \mu\text{m}$ at the position of the ion. The linewidth of the CO_2 laser is assumed to be significantly smaller than $0.03\ \mu\text{m}$. The laser power can also be attenuated with neutral density filters, if necessary. The CO_2 laser is aligned at an angle of 15° with respect to the trap axis as shown in Fig. 3.8.

In addition, some of the measurements are also repeated with a QCL operating at a wavelength of $8.568\ \mu\text{m}$ and entering the vacuum chamber along the same path. The center frequency of the laser is determined from the supplied datasheet shown in Fig. 5.1 with a sum of 5 gaussian peaks that follows the spectral distribution. The antireflection coating of the ZnSe window through which the MIR beams are transmitted spans wavelengths from $8.0\ \mu\text{m}$ to $12.0\ \mu\text{m}$, so no significant effect on the spectral distribution is expected. Due to the change of the clock transition polarizabilities with the wavelength, the non-symmetric distribution of the spectral intensity causes a modification of the Stark shift when measured with the QCL compared to a monochromatic laser with a center wavelength of $8.568\ \mu\text{m}$. The linear variations of the polarizability of the clock transitions are summarized in Table 5.1 and corresponding correction factors c_λ of the measured polarizabilities $\Delta\alpha^{\text{meas}}$

$$\Delta\alpha(\lambda) = \Delta\alpha^{\text{meas}} / (1 + c_\lambda) \quad (5.2)$$

are shown in Table 5.2. The results in this chapter already take this correction into account.

The laser power is not actively stabilized and correspondingly changes over time in addition to its short-term noise with a fractional RMS magnitude of approximately 1 %. A maximum fractional power drift of 1.5 %/h is observed with the CO_2 laser and less than 0.05 %/h with the QCL.

To directly determine the quadratic Stark shift induced by the CO_2 laser, a

5.1. Common experimental setup for polarizability ratio measurements

measurement of the center frequency of each interrogated transition without the additional perturbation by the MIR radiation is interleaved with cycles when the perturbed frequency is measured. During the non-perturbed measurements, the CO₂ laser is redirected into a beam dump with an electrically controlled flip mirror before entering the ion trap to keep the power stable and completely extinguish the light shift. The QCL is blocked by a mechanical shutter instead, due to its reduced intensity and corresponding heat load on the absorbing element. This interleaved measurement makes the determined light shift insensitive to variations of the reference frequency, such as Stark shifts due to the clock laser intensity on the E3 transition.

M1 polarizability The lasers produce an electromagnetic field consisting of the electric field $E(t)$ and the magnetic field $B(t)$. The mean squared magnetic field is connected to the mean squared electric field via the speed of light c

$$\langle B^2 \rangle = \frac{\langle E^2 \rangle}{c^2}. \quad (5.3)$$

$B(t)$ couples to M1 transitions and causes a quadratic Zeeman shift $\Delta\nu_{Z2}$ in the same manner as $E(t)$ causes a quadratic Stark shift [LSR13; Gan+18]. If one defines the magnetic differential polarizability $\Delta\alpha^{\text{M1}}(\omega)$ as

$$\Delta\alpha^{\text{M1}}(\omega) = \frac{\Delta\beta^{\text{M1}}(\omega)}{c^2}, \quad (5.4)$$

where $\Delta\beta^{\text{M1}}(\omega)$ is the sensitivity coefficient for the quadratic Zeeman shift according to

$$\Delta\nu_{Z2} = -\frac{1}{2h}\Delta\beta^{\text{M1}}(\omega)\langle B^2 \rangle = -\frac{1}{2h}\Delta\alpha^{\text{M1}}(\omega)\langle E^2 \rangle, \quad (5.5)$$

then the standard differential polarizability $\Delta\alpha(\omega)$ and $\Delta\alpha^{\text{M1}}(\omega)$ can be compared on equal footing to determine the ratio of the quadratic Zeeman and quadratic Stark shift due to electromagnetic radiation with an angular frequency ω

$$\varepsilon_{\text{E1}}^{\text{M1}}(\omega) = \frac{\Delta\nu_{Z2}(\omega)}{\Delta\nu_{\text{Stark}}(\omega)} = \frac{\Delta\alpha^{\text{M1}}(\omega)}{\Delta\alpha(\omega)}. \quad (5.6)$$

$\Delta\alpha^{\text{M1}}(\omega)$ is determined from a single-pole model [Gan+18]

$$\Delta\alpha^{\text{M1}}(\omega) = \frac{1}{2}\Delta\alpha^{\text{M1}}(0)\left(\frac{1}{1-\omega/\omega_0} + \frac{1}{1+\omega/\omega_0}\right), \quad (5.7)$$

5. Polarizability ratio measurements between $^{88}\text{Sr}^+$ and $^{171}\text{Yb}^+$

where ω_0 is the resonance frequency of the lowest-frequency M1 transition from either the ground or excited state that has a frequency of at least 1 THz, and $\Delta\alpha^{\text{M1}}(0)$ is the DC quadratic Zeeman polarizability connected to that transition. Transitions at a lower frequency, such as hyperfine transitions with GHz frequencies, do not play a significant role, because their contributions are heavily suppressed at the frequencies of the MIR laser radiation. $\Delta\alpha^{\text{M1}}(0)$ is calculated from the transition element of the M1 transition, which is found in [Tan+23] for many optical clock transitions and ranges from $1.553 \mu_B$ and $1.856 \mu_B$ in this case. The scalar values of $\varepsilon_{\text{E1}}^{\text{M1}}$ for the $^{88}\text{Sr}^+$, $^{171}\text{Yb}^+$ E2 and $^{171}\text{Yb}^+$ E3 clock transitions when perturbed at the center wavelengths of the CO_2 laser and the QCL are listed in Table 5.3. All have a magnitude smaller than 0.1×10^{-3} and are negligible compared to the total measurement uncertainty. For this reason, the correction is disregarded when analyzing the data. The tensorial values are expected to be of similar magnitude, since all M1 resonances have the excited state as one part of the corresponding transition pair. So they also produce a negligible offset for the results in this chapter.

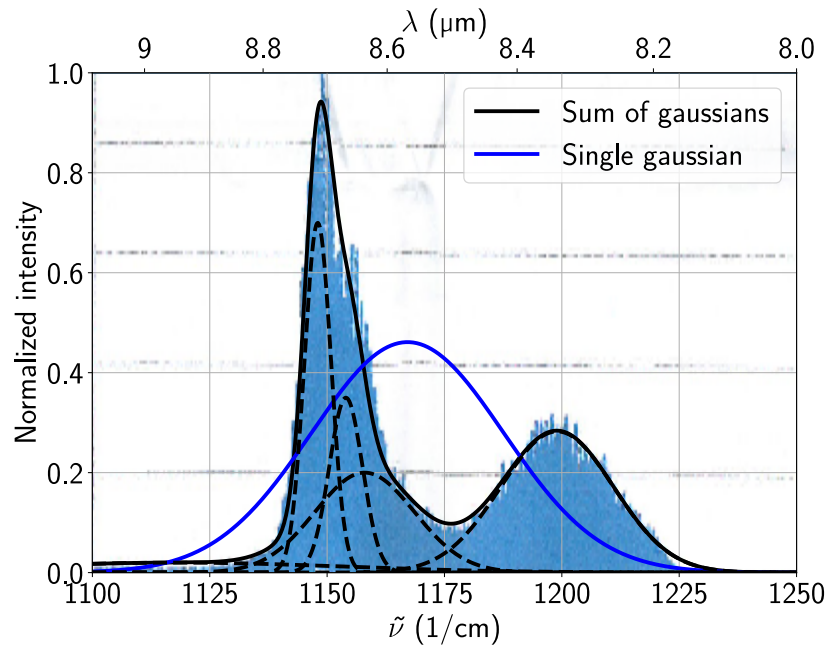


Figure 5.1.: *Spectrum of the QCL laser. The normalized spectral intensity of the QCL laser for different wavenumbers $\tilde{\nu}$ is shown as supplied by the manufacturer of the laser. It is approximated visually by a sum of 5 gaussian peaks shown with dashed lines to determine the center wavelength of the laser and to calculate the effect of the spectral distribution on the measured Stark shifts. A single gaussian with the same center wavelength $\lambda_0 = 8.568 \mu\text{m}$ and standard deviation $\sigma = 0.21 \mu\text{m}$ as the sum of gaussians is shown as well for reference.*

5.1. Common experimental setup for polarizability ratio measurements

Clock transition	λ	$\partial\Delta\tilde{\alpha}_S/\partial\lambda(10^{-3}/\mu\text{m})$	$\partial\Delta\tilde{\alpha}_T/\partial\lambda(10^{-3}/\mu\text{m})$
$^{88}\text{Sr}^+$	10.6 μm	1.889(57)	-1.479(14)
$^{88}\text{Sr}^+$	8.568 μm	3.65(11)	-2.817(27)
$^{171}\text{Yb}^+$ E2	10.6 μm	-19.1(1.7)	-9.53(27)
$^{171}\text{Yb}^+$ E2	8.568 μm	-36.4(3.1)	-18.64(52)
$^{171}\text{Yb}^+$ E3	10.6 μm	0.2804(50)	-0.513(27)
$^{171}\text{Yb}^+$ E3	8.568 μm	0.5332(96)	-0.973(52)

Table 5.1.: Variation of the clock transition polarizabilities. The table lists the fractional linear variation of the differential polarizabilities $\partial\Delta\tilde{\alpha}/\partial\lambda = (\partial\Delta\alpha/\partial\lambda)/\Delta\alpha$ for all three clock transitions investigated in this thesis at the two wavelengths for which $\Delta\alpha$ is measured. They are calculated from the polarizability models in Section 4.1.

Clock transition	Laser (λ)	$c_\lambda(\Delta\alpha_S)(10^{-3})$	$c_\lambda(\Delta\alpha_T)(10^{-3})$
$^{88}\text{Sr}^+$	CO ₂ (10.6 μm)	0.000(57)	0.000(44)
$^{88}\text{Sr}^+$	QCL (8.568 μm)	-0.0642(28)	0.0494(75)
$^{171}\text{Yb}^+$ E2	CO ₂ (10.6 μm)	0.00(57)	0.00(29)
$^{171}\text{Yb}^+$ E2	QCL (8.568 μm)	0.661(54)	0.3384(76)
$^{171}\text{Yb}^+$ E3	CO ₂ (10.6 μm)	0.0000(84)	0.000(15)
$^{171}\text{Yb}^+$ E3	QCL (8.568 μm)	-0.009(13)	0.017(59)

Table 5.2.: Fractional correction of the polarizability due to laser spectral intensity distributions. The table lists the correction factors of the measured polarizability values to determine the clock transition polarizability at the specified wavelength as defined in Eq. (5.2). They are determined from the models in Section 4.1 and the spectral distribution of the laser radiation. The CO₂ laser is assumed to be monochromatic with the specified wavelength uncertainty of 0.03 μm . The QCL distribution is depicted in Fig. 5.1.

Clock transition	Laser (λ)	$\varepsilon_{E1}^{M1}(\lambda)(10^{-3})$
$^{88}\text{Sr}^+$	CO ₂ (10.6 μm)	-0.0094
$^{88}\text{Sr}^+$	QCL (8.568 μm)	-0.0060
$^{171}\text{Yb}^+$ E2	CO ₂ (10.6 μm)	0.053
$^{171}\text{Yb}^+$ E2	QCL (8.568 μm)	0.096
$^{171}\text{Yb}^+$ E3	CO ₂ (10.6 μm)	0.012
$^{171}\text{Yb}^+$ E3	QCL (8.568 μm)	0.012

Table 5.3.: M1/E1 polarizability ratio values. The table lists the ratio between the M1 and E1 polarizability for the different clock transitions and MIR lasers employed in this thesis. All of them have a magnitude below 1×10^{-4} , so the light shift is completely determined by the quadratic Stark shift within the uncertainty of the measurement.

5.2. Tensorial polarizability of $^{88}\text{Sr}^+$

As discussed in Chapter 4, the quadratic Stark shift $\Delta\nu_L$ of a laser at wavelength λ with time-averaged intensity $\langle I \rangle$ and negligible linewidth on an electronic transition with differential polarizability $\Delta\alpha(\lambda)$ is

$$\Delta\nu_L(\lambda) = -\Delta\alpha(\lambda) \frac{\langle I \rangle}{2h\varepsilon_0 c}, \quad (5.8)$$

where $\Delta\alpha$ consists of the scalar ($\Delta\alpha_S$) and tensorial ($\Delta\alpha_T$) polarizability

$$\Delta\alpha(\lambda) = \Delta\alpha_S(\lambda) + \frac{3 \cos^2(\theta_p) - 1}{2} \frac{3m_J^2 - J(J+1)}{J(2J-1)} \Delta\alpha_T(\lambda), \quad (5.9)$$

with the excited state quantum number J , excited state magnetic quantum number m_J and the angle θ_p between the magnetic field \vec{B} and laser polarization direction $\vec{\epsilon}$. Any vector light shifts due to residual circular laser polarisation are proportional to m_J , the same as linear Zeeman shifts. This means that the $^{171}\text{Yb}^+$ clock transitions $S_{1/2}(F=0, m_F=0) \rightarrow D_{3/2}(F=2, m_F=0)$ (E2) and $S_{1/2}(F=0, m_F=0) \rightarrow F_{7/2}(F=3, m_F=0)$ (E3) do not show a vector light shift. For the $^{88}\text{Sr}^+$ transition $S_{1/2} \rightarrow D_{5/2}$ on the other hand, all individual transitions $|S, m_S\rangle \rightarrow |D, m_D\rangle$ are sensitive to circular polarisation. But the average transition frequency

$$\Delta\nu_{m_S}^{m_D} = \frac{\Delta\nu_{+m_S}^{+m_D} + \Delta\nu_{-m_S}^{-m_D}}{2} \quad (5.10)$$

is linearly insensitive to Zeeman shifts, where $\Delta\nu_{\pm m_S}^{\pm m_D}$ is the frequency of the $|S, \pm m_S\rangle \rightarrow |D, \pm m_D\rangle$ transition. Consequently, this average also shows no vector light shift, so it can be disregarded.

Tensor shifts proportional to $\Delta\alpha_T$ remain for all transitions though and need to be corrected for to extract $\Delta\alpha_S$ from any light shift measurement. This is achieved with two techniques, magnetic field direction averaging [Ita00] and magnetic quantum number averaging [Dub+13]. Using the first technique, it is required to interrogate the clock transition and measure the light shift in three mutually orthogonal magnetic field directions. The average frequency is free of tensorial shifts with an uncertainty given by the orthogonality of the field directions. If the non-orthogonality is small ($|\varepsilon_{jk}| \ll 1$), the magnetic field vectors defining the coordinate system are

$$\vec{e}_{B,x} = \begin{pmatrix} 1 \\ \varepsilon_{xy} \\ \varepsilon_{xz} \end{pmatrix}, \vec{e}_{B,y} = \begin{pmatrix} \varepsilon_{yx} \\ 1 \\ \varepsilon_{yz} \end{pmatrix}, \vec{e}_{B,z} = \begin{pmatrix} \varepsilon_{zx} \\ \varepsilon_{zy} \\ 1 \end{pmatrix}, \quad (5.11)$$

which are normalized up to quadratic terms $\varepsilon_{jk}\varepsilon_{jk}$. Then the residual tensor shift after averaging the frequency over all three magnetic field directions is equal to

$$\langle \Delta\nu_T \rangle = \frac{\Delta\nu_{T,x} + \Delta\nu_{T,y} + \Delta\nu_{T,z}}{3} \quad (5.12)$$

$$= \frac{1}{6} \left(\left((\varepsilon_{yx}^2 + \varepsilon_{zx}^2) \cos^2 \varphi_p^2 + (\varepsilon_{xy}^2 + \varepsilon_{zy}^2) \sin^2 \varphi_p \right) \sin^2 \vartheta_p \right) \quad (5.13)$$

$$+ \left(\varepsilon_{xz}^2 + \varepsilon_{yz}^2 \right) \cos^2 \vartheta_p \left) \frac{3m_J^2 - J(J+1)}{J(2J-1)} \Delta\alpha_T + O(\varepsilon^4), \quad (5.14)$$

where ϑ_k and φ_p are the spherical angles of the polarization vector in the basis of the orthogonal ($\varepsilon_{jk}=0$) magnetic field direction. If all ε_{jk} have the same magnitude ε , this reduces to

$$\langle \Delta\nu_T \rangle = \frac{\varepsilon^2}{3} \frac{3m_J^2 - J(J+1)}{J(2J-1)} \Delta\alpha_T + O(\varepsilon^4). \quad (5.15)$$

The magnetic field directions are calibrated by measurements of the Zeeman shift at various currents applied to the Helmholtz coil pairs discussed in Section 3.5, assuming a linear relationship between the coil coordinate system and the orthogonal basis aligned with the trap geometry. Approximately, the x-axis is the imaging direction, the y-axis is the vertical direction and the z-axis is the trap axis direction. Then, the relationship between the magnetic field vector \vec{B} and the input voltage \vec{U} to the current source controlled by the analog output of the experimental control hardware is given by

$$\vec{B} = \mathbf{A}\vec{U} + \vec{B}_0 = \begin{pmatrix} a_{xx} & 0 & 0 \\ a_{yx} & a_{yy} & 0 \\ a_{zx} & a_{zy} & a_{zz} \end{pmatrix} \vec{U} + \begin{pmatrix} b_{x,0} \\ b_{y,0} \\ b_{z,0} \end{pmatrix}, \quad (5.16)$$

which can be numerically inverted to find the vector \vec{U} necessary to produce any magnetic field \vec{B} . The fractional error of the calibration can be estimated from the offset of the measured Zeeman shift compared to the calibration target value and is smaller than 10^{-4} among the x , y and z directions. This means that the fractional tensor shift after averaging is expected to be smaller than 10^{-8} , but without frequent recalibration this error increases over time due to changes in the magnetic background field. Consequently, I assume a maximum fractional offset of less than 10^{-5} on the tensor shift due to magnetic field calibration uncertainties for the following measurements.

With magnetic quantum number averaging [Dub+13], the tensor shift can be averaged out at any magnetic field direction by interrogating the transitions

5. Polarizability ratio measurements between $^{88}\text{Sr}^+$ and $^{171}\text{Yb}^+$

$|S, \pm 1/2\rangle \rightarrow |D, \pm 3/2\rangle$ and $|S, \pm 1/2\rangle \rightarrow |D, \pm 5/2\rangle$ of $^{88}\text{Sr}^+$ in the same way as in Section 4.2, allowing calculating the scalar light shift $\Delta\nu_S$ and tensorial light shift $\Delta\nu_T$

$$\Delta\nu_S = -\Delta\alpha_S \frac{\langle I \rangle}{2h\varepsilon_0 c} = \frac{1}{6}\nu^{5/2} + \frac{5}{6}\nu^{3/2} \quad (5.17)$$

$$\Delta\nu_T = -\Delta\alpha_T \frac{\langle I \rangle}{2h\varepsilon_0 c} \frac{3\cos^2\theta_p - 1}{2} = \frac{5}{6}(\nu^{5/2} - \nu^{3/2}). \quad (5.18)$$

By measuring the average frequency of the $|S, m_S = \pm 1/2\rangle \rightarrow |D, m_D = \pm 3/2\rangle$ and $|S, m_S = \pm 1/2\rangle \rightarrow |D, m_D = \pm 5/2\rangle$ transitions along 3 mutually orthogonal magnetic field directions and comparing it to the scalar shift derived from the weighted average Eq. (5.17), the agreement between these methods can be compared. They agree with each other up to a fractional uncertainty of 0.4×10^{-3} , showing the consistency between the two approaches of extracting the scalar light shift.

By measuring the tensor/scalar $^{88}\text{Sr}^+$ light shift ratio $\Delta\nu_T/\Delta\nu_S$ at 4 different magnetic field angles, the polarizability ratio $\Delta\alpha_T^{\text{Sr}}/\Delta\alpha_S^{\text{Sr}}$ can be determined. The magnetic field directions are chosen such that two of them cause a tensor shift with maximum magnitude while still being orthogonal vectors. This effectively results in the approximate geometric factors $\Lambda(\theta_p) = (3\cos^2\theta_p - 1)/2$

$$\Lambda(\theta_1) = 1, \Lambda(\theta_2) = -0.5, \quad (5.19)$$

but the precise values of $\Lambda(\theta_p)$ are not known. For this reason, also measurements along two magic angles where the tensorial shift is approximately zero

$$\Lambda(\theta_3) = 0, \Lambda(\theta_4) = 0 \quad (5.20)$$

are performed. With this set it is possible to identify $\Lambda(\theta_p)$ from a fit of the expected analytical relationship between θ_p and the tensor shift magnitude with a well-defined uncertainty.

For this measurement, the magnetic field is calibrated using the $^{171}\text{Yb}^+$ E2 transition at an offset frequency for the $\Delta m = +1$ transition of 100 kHz with a total settle time of 35 ms after turning off the large magnetic field for $^{171}\text{Yb}^+$ cooling. Even though the large magnetic field is not necessary for cooling of $^{88}\text{Sr}^+$, it is still switched in the same manner as for $^{171}\text{Yb}^+$ to keep the magnetic field calibration consistent. The light shift is provided by the full power of the 10.6 μm CO_2 laser. Due to the laser intensity noise with an approximate fractional RMS magnitude of 1% on timescales shorter than 10 s and the scalar shift magnitude of approximately 9400 Hz, the $^{88}\text{Sr}^+$ transitions $|S, \pm 1/2\rangle \rightarrow |D, \pm 3/2\rangle$ and $|S, \pm 1/2\rangle \rightarrow |D, \pm 5/2\rangle$ are interrogated with 2.5 ms and 1.0 ms long pulses, respectively. The magnetic

field magnitude varies by less than 0.3×10^{-3} among any direction between the interrogation times, inferred from the decay measurement in Section 3.5. This results in a maximum fractional error of the inferred tensor shift of 10^{-6} , negligible compared to the total measurement uncertainty.

The measurement data is consistent with the following values for the geometric factors

$$\Lambda(\theta_1) = 0.9862(31), \Lambda(\theta_2) = -0.4953(42) \quad (5.21)$$

$$\Lambda(\theta_3) = 0.2044(24), \Lambda(\theta_4) = 0.0585(33), \quad (5.22)$$

which are reasonably close to the target Eq. (5.19) and Eq. (5.20). This measurement results in the polarizability ratio

$$\Delta\alpha_T^{\text{Sr}}(10.6 \mu\text{m})/\Delta\alpha_S^{\text{Sr}}(10.6 \mu\text{m}) = 1.6702(41), \quad (5.23)$$

with a fractional uncertainty of 2.5×10^{-3} . This value is consistent with a theoretical calculation of the same quantity using the polarizability model discussed in Section 4.1, which results in $\Delta\alpha_T^{\text{Sr}}(10.6 \mu\text{m})/\Delta\alpha_S^{\text{Sr}}(10.6 \mu\text{m}) = 1.61(6)$. This quantity allows determinations of the geometric factor $\lambda(\theta_p)$ from the measured tensor/scalar light shift ratio of the $^{88}\text{Sr}^+$ clock transition at an arbitrary magnetic field direction.

5.3. Polarizability ratio measurements for $^{171}\text{Yb}^+$

To determine all polarizability ratios involving the E2 and E3 transition in $^{171}\text{Yb}^+$, magnetic field directions need to be chosen at which both transitions have sufficient coupling strengths to their respective clock lasers (see Section 2.4) and a sufficiently large difference in their tensor shift magnitude. The latter point is necessary to determine the tensor polarizabilities of the $^{171}\text{Yb}^+$ clock transitions. As an additional feature, the tensor shift magnitude is less sensitive to magnetic field direction changes close to the maximum and minimum of $\Lambda(\theta)$. With the tensor/scalar polarizability ratio of the $^{88}\text{Sr}^+$ clock transition from Section 5.2, the geometric factors $\Lambda(\theta_p)$ along two angles $\theta_{1,2}$ which fulfill these criteria are determined to be

$$\Lambda(\theta_1) = 0.7131(18), \Lambda(\theta_2) = -0.4862(14). \quad (5.24)$$

Since the intensity fluctuations of the CO_2 laser are too large at maximum power for coherent interrogation of the E3 transition (because the minimum pulse length is approximately 60 ms even at maximum coupling strength), for this measurement

5. Polarizability ratio measurements between $^{88}\text{Sr}^+$ and $^{171}\text{Yb}^+$

the laser power is reduced to approximately 7% of the maximum with a reflective filter. This results in an approximate scalar shift of -1100 Hz on the E2 transition and -150 Hz on the E3 transition. Tensor shift changes due to temporal variations of the magnetic field contribute with a fractional magnitude of 1×10^{-5} at these settings.

The total light shift $\Delta\nu_{1/2}^{\text{E2/E3}}$ for the E2/E3 transition is measured in both magnetic field directions $\Lambda_{1/2} = \Lambda(\theta_{1/2})$, which allows for the determination of the corresponding scalar $\Delta\nu_S$ and normalized tensorial $\Delta\bar{\nu}_T = -\Delta\alpha_T\langle I \rangle / (2h\varepsilon_0c)$ light shifts

$$\Delta\nu_S^{\text{E2}} = \frac{\Lambda_2\Delta\nu_1^{\text{E2}} - \Lambda_1\Delta\nu_2^{\text{E2}}}{\Lambda_2 - \Lambda_1} \quad (5.25)$$

$$\Delta\bar{\nu}_T^{\text{E2}} = \frac{\Delta\nu_1^{\text{E2}} - \Delta\nu_2^{\text{E2}}}{\Lambda_2 - \Lambda_1} \quad (5.26)$$

$$\Delta\nu_S^{\text{E3}} = \frac{\Lambda_2\Delta\nu_1^{\text{E3}} - \Lambda_1\Delta\nu_2^{\text{E3}}}{\Lambda_2 - \Lambda_1} \quad (5.27)$$

$$\Delta\bar{\nu}_T^{\text{E3}} = \frac{5}{4} \frac{28}{25} \frac{\Delta\nu_1^{\text{E3}} - \Delta\nu_2^{\text{E3}}}{\Lambda_2 - \Lambda_1}, \quad (5.28)$$

where the scalar and tensor polarizability of the $^{171}\text{Yb}^+$ transitions are defined as

$$\Delta\nu = -\frac{\langle I \rangle}{2h\varepsilon_0c} \left(\Delta\alpha_S + \Lambda(\theta_p) \frac{3m_F^2 - F(F+1)}{F(2F-1)} K_F \Delta\alpha_T \right), \quad (5.29)$$

with the hyperfine factors $K_2 = 1, K_3 = 25/28$ calculated from the corresponding Wigner $6j$ -symbol in Eq. (4.14). The polarizability ratios are calculated as the time-resolved ratio between these light shifts. The light shifts caused by the CO_2 laser result in the polarizability ratios are listed in Table 5.4 along with the determinations of the same quantities by NPL [Bay+20] and PTB [SPT05; Hun+16; Hun14] at different perturbing wavelengths. The extrapolation of the E3 polarizability in [Hun14; Hun+16] to the DC value is employed instead of the measured values in the NIR to determine the polarizability ratios at approximately $10^7 \mu\text{m}$. While the differential polarizability is also measured for the E2 transition in [Hun14], an extrapolation in this manner is not possible due to the strong resonances at a wavelength longer than 1545 nm.

The uncertainty of the polarizability ratios determined here is smaller by a factor of 5 to 14 compared to [Bay+20] and 20 to 120 compared to [SPT05; Hun14; Hun+16]. To compare these ratios with existing data, the polarizability values from [SPT05; Hun14; Hun+16; Bay+20] for the E2 and E3 transition are adjusted by the theoretically calculated polarizability ratios summarized in Table 5.5. All

values are consistent with each other within their combined uncertainty. The fractional offsets between the data from [Bay+20; SPT05; Hun+16; Hun14] and the data from this thesis are shown in Fig. 5.2.

Source λ	[SPT05; Hun14; Hun+16] $10^7 \mu\text{m}$	CO_2 $10.6 \mu\text{m}$
$\Delta\alpha_T^{\text{E2}}/\Delta\alpha_S^{\text{E2}}$	-1.97(51)	-1.6288(41)
$\Delta\alpha_S^{\text{E3}}/\Delta\alpha_S^{\text{E2}}$	0.129(26)	0.125 35(32)
$\Delta\alpha_T^{\text{E3}}/\Delta\alpha_S^{\text{E2}}$	-0.0354(74)	-0.033 70(11)
$\Delta\alpha_T^{\text{E2}}/\Delta\alpha_S^{\text{E3}}$	-15.3(2.5)	-12.995(33)
$\Delta\alpha_T^{\text{E3}}/\Delta\alpha_S^{\text{E3}}$	-0.275(16)	-0.268 84(81)
$\Delta\alpha_T^{\text{E2}}/\Delta\alpha_T^{\text{E3}}$	55.7(9.5)	48.38(15)

Source λ	QCL $8.568 \mu\text{m}$	[Bay+20] $7.17 \mu\text{m}$
$\Delta\alpha_T^{\text{E2}}/\Delta\alpha_S^{\text{E2}}$	-1.5835(71)	-1.524(44)
$\Delta\alpha_S^{\text{E3}}/\Delta\alpha_S^{\text{E2}}$	0.118 98(54)	0.1095(17)
$\Delta\alpha_T^{\text{E3}}/\Delta\alpha_S^{\text{E2}}$	-0.031 84(15)	-0.029 70(85)
$\Delta\alpha_T^{\text{E2}}/\Delta\alpha_S^{\text{E3}}$	-13.309(60)	-13.92(46)
$\Delta\alpha_T^{\text{E3}}/\Delta\alpha_S^{\text{E3}}$	-0.2676(15)	-0.2712(66)
$\Delta\alpha_T^{\text{E2}}/\Delta\alpha_T^{\text{E3}}$	49.85(23)	51.3(2.1)

Table 5.4.: Polarizability ratios of the $^{171}\text{Yb}^+$ clock transitions. The table lists the measured (bold) and inferred scalar and tensorial polarizability ratios for the $^{171}\text{Yb}^+$ E2 and E3 clock transitions at different wavelengths λ . The values at $\lambda \approx 10^7 \mu\text{m}$ are a combination of the E2 and E3 polarizabilities determined in [SPT05; Hun+16; Hun14], the values at $\lambda = 7.17 \mu\text{m}$ are taken from [Bay+20]. The other two columns are measured in this work with a CO_2 laser and a QCL. These quantities can be used to constrain the polarizability model for the $^{171}\text{Yb}^+$ clock transitions in the MIR range relevant for room-temperature BBR. The fractional differences between these values are shown in Fig. 5.2.

λ	$10^7 \mu\text{m}$	$8.568 \mu\text{m}$	$7.17 \mu\text{m}$
$\Delta\alpha_S^{\text{E2}}$	1.106(10)	0.9475(42)	0.8861(86)
$\Delta\alpha_T^{\text{E2}}$	1.0503(10)	0.973 13(52)	0.9398(11)
$\Delta\alpha_S^{\text{E3}}$	0.998 52(13)	1.000 79(11)	1.001 77(10)
$\Delta\alpha_T^{\text{E3}}$	1.0027(25)	0.9986(27)	0.9968(27)

Table 5.5.: Polarizability scale factors for $^{171}\text{Yb}^+$ in the MIR range. The table lists the polarizability ratios $\Delta\alpha(10.6 \mu\text{m})/\Delta\alpha(\lambda)$ for the E2 and E3 clock transitions of $^{171}\text{Yb}^+$. They are determined with the polarizability models in Section 4.1.

5. Polarizability ratio measurements between $^{88}\text{Sr}^+$ and $^{171}\text{Yb}^+$

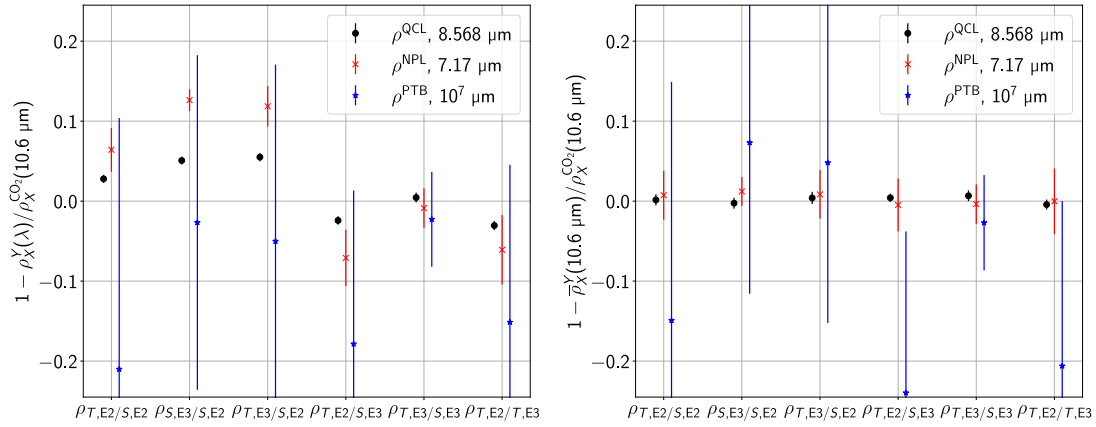


Figure 5.2.: Fractional offsets of the $^{171}\text{Yb}^+$ polarizability ratios. The scalar (S) and tensorial (T) polarizability ratios $\rho_X^Y(\lambda)$ of the $^{171}\text{Yb}^+$ $E2$ and $E3$ clock transitions are measured with the CO_2 ($Y = \text{CO}_2$) laser at a wavelength $\lambda = 10.6 \mu\text{m}$ and compared with the values from [Bay+20] ($Y = \text{NPL}, \lambda = 7.17 \mu\text{m}$), [SPT05; Hun+16; Hun14] ($Y = \text{PTB}, \lambda \approx 10^7 \mu\text{m}$) and those determined with the QCL laser ($Y = \text{QCL}, \lambda = 8.568 \mu\text{m}$). As shown in the left-hand figure, the polarizability ratios involving the $E2$ transition differ from each other, primarily due to the dipole transition from the $D_{3/2}$ state at $2.4 \mu\text{m}$ [Bié+98; LWB06]. The only ratio not involving the $E2$ transition $\rho_{T,E3/S,E3}$ produces the same value within the uncertainty of all three measurements. On the right-hand side, the normalized polarizability ratio $\bar{\rho}(10.6 \mu\text{m}) = \varepsilon(\lambda)\rho(\lambda)$ is calculated for all data. The scale factors $\varepsilon(\lambda)$ are determined from the polarizability models discussed in Section 4.1 for each transition and are listed in Table 5.5. All of these differences are consistent with zero within their uncertainty. This shows that the data collected at different wavelengths follow the curvature of the $E2$ and $E3$ polarizability and can potentially be employed to improve the polarizability models.

The same values are also determined using the QCL laser operating at a wavelength of $8.568 \mu\text{m}$. The $^{88}\text{Sr}^+$ tensor/scalar polarizability ratio $\rho_{T,\text{Sr}/S,\text{Sr}}(8.568 \mu\text{m}) = 1.009\,58(24) \times \rho_{T,\text{Sr}/S,\text{Sr}}(10.6 \mu\text{m}) = 1.6860(42)$ is determined from the measurement at $10.6 \mu\text{m}$ in Section 5.2 and the theoretical correction based on the polarizability model discussed in Section 4.1. This value also takes the spectral correction from Table 5.2 into account. This allows for the determination of the geometric factors with the light shifts on the $^{88}\text{Sr}^+$ transition as

$$\Lambda(\theta_1) = -0.4904(22), \Lambda(\theta_2) = 0.5157(14) \quad (5.30)$$

and subsequently a measurement of the light shift of the $^{171}\text{Yb}^+$ clock transitions at these settings in the same way as for the CO_2 laser. Tensor shift changes due to temporal variations of the magnetic field contribute with a fractional magnitude of 2×10^{-5} . Due to the reduced power of the QCL laser compared to the CO_2 laser,

the approximate scalar shifts on the E2 and E3 transition are -490 Hz and -60 Hz, respectively. The polarizability ratios at the wavelength of 8.568 μm are listed in Table 5.4, the increased fractional uncertainty compared to the CO_2 data is due to the higher fractional uncertainty in the geometric factors. If the polarizability variations of the E2 and E3 transition between 10.6 μm and 8.568 μm listed in Table 5.5 are taken into account, the QCL polarizability ratios are also consistent with the CO_2 polarizability ratios as shown in Fig. 5.2.

These data in combination with the polarizability measurements in [Hun+16] and [Bay+20] can be used to improve the knowledge of the dynamic correction for the E2 and E3 clock transitions. The current polarizability model described in Section 4.1 is consistent with the data within the uncertainty, but now measurements with significantly smaller uncertainty are available in the MIR region relevant for BBR shifts at room temperature.

5.4. Polarizability ratio of $^{88}\text{Sr}^+$ and $^{171}\text{Yb}^+$ clock transitions

The measurements in Section 5.2 and Section 5.3 do not allow for a determination of the absolute polarizability $\Delta\alpha_S^{\text{E}2}(10.6 \mu\text{m})$ and $\Delta\alpha_S^{\text{E}3}(10.6 \mu\text{m})$ with an uncertainty smaller than quoted in [Hun+16; Bay+20] on their own. For this, a measurement of the polarizability ratio $\rho_{S,\text{E}2/S,\text{Sr}}(10.6 \mu\text{m}) = \Delta\alpha_S^{\text{E}2}(10.6 \mu\text{m})/\Delta\alpha_S^{\text{Sr}}(10.6 \mu\text{m})$ is necessary. All other absolute polarizabilities can then be calculated from this quantity and the polarizability ratios discussed in Section 5.3. Finally, this allows for a reduction of the BBR shift uncertainty on the $^{171}\text{Yb}^+$ E2 and E3 clock transition due to the $^{88}\text{Sr}^+$ reference polarizability $\Delta\alpha_{\text{dc}}^{\text{Sr}} = -4.8314(20) \times 10^{-40} \text{ Jm}^2/\text{V}^2$ [Lin+25b].

Since the CO_2 laser intensity $\langle I \rangle(10.6 \mu\text{m})$ is calibrated with $^{88}\text{Sr}^+$, but employed for $^{171}\text{Yb}^+$, the potential spatial intensity variation between the respective positions of the ions has to be taken into account. The variation might occur due to the ion location in a linear crystal, if they are co-trapped in the same potential, or due to position offsets between two single trapped ions, because of their differing mass. In the linear confinement regime where the coupled radial secular frequencies $\omega_{x,j}, \omega_{y,j}$ are larger than the coupled axial secular frequencies $\omega_{z,j}$, the radial equilibrium positions between the ions differ by $0.29 \text{ nm}/(\text{V}/\text{m}) \times E_{\text{ext}}$ for a given radial displacement field E_{ext} at normal operating conditions, calculated from Eq. (2.22). This field can be determined from micromotion measurements and is kept below 200 V/m. This means that the equilibrium positions differ by 57 nm at most, a factor of approximately 4000 below the smaller CO_2 beam waist of 225.4(6.8) μm (determined in Section 4.3). This means that even if the ions would be positioned close to the beam waist, where the intensity gradient is the largest, the intensity between the ions would differ by 0.5×10^{-3} in the worst case. Since

5. Polarizability ratio measurements between $^{88}\text{Sr}^+$ and $^{171}\text{Yb}^+$

the ions are positioned close to the maximum of the gaussian intensity profile, the effect is even further suppressed and expected to cause a negligibly small correction. As a test of the radial displacement effect, a total light shift of -3150 Hz is applied on the E2 transition a single trapped $^{171}\text{Yb}^+$ and compared between the normal operating RF setting and a reduced RF power by 10 dB. The light shift is measured for each setting for approximately 10 s and then the RF power is changed. Any radial displacement due to external fields is magnified by a factor of 3.2 using this technique. Between the two settings a fractional light shift offset of $1.14(64) \times 10^{-3}$ is observed, consistent with zero at 2σ . The difference might be due to radial magnetic field gradients and consequently different tensor shift magnitudes and position shifts of the ions with respect to the laser beam due to the temperature difference of the trap between the two settings. This means that at normal operating conditions, a fractional light shift offset between the two ions of $0.36(20) \times 10^{-3}$ due to radial displacement between them is expected, smaller than the overall measurement uncertainty.

However, the position of the ions in a crystal along the trap axis differs by several μm , dependent on the axial confinement quantified by the secular frequency ω_z . To estimate the magnitude of the light shift difference along the trap axis, I measure it on the $^{171}\text{Yb}^+$ E2 transition in a $^{88}\text{Sr}^+ - ^{171}\text{Yb}^+$ crystal with ω_z reduced by a factor of 1.8 compared to the single-ion operating conditions. Due to collisions with the background gas, the ions switch positions every couple of minutes, which causes them to be perturbed by different intensities of the CO_2 beam. The difference in the light shift between these two configurations is a measure for the axial inhomogeneity of the intensity distribution. Any axial DC fields are compensated with an opposing field generated through a voltage imbalance on the axial confinement electrodes such that there is no movement of the ion visible on the camera when increasing the confinement voltage by a factor of 50. An average total light shift of -3120 Hz is observed on the E2 transition, which a fractional difference between the two crystal configurations of $24.1(1.8) \times 10^{-3}$. This is a factor of 1.6 larger than the expected maximum variation of 15×10^{-3} of the gaussian beam intensity with a waist of $225.4(6.8) \mu\text{m}$, the distance $11.5 \mu\text{m}$ of the two equilibrium positions along the trap axis calculated from the $^{171}\text{Yb}^+$ mass and $\omega_z = 2\pi \times 330$ kHz as well as the projection $\sin(15^\circ)$ of the gaussian beam minor axis on the trap axis direction. This difference might be due to variations of the tensor shift along the trap axis due to magnetic field gradients. At high confinement, this variation is expected to be reduced to $14.6(1.0) \times 10^{-3}$. This would limit the fractional uncertainty of the polarizability ratio measurement to approximately 10×10^{-3} without more careful investigation of this discrepancy.

Instead, to determine the polarizability ratio without being limited by the variation of the light shift along the ion chain, only a single ion is trapped in the potential at any point during the measurement. Since the axial position is solely determined by the electric charge and independent of the mass, both $^{88}\text{Sr}^+$ and $^{171}\text{Yb}^+$ are trapped at the same location along z . This is also supported by camera observations of

the center-of-mass position of a $^{88}\text{Sr}^+ - ^{171}\text{Yb}^+$ crystal, which coincides with the position of both a single trapped $^{88}\text{Sr}^+$ and $^{171}\text{Yb}^+$, respectively. The intensity variations due to radial displacement are still relevant with a fractional magnitude of $0.36(20) \times 10^{-3}$.

The experimental sequence is as follows with the CO_2 laser is operated at full intensity, causing a scalar light shift of approximately $-15\,600$ Hz and 9300 Hz on the E2 and $^{88}\text{Sr}^+$ clock transition, respectively:

1. Manually load a $^{171}\text{Yb}^+$ ion in segment 2 using the oven source.
2. Determine the E2 center frequency at three different mutually orthogonal magnetic field directions with geometric factors $\Lambda_1, \Lambda_2, \Lambda_3$ with and without the CO_2 laser induced light shift. This allows for the determination of the scalar light shift of the E2 transition $\Delta\nu_S^{\text{E2}}$.
3. After approximately 5 minutes, stop the interrogation and move the trapped $^{171}\text{Yb}^+$ to segment 6, where it stays uncooled for the following steps.
4. Automatically load a $^{88}\text{Sr}^+$ using the ablation laser in segment 2 and detect the ion number using the fluorescence collected with the PMT. At the settings in this measurement, a single ion is loaded within at most 5 attempts.
5. Determine the $^{88}\text{Sr}^+$ clock transition frequency among the same magnetic field directions with geometric factors $\Lambda_1, \Lambda_2, \Lambda_3$ with and without the CO_2 laser induced light shift. This allows for the determination of the scalar $\Delta\nu_S^{\text{Sr}}$ light shift of the $^{88}\text{Sr}^+$ transition.
6. After approximately 5 minutes, stop the interrogation, throw out $^{88}\text{Sr}^+$ by removing the axial confinement voltage of segment 1 and raise this voltage again. Move the stored $^{171}\text{Yb}^+$ back to segment 2 and continue with step 2 of the experimental sequence.

This sequence can operate without manual intervention for several hours. The three magnetic field directions are oriented to maximize the magnitude of the tensorial shifts and be minimally sensitive to temporal variations of the magnetic field direction. They are determined from the tensorial shifts on the $^{88}\text{Sr}^+$ transition in combination with the polarizability ratio $\rho_{T,\text{Sr}/S,\text{Sr}}$ to be

$$\Lambda_1 = 0.9729(30), \Lambda_2 = -0.4865(12), \Lambda_3 = -0.4836(35), \quad (5.31)$$

which are mutually orthogonal with a residual fractional tensor shift of $0.9(1.6) \times 10^{-3}$, limited by the statistical uncertainty of the measurement. The remaining fractional tensor shift is expected to be smaller than 1×10^{-5} . The interrogation times of the $^{88}\text{Sr}^+ |S, \pm 1/2\rangle \rightarrow |D, \pm 3/2\rangle$ and $|S, \pm 1/2\rangle \rightarrow |D, \pm 5/2\rangle$ transitions are 2.5 ms and 1.0 ms, respectively. The E2 transition is interrogated for 2.8 ms at the setting λ_1 and for 31 ms along the settings λ_2 and λ_3 due to the large variation in the total light shift from the addition and subtraction of the

5. Polarizability ratio measurements between $^{88}\text{Sr}^+$ and $^{171}\text{Yb}^+$

scalar and tensorial component. This results in a maximum fractional contribution of the residual tensorial shift of approximately 3×10^{-5} , significantly smaller than the total measurement uncertainty.

Each E2 light shift measurement except for the first one is interleaved between two $^{88}\text{Sr}^+$ light shift measurements, which calibrate the laser intensity at their respective points in time. The laser intensity is then linearly interpolated to the measurement time of the E2 light shift and used to determine the differential polarizability ratio

$$\rho_{S,E2/S,Sr}(10.6 \mu\text{m}) = \frac{\Delta\alpha_S^{E2}(10.6 \mu\text{m})}{\Delta\alpha_S^{Sr}(10.6 \mu\text{m})} = -1.6725(21), \quad (5.32)$$

where the fractional uncertainty of 1.3×10^{-3} is largely limited by the statistical uncertainty of the measurement, but also includes the observed fractional light shift offset along the radial direction of $0.36(20) \times 10^{-3}$. The statistical uncertainty is calculated as the standard error of the mean $\hat{\sigma} = \sigma/\sqrt{N}$, where σ is the standard deviation of the measurement and N is the number of measurement points. The time-resolved value of $\rho_{S,E2/S,Sr}(10.6 \mu\text{m})$ is shown in Fig. 5.3. No significant deviation of the data from white noise is observed.

The measured polarizability ratio $\rho_{S,E2/S,Sr}(10.6 \mu\text{m})$ together with the reference $^{88}\text{Sr}^+$ polarizability $\Delta\alpha_{dc}^{Sr} = -4.8314(20) \times 10^{-40} \text{ Jm}^2/\text{V}^2$ [Lin+25b] and the extrapolation $\Delta\alpha_S^{Sr}(10.6 \mu\text{m})/\Delta\alpha_{dc}^{Sr} = 0.99021(42)$ from $\lambda \approx 10^7 \mu\text{m}$ to $\lambda = 10.6 \mu\text{m}$ allows for the calculation of the scalar $^{171}\text{Yb}^+$ E2 polarizability $\Delta\alpha_S^{E2}(10.6 \mu\text{m})$. To determine the other polarizabilities for the E2 and E3 transition, the appropriate ratios in Table 5.4 are multiplied with $\Delta\alpha_S^{E2}(10.6 \mu\text{m})$. The absolute polarizability values at a wavelength of $8.568 \mu\text{m}$ are calculated from the same data under the assumption that the E3 scalar polarizability ratio $\Delta\alpha_S^{E3}(10.6 \mu\text{m})/\Delta\alpha_S^{E3}(8.568 \mu\text{m})$ is equal to the value derived from the polarizability model. They are summarized together with the corresponding values from [SPT05; Hun+16; Hun14; Bay+20] in Table 5.6 and their offsets are depicted in Fig. 5.4.

5.4. Polarizability ratio of $^{88}\text{Sr}^+$ and $^{171}\text{Yb}^+$ clock transitions

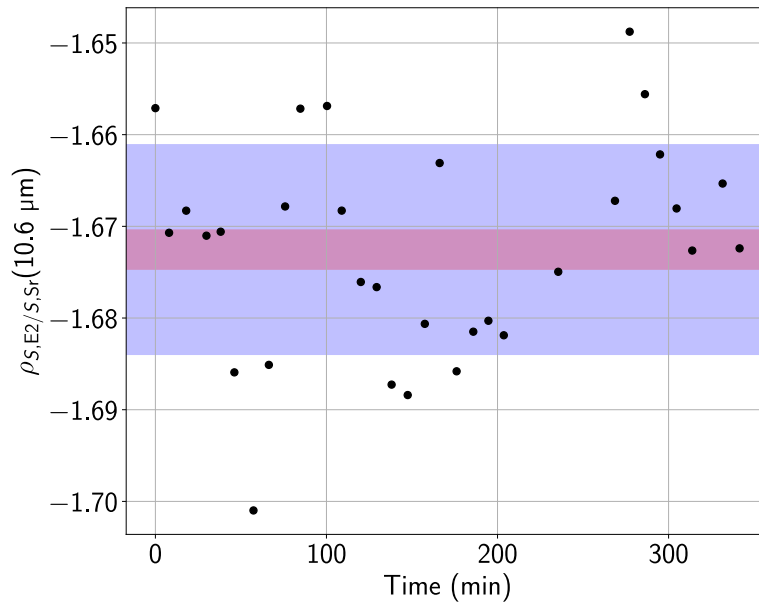


Figure 5.3.: Polarizability ratio of the $^{171}\text{Yb}^+$ E2 and $^{88}\text{Sr}^+$ clock transitions. The figure shows the time-resolved polarizability ratio $\rho_{S,E2/S,Sr}$ at the CO_2 laser wavelength of $10.6 \mu\text{m}$. The standard deviation $\sigma = 0.011$ of the data is shaded blue and the uncertainty of the mean value $\rho_{S,E2/S,Sr} = -1.6725(21)$ is shaded red. The uncertainty is calculated as the standard error of the mean $\hat{\sigma} = \sigma/\sqrt{N}$ with the number of measurements $N = 31$. It also includes the systematic uncertainty due to the observed fractional light shift offset along the radial direction of $0.36(20) \times 10^{-3}$.

5. Polarizability ratio measurements between $^{88}\text{Sr}^+$ and $^{171}\text{Yb}^+$

Source λ	PTB [SPT05; Hun+16; Hun14] $10^7\mu\text{m}$	CO ₂ , RF $10.6\mu\text{m}$	CO ₂ , LS $10.6\mu\text{m}$
$\Delta\alpha_S^{E2}$	6.9(1.4) [SPT05]	8.001(11)	6.93(12)
$\Delta\alpha_T^{E2}$	-13.6(2.2) [SPT05]	-13.033(38)	-11.29(20)
$\Delta\alpha_S^{E3}$	0.888(16) [Hun+16]	1.0030(29)	0.869(15)
$\Delta\alpha_T^{E3}$	-0.244(13) [Hun14]	-0.26964(93)	-0.2336(41)

Source λ	QCL, RF $8.568\mu\text{m}$	QCL, LS $8.568\mu\text{m}$	NPL [Bay+20] $7.17\mu\text{m}$
$\Delta\alpha_S^{E2}$	8.423(45)	7.30(13)	7.79(20)
$\Delta\alpha_T^{E2}$	-13.337(79)	-11.55(21)	-11.88(46)
$\Delta\alpha_S^{E3}$	1.0022(29)	0.868(15)	0.854(18)
$\Delta\alpha_T^{E3}$	-0.2706(19)	-0.2344(43)	-0.2315(75)

Table 5.6.: Absolute polarizabilities of the $^{171}\text{Yb}^+$ clock transitions. The table lists the measured scalar and tensorial differential polarizabilities $\Delta\alpha$ for the $^{171}\text{Yb}^+$ E2 and E3 clock transitions at different wavelengths λ given in units of $10^{-40}\text{Jm}^2/\text{V}^2$. The values at $\lambda \approx 10^7\mu\text{m}$ are a combination of the E2 and E3 polarizabilities measured in [SPT05; Hun+16; Hun14] (column PTB), the values at $\lambda = 7.17\mu\text{m}$ are taken from [Bay+20] (column NPL). The polarizabilities at $10.6\mu\text{m}$ in the column CO₂, RF are determined in this work with a CO₂ laser using the $^{88}\text{Sr}^+$ polarizability $\Delta\alpha_{dc}^{\text{Sr}}$ [Lin+25b] as a reference value in combination with the polarizability ratios in Table 5.4. The values in the column CO₂, LS use the light-shift-based polarizability measurement of $\Delta\alpha_S^{\text{Sr}}$ Eq. (4.54), instead. The values at $8.568\mu\text{m}$ are calculated from the polarizabilities at $10.6\mu\text{m}$ under the assumption that the E3 scalar polarizability ratio $\Delta\alpha_S^{E3}(10.6\mu\text{m})/\Delta\alpha_S^{E3}(8.568\mu\text{m})$ is equal to the value derived from the polarizability model. All in all, there is a consistent discrepancy of approximately 14% between the values from [SPT05; Hun+16; Hun14; Bay+20] and the ones determined in this thesis based on the rf-based measurement of $\Delta\alpha_{dc}^{\text{Sr}}$. This is consistent with the discrepancy in the absolute $^{88}\text{Sr}^+$ polarizability discussed in Section 4.3. The offset between these values is shown in Fig. 5.4.

The fractional BBR shift at a temperature of 300 K can be determined with significantly reduced uncertainty for both the E2 and E3 transition

$$\frac{\Delta\nu_{\text{BBR}}^{E2}}{\nu^{E2}} = -606.11(84) \times 10^{-18}, \quad \frac{\Delta\nu_{\text{BBR}}^{E3}}{\nu^{E3}} = -81.59(24) \times 10^{-18}, \quad (5.33)$$

where the correction $\xi^{E2}(10.6\mu\text{m}) = -1.61(12) \times 10^{-3}$ and $\xi^{E3}(10.6\mu\text{m}) = 0.12(8) \times 10^{-3}$ defined as in Eq. (4.28) is applied. Due to the significant discrepancy in $\Delta\alpha_S^{E2}$ and $\Delta\alpha_S^{E3}$ between the value based on RF-induced frequency shifts and light-induced frequency shifts discussed in section 4.3, the BBR shift changes significantly when compared to the determination by NPL in [Bay+20]

$$\frac{\Delta\nu_{\text{BBR}}^{\text{E2}} - \Delta\nu_{\text{BBR}}^{\text{E2, NPL}}}{\nu^{\text{E2}}} = -99(28) \times 10^{-18}, \quad \frac{\Delta\nu_{\text{BBR}}^{\text{E3}} - \Delta\nu_{\text{BBR}}^{\text{E3, NPL}}}{\nu^{\text{E3}}} = -11.9(1.5) \times 10^{-18}. \quad (5.34)$$

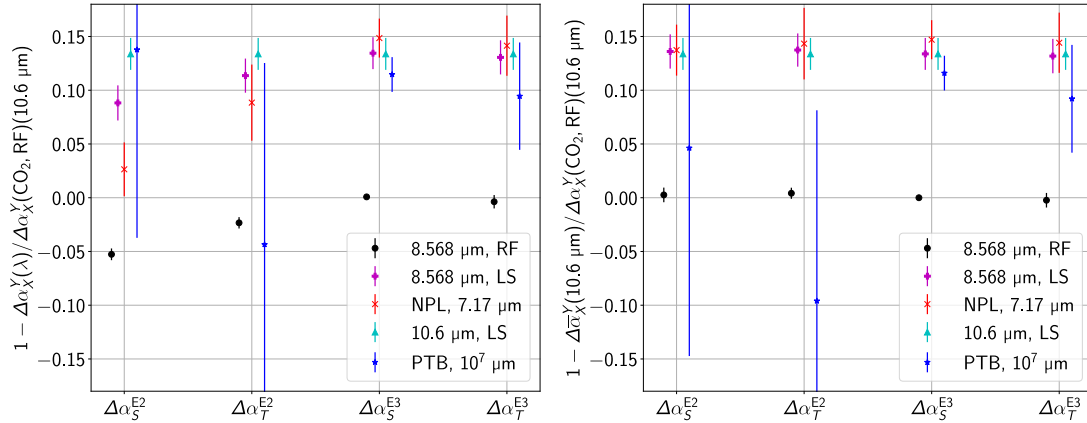


Figure 5.4.: Fractional offsets of the $^{171}\text{Yb}^+$ polarizability values. The scalar (S) and tensorial (T) polarizabilities $\Delta\alpha_X^Y(\lambda)$ of the $^{171}\text{Yb}^+$ E2 and E3 clock transitions are measured with the CO_2 laser at a wavelength $\lambda=10.6\mu\text{m}$ using the rf-based determination of $\Delta\alpha_{\text{dc}}^{\text{Sr}}$ in [Lin+25b] as a reference (shown as RF) and compared with the values from [Bay+20] (NPL, $\lambda=7.17\mu\text{m}$), [SPT05; Hun14; Hun+16] (PTB, $\lambda\approx 10^7\mu\text{m}$). $\Delta\alpha_X^Y(8.568\mu\text{m})$ is calculated from $\Delta\alpha_X^Y(10.6\mu\text{m})$ under the assumption that the E3 scalar polarizability ratio $\Delta\alpha_S^{\text{E3}}(10.6\mu\text{m})/\Delta\alpha_S^{\text{E3}}(8.568\mu\text{m})$ is equal to the value derived from the polarizability model. Additionally, the same polarizabilities are determined using the light-shift based measurement of $\Delta\alpha_S^{\text{Sr}}$ Eq. (4.54) (shown as LS). $\Delta\bar{\alpha}_X^Y(10.6\mu\text{m}) = \varepsilon(\lambda)\Delta\alpha_X^Y$ is calculated from the polarizability models discussed in Section 4.1. The RF determinations show a consistent discrepancy from the LS values of approximately 14 %, consistent with the offset discussed in Section 4.3.

Conclusion The measurements presented in this chapter allow for determination of both polarizability ratios and absolute polarizabilities with significantly reduced uncertainty compared to other measurements of the same quantities for $^{171}\text{Yb}^+$ clock transitions [SPT05; Hun+16; Hun14; Bay+20], relying on the accuracy of the polarizability of the $^{88}\text{Sr}^+$ clock transition [Dub+14; Lin+25b]. Since the light shifts are induced with MIR lasers, the measurements also result in a smaller fractional uncertainty for the differential polarizability around $10.6\mu\text{m}$ compared to the polarizability ratio measurement presented in [Wei+24]. All of this results in a reduction of the $^{171}\text{Yb}^+$ E2 and E3 fractional BBR shift uncertainty to 0.84×10^{-18} and 0.24×10^{-18} , allowing for operation of an E2 and E3 clock with below 1×10^{-18} total uncertainty. These uncertainties can be further reduced by gathering more data and by performing the measurement at the magic angle where the tensor

5. Polarizability ratio measurements between $^{88}\text{Sr}^+$ and $^{171}\text{Yb}^+$

shift is zero. In this setting, magnetic field variations have a significantly larger effect and have to be characterized more carefully, though.

However, due to the difference in the polarizability determined with laser radiation and RF fields presented in Section 4.3, the BBR shift magnitude changes by a significant amount. Whether $\Delta\alpha_{\text{Sr}}^{\text{Sr}}$ determined from magic frequency measurements [Dub+14; Lin+25b] is correct has to be investigated further to decide whether to use the results presented here for correction of the BBR shift.

6. $^{88}\text{Sr}^+ / ^{171}\text{Yb}^+$ E3 frequency ratio measurement

The system described in this thesis is also operated as a single ion $^{88}\text{Sr}^+$ clock to realize the unperturbed frequency ν_{Sr^+} of the $^2S_{1/2} \rightarrow ^2D_{5/2}$ E2 transition. It is a recognized secondary representation of the second and various NMIs in the world operate $^{88}\text{Sr}^+$ clocks [Bar+14; Mar+25a; Lin+25b]. Past determinations show a disagreement between the values of ν_{Sr^+} when measured against Cs clocks [Bar+14; Jia+22]. Determining the optical frequency ratio between the $^{88}\text{Sr}^+$ and the $^{171}\text{Yb}^+$ E3 clock transitions allows for determination of ν_{Sr^+} with reference to the absolute frequency of the E3 transition [Lan+21a]. This may resolve the disagreement and provides input data for a redefinition of the second based on $^{88}\text{Sr}^+$ [Dim+24]. The content of this chapter is published in [Ste+23] to a large extent.

6.1. Clock transition interrogation sequence

Due to the lack of $m=0$ states in both the ground state and excited state, each individual $\nu_{m_S}^{m_D} := |S, m_S\rangle \rightarrow |D, m_D\rangle$ transition frequency $\nu_{m_S}^{m_D}$ is linearly dependent on the magnetic field B at the ion position. In addition, tensorial effects such as the electric quadrupole shift induced by electric field gradients, perturb the transition frequency proportional to m_D^2 [Dub+13]. To realize the unperturbed frequency, these effects can be canceled by choosing appropriate interrogation sequences of the individual $\nu_{m_S}^{m_D}$ transitions and computing the weighted average $\bar{\nu}$ of their center frequencies $\nu_{m_S}^{m_D}$ [Dub+13]

$$\bar{\nu} = \sum_{m_S, m_D} w_{m_D}^{m_S} \nu_{m_S}^{m_D}. \quad (6.1)$$

Zeeman shift Cancelling the linear Zeeman shift is achieved by interrogating pairs of transitions with linear magnetic sensitivities of equal magnitude but opposite sign as the Zeeman shift is given by

$$\Delta\nu_{m_S}^{m_D}(\vec{B}) = \frac{\mu_B}{h} |\vec{B}| (g_D m_D - g_S m_S) \quad (6.2)$$

$$+ a_{m_D} \left(\frac{\mu_B}{h} |\vec{B}| \right)^2 \frac{(g_e + 1)^2}{\nu_{DD}} \quad (6.3)$$

$$+ O(|\vec{B}|^3), \quad (6.4)$$

where g_D, g_S are the Landé factors of the excited and ground state respectively, $a_{\pm 1/2} = 6/25$, $a_{\pm 3/2} = 4/25$, $a_{\pm 5/2} = 0$ is an m_D -dependent prefactor, g_e is the electron-spin Landé factor and $\nu_{DD} = 8.404\,382$ THz is the energy separation of the $^2\text{D}_{3/2}$ and $^2\text{D}_{5/2}$ electronic states [Dub+13].

The quadratic Zeeman shift remains for the mean frequency $\nu_Z^{m_D} := (\nu_{+1/2}^{+m_D} + \nu_{-1/2}^{-m_D})/2$ and needs to be corrected separately. The field B is approximated from the measured linear shift

$$B(t) = \frac{(\nu_{+1/2}^{+m_D} - \nu_{-1/2}^{-m_D})}{2\mu_B(g_D m_D - g_S/2)} \quad (6.5)$$

and then used to correct $\nu_Z^{m_D}$ dynamically to compensate magnetic field changes over time. For magnetic fields below 100 μT the fractional error on the unperturbed transition frequency introduced by disregarding the third order shift is smaller than 10^{-25} and thus negligible. The second-order Zeeman shift does not introduce any error for the inferred magnetic field, since it is common to the positive and negative Zeeman shift transition.

Tensorial shifts There are a variety of effects that cause a shift that is tensorial in nature. This means that the magnitude of the shift is proportional to tensorial properties of the energy levels such as their quadrupole moment Θ or the tensorial part of the polarizability $\Delta\alpha_T$ [Dub+13]. Since the wavefunction of the $S_{1/2}$ ground state is spherically symmetric, it is immune to these effects [AS68, p. 132]. The excited state $D_{5/2}$ on the other hand is sensitive to tensorial shift effects, with each m_D substate having a different sensitivity to the perturbation. The tensorial shift $\Delta\nu_T$ due to an electric field or its gradient is given by [Ita00]

$$\Delta\nu_T = A \frac{3\cos^2(\vartheta) - 1}{2} \left(\frac{3m_D^2 - J(J+1)}{J(2J-1)} \right), \quad (6.6)$$

where A is a factor proportional to the perturbation, ϑ is the angle between the magnetic field at the ion position \vec{B} , and the electric field or its gradient and J is the total angular momentum of the excited state.

There are two significant tensor shift contributions for the system considered here:

1. The electric quadrupole shift $\Delta\nu_Q$ with $A = -2\vec{\nabla}\vec{E}\Theta/h$ [Ita00] with the electric field gradient $\vec{\nabla}\vec{E}$ and the angle ϑ between \vec{B} and each component of the field gradient. In linear ion traps the gradient is usually dominated by the axial trapping potential [Kel+19].
2. The tensorial Stark shift $\Delta\nu_{\text{Stark},T}$ with $A = -1/(2h)\Delta\alpha_T\langle\vec{E}^2\rangle$ [SSA16], where ϑ is the angle between \vec{B} and \vec{E} . The electric field is usually caused by electromagnetic radiation or the RF trapping field.

Especially $\Delta\nu_Q$ can reach a magnitude of 1-300 Hz for field gradients of 1-100 V/mm² typically found in ion traps [Lan+20; Für+20]. While the shift magnitude can be calculated, it is difficult to reach low uncertainties and drifts in the shift need to be accounted for. Alternatively, the tensorial shifts can be zeroed using three different methods which can all be derived from Eq. (6.6):

1. If $3\cos^2(\vartheta) - 1 = 0$, $\vartheta \approx 54.7^\circ$, $\Delta\nu_T$ is equal to zero, so by choosing the appropriate direction of \vec{B} , one tensorial shift can be heavily suppressed. Since $\vec{\nabla}\vec{E}$ and the electric fields responsible for the Stark shift are not collinear in general, not all tensorial shifts can be zeroed simultaneously using this method. In addition, there may be other constraints on the magnetic field direction from the experimental design and fluctuations in the background magnetic field need to be corrected for.
2. If the transition susceptible to tensor shifts is probed three times where the magnetic field directions for each interrogation are mutually orthogonal, the mean frequency of all three interrogations is free of tensor shifts [Ita00]. This method has successfully been used in a variety of optical clocks [Hun+16; Lan+21a], but requires careful calibration of the applied magnetic field. Also it is sensitive to changes in the magnetic background field unless recalibration sequences are applied when necessary.
3. The third option is to interrogate multiple transitions with different $|m_D| = 1/2, 3/2, 5/2$. If all $|m_D|$ are interrogated, their mean frequency is intrinsically free of tensor shifts, since the corresponding Hamiltonian is trace-free [Dub+13]. By only interrogating two of three options and calculating a weighted average such that the tensor shift is removed, higher cycle rates and subsequent lower instabilities can be achieved, but only the first order of the tensor shift is canceled [Dub+13]. In that case, third-order and higher contributions remain, since the second order of the tensor shift expansion is zero [Dub+13]. This method requires interrogating linearly magnetically sensitive transitions, so it is a good option for ions such as $^{88}\text{Sr}^+$ and $^{40}\text{Ca}^+$ where no transition $|S, m_S=0\rangle \rightarrow |D, m_D=0\rangle$ exists.

I choose the third option for the $^{88}\text{Sr}^+$ clock since it is the most easily applicable for

6. $^{88}\text{Sr}^+ / ^{171}\text{Yb}^+$ E3 frequency ratio measurement

the described experimental apparatus. To reach the smallest instability possible, I optimize the number of interrogations on each transition $\nu_{m_s}^{m_D}$ given their respective maximum coherent interrogation times. These differ because the coherence time is limited by magnetic field noise, so more magnetically sensitive transitions are more susceptible to this noise compared to the innermost $\nu_{\pm 1/2}^{\pm 1/2}$ transitions.

Specifically, if the coherent interrogation time of the clock transition is limited by magnetic field noise, the minimum linewidths $\delta\nu$ of the transitions between individual Zeeman states are related in the following way:

$$\delta\nu_{\pm 1/2}^{\pm 3/2} = 2\delta\nu_{\pm 1/2}^{\pm 1/2}, \quad \delta\nu_{\pm 1/2}^{\pm 5/2} = 5\delta\nu_{\pm 1/2}^{\pm 1/2} \quad (6.7)$$

The weighted average frequency of each transition needs to be chosen in such a way that the result is free of all tensorial shifts

$$\nu_{\text{Sr}^+} = w_1\nu^{1/2} + w_3\nu^{3/2} + w_5\nu^{5/2}, \quad (6.8)$$

where $\nu^k = (\nu_{+1/2}^{+k} + \nu_{-1/2}^{-k})/2$ and $w_1 + w_3 + w_5 = 1$. The instability of ν_{Sr^+} is proportional to the uncertainty $\Delta\nu_{\text{Sr}^+}$

$$\Delta\nu_{\text{Sr}^+} = \sqrt{(w_1\Delta\nu^{1/2})^2 + (w_3\Delta\nu^{3/2})^2 + (w_5\Delta\nu^{5/2})^2}, \quad (6.9)$$

where the uncertainty of each individual transition is related to the linewidth and number of interrogations during each clock cycle n_j

$$\Delta\nu_{\text{Sr}^+} = \sqrt{\left(w_1 \frac{\delta\nu^{1/2}}{\sqrt{n_1}}\right)^2 + \left(w_3 \frac{\delta\nu^{3/2}}{\sqrt{n_3}}\right)^2 + \left(w_5 \frac{\delta\nu^{5/2}}{\sqrt{n_5}}\right)^2}, \quad (6.10)$$

which in combination with Eq. (6.7) allows for a numerical optimization of the number of interrogations of each transition to reach the smallest instability

$$\Delta\nu_{\text{Sr}^+} = \sqrt{\frac{w_1^2}{n_1} + 4\frac{w_3^2}{n_3} + 25\frac{w_5^2}{n_5}}\delta\nu^{1/2}. \quad (6.11)$$

The optimum occurs for $w_1 = 0$, $w_3 = 5/6$, $w_5 = 1/6$ and $n_3 = 2$, $n_5 = 1$ and is approximately

$$\Delta\nu_{\text{Sr}^+} \approx 1.44\delta\nu^{1/2}, \quad (6.12)$$

which is a factor of 1.26 smaller than the simple average over all transitions with the same interrogation time.

Experimental sequence The clock cycles through the same experimental sequence continuously until it is manually stopped or the ion is lost. A sketch of the primary steps is shown in Fig. 6.1 along with the lasers in use for each step. Every clock cycle starts with 5 ms of Doppler cooling with the 422 nm as well as 1033 nm and 1092 nm radiation. By comparing the accumulated fluorescence during cooling to a threshold value, it is determined whether the ion is still bright and has not left the trap or gained significant amounts of kinetic energy. If the ion is dark, all 422 nm lasers are red-detuned by approximately 500 MHz and turned to full power to re-cool the ion in the trap. This procedure continues until the ion is cooled close to the Doppler limit again.

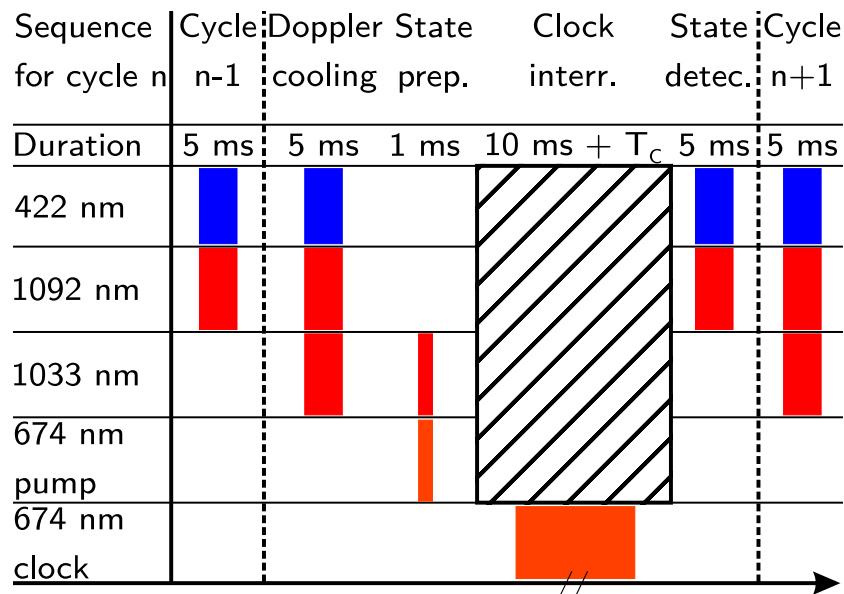


Figure 6.1.: *Experimental pulse sequence for the $^{88}\text{Sr}^+$ clock. The active periods of all lasers involved in the interrogation cycle of the $^{88}\text{Sr}^+$ clock transition are illustrated along with the duration of each period. Doppler cooling and state detection requires the 422 nm and 1092 nm lasers, while the 1033 nm laser clears out the excited state of the clock. State preparation is implemented with the clock and clear out laser. During spectroscopy, all lasers other than the clock laser are mechanically blocked with shutters. Their opening and closing takes 5 ms, each. T_C varies between 35 ms and 87.5 ms, depending on the magnetic field sensitivity of the interrogated transition.*

After Doppler cooling, the cooling lasers are turned off and the Sr clock laser entering the ion trap along the vertical axis in Fig. 3.8 is pulsed at full power for 1 ms at the detuning of the $|S, m_S = \pm 1/2\rangle \rightarrow |D, m_D = \mp 3/2\rangle$ transition. This prepares the ion in the $|S, m_S = \mp 1/2\rangle$ state with more than 95 % fidelity, see Section 2.4 for more details. Afterwards, all beams other than the path-length stabilized Sr clock laser are blocked with mechanical shutters, which takes 5 ms. Then, the clock laser drives the clock transition to perform a π -pulse at either the

6. $^{88}\text{Sr}^+ / ^{171}\text{Yb}^+$ E3 frequency ratio measurement

positive or negative half-maximum detuning with respect to the resonance frequency from the last completed cycle. The $|S, \pm 1/2\rangle \rightarrow |D, \pm 3/2\rangle$ transitions have an interrogation time $T_C = 87.5$ ms and for the $|S, \pm 1/2\rangle \rightarrow |D, \pm 5/2\rangle$ transitions, $T_C = 35$ ms. The shutters are opened again, taking 5 ms, and the 422 nm and 1092 nm lasers illuminate the ion for an additional 5 ms to determine whether it remained in the ground state or was excited. The fidelity of this state detection is greater than 99 % as determined from a histogram of photon counts with and without the repump laser active. The Doppler cooling section of the subsequent cycle measures if the ion is still cool in the trap and marks the previous interrogation cycle as invalid, if this is not the case. Invalid cycles are repeated immediately before resuming the interrogation sequence.

Once 4 valid clock excitation attempts are recorded, the number of excitations at positive n_+ and negative n_- detunings corrects the center frequency of the interrogated transition by $0.15(n_+ - n_-)\Delta_{\text{HWHM}}$, where Δ_{HWHM} is the half-width-half-maximum detuning of the transition. The number of successful excitations is also recorded and used in conjunction with fluorescence data and phase-slips of the clock laser fiber-length stabilizations to exclude invalid data from the recorded frequency.

6.2. Systematic frequency shifts and their uncertainty

The measured frequency of an interrogated clock transition is affected by a variety of physical effects. These effects can only be quantified with a finite uncertainty, which are listed in the so-called *uncertainty budget*. The systematic uncertainty to which the unperturbed transition frequency ν_0 can be realized is the combined uncertainty of all frequency shifts listed in the uncertainty budget. The uncertainty budget for the lowest systematic uncertainty achieved in YbSr1 is shown in Table 6.1.

Shift effect	$\Delta\nu/\nu_0(10^{-18})$	$u(\Delta\nu)/\nu_0(10^{-18})$
Blackbody radiation	537.9	7.6
Excess micromotion	-15.1	6.6
Collisions	0	1.1
Servo error	0	0.70
Thermal motion	-3.01	0.31
AOM chirp	0	0.10
Clock laser AC Stark	0.126	0.065
Quadratic Zeeman	0.1928	0.0008
Total	520	10

Table 6.1.: *Systematic uncertainty budget. A summary of all systematic frequency shifts from the unperturbed reference value and their uncertainties with the trap operated at the smallest employed RF power. The overall uncertainty is dominated by the BBR shift due to the limited knowledge of trap heating and the excess micromotion shift due to uncompensable micromotion.*

Stark effect As discussed in Chapter 4, the Stark effect causes a shift of the atomic transition frequency due to a perturbing electric field. Several sources of electric fields in an optical clock based on trapped ions exist and their shifts have to be corrected for.

Blackbody radiation At room temperature, the BBR shift usually has one of the largest magnitudes and contributes significantly to the systematic uncertainty [San+19; Lan+21a]. While there exist ion species that feature BBR insensitive clock transitions, such as $^{27}\text{Al}^+$ [Mar+25b] and In^+ [Hau+25], they tend to not possess Doppler cooling transitions in the visible range, necessitating sophisticated cooling and detection techniques. One notable exception is Lu^+ , which possesses a BBR shift-insensitive clock transition while still allowing for classic cooling and detection methods [Arn+18]. An accurate determination of the BBR shift requires a precise measurement of the dynamic polarizability $\Delta\alpha(\lambda)$ in the infrared as well as an inference of the effective BBR temperature T_{eff} the ion experiences. For methods to determine $\Delta\alpha(\lambda)$ with low uncertainty, refer to Chapter 4 and Chapter 5.

$T_{\text{eff}} = T_0 + \delta T$ for ion traps consists of two components: the background temperature T_B of the laboratory the ion trap is situated in and the effective heating δT of the ion trap due to RF currents induced by the trap drive. T_B is measured with sufficiently high accuracy using multiple Pt100 sensors around the vacuum chamber and is not the limiting factor for ion trap BBR shifts in this setup. δT on the other hand, is more difficult to determine, since the generated heat in the trap can be distributed very inhomogeneously, if the trap is not specifically designed using materials with high thermal conductivity [Dol+15; Nor+20]. In addition, the ion

6. $^{88}\text{Sr}^+ / ^{171}\text{Yb}^+$ E3 frequency ratio measurement

does not have a line of sight with all heated elements, which leads to a reduction of the effective temperature depending on the trap geometry [Dol+15; Nor+20]. All in all, the accurate determination of δT usually necessitates special ion traps and extensive Finite Element Modelling (FEM) to reach a sub-Kelvin effective temperature uncertainty. A comprehensive study of effective temperature increase determinations and subsequent BBR shift uncertainty calculations is found in [Dol+15]. The ion trap design used in this work is specifically studied in [Nor+20], but relies on the high thermal conductivity $\kappa = 175 \text{ W}/(\text{m K})$ of the AlN carrier material [Nor+20]. The system in use here uses Rogers 4350B with a thermal conductivity of $\kappa = 0.7 \text{ W}/(\text{m K})$ [Nor+20], significantly altering the temperature distribution when the RF trap is operating. This makes the BBR shift estimate based on [Nor+20] unreliable for the system discussed here.

In contrast, I employ a different method to estimate the effective heating δT for traps that are not specially designed for low and homogeneous heating. The dominant heating source is the ohmic resistance of the trap material, which causes Joule heating Q_J proportional to the power circulating in the trap P_{RF} . The effective temperature increase δT is linearly related to Q_J under the assumption that thermal radiation does not contribute significantly to the balance of all heating and cooling sources of the system as a whole. This means that the effective heating at two different RF power settings P_1 and $P_2 = kP_1$ leads to a difference in the BBR shift $\Delta\nu_{12}$ of

$$\Delta\nu_{12} = \nu_2 - \nu_1 = -\frac{2\sigma}{h\varepsilon_0 c} \Delta\alpha_{\text{dc}}(1 + \eta) \left((T_0 + k\delta T)^4 - (T_0 + \delta T)^4 \right), \quad (6.13)$$

which can be used to determine δT and consequently extrapolate the measured frequency to $\delta T = 0$ or the well-known background temperature T_0 . The only requirements for this method to produce the correct unperturbed frequency are that the effective temperature increase is proportional to the RF power and that all other potential frequency variations have been taken into account correctly.

Heat flow due to thermal radiation P_R is proportional to the surface area A of the hot body and its temperature T to the fourth power

$$P_R = \varepsilon\sigma AT^4, \quad (6.14)$$

where σ is the Stefan-Boltzmann constant and ε is the emissivity of the body. Let's assume for now that this is the only heat conduction mechanism and the power P_{RF} is dissipated purely by radiation. Then it follows that the increased temperature $T = T_0 + \Delta T$ above the reference temperature T_0 without RF is given by

$$P_{\text{RF}} = P_R(T) - P_R(T_0) = \varepsilon\sigma A\left((T_0 + \Delta T)^4 - T_0^4\right) \quad (6.15)$$

$$= \varepsilon AT_0^4 \left(4\frac{\Delta T}{T_0} + 6\left(\frac{\Delta T}{T_0}\right)^2 + 4\left(\frac{\Delta T}{T_0}\right)^3 + \left(\frac{\Delta T}{T_0}\right)^4 \right). \quad (6.16)$$

Importantly, the first term in the expansion is still linear with respect to ΔT and thus does not cause any error when relying on the linearity between the effective temperature increase δT and the applied RF power. For the ion trap in this thesis, $A \approx 2 \times 50 \text{ mm} \times 50 \text{ mm} = 5 \times 10^{-3} \text{ m}^2$, $T_0 = 296 \text{ K}$, $\varepsilon = 1$ and $P_{\text{RF}} \approx 0.5 \text{ W}$ as a worst case scenario where about half of all RF power is dissipated via radiation. This is more than a factor of 10 higher than the typical radiative losses in ion traps [Dol+15]. With these parameters $\Delta T = 15.7 \text{ K}$ and the relative nonlinearity μ is equal to

$$\mu = \frac{6(\Delta T/T_0)^2 + 4(\Delta T/T_0)^3 + (\Delta T/T_0)^4}{4\Delta T/T_0} \quad (6.17)$$

$$= \frac{3}{2}\Delta T/T_0 \left(1 + \frac{2}{3}\Delta T/T_0 + \frac{1}{6}(\Delta T/T_0)^2 \right) \approx 8.2\%, \quad (6.18)$$

so any relative uncertainty $u(\delta T)/\delta T$ smaller than 10% may have to take radiative nonlinearities into account. However, most of the heat is dissipated due to thermal conductance between the ion trap and the optical table at a lower temperature. So, the nonlinearity does not need to be taken into account in this measurement.

This measurement allows for a small uncertainty, because the differential polarizability of the $^{88}\text{Sr}^+$ clock transition is known with comparatively high accuracy $\Delta\alpha_{\text{dc}} = -4.7938(71) \times 10^{-40} \text{ Jm}^2/\text{V}^2$ [Dub+14]. More details on this quantity and a disagreement between different methods to determine it are discussed in Chapter 4. Three different powers $P_{\text{RF}} = (+0 \text{ dB}, +3 \text{ dB}, +6 \text{ dB}) \approx (P_0, 1.995P_0, 3.981P_0)$ are input into the ion trap and the frequency ratio $\mathcal{R}_T(T_0 + P/P_0 \times \delta T) = \nu_{\text{Sr}}/\nu_{\text{E3}}(T_0 + P/P_0 \times \delta T)$ is measured against a separate unperturbed $^{171}\text{Yb}^+$ E3 single-ion clock Yb1 [San+19]. T_0 can be determined with an uncertainty of 0.2 K using a Pt100 sensor and is 296.7(2) K. From these measurements and a nonlinear least-squared regression of the data with Eq. (6.13) an effective temperature increase at $P_{\text{RF}} = P_0$ of $\delta T = 0.6(1.0) \text{ K}$ is determined. The data, their corresponding uncertainty and the best-fit line are shown in Figure 6.2. This results in a fractional BBR shift of $537.9(7.6) \times 10^{-18}$ at this setting. Due to the linear increase in δT , the uncertainty increases correspondingly at higher RF powers.

6. $^{88}\text{Sr}^+ / ^{171}\text{Yb}^+$ E3 frequency ratio measurement

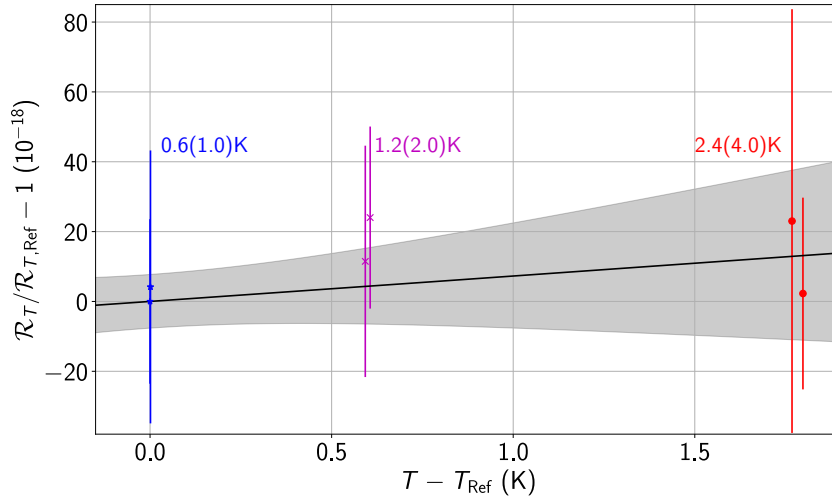


Figure 6.2.: *BBR shift estimate due to trap heating.* The frequency ratio \mathcal{R}_T between the $^{88}\text{Sr}^+$ clock and an unperturbed $^{171}\text{Yb}^+$ E3 clock [San+19] is measured for three different RF power settings $P_{RF} = (+0 \text{ dB}, +3 \text{ dB}, +6 \text{ dB})$ relative to an initial setting P_0 , shown in blue, purple and red, respectively. At this initial setting, the frequency ratio $\mathcal{R}_{T, \text{Ref}}$ at the temperature $T_{\text{Ref}} = T_0 + \delta T(P_0)$ is determined. The error bars only indicate statistical uncertainties. The background temperature T_0 varies slightly over the measurement period and is determined with a Pt100 sensor in the laboratory. The black line shows the best-fit curve of Eq. (6.13) as determined by nonlinear least-squares regression and the gray shading corresponds to the uncertainty when all differences in temperature are attributed to heating of the trap. With this data, it is possible to determine $\delta T(P_0) = 0.6(1.0) \text{ K}$ and corresponding higher values for the other RF power settings.

AC Stark shifts The second relevant source of Stark shifts for an ion clock is the intensity $I(\lambda)$ of radiation with wavelength λ at the position of the ion, so-called *AC Stark shifts*. These appear to residual laser radiation from the cooling beams or the clock laser itself. As discussed in Section 4.3, only the averaged Stark shift over many oscillation periods is observable. Only the scalar shift proportional to $\Delta\alpha_S(\lambda)$ is relevant for the shift of the clock frequency, because the tensorial shift is averaged with the same technique as the electric quadrupole shift. This requires that the tensorial shift is equal for each cycle averaged, which may not be the case, if e.g. the clock laser intensity is varied between each cycle.

During the interrogation of the clock transition all beams other than the clock laser are blocked with mechanical shutters as described in Section 3.2. This means that the only laser-induced Stark shift is due to the 674 nm laser itself with a scalar differential polarizability $\Delta\alpha_S(\lambda) = -28.1(7.0) \times 10^{-40} \text{ Jm}^2/\text{V}^2$ [Mad+04]. The maximum intensity of the clock laser at the ion position is $7.0(3.5) \text{ nW}/\text{mm}^2$ which corresponds to a fractional AC Stark shift is $0.126(65) \times 10^{-18}$, negligible compared to the overall systematic uncertainty.

Motional Stark shifts The third source of Stark shifts in ion traps is due to ion motion. In the center ($\vec{r}=(0,0,0)^T$) of the ion trap, no electric fields $\vec{E}=m/e\frac{d^2}{dt^2}\vec{r}$ originating from the trapping potential perturb the particle (as can be seen in Eq. (2.15)). This is in contrast to optical clocks with neutral atoms, which require large laser intensities to confine atoms sufficiently well, which incurs substantial Stark shifts, if they are not operated at a magic wavelength [TK03].

But the ion does not reside in the center of the trap during the whole interrogation of the clock transition. As discussed in Section 2.1, secular motion and micromotion both cause the ion to leave the center and it experiences an electric field. This causes a Stark shift, which has to be determined and corrected for. In general, for an oscillatory motion caused purely by an electric field $E(t)$ with RMS amplitude a_{RMS} and angular frequency ω results in the following averaged squared electric field $\langle E^2(t) \rangle$

$$\langle E^2(t) \rangle = a_{\text{RMS}}^2 \omega^4 \frac{m^2}{q^2}, \quad (6.19)$$

where m is the ion mass and q the ion charge. If the ion possesses a temperature T along one axis of motion, $\langle E^2(t) \rangle$ can be expressed as

$$\langle E^2(t) \rangle = k_B T \omega^2 \frac{m}{q^2}, \quad (6.20)$$

with the Boltzmann constant k_B , since $a_{\text{RMS}}^2 = k_B T / (m\omega^2)$ when the ion velocity is well described by a Maxwell-Boltzmann distribution. If all three axes of motion have the same temperature, $\langle E^2(t) \rangle = 3k_B T \omega^2 m / q^2$. The Stark shift due to this ion motion is then given by [Dub+13]

$$\Delta\nu_{\text{Stark}} = -\frac{3}{2} k_B T \Delta\alpha(\omega) \frac{m\omega^2}{q^2}. \quad (6.21)$$

An important point is that $\Delta\alpha(\omega)$ is the combination of the scalar $\Delta\alpha_S$, vectorial $\Delta\alpha_V$ and tensorial $\Delta\alpha_T$ dynamic differential polarizability at the angular frequency ω , and thus depends on the direction of the magnetic field. The vectorial shifts are averaged to zero by interrogating positive and negative Zeeman states (the same way as linear Zeeman shifts) and the tensorial shifts are averaged to zero by interrogating states with different m_j^2 as described in Section 6.1. Consequently, only $\Delta\alpha_S(\omega)$ remains and since the motion of the ion is determined by RF fields, $\Delta\alpha_S(\omega) \approx \Delta\alpha_{\text{dc}}$.

Doppler effect If the ion moves with the velocity \vec{v} with respect to a laser beam propagating along the direction \vec{k} , the frequency of the laser is shifted by [HMS79]

6. $^{88}\text{Sr}^+ / ^{171}\text{Yb}^+$ E3 frequency ratio measurement

$$\frac{\Delta\nu_D}{\nu_0} = 1 - \frac{1 - \beta \cos(\theta)}{\sqrt{1 - \beta^2}} = \cos(\theta)\beta - \frac{1}{2}\beta^2 \quad (6.22)$$

$$+ \frac{1}{2} \cos(\theta)\beta^3 - \frac{3}{8}\beta^4 + O(\beta^5), \quad (6.23)$$

with $\beta = |\vec{v}|/c$ and $\theta = \angle(\vec{v}, \vec{k})$. Since the ion is confined within the Lamb-Dicke regime [Dic53] and interrogated over many cycles of its motion [Fis97; Cho+10], all terms of $\Delta\nu_D$ proportional to $\cos(\theta)$ average to zero and the remaining Doppler shift is

$$\left\langle \frac{\Delta\nu_D}{\nu_0} \right\rangle = -\frac{1}{2} \frac{\langle |\vec{v}|^2 \rangle}{c^2} - \frac{3}{8} \frac{\langle |\vec{v}|^4 \rangle}{c^4} + O\left(\frac{\langle |\vec{v}|^6 \rangle}{c^6}\right). \quad (6.24)$$

The terms proportional to β^4 and higher are disregarded due to their small magnitude. The motional sidebands of the ion can additionally lead to a line-pulling effect that disturbs the center frequency, but this effect is usually small in optical clocks with well-separated sidebands [LME07].

If the motion is thermal at a temperature T , the Doppler shift can be specified more explicitly, since $\langle v^2 \rangle = k_B T/m$ per motional degree of freedom. Then the Doppler shift for motion in 3D at a temperature T is

$$\left\langle \frac{\Delta\nu_D}{\nu_0} \right\rangle \approx -\frac{3k_B T}{2mc^2}. \quad (6.25)$$

If on the other hand the motion is due to an oscillation with RMS amplitude a_{RMS} and angular frequency ω , the Doppler shift is equal to

$$\left\langle \frac{\Delta\nu_D}{\nu_0} \right\rangle \approx -\frac{a_{\text{RMS}}^2 \omega^2}{2c^2}. \quad (6.26)$$

Total motional shift The Doppler and Stark shift due to ion motion are not independent of each other, since they have the same source: the motion of the ion itself. For this reason, it makes sense to combine them and potentially profit from cancellation effects, e.g. the magic frequency discussed in Section 4.1. For oscillatory motion along one axis with RMS amplitude a_{RMS} and angular frequency ω , the combined Stark and Doppler shift is [Dub+13]

$$\left\langle \frac{\Delta\nu_M}{\nu_0} \right\rangle = \left\langle \frac{\Delta\nu_D + \Delta\nu_{\text{Stark}}}{\nu_0} \right\rangle = -\frac{a_{\text{RMS}}^2 \omega^2}{2c^2} \left(1 + \frac{m^2 c^2 \omega^2 \Delta\alpha_{\text{dc}}}{q^2 h\nu_0} \right). \quad (6.27)$$

If the motion is thermal with temperature T , the combined motional shift is

$$\left\langle \frac{\Delta\nu_M}{\nu_0} \right\rangle = \left\langle \frac{\Delta\nu_D + \Delta\nu_{\text{Stark}}}{\nu_0} \right\rangle = -\frac{k_B T}{2mc^2} \left(1 + \frac{m^2 c^2 \omega^2 \Delta\alpha_{\text{dc}}}{q^2 h\nu_0} \right). \quad (6.28)$$

These relations describe frequency shifts due to intrinsic micromotion ($\Delta\nu_{M,\text{int}}$), excess micromotion ($\Delta\nu_{M,\text{exc}}$) and secular motion ($\Delta\nu_{M,\text{sec}}$) along the radial axes of the ion trap. The axial motion, on the other hand, does not have an intrinsic micromotion component in a linear trap, since the confinement is due to a static potential. This results in the following total motional shift

$$\left\langle \frac{\Delta\nu_{M,\text{total}}}{\nu_0} \right\rangle = \sum_{x,y} \left\langle \frac{\Delta\nu_{M,\text{int}}}{\nu_0} \right\rangle + \sum_{x,y,z} \left(\left\langle \frac{\Delta\nu_{M,\text{exc}}}{\nu_0} \right\rangle + \left\langle \frac{\Delta\nu_{M,\text{sec}}}{\nu_0} \right\rangle \right), \quad (6.29)$$

which can be rewritten as

$$\left\langle \frac{\Delta\nu_{M,\text{total}}}{\nu_0} \right\rangle = -\frac{k_B}{2mc^2} \left(2(T_x + T_y) + T_z \right) \quad (6.30)$$

$$+ \frac{m^2 c^2 \Omega^2 \Delta\alpha_{\text{dc}}}{q^2 h\nu_0} \left(T_x \left(1 + 2\frac{\omega_x^2}{\Omega^2} \right) + T_y \left(1 + 2\frac{\omega_y^2}{\Omega^2} \right) + T_z \frac{\omega_z^2}{\Omega^2} \right) \quad (6.31)$$

$$+ \sum_{x,y,z} \left\langle \frac{\Delta\nu_{M,\text{exc}}}{\nu_0} \right\rangle, \quad (6.32)$$

with the temperatures (T_x, T_y, T_z) and angular secular frequencies ($\omega_x, \omega_y, \omega_z$) along the three axes of motion as well as the trap RF angular frequency Ω . Since $\omega/\Omega \approx 0.1$, the Stark shifts due to secular motion are suppressed by a factor of 100 compared to the Stark shifts due to micromotion and often ignored [Dub+13]. The temperatures of the ion along the three axes including motional heating during the clock pulse are (T_x, T_y, T_z) = (0.5(1), 2.0(3), 2.5(4)) mK, leading to a fractional thermal motional shift of $-3.01(31) \times 10^{-18}$.

A mean squared electric field $\langle E^2 \rangle$ the ion experiences due to excess micromotion can be related to Eq. (6.27) with $a_{\text{RMS}}^2 = q^2/m^2/\Omega^4 \langle E^2 \rangle$. This results in the total excess micromotion shift

$$\sum_{x,y,z} \left\langle \frac{\Delta\nu_{M,\text{exc}}}{\nu_0} \right\rangle = -\frac{q^2}{2m^2 c^2 \Omega^2} \left(1 + \frac{m^2 c^2 \Omega^2 \Delta\alpha_{\text{dc}}}{q^2 h\nu_0} \right) \left(\langle E_x^2 \rangle + \langle E_y^2 \rangle + \langle E_z^2 \rangle \right). \quad (6.33)$$

Equation (6.33) implies that the excess micromotion has to be measured along all three directions of motion to accurately correct for it. Equation (6.27) shows that

6. $^{88}\text{Sr}^+ / ^{171}\text{Yb}^+$ E3 frequency ratio measurement

all shifts due to an oscillation at angular frequency ω are suppressed if [Ber+98; Dub+14]

$$\Omega^2 = -\frac{q^2}{m^2 c^2} \frac{h\nu_0}{\Delta\alpha_{\text{dc}}}, \quad (6.34)$$

in which case Ω is called the magic frequency as discussed in Section 4.1. Typically, intrinsic and excess micromotion shifts are suppressed this way (if possible), since Stark shifts due to secular motion are small anyway. Excess micromotion is determined with the photon-correlation method discussed in Section 2.2 and [Kel+15]. $\langle E^2 \rangle$ is minimized by applying DC electric fields to the ion to move it to the trap center. In a linear trap, this allows for zeroing $\langle E_x^2 \rangle$ and $\langle E_y^2 \rangle$, but the component along the trap axis $\langle E_z^2 \rangle$ cannot be influenced. In this trap, for the lowest trap depth employed (+0 dB) the axial RMS electric field due to excess micromotion is $\sqrt{\langle E_z^2 \rangle} = 320(70)$ V/m at an RF frequency of 13.28 MHz, leading to a fractional shift of $-15.1(6.6) \times 10^{-18}$. A different RF frequency of 12.8 MHz was employed as well for some part of the data, leading to a different micromotion shift. This is also the case for larger RF powers, since $\langle E_z^2 \rangle \sim P_{\text{RF}}$, so all data are corrected for their excess micromotion shift by different amounts.

Collisional shift Collisions of the background gas with the single trapped ion cause frequency shifts in two ways [Han+19a]. On the one hand, a collision imparts kinetic energy onto the ion without disturbing the coherence of the ion with respect to the laser directly. This effectively increases the Doppler shift due to thermal motion of the ion for a single cycle and is called the *time-dilation component* [Han+19a]. On the other hand, a Langevin spiraling collision completely dephases the ion with respect to the laser, causing a $\pi/2$ phase shift in the worst case. Due to the high mass of $^{88}\text{Sr}^+$ compared to hydrogen, the dominant component of the background gas, the Langevin collisions dominate the collisional shift estimate. Since the presence of the ion in the trap after spectroscopy is checked before using the frequency information for the servo, collisions that heat the ion so much that it is in a high motional state are discarded. This further reduces the collisional shift. With the background pressure of 6.2 nPa determined in Section 3.6 and the shift coefficient $\Delta\nu_{\text{coll}} = 80$ kHz/Pa [Mad+04] the maximum fractional shift is 1.1×10^{-18} , which I take as the full uncertainty.

Servo error Usually, the angular laser frequency ω_L drifts during the interrogation of the clock transition, leading to an offset between ω_L and ω_0 of

$$\Delta\omega_L(t) = \omega_L(t) - \omega_0 = \Delta\omega_L(0) + \alpha \times t, \quad (6.35)$$

where α is the drift rate of the laser. Since the clock transition has to be interrogated multiple times (four times in this work) before an error signal is generated and the

clock laser frequency corrected, the laser drift causes an offset of the frequency the clock produces from its unperturbed reference value [PST05]. A review on drift and noise induced servo errors is found in [Lin+23].

In the case of the Sr clock laser, it is directly phase-locked to the E3 clock laser steered by the optical clock Yb1 as described in Section 3.7. This clock utilizes a second-order integrating servo to correct for the laser drift, producing a linearly drift-free laser frequency ($\alpha=0/(ss)$). For this reason, the servo error due to laser drift is equal to zero for sufficiently long averaging times. Magnetic field and tensor shift drifts, on the other hand, affect the frequency of each individual interrogated transition in a similiar way to a drifting clock laser. To limit the effect of these drifts, the transitions $\nu_{m_S}^{m_D}$ are interrogated in the following order

$$\nu_{-1/2}^{-5/2} \rightarrow \nu_{-1/2}^{-3/2} \rightarrow \nu_{+1/2}^{+3/2} \rightarrow \nu_{+1/2}^{+5/2} \rightarrow \nu_{+1/2}^{+3/2} \rightarrow \nu_{-1/2}^{-3/2} \quad (6.36)$$

$$\rightarrow \nu_{-1/2}^{-3/2} \rightarrow \nu_{+1/2}^{+3/2} \rightarrow \nu_{+1/2}^{+5/2} \rightarrow \nu_{+1/2}^{+3/2} \rightarrow \nu_{-1/2}^{-3/2} \rightarrow \nu_{-1/2}^{-5/2}, \quad (6.37)$$

which reduces the servo error due to cancellations of linear perturbations. The residual servo error is determined with a Monte-Carlo simulation of the servo algorithm with a magnetic field drift rate of 51 pT/h and tensor shift drift rate of 28 mHz/h, which is the upper limit of the drift rates from available data. No significant frequency offset is found with a fractional uncertainty of 0.70×10^{-18} .

Acousto-optic modulator chirp Within the clock interrogation sequence, the clock laser beam intensity is changed by adjusting the RF power of an AOM on the ion trap table. RF losses within the AOM cause a temperature increase of the crystal, which lengthens it. This length change causes a first order Doppler shift in the clock laser beam, changing its frequency with respect to the unperturbed transition in the ion [Kaz+16]. Phase differences $\Delta\phi$ due to the Doppler shift are investigated directly in [Kaz+16] and $\Delta\phi=9$ mrad, 2 mrad are found for 1 W of RF power and $t_W=2$ ms or $t_W=0.5$ ms waiting time, respectively, with a minimum cycle time of 30 ms. Then, the expected phase error $\Delta\phi$ for a clock pulse with time t and a total cycle time t_0 at an RF power P is

$$\Delta\phi = \frac{P}{1 \text{ W}} \frac{9 \text{ mrad} - 2 \text{ mrad}}{2 \text{ ms} - 0.5 \text{ ms}} \frac{30 \text{ ms}}{t_0} \times \min(t, t_0 - t). \quad (6.38)$$

The maximum effect in the clock sequence of this measurement occurs for $P=5$ mW, $t=35$ ms, $t_0=55$ ms and results in $\Delta\phi=0.31$ mrad. For the Sr clock laser at a frequency of 445 THz, this corresponds to a fractional shift of $\Delta\nu/\nu_0 = \Delta\phi/\pi \times 1 \text{ Hz}/\nu_0 = 0.22 \times 10^{-18}$. Additionally, the undiffracted beam transmitted through the AOM is path-length-stabilized with a bandwidth of 10 kHz, primarily to mitigate path-length fluctuations of the fiber connecting the clock laser setup

6. $^{88}\text{Sr}^+ / ^{171}\text{Yb}^+$ E3 frequency ratio measurement

with the ion trap. Since the temperature-change induced phase errors are common mode to the diffracted and undiffracted beam to first order, a large suppression of the AOM chirp is expected, further reducing the effect on the clock laser frequency. All in all, a fractional uncertainty of the clock of 0.10×10^{-18} is assumed due to AOM chirps.

Second-order Zeeman shift The quadratic Zeeman shift due to the magnetic field \vec{B} is caused by magnetic field-induced mixing of the $^2D_{5/2}$ and $^2D_{3/2}$ states with the transition frequency of the corresponding M1 transition of $\nu_{DD} = 8.404\,382$ THz [Dub+13]. Independent of the averaging scheme employed, the center frequency free of linear Zeeman and tensorial shifts is offset from its unperturbed value by [Dub+13]

$$\Delta\nu_{\text{Zeeman, Quadratic}} = \frac{2}{15} \left(\frac{\mu_B}{h} |\vec{B}| \right)^2 \frac{(g_e - 1)^2}{\nu_{DD}}. \quad (6.39)$$

During this measurement a static field of $4.48 \mu\text{T}$ is applied to define a quantization axis, which causes a fractional frequency shift of $0.1409(3) \times 10^{-18}$. Additionally, the magnetic component of the BBR field causes a fractional frequency shift of $0.0519(7) \times 10^{-18}$ [Dub+13]. The fractional third order-shift is expected to be on the order of 10^{-26} from the relative scaling of the linear and quadratic shift and negligible. The AC Zeeman shift due to currents induced by the trap drive causes a fractional shift of $7.67(70) \times 10^{-21}$ as discussed in Section 3.5, negligible compared to other systematic shifts.

6.3. Frequency instability and multi-ion operation

The frequency offset between the Sr clock laser and the optical transition is adjusted based on the weighted average of all interrogated transition frequencies. This allows for the determination of the optical frequency ratio $\mathcal{R}(t) = \nu_{\text{Sr}^+}(t) / \nu_{\text{E3}}(t)$ between the $^{88}\text{Sr}^+$ clock and the $^{171}\text{Yb}^+$ E3 clock Yb1 [San+19]. Due to the comparatively small signal-to-noise ratio of single-ion clocks, $\mathcal{R}(t)$ is dominated by QPN, so averaging of $\mathcal{R}(t)$ over time is necessary to reduce its statistical uncertainty u_{stat} . The Allan deviation $\sigma_y(\tau)$ of $\mathcal{R}(t)$ discussed in Section 1.1 after averaging time τ determines u_{stat} and follows the white noise scaling $\sigma_y(\tau) \sim 1/\sqrt{\tau}$ for $\tau > 100$ s as shown in Fig. 6.3. For shorter times the instability is below the QPN limit, because the Sr clock laser is phase-locked to the E3 clock laser with low instability essentially given by the Si resonator [Mat+17].

If the noise sources are known, the expected instability can be estimated by a Monte-Carlo estimation of the servo algorithm. This produces an instability of $\sigma_y(t) = 4.8 \times 10^{-15} / \sqrt{\tau/\text{s}}$ for the $^{88}\text{Sr}^+$ frequency ν_{Sr} , in agreement with the data.

This confirms that the clock is limited by QPN from the interrogation time of the individual transitions, limited by magnetic field noise.

The system is also operated with three $^{88}\text{Sr}^+$ ions simultaneously, which all produce an error signal for the clock servo. This increases the signal-to-noise ratio and can reduce the instability of the clock frequency by up to a factor $\sqrt{3}$. Due to the position along the trap axis and the presence of other ions, the electric field gradient is different for each ion, causing variations in the quadrupole shift [Kel+19]. Since only a single beam interrogates all ions simultaneously, these frequency shifts need to be minimized as much as possible to not observe broadening of the excitation spectrum. This is achieved by setting the quantization axis at the magic angle of $54.7(4)^\circ$ with respect to the trap axis, where any shift due to an axial field gradient is minimized. Additionally, the cooling and detection time of the overall excitation of the crystal are increased to 15 ms to distinguish between all four excitation states (0-3 ions dark) reliably with the spatially integrating PMT.

Running the clock with these settings reduces the instability to $\sigma_y(\tau) = 3.3 \times 10^{-15} / \sqrt{\tau/\text{s}}$, consistent with a Monte-Carlo simulation of the servo algorithm, taking the additional delay due to cooling and detection into account. This was the first direct observation of instability reduction by interrogating multiple ions in a linear trap to my knowledge. Additionally, the observed frequency ratio with three ions is consistent with the single-ion ratio up to a fractional difference of $27(33) \times 10^{-18}$, consistent with zero. This supports the assumption that no unrecognized frequency shift changes the frequency of the multi-ion clock by a significant amount.

6. $^{88}\text{Sr}^+ / ^{171}\text{Yb}^+$ E3 frequency ratio measurement

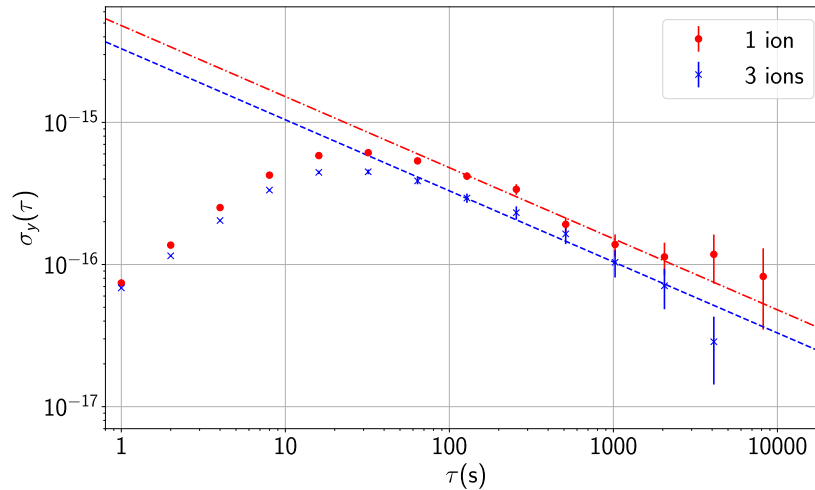


Figure 6.3.: Allan deviation of Sr/E3 frequency ratio. The Allan deviation of the optical frequency ratio $\mathcal{R}(t) = \nu_{\text{Sr}^+}(t) / \nu_{\text{E3}}(t)$ is dominated by the instability of the $^{88}\text{Sr}^+$ clock, since $\sigma_y(1\text{ s}) = 1 \times 10^{-15}$ for the E3 reference clock [Dör+21]. For averaging times below 100 s, the instability is below the QPN limit, because the respective clock lasers are phase-locked to each other and referenced to the Si resonator [Mat+17]. From an averaging time of 100 s onwards, the instability follows the expected white-noise behaviour consistent with QPN at an instability of $\sigma_y(t) = 4.8 \times 10^{-15} / \sqrt{\tau/\text{s}}$. This value is determined independent from the data with a Monte-Carlo simulation of the servo algorithm, shown as a dashed-dotted line. The instability reduces to $\sigma_y(t) = 3.3 \times 10^{-15} / \sqrt{\tau/\text{s}}$ when interrogating three $^{88}\text{Sr}^+$ ions, consistent with the servo algorithm simulation when the additional dead time during cooling and state detection is taken into account.

6.4. Frequency ratio measurement and absolute frequency determination

By operating the $^{88}\text{Sr}^+$ $S_{1/2} \rightarrow D_{5/2}$ and $^{171}\text{Yb}^+$ E3 $S_{1/2}(F=0) \rightarrow F_{7/2}(F=3)$ single-ion clock in between October 2021 and July 2022, the optical frequency ratio $\mathcal{R} = \nu_{\text{Sr}^+} / \nu_{\text{E3}}$ is determined at three different RF power settings and is shown in Fig. 6.4. The systematic frequency offsets from the unperturbed reference are determined separately for each measurement run and are corrected for. The statistical uncertainty is determined from the Allan deviation extrapolated to the total measurement time under the assumption of white frequency noise. All data are consistent with a single mean value $\overline{\mathcal{R}} = 0.692\,671\,163\,215\,966\,061(16)$ where the fractional total uncertainty of 23×10^{-18} consists of a statistical uncertainty of 9.8×10^{-18} and a systematic uncertainty of 20.5×10^{-18} . The systematic uncertainty is larger than the minimum in Table 6.1, because the BBR shift and micromotion shift uncertainties increase with the RF trap power. This is the

6.4. Frequency ratio measurement and absolute frequency determination

first determination of this optical frequency ratio and it has a total uncertainty about a factor of 5 smaller than the best systematic uncertainties of primary Cs standards [Szy+16; Wey+18; Hot+23; Bea+25]. After publication of [Ste+23], an international clock comparison campaign allowed for determination of the optical frequency ratio \mathcal{R}_{VTT} between the VTT $^{88}\text{Sr}^+$ clock and Yb1 at PTB via a Global Navigation Satellite System (GNSS) link [Lin+25c]. The fractional difference in the optical frequency ratio $\Delta\mathcal{R}/\bar{\mathcal{R}} = 1 - \mathcal{R}_{\text{VTT}}/\bar{\mathcal{R}} = 0.05(12) \times 10^{-15}$ is consistent with zero [Lin+25c], further supporting the performance of $^{88}\text{Sr}^+$ as an optical frequency standard. The increased uncertainty compared to the systematic uncertainty of both ion clocks is due to the GNSS link uncertainty.

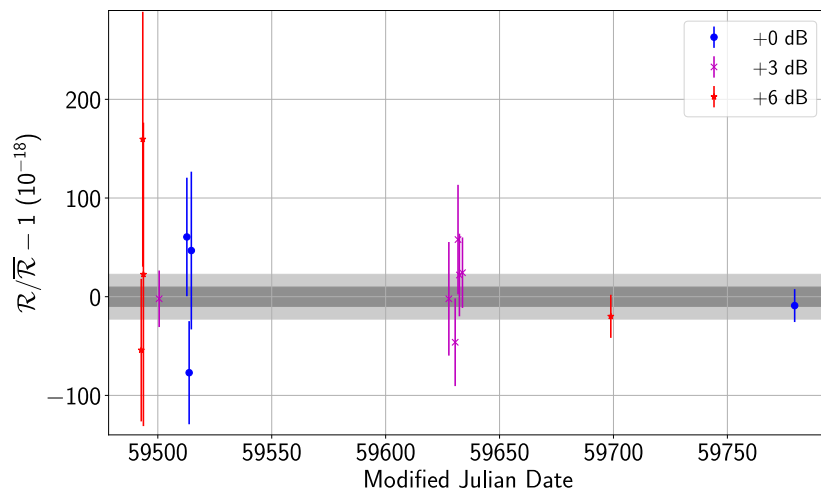


Figure 6.4.: *Frequency ratio measurement.* The frequency ratio $\mathcal{R} = \nu_{\text{Sr}^+} / \nu_{\text{E3}}$ is shown as a fractional deviation from its mean value $\bar{\mathcal{R}}$ for various measurement intervals between October 2021 and July 2022. The measurement is carried out at three different RF trap settings to determine the effective temperature increase of the ion trap above the laboratory temperature. All data are consistent with a single mean value with the statistical uncertainty shown in dark gray and a total uncertainty shown in light gray.

Since both ion traps are situated in Earth’s gravitational potential Φ at different positions, there exists a gravitational redshift between them, which affects \mathcal{R} [Ein16; Tak+16; Tak+20]. Since the clocks are set up in the same laboratory space, the primary difference in Φ is due to the height difference Δh between the ions. This causes a gravitational redshift [Ein16]

$$\frac{\Delta\nu_{\text{grav}}}{\nu_0} = \frac{g\Delta h}{c^2}, \quad (6.40)$$

where g is the local gravitational acceleration. An absolute value of g is determined by a measurement with a gravimeter on PTB campus and geometric levelling

6. $^{88}\text{Sr}^+ / ^{171}\text{Yb}^+$ E3 frequency ratio measurement

from the measurement point to a reference position in the clock laboratory. The result is that $g = 9.725(4) \text{ m/s}^2$ in the clock laboratory. A review of geodetic methods to determine gravitational redshifts for clocks is found in [Den+18]. Δh is measured via geometric levelling between the optical tables and an estimate of the ion position relative to the optical table by a laser beam that is focussed onto the respective ion. This results in $\Delta h = h_{\text{Sr}^+} - h_{\text{E3}} = 0.121(3) \text{ m}$ and a fractional gravitational redshift of $-13.16(33) \times 10^{-18}$. The value of $\overline{\mathcal{R}}$ already takes this correction into account.

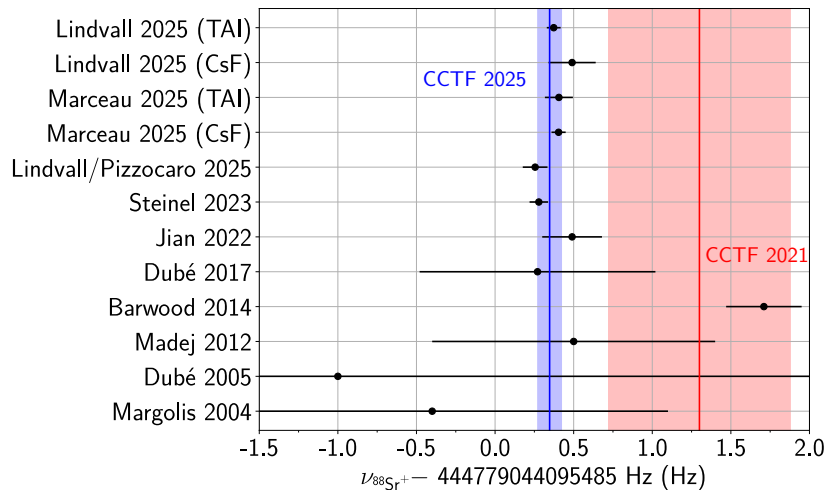


Figure 6.5.: Absolute frequency of the $^{88}\text{Sr}^+$ clock transition. The determination of the absolute frequency of the $^{88}\text{Sr}^+$ clock transition by various research institutions over time is shown. [Dub+05; Mad+12; DBG17; Jia+22; Mar+25a] were performed at NRC [Mar+04; Bar+14] at NPL and [Lin+25a; Lin+25a] at VTT. Additionally, after publication of [Ste+23] an additional frequency ratio measurement between the $^{88}\text{Sr}^+$ clock of VTT and the same $^{171}\text{Yb}^+$ E3 clock of PTB Yb1 was published via a GNSS link in an international clock comparison campaign [Lin+25c]. Both this value and the one presented in this thesis [Ste+23] are the absolute frequency derived from the optical frequency ratio and the $^{171}\text{Yb}^+$ E3 frequency [Lan+21a]. New measurements from NRC [Mar+25a] and VTT [Lin+25a] with reduced uncertainty against both a local Cs clock and the Temps Atomique International (TAI) ensemble were also published recently. All data except for [Bar+14] are consistent within 2σ , while the latter point shows a significant deviation. It heavily influences the current recommended frequency of the $^{88}\text{Sr}^+$ clock transition as a secondary representation of the second (CCTF 2021) depicted as a red line with the red shading being its uncertainty [Mar+24]. A new evaluation of the recommended frequency was presented recently (CCTF 2025) and is shown as a blue line with its uncertainty shaded in blue [CCT25]. It agrees with the recent determinations of the $^{88}\text{Sr}^+$ clock transition frequency and has the same fractional uncertainty of 0.17×10^{-15} as the other optical standards limited by Cs clocks.

To compare the result with values already measured in other works, $\overline{\mathcal{R}}$ is multiplied with the E3 absolute frequency $\nu_{\text{E3}} = 642\,121\,496\,772\,645.10(8)$ Hz [Lan+21a] to determine the absolute frequency of the $^{88}\text{Sr}^+$ clock transition $\nu_{\text{Sr}^+} = 444\,779\,044\,095\,485.278(59)$ Hz. The uncertainty of ν_{Sr^+} is limited by the systematic uncertainty of the Cs fountain clock against which ν_{E3} is measured [Wey+18; Lan+21a]. The value is shown in Fig. 6.5 together with determinations of the same quantity by NPL, NRC and VTT [Mar+04; Dub+05; Mad+12; Bar+14; DBG17; Jia+22; Lin+25c; Mar+25a; Lin+25a].

ν_{Sr^+} is consistent with all but one ([Bar+14]) previous measurements and has a reduced uncertainty by a factor of 3 compared to the previous record [Jia+22]. A new measurement from NRC against a local Cs clock with further reduced uncertainty was published recently [Mar+25a] and is offset from ν_{Sr^+} by 0.126(74) Hz, a significance of 1.7σ . Similarly, a recent measurement from VTT against the TAI ensemble results in an offset from ν_{Sr^+} of 0.095(74) Hz, a significance of 1.3σ . These measurements produce the most accurate absolute frequencies to date. Since these offsets are very similar for the value of ν_{Sr^+} derived from the optical ratio in [Lin+25c] using [Lan+21a] as a reference for the $^{171}\text{Yb}^+$ absolute frequency ν_{E3} , it is likely that ν_{E3} is the source of this slight disagreement. Importantly, the recommended frequency as a secondary representation of the second [Mar+24] is not consistent with all determinations from 2022 onwards [Jia+22; Ste+23; Lin+25c; Mar+25a; Lin+25a]. This is because the value in [Mar+24] is heavily influenced by the inconsistent value from [Bar+14]. A new evaluation of the recommended frequency by the Consultative Committee for Time and Frequency (CCTF) was presented recently [CCT25] with the value $\nu_{\text{Sr}^+} = 444\,779\,044\,095\,485.347(76)$ Hz, consistent with all recent determinations of this quantity. This shows that measurements of clock frequencies by multiple entities are important to check potential inconsistencies, particularly if an optical standard is supposed to replace Cs as the primary frequency reference [Dim+24].

Conclusion Operation of YbSr1 as a single-ion optical frequency standard in combination with a novel method to determine the trap-induced BBR shift allows for the first determination of an optical frequency ratio \mathcal{R} with a $^{88}\text{Sr}^+$ clock. The total uncertainty of \mathcal{R} between the $^{88}\text{Sr}^+$ clock transition and the $^{171}\text{Yb}^+$ clock transition of 23×10^{-18} is significantly smaller than the systematic uncertainty of the best Cs clocks [Szy+16; Wey+18; Hot+23; Bea+25]. The absolute frequency calculated from \mathcal{R} and ν_{E3} [Lan+21a] supports a readjustment of the recommended value for ν_{Sr^+} together with other recent determinations of this quantity [Jia+22; Lin+25c; Mar+25a]. Additionally, multi-ion operation of the clock with three $^{88}\text{Sr}^+$ ions shows a reduction of the clock instability consistent with the expectation from servo simulations, a key feature of multi-ion clocks.

An ion trap with reduced axial micromotion and better thermal conductivity is a straight-forward path towards a $^{88}\text{Sr}^+$ clock with smaller systematic uncertainty.

6. $^{88}\text{Sr}^+ / ^{171}\text{Yb}^+$ E3 frequency ratio measurement

YbSr2, a second-generation apparatus, fulfills these requirements and is currently being evaluated. Axial micromotion is reduced to below 100 V/m at sufficiently high trapping depths and the resonator is modified such that operation at the magic frequency is possible. The trap is the version presented in [Nor+20] with similar heating of the trap body. All in all, this positions *YbSr2* as a $^{88}\text{Sr}^+$ clock with an uncertainty in the mid 10^{-19} regime. Also, up to 10 ions are already interrogated simultaneously with a significant reduction in the instability. This shows that $^{88}\text{Sr}^+$ is a serious contender for the redefinition of the second based on an optical transition [Dim+24].

7. Summary and outlook

This thesis reports on the setup, operation and evaluation of the first multi-ion, multi-species optical clock *YbSr1* in the group *Optical clocks based on trapped ions* at PTB. It employs the E2 $^2S_{1/2}(F=0) \rightarrow ^2D_{3/2}(F=2)$ and $^2S_{1/2}(F=0) \rightarrow ^2F_{7/2}(F=3)$ E3 transitions of $^{171}\text{Yb}^+$ and the $^2S_{1/2} \rightarrow ^2D_{5/2}$ E2 transition of $^{88}\text{Sr}^+$. Measurements on the $^{88}\text{Sr}^+$ clock transition allow for more accurate determinations of systematic frequency shifts on the $^{171}\text{Yb}^+$ clock transitions and it is also operated as an optical clock on its own.

7.1. Polarizability ratio measurement and BBR shift uncertainty reduction

Quadratic Stark shifts on the clock transitions are a key effect investigated in this thesis. They limit the fractional uncertainty of the $^{171}\text{Yb}^+$ E2 and E3 clocks operating at room temperature to 28×10^{-18} and 1.5×10^{-18} , respectively, due to the Stark shift induced by BBR Eq. (4.25). $\Delta\alpha_{\text{dc}}$ is determined from optical power measurements of infrared laser radiation with a fractional uncertainty of approximately 2% [Hun+16; Bay+20], which limits the uncertainty of the clocks even if T is known with low uncertainty. For $^{88}\text{Sr}^+$ $\Delta\alpha_{\text{dc}}$ is known with a fractional uncertainty of 0.04% [Dub+14; Lin+25b], which allows for operation of an optical clock based on this transition at room temperature with a fractional frequency uncertainty below 1×10^{-18} .

The scalar quadratic Stark shift $\Delta\nu_{\text{Stark}}$ due to a laser with center wavelength λ and intensity $I(\lambda)$ also is related to the scalar differential polarizability $\Delta\alpha_S(\lambda)$ Eq. (5.8). At a wavelength of $10.6 \mu\text{m}$, close to the maximum spectral energy density for room temperature BBR, the fractional difference between $\Delta\alpha_S(10.6 \mu\text{m})$ and $\Delta\alpha_{\text{dc}}$ is smaller than 1% for the $^{88}\text{Sr}^+$ clock transition. This means that measuring the $^{88}\text{Sr}^+$ frequency shift induced by a CO_2 laser allows one to determine $I(10.6 \mu\text{m})$ with small uncertainty. Consequently, by measuring the light shift on the $^{171}\text{Yb}^+$ clock transitions perturbed by the calibrated laser intensity, $\Delta\alpha_S(10.6 \mu\text{m})$ is determined with an uncertainty ultimately limited by the knowledge of the $^{88}\text{Sr}^+$ polarizability. This method was first proposed in [BAS19] and employed in [Wei+24] for measuring the differential polarizability of the Al^+ clock transition at a perturbing wavelength of 1068 nm . Due to the large polarizability difference

7. Summary and outlook

between $\Delta\alpha_{\text{dc}}$ and $\Delta\alpha_S(1068\text{ nm})$ for the clock transition of Ca^+ , the measurement uncertainty is limited to a fractional value of 2.9 %.

In contrast, here the difference is smaller and in addition is confirmed from a measurement of the magic wavelength at 1538.75(10) nm consistent with the theoretical prediction while reducing the uncertainty by a factor 150 [Bar+22]. This enables polarizability ratio measurements with negligible additional uncertainty due to the extrapolation from $\Delta\alpha_{\text{dc}}$ to $\Delta\alpha_S(10.6\text{ }\mu\text{m})$. Such a polarizability ratio measurement is performed between the E2 transitions of $^{88}\text{Sr}^+$ and $^{171}\text{Yb}^+$ to a fractional uncertainty of 0.13 %, limited by statistical uncertainty and with significantly reduced uncertainty compared to previous determinations [SPT05; Bay+20]. With separate polarizability ratio measurements between the $^{171}\text{Yb}^+$ E2 and E3 transitions, $\Delta\alpha_S(10.6\text{ }\mu\text{m})$ for the E3 clock is determined with a fractional uncertainty of 0.33 %, limited by the measurement of the tensorial polarizability contribution. This is also a significant reduction of the uncertainty for this quantity [Hun+16; Bay+20] and allows for operation of the E2 and E3 clock at room temperature with a fractional uncertainty of 0.84×10^{-18} and 0.24×10^{-18} , respectively. This allows for a total fractional uncertainty of both $^{171}\text{Yb}^+$ clock transitions below 1×10^{-18} . But the values of $\Delta\alpha_S$ for the $^{171}\text{Yb}^+$ clock transitions determined with reference to the $^{88}\text{Sr}^+$ polarizability differ by a fractional value of approximately 14 % from the values determined in [Hun+16; Bay+20]. This changes the BBR shift by $-99(28) \times 10^{-18}$ and $-11.9(1.5) \times 10^{-18}$ compared to the determination in [Bay+20] for the E2 and E3 transition, respectively, if the new value for $\Delta\alpha_S$ is adopted. To summarize, if the optical intensity measurements are employed for the BBR shift correction at a temperature of 300 K, then

$$\frac{\Delta\nu_{\text{BBR}}^{\text{Sr}}}{\nu^{\text{Sr}}} = 486.9(8.3) \times 10^{-18} \quad (7.1)$$

$$\frac{\Delta\nu_{\text{BBR}}^{\text{E2}}}{\nu^{\text{E2}}} = -525.0(9.0) \times 10^{-18} \quad (7.2)$$

$$\frac{\Delta\nu_{\text{BBR}}^{\text{E3}}}{\nu^{\text{E3}}} = -70.7(1.2) \times 10^{-18}, \quad (7.3)$$

while the magic-RF-based measurements result in

$$\frac{\Delta\nu_{\text{BBR}}^{\text{Sr}}}{\nu^{\text{Sr}}} = 562.06(42) \times 10^{-18} \quad (7.4)$$

$$\frac{\Delta\nu_{\text{BBR}}^{\text{E2}}}{\nu^{\text{E2}}} = -606.11(84) \times 10^{-18} \quad (7.5)$$

$$\frac{\Delta\nu_{\text{BBR}}^{\text{E3}}}{\nu^{\text{E3}}} = -81.59(24) \times 10^{-18}. \quad (7.6)$$

These uncertainties can be reduced further by accumulating more measurement time and by minimizing the tensorial contribution to the overall Stark shift at the

magic angle of the magnetic field direction with respect to the laser polarization vector. Since the tensor shift is also more sensitive to temporal and spatial magnetic field gradients at the magic angle, this requires an investigation of the magnetic field differences between the $^{88}\text{Sr}^+$ and $^{171}\text{Yb}^+$ clock transition interrogation time with higher accuracy to measure $\Delta\alpha_S$ with a fractional uncertainty significantly below 0.04%. This then allows for $^{171}\text{Yb}^+$ E3 room-temperature clocks with below 1×10^{-19} fractional BBR shift uncertainty, if sufficiently precise temperature measurements are available.

7.2. Comparison between polarizability measurement methods

The values of $\Delta\alpha_S$ for the $^{171}\text{Yb}^+$ clock transitions determined here differ by a fractional value of approximately 14% from the values measured in [Hun+16; Bay+20]. To investigate this offset, $\Delta\alpha_S(10.6\ \mu\text{m})$ is measured independently from the method in [Dub+14; Lin+25b]. Instead, the same method employed in [Hun+16; Bay+20] is used in this thesis. Since the scalar Stark shift $\Delta\nu_{\text{Stark}}$ of the clock transition frequency due to laser radiation with center wavelength λ and intensity $I(\lambda)$ is given by Eq. (5.8), a measurement of $I(\lambda)$ and the light shift corresponding to this intensity allows for a determination of $\Delta\alpha_S(\lambda)$. For a circular Gaussian beam with waist w_0 and optical power P , the time averaged intensity is proportional to P/w_0^2 , which means that both P and w_0 need to be known to with sufficiently low uncertainty to infer $I(\lambda)$. P is determined from optical power measurements with a calibrated photodetector and w_0 is inferred from displacement of the beam over the ion while recording the scalar Stark shift. This way, the peak intensity and peak light shift are measured and used to calculate $\Delta\alpha_S(\lambda)$. For $^{88}\text{Sr}^+$, the value of the differential polarizability shows the same discrepancy from the value determined with RF-induced frequency shifts [Dub+14; Lin+25b] of approximately 14% as observed between the polarizability values on the $^{171}\text{Yb}^+$ clock transitions. This reveals that the discrepancy is sourced in the two different methods to determine $\Delta\alpha_S$, not the ratio measurement. If one takes the average of all light-shift based polarizability values, it is offset from the RF based values by 13.7(1.6) %.

Which of the two methods, if not both of them, has an unrecognized systematic error is currently unknown. Both methods produce internally mostly consistent results between different laboratories, clock transitions, photodetectors, perturbing laser wavelengths and evaluation procedures. This suggests that a common mode effect inherent to the method itself is at fault. To gain more insight, a third independent method to measure $\Delta\alpha_S$ in the MIR wavelength range is advantageous. One such method is to increase or decrease the BBR temperature T of the $^{88}\text{Sr}^+$ optical clock and check, whether the observed BBR shift agrees with either of

7. Summary and outlook

the two polarizability values. Such a measurement was performed between a room-temperature and cryogenic Ca^+ clock in [Hua+24], which shows agreement between the RF based polarizability value and the observed frequency difference between the clocks. This is not feasible in the current setup of YbSr1, since the uncompensable micromotion shift is of similar magnitude as the difference in BBR shift. But the upgraded system YbSr2 with lower micromotion and a more accurate determination of T allows for such a measurement.

In general, reducing the overall BBR shift reduces the sensitivity to the accuracy of the polarizability measurements. This is possible with a cryogenic setup operating at the temperature of liquid nitrogen (77 K) or liquid helium (4.2 K). At these temperatures the BBR shift magnitude is reduced to 4.3×10^{-3} and 38×10^{-9} of its value at 300 K, respectively. In addition, vacuum pressure [Pag+18] and heating rates [Lab+08] are observed to be significantly reduced, which also have to be determined with sufficient precision for optical clocks with a fractional uncertainty below 1×10^{-18} . But these systems require more technical complexity and optical clocks are susceptible to vibrations induced by the cooling systems, so these challenges have to be weighed against the benefit of operating at low temperatures.

7.3. Measurement of the $^{88}\text{Sr}^+ / ^{171}\text{Yb}^+$ E3 optical frequency ratio

$^{88}\text{Sr}^+$ is a recognized frequency standard, listed as a secondary representation of the second by the BIPM [Mar+24]. But no frequency ratio measurements between it and other optical standards were available at the start of the work in this thesis. For this reason, a measurement of the optical frequency ratio between the $^{88}\text{Sr}^+$ clock transition and the $^{171}\text{Yb}^+$ E3 transition is relevant to investigate $^{88}\text{Sr}^+$ as a potential candidate for the redefinition of the second [Dim+24].

The dominant frequency offset from the unperturbed reference is the BBR shift, which requires an accurate knowledge of the effective temperature T at the ion position. It consists of the background temperature T_0 of the laboratory, determined with temperature sensors outside of the vacuum system, and the effective heating δT due to RF losses in the ion trap. Due to the low thermal conductivity of the trap material, temperature measurements on the trap body do not provide a reliable way to measure δT . Instead, the linearity between the RF power P_{RF} and δT is exploited by measuring the frequency difference between the $^{88}\text{Sr}^+$ clock and an unperturbed reference system at different values of P_{RF} . This allows for an extrapolation of the trap-induced BBR shift to $\delta T = 0$ K, where $T = T_0$. The uncertainties with which T and the excess axial micromotion magnitude are determined, dominate the total the systematic uncertainty of the clock, contributing about 10×10^{-18} .

7.3. Measurement of the $^{88}\text{Sr}^+ / ^{171}\text{Yb}^+$ E3 optical frequency ratio

In this way, a measurement of the optical frequency ratio \mathcal{R} between the $^{88}\text{Sr}^+$ and $^{171}\text{Yb}^+$ E3 clock transitions is performed with a total fractional uncertainty of 23×10^{-18} , significantly below the uncertainty of the best primary frequency standards [Szy+16; Wey+18; Hot+23; Bea+25]. This allows determination of the absolute frequency of the $^{88}\text{Sr}^+$ clock transition using the measurement of the E3 frequency in [Lan+21a], limited by the uncertainty of the reference caesium clock [Wey+18]. The value is consistent with all but one previous determinations of the same quantity at a reduced fractional uncertainty of 0.13×10^{-15} [Mar+04; Dub+05; Mad+12; Bar+14; DBG17; Jia+22]. Additional measurements after publication of this result in [Ste+23] with similar or further reduced uncertainty corroborate this value as well [Lin+25c; Mar+25a]. But all recent measurements [Jia+22; Ste+23; Lin+25c; Mar+25a] of the $^{88}\text{Sr}^+$ frequency lie outside of the range of the recommended frequency [Mar+24], which is heavily influenced by the single measurement in [Bar+14] that as now been identified as inconsistent. This suggests an unrecognized systematic shift that affects this value and provides the basis for an adjustment of the recommended frequency. A new evaluation of the recommended frequency by the CCTF was presented recently [CCT25] with the value $\nu_{\text{Sr}^+} = 444\,779\,044\,095\,485.347(76)$ Hz, consistent with all recent determinations of this quantity. This shows the importance of multiple independent measurements of optical frequencies and frequency ratios with small uncertainty.

Additionally, the viability of YbSr1 as a multi-ion clock is also investigated. Three simultaneously interrogated $^{88}\text{Sr}^+$ ions show a reduced instability of the observed frequency ratio consistent with expectation once additional deadtime is taken into account. The optical frequency ratio also shows no significant offset from the single ion result, supporting the assumption that all inhomogeneities are sufficiently well under control at a fractional frequency uncertainty of 33×10^{-18} .

A $^{88}\text{Sr}^+$ clock with better-known temperature T and smaller axial micromotion magnitude allows for systematic uncertainties below 1×10^{-18} using the new differential polarizability value [Lin+25b]. This system already exists and is the second-generation apparatus, *YbSr2*. It is informed by the successes and limitations of YbSr1 and focuses on multi-ion clock operation with up to 10 trapped ions. While it is currently being evaluated, it is likely that the instability reduction scales up to at least 6 ions and its systematic uncertainty is below 1×10^{-18} . Optical frequency ratio measurements against the $^{171}\text{Yb}^+$ E3 clock Yb1 also show no deviations from white noise while resulting in a frequency ratio consistent with the one presented here at a significantly reduced uncertainty. This positions $^{88}\text{Sr}^+$ as a strong contender for the redefinition of the second based on an optical reference transition [Dim+24].

Appendices

A. Legend for optical elements

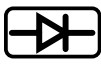
	Fiber coupler		Biconvex lens		Acousto-optic modulator
	Half waveplate		Planoconvex lens		Electro-optic modulator
	Quarter waveplate		Cylindrical planoconvex lens		Optical resonator
	Photodiode		Planoconcave lens		Optical isolator
	Mechanical shutter		Flip mirror		Faraday rotator
	Dichroic mirror		Aperture		Tapered amplifier
	Planar Mirror		Polarizing beamsplitter		
	Window				

Figure A.1.: *The legend for optical elements used in the thesis.*

Bibliography

- [Aep+24] Alexander Aepli et al. “Clock with 8×10^{-19} Systematic Uncertainty.” In: *Phys. Rev. Lett.* 133 (2 July 2024), p. 023401. DOI: 10.1103/PhysRevLett.133.023401. URL: <https://link.aps.org/doi/10.1103/PhysRevLett.133.023401> (cited on page 3).
- [All66] D.W. Allan. “Statistics of atomic frequency standards.” In: *Proceedings of the IEEE* 54.2 (1966), pp. 221–230. DOI: 10.1109/PROC.1966.4634 (cited on page 7).
- [And+23] E. K. Anderson et al. “Observation of the effect of gravity on the motion of antimatter.” en. In: *Nature* 621.7980 (2023), pp. 716–722. ISSN: 1476-4687. DOI: 10.1038/s41586-023-06527-1. URL: <https://www.nature.com/articles/s41586-023-06527-1> (cited on page 18).
- [Arn+18] Kyle J Arnold et al. “Blackbody radiation shift assessment for a lutetium ion clock.” In: *Nature communications* 9.1 (2018), p. 1650. DOI: 10.1038/s41467-018-04079-x (cited on pages 91, 127).
- [Arn+20] K. J. Arnold et al. “Precision Measurements of the $^{138}\text{Ba}^+ 6s^2S_{1/2} - 5d^2D_{5/2}$ Clock Transition.” In: *Phys. Rev. Lett.* 124 (19 May 2020), p. 193001. DOI: 10.1103/PhysRevLett.124.193001. URL: <https://link.aps.org/doi/10.1103/PhysRevLett.124.193001> (cited on page 66).
- [AS68] James Roger Prior Angel and PGH Sandars. “The hyperfine structure Stark effect I. Theory.” In: *Proceedings of the Royal Society of London. Series A. Mathematical and Physical Sciences* 305.1480 (1968), pp. 125–138. DOI: 10.1098/rspa.1968.0109 (cited on pages 80, 81, 122).
- [AS72] Milton Abramowitz and Irene A. Stegun. *Handbook of Mathematical Functions with Formulas, Graphs, and Mathematical Tables*. National Bureau of Standards, 1972 (cited on page 32).
- [AT55] S. H. Autler and C. H. Townes. “Stark Effect in Rapidly Varying Fields.” In: *Phys. Rev.* 100 (2 Oct. 1955), pp. 703–722. DOI: 10.1103/PhysRev.100.703. URL: <https://link.aps.org/doi/10.1103/PhysRev.100.703> (cited on page 66).

- [BA25] M D Barrett and K J Arnold. “An extrapolation method for polarisability assessments of ion-based optical clocks.” In: *New Journal of Physics* 27.1 (Jan. 2025), p. 013005. DOI: 10.1088/1367-2630/ada4d1. URL: <https://dx.doi.org/10.1088/1367-2630/ada4d1> (cited on pages 83, 86).
- [BAJ12] Stephan Bernadotte, Andrew J. Atkins, and Christoph R. Jacob. “Origin-independent calculation of quadrupole intensities in X-ray spectroscopy.” In: *The Journal of Chemical Physics* 137.20 (Nov. 2012), p. 204106. ISSN: 0021-9606. DOI: 10.1063/1.4766359. URL: <https://doi.org/10.1063/1.4766359> (cited on page 29).
- [Bar+14] G. P. Barwood et al. “Agreement between two $^{88}\text{Sr}^+$ optical clocks to 4 parts in 10^{17} .” In: *Phys. Rev. A* 89 (5 May 2014), p. 050501. DOI: 10.1103/PhysRevA.89.050501. URL: <https://link.aps.org/doi/10.1103/PhysRevA.89.050501> (cited on pages 121, 140, 141, 147).
- [Bar+22] Parinaz Barakhshan et al. Portal for High-Precision Atomic Data and Computation (version 2.0). University of Delaware, Newark, DE, USA. URL: <https://www.udel.edu/atom>. Feb. 2022 (cited on pages 83, 86, 88, 90, 98, 144).
- [BAS19] M. D. Barrett, K. J. Arnold, and M. S. Safronova. “Polarizability assessments of ion-based optical clocks.” In: *Phys. Rev. A* 100 (4 Oct. 2019), p. 043418. DOI: 10.1103/PhysRevA.100.043418. URL: <https://link.aps.org/doi/10.1103/PhysRevA.100.043418> (cited on pages 101, 143).
- [Bau05] Andreas Bauch. “The PTB primary clocks CS1 and CS2.” In: *Metrologia*. Vol. 42. June 2005. DOI: 10.1088/0026-1394/42/3/S06 (cited on page 3).
- [Bay+20] C F A Baynham et al. “Measurement of differential polarizabilities at a mid-infrared wavelength in $^{171}\text{Yb}^+$.” 2020. arXiv: 1801.10134 [physics.atom-ph]. URL: <https://arxiv.org/abs/1801.10134> (cited on pages 11, 12, 14, 91, 96–98, 101, 110–113, 116, 118, 119, 143–145).
- [BB02] D. J. Berkeland and M. G. Boshier. “Destabilization of dark states and optical spectroscopy in Zeeman-degenerate atomic systems.” In: *Phys. Rev. A* 65 (3 Feb. 2002), p. 033413. DOI: 10.1103/PhysRevA.65.033413. URL: <https://link.aps.org/doi/10.1103/PhysRevA.65.033413> (cited on pages 27, 28).
- [Bea+25] Scott Beattie et al. “Advancements in the NRC-FCs2 primary frequency standard.” In: *Metrologia* 62.3 (May 2025), p. 035003. DOI: 10.1088/1681-7575/adcd7b. URL: <https://dx.doi.org/10.1088/1681-7575/adcd7b> (cited on pages 3, 6, 9, 139, 141, 147).

- [Ben+19] Erik Benkler et al. “End-to-end topology for fiber comb based optical frequency transfer at the 10^{-21} level.” In: *Opt. Express* 27.25 (Dec. 2019), pp. 36886–36902. DOI: 10.1364/OE.27.036886. URL: <https://opg.optica.org/oe/abstract.cfm?URI=oe-27-25-36886> (cited on pages 73, 76).
- [Ber+98] D. J. Berkeland et al. “Minimization of ion micromotion in a Paul trap.” In: *Journal of Applied Physics* 83.10 (May 1998), pp. 5025–5033. ISSN: 0021-8979. DOI: 10.1063/1.367318. eprint: https://pubs.aip.org/aip/jap/article-pdf/83/10/5025/18699946/5025_1_online.pdf. URL: <https://doi.org/10.1063/1.367318> (cited on pages 23, 28, 87, 134).
- [Bié+98] E Biémont et al. “Lifetime calculations in Yb II.” In: *Journal of Physics B: Atomic, Molecular and Optical Physics* 31.15 (Aug. 1998), p. 3321. DOI: 10.1088/0953-4075/31/15/006. URL: <https://dx.doi.org/10.1088/0953-4075/31/15/006> (cited on pages 85, 112).
- [BIP19] BIPM. *Le Système international d’unités / The International System of Units (‘The SI Brochure’)*. Ninth. Bureau international des poids et mesures, 2019. ISBN: 978-92-822-2272-0. URL: http://www.bipm.org/en/si/si_brochure/ (cited on pages 3, 4, 37).
- [BKW92] Gerhard Birkl, Sven Kassner, and Herbert Walther. “Multiple-shell structures of laser-cooled $^{24}\text{Mg}^+$ ions in a quadrupole storage ring.” In: *Nature* 357.6376 (1992), pp. 310–313. DOI: doi.org/10.1038/357310a0 (cited on page 23).
- [Blo+00] M Block et al. “Crystalline ion structures in a Paul trap.” In: *Journal of Physics B: Atomic, Molecular and Optical Physics* 33.11 (June 2000), p. L375. DOI: 10.1088/0953-4075/33/11/101. URL: <https://dx.doi.org/10.1088/0953-4075/33/11/101> (cited on page 23).
- [Blü+88] R Blümel et al. “Phase transitions of stored laser-cooled ions.” In: *Nature* 334.6180 (1988), pp. 309–313. DOI: 10.1038/334309a0 (cited on page 23).
- [Boc+18] Matthias Bock et al. “High-fidelity entanglement between a trapped ion and a telecom photon via quantum frequency conversion.” en. In: *Nature Communications* 9.1 (2018), p. 1998. ISSN: 2041-1723. DOI: 10.1038/s41467-018-04341-2. URL: <https://www.nature.com/articles/s41467-018-04341-2> (cited on page 18).
- [Bre+19] S. M. Brewer et al. “ $^{27}\text{Al}^+$ Quantum-Logic Clock with a Systematic Uncertainty below 10^{-18} .” In: *Phys. Rev. Lett.* 123 (3 July 2019), p. 033201. DOI: 10.1103/PhysRevLett.123.033201. URL: <https://link.aps.org/doi/10.1103/PhysRevLett.123.033201> (cited on page 3).

- [Bri20] Malte Brinkmann. “Design und Fabrikation skalierbarer Ionenfallen für neuartige Anwendungen der Quantenmetrologie.” Master thesis. Leibniz Universität Hannover, 2020 (cited on page 49).
- [BWR00] T. A. Birks, W. J. Wadsworth, and P. St. J. Russell. “Supercontinuum generation in tapered fibers.” In: *Opt. Lett.* 25.19 (Oct. 2000), pp. 1415–1417. DOI: 10.1364/OL.25.001415. URL: <https://opg.optica.org/ol/abstract.cfm?URI=ol-25-19-1415> (cited on page 5).
- [Cai+17] William B. Cairncross et al. “Precision Measurement of the Electron’s Electric Dipole Moment Using Trapped Molecular Ions.” In: *Phys. Rev. Lett.* 119 (15 2017), p. 153001. DOI: 10.1103/PhysRevLett.119.153001. URL: <https://link.aps.org/doi/10.1103/PhysRevLett.119.153001> (cited on page 18).
- [CCT25] WGFS 1 CCTF. “CCTF Recommendation 24-2 CCL CCTF WGFS on updates to the CIPM list of standard frequencies, approved by CCTF during its 24th meeting.” Sept. 2025 (cited on pages 140, 141, 147).
- [Cho+10] Chin-Wen Chou et al. “Optical clocks and relativity.” In: *Science* 329.5999 (2010), pp. 1630–1633. DOI: 10.1126/science.1192720 (cited on page 132).
- [Coh75] C. Cohen-Tannoudji. “Optical Pumping with Lasers.” In: *Atomic Physics 4*. Ed. by G. zu Putlitz, E. W. Weber, and A. Winnacker. Boston, MA: Springer US, 1975, pp. 589–614. ISBN: 978-1-4684-2964-0. DOI: 10.1007/978-1-4684-2964-0_29. URL: https://doi.org/10.1007/978-1-4684-2964-0_29 (cited on page 28).
- [Col+21] Boulder Atomic Clock Optical Network BACON Collaboration et al. “Frequency ratio measurements at 18-digit accuracy using an optical clock network.” In: *Nature* 591.7851 (2021), pp. 564–569. DOI: 10.1038/s41586-021-03253-4 (cited on page 12).
- [Cor21] Magnetic Shield Corporation. *MuMetal Properties*. 2021. URL: <http://www.mu-metal.com/technical-data.html> (cited on page 64).
- [Cor22] Rogers Corporation. *RO4000® Series*. RO4350B. 2022. URL: <https://rogerscorp.com/advanced-electronics-solutions/ro4000-series-laminates/ro4350b-laminates> (cited on page 49).
- [Cow81] Robert D. Cowan. *The theory of atomic structure and spectra*. University of California Press, 1981 (cited on pages 26, 38).
- [DBG17] Pierre Dubé, John E Bernard, and Marina Gertszov. “Absolute frequency measurement of the $^{88}\text{Sr}^+$ clock transition using a GPS link to the SI second.” In: *Metrologia* 54.3 (Mar. 2017), p. 290. DOI: 10.1088/1681-7575/aa5e60. URL: <https://dx.doi.org/10.1088/1681-7575/aa5e60> (cited on pages 140, 141, 147).

- [Dem12] Wolfgang Demtröder. *Experimentalphysik 2: Elektrizität und Optik*. Springer, 2012 (cited on page 17).
- [Dem13] Wolfgang Demtröder. *Laserspektroskopie 2. Experimentelle Techniken*. Springer Berlin, Heidelberg, Feb. 2013. ISBN: 978-3-642-21447-9. DOI: 10.1007/978-3-642-21447-9. URL: <https://doi.org/10.1007/978-3-642-21447-9> (cited on page 26).
- [Dem16] Wolfgang Demtröder. *Experimentalphysik 3: Atome, Moleküle und Festkörper*. Springer-Verlag, 2016 (cited on page 79).
- [Den+18] Heiner Denker et al. “Geodetic methods to determine the relativistic redshift at the level of 10^{-18} in the context of international timescales: a review and practical results.” In: *Journal of Geodesy* 92 (2018), pp. 487–516 (cited on page 140).
- [Dic53] R. H. Dicke. “The Effect of Collisions upon the Doppler Width of Spectral Lines.” In: *Phys. Rev.* 89 (2 Jan. 1953), pp. 472–473. DOI: 10.1103/PhysRev.89.472. URL: <https://link.aps.org/doi/10.1103/PhysRev.89.472> (cited on page 132).
- [Die+89] F. Diedrich et al. “Laser Cooling to the Zero-Point Energy of Motion.” In: *Phys. Rev. Lett.* 62 (4 Jan. 1989), pp. 403–406. DOI: 10.1103/PhysRevLett.62.403. URL: <https://link.aps.org/doi/10.1103/PhysRevLett.62.403> (cited on pages 31, 46).
- [Dim+24] N Dimarcq et al. “Roadmap towards the redefinition of the second.” In: *Metrologia* 61.1 (Jan. 2024), p. 012001. DOI: 10.1088/1681-7575/ad17d2. URL: <https://dx.doi.org/10.1088/1681-7575/ad17d2> (cited on pages 4, 121, 141, 142, 146, 147).
- [Dol+15] M Doležal et al. “Analysis of thermal radiation in ion traps for optical frequency standards.” In: *Metrologia* 52.6 (Nov. 2015), p. 842. DOI: 10.1088/0026-1394/52/6/842. URL: <https://dx.doi.org/10.1088/0026-1394/52/6/842> (cited on pages 102, 127–129).
- [Dör+21] S Dörscher et al. “Optical frequency ratio of a $^{171}\text{Yb}^+$ single-ion clock and a ^{87}Sr lattice clock.” In: *Metrologia* 58.1 (Jan. 2021), p. 015005. DOI: 10.1088/1681-7575/abc86f. URL: <https://dx.doi.org/10.1088/1681-7575/abc86f> (cited on pages 12, 138).
- [Dre+83] Ronald WP Drever et al. “Laser phase and frequency stabilization using an optical resonator.” In: *Applied Physics B* 31.2 (1983), pp. 97–105. DOI: 10.1007/BF00702605 (cited on pages 74, 75).
- [Dre+98] M. Drewsen et al. “Large Ion Crystals in a Linear Paul Trap.” In: *Phys. Rev. Lett.* 81 (14 Oct. 1998), pp. 2878–2881. DOI: 10.1103/PhysRevLett.81.2878. URL: <https://link.aps.org/doi/10.1103/PhysRevLett.81.2878> (cited on page 23).

Bibliography

- [Dub+05] P. Dubé et al. “Electric Quadrupole Shift Cancellation in Single-Ion Optical Frequency Standards.” In: *Phys. Rev. Lett.* 95 (3 July 2005), p. 033001. DOI: 10.1103/PhysRevLett.95.033001. URL: <https://link.aps.org/doi/10.1103/PhysRevLett.95.033001> (cited on pages 140, 141, 147).
- [Dub+10] P. Dubé et al. “Recent progress on the NRC $^{88}\text{Sr}^+$ single-ion optical frequency standard.” In: *2010 IEEE International Frequency Control Symposium*. June 2010, pp. 65–70. DOI: 10.1109/FREQ.2010.5556371 (cited on page 26).
- [Dub+13] Pierre Dubé et al. “Evaluation of systematic shifts of the $^{88}\text{Sr}^+$ single-ion optical frequency standard at the 10^{-17} level.” In: *Phys. Rev. A* 87 (2 2013), p. 023806. DOI: 10.1103/PhysRevA.87.023806. URL: <https://link.aps.org/doi/10.1103/PhysRevA.87.023806> (cited on pages 89, 95, 106, 107, 121–123, 131–133, 136).
- [Dub+14] Pierre Dubé et al. “High-Accuracy Measurement of the Differential Scalar Polarizability of a $^{88}\text{Sr}^+$ Clock Using the Time-Dilation Effect.” In: *Phys. Rev. Lett.* 112 (17 Apr. 2014), p. 173002. DOI: 10.1103/PhysRevLett.112.173002. URL: <https://link.aps.org/doi/10.1103/PhysRevLett.112.173002> (cited on pages 12–14, 87, 88, 96, 98, 119, 120, 129, 134, 143, 145).
- [Ear39] Samuel Earnshaw. “On the Nature of the Molecular Forces which regulate the Constitution of the Luminiferous Ether.” In: *Transactions of the Cambridge Philosophical Society* 7 (1839), pp. 97–112 (cited on page 18).
- [Ein05] A. Einstein. “Zur Elektrodynamik bewegter Körper.” In: *Annalen der Physik* 322.10 (1905), pp. 891–921. DOI: <https://doi.org/10.1002/andp.19053221004>. eprint: <https://onlinelibrary.wiley.com/doi/pdf/10.1002/andp.19053221004>. URL: <https://onlinelibrary.wiley.com/doi/abs/10.1002/andp.19053221004> (cited on page 3).
- [Ein16] A. Einstein. “Die Grundlage der allgemeinen Relativitätstheorie.” In: *Annalen der Physik* 354.7 (1916), pp. 769–822. DOI: <https://doi.org/10.1002/andp.19163540702>. eprint: <https://onlinelibrary.wiley.com/doi/pdf/10.1002/andp.19163540702>. URL: <https://onlinelibrary.wiley.com/doi/abs/10.1002/andp.19163540702> (cited on pages 3, 139).
- [Ejt10] Sara Ejtemaee. “A fluorescence study of single trapped Ytterbium ions for quantum information applications.” Master thesis. Simon Fraser University, Aug. 2010 (cited on pages 27, 28).

- [ETH10] S. Ejtemaee, R. Thomas, and P. C. Haljan. “Optimization of Yb⁺ fluorescence and hyperfine-qubit detection.” In: *Phys. Rev. A* 82 (6 Dec. 2010), p. 063419. DOI: 10.1103/PhysRevA.82.063419. URL: <https://link.aps.org/doi/10.1103/PhysRevA.82.063419> (cited on pages 27, 28).
- [Fal+11] St Falke et al. “The ⁸⁷Sr optical frequency standard at PTB.” In: *Metrologia* 48.5 (Sept. 2011), p. 399. DOI: 10.1088/0026-1394/48/5/022. URL: <https://dx.doi.org/10.1088/0026-1394/48/5/022> (cited on page 10).
- [FB19] Tara Fortier and Esther Baumann. “20 years of developments in optical frequency comb technology and applications.” In: *Communications Physics* 2.1 (2019), p. 153. DOI: 10.1038/s42005-019-0249-y (cited on pages 5, 6).
- [Fig+19] C. Figgatt et al. “Parallel entangling operations on a universal ion-trap quantum computer.” en. In: *Nature* 572.7769 (2019), pp. 368–372. ISSN: 1476-4687. DOI: 10.1038/s41586-019-1427-5. URL: <https://www.nature.com/articles/s41586-019-1427-5> (cited on page 18).
- [Fil+23] M. Filzinger et al. “Improved Limits on the Coupling of Ultralight Bosonic Dark Matter to Photons from Optical Atomic Clock Comparisons.” In: *Phys. Rev. Lett.* 130 (25 June 2023), p. 253001. DOI: 10.1103/PhysRevLett.130.253001. URL: <https://link.aps.org/doi/10.1103/PhysRevLett.130.253001> (cited on pages 11, 12).
- [Fis97] Peter TH Fisk. “Trapped-ion and trapped-atom microwave frequency standards.” In: *Reports on Progress in Physics* 60.8 (1997), p. 761. DOI: 10.1088/0034-4885/60/8/001 (cited on page 132).
- [Für+19] Henning Alexander Fürst et al. “Trapped ions in a bath of ultracold atoms.” University of Amsterdam, 2019 (cited on page 69).
- [Für+20] H. A. Fürst et al. “Coherent Excitation of the Highly Forbidden Electric Octupole Transition in ¹⁷²Yb⁺.” In: *Phys. Rev. Lett.* 125 (16 Oct. 2020), p. 163001. DOI: 10.1103/PhysRevLett.125.163001. URL: <https://link.aps.org/doi/10.1103/PhysRevLett.125.163001> (cited on pages 41, 123).
- [Gan+18] H. C. J. Gan et al. “Oscillating-magnetic-field effects in high-precision metrology.” In: *Phys. Rev. A* 98 (3 Sept. 2018), p. 032514. DOI: 10.1103/PhysRevA.98.032514. URL: <https://link.aps.org/doi/10.1103/PhysRevA.98.032514> (cited on pages 14, 66–68, 80, 103).

Bibliography

- [God+14] R. M. Godun et al. “Frequency Ratio of Two Optical Clock Transitions in $^{171}\text{Yb}^+$ and Constraints on the Time Variation of Fundamental Constants.” In: *Phys. Rev. Lett.* 113 (21 Nov. 2014), p. 210801. DOI: 10.1103/PhysRevLett.113.210801. URL: <https://link.aps.org/doi/10.1103/PhysRevLett.113.210801> (cited on page 12).
- [Han+19a] A. M. Hankin et al. “Systematic uncertainty due to background-gas collisions in trapped-ion optical clocks.” In: *Phys. Rev. A* 100 (3 Sept. 2019), p. 033419. DOI: 10.1103/PhysRevA.100.033419. URL: <https://link.aps.org/doi/10.1103/PhysRevA.100.033419> (cited on pages 69–71, 134).
- [Han+19b] S. Hannig et al. “Towards a transportable aluminium ion quantum logic optical clock.” In: *Review of Scientific Instruments* 90.5 (May 2019), p. 053204. ISSN: 0034-6748. DOI: 10.1063/1.5090583. eprint: https://pubs.aip.org/aip/rsi/article-pdf/doi/10.1063/1.5090583/14695430/053204_1_online.pdf. URL: <https://doi.org/10.1063/1.5090583> (cited on page 10).
- [HAP72] WILLIAM HAPPER. “Optical Pumping.” In: *Rev. Mod. Phys.* 44 (2 Apr. 1972), pp. 169–249. DOI: 10.1103/RevModPhys.44.169. URL: <https://link.aps.org/doi/10.1103/RevModPhys.44.169> (cited on page 42).
- [Har06] HartmutG. “FrequencyComb-CEOphase.” This work is licensed under the Creative Commons Attribution-Share Alike 3.0 Unported License. To view a copy of this license, visit <https://creativecommons.org/licenses/by-sa/3.0/>. 2006. URL: <https://en.wikipedia.org/wiki/File:FrequencyComb-CEOphase.svg> (cited on pages 6, 73).
- [Hau+25] H. N. Hausser et al. “ $^{115}\text{In}^+ - ^{172}\text{Yb}^+$ Coulomb Crystal Clock with 2.5×10^{-18} Systematic Uncertainty.” In: *Phys. Rev. Lett.* 134 (2 Jan. 2025), p. 023201. DOI: 10.1103/PhysRevLett.134.023201. URL: <https://link.aps.org/doi/10.1103/PhysRevLett.134.023201> (cited on pages 10, 49, 127).
- [Her+12] N. Herschbach et al. “Linear Paul trap design for an optical clock with Coulomb crystals.” In: *Appl Phys B* 107 (2012), pp. 891–906. DOI: 10.1007/s00340-011-4790-y. URL: <https://doi.org/10.1007/s00340-011-4790-y> (cited on page 10).
- [Het+15] M. Hettrich et al. “Measurement of Dipole Matrix Elements with a Single Trapped Ion.” In: *Phys. Rev. Lett.* 115 (14 Oct. 2015), p. 143003. DOI: 10.1103/PhysRevLett.115.143003. URL: <https://link.aps.org/doi/10.1103/PhysRevLett.115.143003> (cited on page 83).

- [HMS79] D Hasselkamp, E Mondry, and A Scharmann. “Direct observation of the transversal Doppler-shift.” In: *Zeitschrift für Physik A Atoms and Nuclei* 289.2 (1979), pp. 151–155. DOI: 10.1007/BF01435932 (cited on page 131).
- [Höf+97] J.T Höffges et al. “Heterodyne measurement of the fluorescent radiation of a single trapped ion.” In: *Optics Communications* 133.1 (1997), pp. 170–174. ISSN: 0030-4018. DOI: [https://doi.org/10.1016/S0030-4018\(96\)00621-9](https://doi.org/10.1016/S0030-4018(96)00621-9). URL: <https://www.sciencedirect.com/science/article/pii/S0030401896006219> (cited on page 28).
- [Hot+23] Gregory W. Hoth et al. “NIST-F3, a Cesium Fountain Frequency Reference.” In: *Proceedings of the 54th Annual Precise Time and Time Interval Systems and Applications Meeting* (2023), pp. 183–188. DOI: 10.33012/2023.18691 (cited on pages 3, 6, 9, 139, 141, 147).
- [HRS02] Gerhard Heinzel, Albrecht Rüdiger, and Reinhard Schilling. *Spectrum and spectral density estimation by the Discrete Fourier transform (DFT), including a comprehensive list of window functions and some new at-top windows*. 2002. URL: <https://hdl.handle.net/11858/00-001M-0000-0013-557A-5> (cited on page 22).
- [Hua+24] Yao Huang et al. “Measurement of infrared magic wavelength for an all-optical trapping of $^{40}\text{Ca}^+$ ion clock.” In: *New Journal of Physics* 26.4 (Apr. 2024), p. 043021. DOI: 10.1088/1367-2630/ad3ea8. URL: <https://dx.doi.org/10.1088/1367-2630/ad3ea8> (cited on pages 82, 83, 99, 146).
- [Hun+12] N. Huntemann et al. “High-Accuracy Optical Clock Based on the Octupole Transition in $^{171}\text{Yb}^+$.” In: *Phys. Rev. Lett.* 108 (9 Feb. 2012), p. 090801. DOI: 10.1103/PhysRevLett.108.090801. URL: <https://link.aps.org/doi/10.1103/PhysRevLett.108.090801> (cited on page 10).
- [Hun+14] N. Huntemann et al. “Improved Limit on a Temporal Variation of m_p/m_e from Comparisons of Yb^+ and Cs Atomic Clocks.” In: *Phys. Rev. Lett.* 113 (21 Nov. 2014), p. 210802. DOI: 10.1103/PhysRevLett.113.210802. URL: <https://link.aps.org/doi/10.1103/PhysRevLett.113.210802> (cited on page 12).
- [Hun+16] N. Huntemann et al. “Single-Ion Atomic Clock with 3×10^{-18} Systematic Uncertainty.” In: *Phys. Rev. Lett.* 116 (6 Feb. 2016), p. 063001. DOI: 10.1103/PhysRevLett.116.063001. URL: <https://link.aps.org/doi/10.1103/PhysRevLett.116.063001> (cited on pages 10–12, 14, 72, 83, 86, 91, 96–98, 101, 110–113, 116, 118, 119, 123, 143–145).
- [Hun14] Nils Huntemann. “High-Accuracy Optical Clock Based on the Octupole Transition in $^{171}\text{Yb}^+$.” PhD thesis. Hannover University, 2014 (cited on pages 14, 83, 86, 110–112, 116, 118, 119).

- [HW91] Ernst Hairer and Gerhard Wanner. *Solving Ordinary Differential Equations II*. Springer Berlin, Heidelberg, 1991. DOI: 10.1007/978-3-662-09947-6 (cited on page 21).
- [Ita00] Wayne M Itano. “External-field shifts of the $^{199}\text{Hg}^+$ optical frequency standard.” In: *Journal of research of the National Institute of Standards and Technology* 105.6 (2000), p. 829. DOI: 10.6028/jres.105.065 (cited on pages 106, 122, 123).
- [Jia+09] Dansha Jiang et al. “Blackbody-radiation shift in a $^{88}\text{Sr}^+$ ion optical frequency standard.” In: *Journal of Physics B: Atomic, Molecular and Optical Physics* 42.15 (July 2009), p. 154020. DOI: 10.1088/0953-4075/42/15/154020. URL: <https://dx.doi.org/10.1088/0953-4075/42/15/154020> (cited on page 84).
- [Jia+22] Bin Jian et al. “Improved absolute frequency measurement of the strontium ion clock using a GPS link to the SI second.” In: *Metrologia* 60.1 (Dec. 2022), p. 015007. DOI: 10.1088/1681-7575/aca615. URL: <https://dx.doi.org/10.1088/1681-7575/aca615> (cited on pages 15, 121, 140, 141, 147).
- [Jor+25] Elena Jordan et al. “Scalable chip-based 3D ion traps.” In: *Quantum Science and Technology* 10.4 (Aug. 2025), p. 045005. DOI: 10.1088/2058-9565/adf2db. URL: <https://dx.doi.org/10.1088/2058-9565/adf2db> (cited on page 49).
- [Jos+24] Manoj K. Joshi et al. “Characterization of ion-trap-induced ac magnetic fields.” In: *Phys. Rev. A* 110 (6 Dec. 2024), p. 063101. DOI: 10.1103/PhysRevA.110.063101. URL: <https://link.aps.org/doi/10.1103/PhysRevA.110.063101> (cited on page 67).
- [Kal+21] D Kalincev et al. “Motional heating of spatially extended ion crystals.” In: *Quantum Science and Technology* 6.3 (May 2021), p. 034003. DOI: 10.1088/2058-9565/abee99. URL: <https://dx.doi.org/10.1088/2058-9565/abee99> (cited on page 47).
- [Kat+03] Hidetoshi Katori et al. “Ultrastable Optical Clock with Neutral Atoms in an Engineered Light Shift Trap.” In: *Phys. Rev. Lett.* 91 (17 Oct. 2003), p. 173005. DOI: 10.1103/PhysRevLett.91.173005. URL: <https://link.aps.org/doi/10.1103/PhysRevLett.91.173005> (cited on page 10).
- [Kaz+16] Michael Kazda et al. “Phase Analysis for Frequency Standards in the Microwave and Optical Domains.” In: *IEEE Transactions on Ultrasonics, Ferroelectrics, and Frequency Control* 63.7 (2016), pp. 970–974. DOI: 10.1109/TUFFC.2016.2515759 (cited on page 135).

- [Kel+15] J. Keller et al. “Precise determination of micromotion for trapped-ion optical clocks.” In: *Journal of Applied Physics* 118.10 (Sept. 2015), p. 104501. ISSN: 0021-8979. DOI: 10.1063/1.4930037. URL: <https://doi.org/10.1063/1.4930037> (cited on pages 23, 28, 134).
- [Kel+19] J. Keller et al. “Controlling systematic frequency uncertainties at the 10^{-19} level in linear Coulomb crystals.” In: *Phys. Rev. A* 99 (1 Jan. 2019), p. 013405. DOI: 10.1103/PhysRevA.99.013405. URL: <https://link.aps.org/doi/10.1103/PhysRevA.99.013405> (cited on pages 10, 49, 123, 137).
- [Kim+25] Kyungtae Kim et al. “Atomic Coherence of 2 Minutes and Instability of 1.5×10^{-18} at 1 s in a Wannier-Stark Lattice Clock.” In: *Phys. Rev. Lett.* 135 (10 Sept. 2025), p. 103601. DOI: 10.1103/3wttv-sty2. URL: <https://link.aps.org/doi/10.1103/3wttv-sty2> (cited on page 8).
- [KK73] Daniel Kleppner and Robert Kolenkow. *An introduction to mechanics*. Cambridge University Press, 1973 (cited on page 17).
- [Kra+24] A. Kramida et al. “NIST Atomic Spectra Database (version 5.12).” <https://physics.nist.gov/asd>. Accessed: 2025-04-23. 2024. DOI: 10.18434/T4W30F (cited on page 83).
- [KRM18] Ivana Kovacic, Richard Rand, and Si Mohamed Sah. “Mathieu’s equation and its generalizations: overview of stability charts and their features.” In: *Applied Mechanics Reviews* 70.2 (2018), p. 020802. DOI: 10.1115/1.4039144 (cited on page 20).
- [Kuh21] Niklas Kuhrmeyer. “Weglängenstabilisierung zur Übertragung hochstabiler optischer Signale mit SDR-Techniken.” Technische Universität Braunschweig, 2021 (cited on page 77).
- [Lab+08] Jaroslaw Labaziewicz et al. “Suppression of Heating Rates in Cryogenic Surface-Electrode Ion Traps.” In: *Phys. Rev. Lett.* 100 (1 Jan. 2008), p. 013001. DOI: 10.1103/PhysRevLett.100.013001. URL: <https://link.aps.org/doi/10.1103/PhysRevLett.100.013001> (cited on page 146).
- [Lan+20] R. Lange et al. “Coherent Suppression of Tensor Frequency Shifts through Magnetic Field Rotation.” In: *Phys. Rev. Lett.* 125 (14 Sept. 2020), p. 143201. DOI: 10.1103/PhysRevLett.125.143201. URL: <https://link.aps.org/doi/10.1103/PhysRevLett.125.143201> (cited on pages 11, 123).
- [Lan+21a] R. Lange et al. “Improved Limits for Violations of Local Position Invariance from Atomic Clock Comparisons.” In: *Phys. Rev. Lett.* 126 (1 Jan. 2021), p. 011102. DOI: 10.1103/PhysRevLett.126.011102. URL: <https://link.aps.org/doi/10.1103/PhysRevLett.126.011102> (cited on pages 10–13, 15, 72, 121, 123, 127, 140, 141, 147).

Bibliography

- [Lan+21b] R. Lange et al. “Lifetime of the $^2F_{7/2}$ Level in Yb^+ for Spontaneous Emission of Electric Octupole Radiation.” In: *Phys. Rev. Lett.* 127 (21 Nov. 2021), p. 213001. DOI: 10.1103/PhysRevLett.127.213001. URL: <https://link.aps.org/doi/10.1103/PhysRevLett.127.213001> (cited on pages 11, 29).
- [Lan21] Richard Lange. “High-Precision Frequency Comparisons and Searches for New Physics with Yb^+ Optical Clocks.” PhD thesis. Leibniz Universität Hannover, 2021 (cited on pages 10, 11, 83, 86).
- [Lei+03] D. Leibfried et al. “Quantum dynamics of single trapped ions.” In: *Rev. Mod. Phys.* 75 (1 2003), pp. 281–324. DOI: 10.1103/RevModPhys.75.281. URL: <https://link.aps.org/doi/10.1103/RevModPhys.75.281> (cited on pages 18, 30, 31, 33, 34).
- [Lei+07] David R. Leibbrandt et al. “Laser ablation loading of a surface-electrode ion trap.” In: *Phys. Rev. A* 76 (5 Nov. 2007), p. 055403. DOI: 10.1103/PhysRevA.76.055403. URL: <https://link.aps.org/doi/10.1103/PhysRevA.76.055403> (cited on page 63).
- [Li+24] Lin Li et al. “Dynamic laser ablation loading of a linear Paul trap.” In: *Journal of Physics D: Applied Physics* 57.31 (May 2024), p. 315205. DOI: 10.1088/1361-6463/ad449f. URL: <https://dx.doi.org/10.1088/1361-6463/ad449f> (cited on page 63).
- [Li07] Yajun Li. “Encircled energy in systems with truncated-Gaussian apertures of different Fresnel numbers. I. Generalization of the Q_{2n} function of E. Wolf and the Y_n function of H. H. Hopkins.” In: *J. Opt. Soc. Am. A* 24.7 (July 2007), pp. 2023–2032. DOI: 10.1364/JOSAA.24.002023. URL: <https://opg.optica.org/josaa/abstract.cfm?URI=josaa-24-7-2023> (cited on page 94).
- [Lin+23] T Lindvall et al. “Noise-induced servo errors in optical clocks utilizing Rabi interrogation.” In: *Metrologia* 60.4 (July 2023), p. 045008. DOI: 10.1088/1681-7575/acdfd4. URL: <https://dx.doi.org/10.1088/1681-7575/acdfd4> (cited on page 135).
- [Lin+25a] T. Lindvall et al. “ $^{88}\text{Sr}^+$ optical clock with 7.9×10^{-19} systematic uncertainty and measurement of its absolute frequency with 9.8×10^{-17} uncertainty.” In: *Phys. Rev. Appl.* (Sept. 2025), pp. –. DOI: 10.1103/cz1f-bfvp. URL: <https://link.aps.org/doi/10.1103/cz1f-bfvp> (cited on pages 13, 140, 141).
- [Lin+25b] T. Lindvall et al. “Measurement of the Differential Static Scalar Polarizability of the $^{88}\text{Sr}^+$ Clock Transition.” In: *Phys. Rev. Lett.* 135 (4 July 2025), p. 043402. DOI: 10.1103/52by-28mr. URL: <https://link.aps.org/doi/10.1103/52by-28mr> (cited on pages 12–14, 88, 96, 101, 113, 116, 118–121, 143, 145, 147).

- [Lin+25c] Thomas Lindvall et al. “Coordinated international comparisons between optical clocks connected via fiber and satellite links.” In: *Optica* 12.6 (June 2025), pp. 843–852. DOI: 10.1364/OPTICA.561754. URL: <https://opg.optica.org/optica/abstract.cfm?URI=optica-12-6-843> (cited on pages 11, 139–141, 147).
- [LL06] Sun Kyung Lee and Hai-Woong Lee. “Damped population oscillation in a spontaneously decaying two-level atom coupled to a monochromatic field.” In: *Phys. Rev. A* 74 (6 Dec. 2006), p. 063817. DOI: 10.1103/PhysRevA.74.063817. URL: <https://link.aps.org/doi/10.1103/PhysRevA.74.063817> (cited on pages 36, 37).
- [LME07] I. Lizuain, J. G. Muga, and J. Eschner. “Motional frequency shifts of trapped ions in the Lamb-Dicke regime.” In: *Phys. Rev. A* 76 (3 Sept. 2007), p. 033808. DOI: 10.1103/PhysRevA.76.033808. URL: <https://link.aps.org/doi/10.1103/PhysRevA.76.033808> (cited on page 132).
- [Lor02] Hendrik Antoon Lorentz. “The fundamental equations for electromagnetic phenomena in ponderable bodies, deduced from the theory of electrons.” In: *Proceedings of the section of sciences* 5 (1902), pp. 254–266. URL: <https://dwc.knaw.nl/DL/publications/PU00014152.pdf> (cited on page 17).
- [Lou00] Rodney Loudon. *The Quantum Theory of Light*. 3rd. Oxford University Press, 2000 (cited on page 31).
- [LSR13] Fam Le Kien, Philipp Schneeweiss, and Arno Rauschenbeutel. “Dynamical polarizability of atoms in arbitrary light fields: general theory and application to cesium.” In: *The European Physical Journal D* 67 (2013), pp. 1–16. DOI: 10.1140/epjd/e2013-30729-x (cited on pages 80, 83, 103).
- [Lud+15] Andrew D. Ludlow et al. “Optical atomic clocks.” In: *Rev. Mod. Phys.* 87 (2 June 2015), pp. 637–701. DOI: 10.1103/RevModPhys.87.637. URL: <https://link.aps.org/doi/10.1103/RevModPhys.87.637> (cited on pages 8–10).
- [LWB06] S. N. Lea, S. A. Webster, and G. P. Barwood. “Polarisabilities and blackbody shifts in Sr^+ and Yb^+ .” In: *Proceedings of the 20th European Frequency and Time Forum* (2006), p. 302 (cited on page 112).
- [Mad+04] A. A. Madej et al. “Absolute frequency of the $^{88}\text{Sr}^+ 5s^2S_{1/2} - 4d^2D_{5/2}$ reference transition at 445 THz and evaluation of systematic shifts.” In: *Phys. Rev. A* 70 (1 July 2004), p. 012507. DOI: 10.1103/PhysRevA.70.012507. URL: <https://link.aps.org/doi/10.1103/PhysRevA.70.012507> (cited on pages 130, 134).

- [Mad+12] Alan A. Madej et al. “ $^{88}\text{Sr}^+$ 445-THz Single-Ion Reference at the 10^{-17} Level via Control and Cancellation of Systematic Uncertainties and Its Measurement against the SI Second.” In: *Phys. Rev. Lett.* 109 (20 Nov. 2012), p. 203002. DOI: 10.1103/PhysRevLett.109.203002. URL: <https://link.aps.org/doi/10.1103/PhysRevLett.109.203002> (cited on pages 140, 141, 147).
- [Mar+04] HS Margolis et al. “Hertz-level measurement of the optical clock frequency in a single $^{88}\text{Sr}^+$ ion.” In: *Science* 306.5700 (2004), pp. 1355–1358. DOI: 10.1126/science.1105497 (cited on pages 140, 141, 147).
- [Mar+24] H S Margolis et al. “The CIPM list ‘Recommended values of standard frequencies’: 2021 update.” In: *Metrologia* 61.3 (Apr. 2024), p. 035005. DOI: 10.1088/1681-7575/ad3afc. URL: <https://dx.doi.org/10.1088/1681-7575/ad3afc> (cited on pages 4, 13, 15, 140, 141, 146, 147).
- [Mar+25a] Claude Marceau et al. “Absolute frequency measurement of a $^{88}\text{Sr}^+$ clock by direct comparison to a primary frequency standard.” In: *Metrologia* 62.4 (June 2025), p. 045001. DOI: 10.1088/1681-7575/ade4d1. URL: <https://dx.doi.org/10.1088/1681-7575/ade4d1> (cited on pages 13, 121, 140, 141, 147).
- [Mar+25b] Mason C. Marshall et al. “High-Stability Single-Ion Clock with 5.5×10^{-19} Systematic Uncertainty.” In: *Phys. Rev. Lett.* 135 (3 July 2025), p. 033201. DOI: 10.1103/hb3c-dk28. URL: <https://link.aps.org/doi/10.1103/hb3c-dk28> (cited on pages 3, 9, 127).
- [Mat+17] D. G. Matei et al. “1.5 μm Lasers with Sub-10 mHz Linewidth.” In: *Phys. Rev. Lett.* 118 (26 June 2017), p. 263202. DOI: 10.1103/PhysRevLett.118.263202. URL: <https://link.aps.org/doi/10.1103/PhysRevLett.118.263202> (cited on pages 4, 6, 72, 73, 136, 138).
- [Mat68] Émile Mathieu. “Mémoire sur le mouvement vibratoire d’une membrane de forme elliptique.” fre. In: *Journal de Mathématiques Pures et Appliquées* 13 (1868), pp. 137–203. URL: <http://eudml.org/doc/234720> (cited on page 19).
- [MF04] Giovanna Morigi and Shmuel Fishman. “Eigenmodes and Thermodynamics of a Coulomb Chain in a Harmonic Potential.” In: *Phys. Rev. Lett.* 93 (17 Oct. 2004), p. 170602. DOI: 10.1103/PhysRevLett.93.170602. URL: <https://link.aps.org/doi/10.1103/PhysRevLett.93.170602> (cited on page 24).
- [MH22] Regina Moser and Natascha Hedrich. “Quantum Physics at Technorama.” en. Feb. 2022. URL: <https://www.phys.ethz.ch/news-and-events/d-phys-news/2022/01/quantum-physics-at-technorama.html> (cited on page 18).

- [MS21] Bonnie L. Schmittberger Marlow and David R. Scherer. “A Review of Commercial and Emerging Atomic Frequency Standards.” In: *IEEE Transactions on Ultrasonics, Ferroelectrics, and Frequency Control* 68.6 (2021), pp. 2007–2022. DOI: 10.1109/TUFFC.2021.3049713 (cited on page 5).
- [MS99] Harold J. Metcalf and Peter Straten. *Laser Cooling and Trapping*. Springer New York, NY, 1999. DOI: 10.1007/978-1-4612-1470-0. URL: <https://doi.org/10.1007/978-1-4612-1470-0> (cited on page 25).
- [MW01] Giovanna Morigi and Hahn Walther. “Two-species Coulomb chains for quantum information.” In: *The European Physical Journal D - Atomic, Molecular, Optical and Plasma Physics* 13 (2 Jan. 2001), pp. 261–269. DOI: 10.1007/s100530170275. URL: <https://doi.org/10.1007/s100530170275> (cited on page 24).
- [Nad+22] D. P. Nadlinger et al. “Experimental quantum key distribution certified by Bell’s theorem.” en. In: *Nature* 607.7920 (2022), pp. 682–686. ISSN: 1476-4687. DOI: 10.1038/s41586-022-04941-5. URL: <https://www.nature.com/articles/s41586-022-04941-5> (cited on page 18).
- [Nor+20] T. Nordmann et al. “Sub-kelvin temperature management in ion traps for optical clocks.” In: *Review of Scientific Instruments* 91.11 (Nov. 2020), p. 111301. ISSN: 0034-6748. DOI: 10.1063/5.0024693. URL: <https://doi.org/10.1063/5.0024693> (cited on pages 102, 127, 128, 142).
- [Nos+25] I. Nosske et al. “Transportable strontium lattice clock with 4×10^{-19} blackbody radiation shift uncertainty.” 2025. arXiv: 2507.14030 [physics.atom-ph]. URL: <https://arxiv.org/abs/2507.14030> (cited on page 10).
- [Oel+19] E Oelker et al. “Demonstration of 4.8×10^{-17} stability at 1 s for two independent optical clocks.” In: *Nature Photonics* 13.10 (2019), pp. 714–719. DOI: 10.1038/s41566-019-0493-4 (cited on page 8).
- [Olm+07] S. Olmschenk et al. “Manipulation and detection of a trapped Yb⁺ hyperfine qubit.” In: *Phys. Rev. A* 76 (5 Nov. 2007), p. 052314. DOI: 10.1103/PhysRevA.76.052314. URL: <https://link.aps.org/doi/10.1103/PhysRevA.76.052314> (cited on page 27).
- [Olv+] F. W. J. Olver et al. “NIST Digital Library of Mathematical Functions.” <https://dlmf.nist.gov/>, Release 1.1.11 of 2023-09-15. URL: <https://dlmf.nist.gov/> (cited on pages 20, 21).

Bibliography

- [Pag+18] G Pagano et al. “Cryogenic trapped-ion system for large scale quantum simulation.” In: *Quantum Science and Technology* 4.1 (Oct. 2018), p. 014004. DOI: 10.1088/2058-9565/aae0fe. URL: <https://dx.doi.org/10.1088/2058-9565/aae0fe> (cited on page 146).
- [Par+13] H L Partner et al. “Dynamics of topological defects in ion Coulomb crystals.” In: *New Journal of Physics* 15.10 (Oct. 2013), p. 103013. DOI: 10.1088/1367-2630/15/10/103013. URL: <https://dx.doi.org/10.1088/1367-2630/15/10/103013> (cited on page 23).
- [Pat+20] Sayan Patra et al. “Proton-electron mass ratio from laser spectroscopy of HD^+ at the part-per-trillion level.” In: *Science* 369.6508 (2020), pp. 1238–1241. DOI: 10.1126/science.aba0453. URL: <https://www.science.org/doi/abs/10.1126/science.aba0453> (cited on page 18).
- [Pau90] Wolfgang Paul. “Electromagnetic traps for charged and neutral particles.” In: *Rev. Mod. Phys.* 62 (3 1990), pp. 531–540. DOI: 10.1103/RevModPhys.62.531. URL: <https://link.aps.org/doi/10.1103/RevModPhys.62.531> (cited on pages 10, 18).
- [PD06] Sergey G. Porsev and Andrei Derevianko. “Multipolar theory of blackbody radiation shift of atomic energy levels and its implications for optical lattice clocks.” In: *Phys. Rev. A* 74 (2 Aug. 2006), p. 020502. DOI: 10.1103/PhysRevA.74.020502. URL: <https://link.aps.org/doi/10.1103/PhysRevA.74.020502> (cited on pages 82–84).
- [Pei+04] E. Peik et al. “Limit on the Present Temporal Variation of the Fine Structure Constant.” In: *Phys. Rev. Lett.* 93 (17 Oct. 2004), p. 170801. DOI: 10.1103/PhysRevLett.93.170801. URL: <https://link.aps.org/doi/10.1103/PhysRevLett.93.170801> (cited on page 12).
- [Pis20] Emilio Pisanty. “Unit relations in the new SI planar.” This work is licensed under the Creative Commons Attribution-Share Alike 4.0 International License. To view a copy of this license, visit <https://creativecommons.org/licenses/by-sa/4.0/>. 2020. URL: https://commons.wikimedia.org/wiki/File:Unit_relations_in_the_new_SI.svg (cited on page 4).
- [Pji22] Daniël Riemer Maria Pjin. “Thermodynamics in Trapped Ion Quantum Processors.” PhD thesis. Johannes Gutenberg-Universität Mainz, 2022 (cited on page 42).
- [Pla01] Max Planck. “Ueber das Gesetz der Energieverteilung im Normalspectrum.” In: *Annalen der Physik* 309.3 (1901), pp. 553–563. DOI: <https://doi.org/10.1002/andp.19013090310>. URL: <https://onlinelibrary.wiley.com/doi/abs/10.1002/andp.19013090310> (cited on page 83).

- [Pog+21] I. Pogorelov et al. “Compact Ion-Trap Quantum Computing Demonstrator.” In: *PRX Quantum* 2 (2 June 2021), p. 020343. DOI: 10.1103/PRXQuantum.2.020343. URL: <https://link.aps.org/doi/10.1103/PRXQuantum.2.020343> (cited on page 42).
- [Pre+91] J. D. Prestage et al. “Dynamics of charged particles in a Paul radio-frequency quadrupole trap.” In: *Phys. Rev. Lett.* 66 (23 June 1991), pp. 2964–2967. DOI: 10.1103/PhysRevLett.66.2964. URL: <https://link.aps.org/doi/10.1103/PhysRevLett.66.2964> (cited on page 23).
- [Pre+92] J. D. Prestage et al. “Ultra-stable Hg⁺ trapped ion frequency standard.” In: *Journal of Modern Optics* 39 (2 1992), pp. 221–232. DOI: 10.1080/09500349214550231. URL: <https://doi.org/10.1080/09500349214550231> (cited on page 10).
- [PST05] Ekkehard Peik, Tobias Schneider, and Christian Tamm. “Laser frequency stabilization to a single ion.” In: *Journal of Physics B: Atomic, Molecular and Optical Physics* 39.1 (Dec. 2005), p. 145. DOI: 10.1088/0953-4075/39/1/012. URL: <https://dx.doi.org/10.1088/0953-4075/39/1/012> (cited on pages 7, 10, 37, 135).
- [Rai+92] M. G. Raizen et al. “Ionic crystals in a linear Paul trap.” In: *Phys. Rev. A* 45 (9 May 1992), pp. 6493–6501. DOI: 10.1103/PhysRevA.45.6493. URL: <https://link.aps.org/doi/10.1103/PhysRevA.45.6493> (cited on page 24).
- [RH08] William J Riley and David A Howe. *Handbook of frequency stability analysis*. Vol. 1065. US Department of Commerce, National Institute of Standards and Technology, 2008 (cited on page 7).
- [Rie06] Fritz Riehle. *Frequency standards: basics and applications*. John Wiley & Sons, 2006 (cited on page 11).
- [Roo00] Christian Felix Roos. “Controlling the quantum state of trapped ions.” Leopold-Franzens-Universität Innsbruck, 2000 (cited on pages 32, 33).
- [Ros+06] T Rosenband et al. “Blackbody radiation shift of the $^{27}\text{Al}^+ \ ^1S_0 \rightarrow \ ^3P_0$ transition.” In: *Proceedings of the 20th European Frequency and Time Forum*. IEEE, 2006, pp. 289–292 (cited on page 91).
- [Sah+06] B. K. Sahoo et al. “Lifetimes of the metastable $^2D_{3/2,5/2}$ states in Ca⁺, Sr⁺, and Ba⁺.” In: *Phys. Rev. A* 74 (6 Dec. 2006), p. 062504. DOI: 10.1103/PhysRevA.74.062504. URL: <https://link.aps.org/doi/10.1103/PhysRevA.74.062504> (cited on pages 27, 29, 45).
- [Sai+22] Tim Sailer et al. “Measurement of the bound-electron g-factor difference in coupled ions.” In: *Nature* 606 (2022), pp. 479–483. DOI: 10.1038/s41586-022-04807-w. URL: <https://doi.org/10.1038/s41586-022-04807-w> (cited on page 18).

Bibliography

- [San+18] Christian Sanner et al. “Autobalanced Ramsey Spectroscopy.” In: *Phys. Rev. Lett.* 120 (5 Jan. 2018), p. 053602. DOI: 10.1103/PhysRevLett.120.053602. URL: <https://link.aps.org/doi/10.1103/PhysRevLett.120.053602> (cited on page 11).
- [San+19] Christian Sanner et al. “Optical clock comparison for Lorentz symmetry testing.” In: *Nature* 567 (2019), pp. 204–208. DOI: 10.1038/s41586-019-0972-2. URL: <https://doi.org/10.1038/s41586-019-0972-2> (cited on pages 10–12, 89, 102, 127, 129, 130, 136).
- [Sas+23] S. Sasidharan et al. “Penning-Trap Mass Measurement of Helium-4.” In: *Phys. Rev. Lett.* 131 (9 2023), p. 093201. DOI: 10.1103/PhysRevLett.131.093201. URL: <https://link.aps.org/doi/10.1103/PhysRevLett.131.093201> (cited on page 18).
- [Sch+05] P. O. Schmidt et al. “Spectroscopy Using Quantum Logic.” In: *Science* 309 (5735 June 2005), pp. 749–752. DOI: 10.1126/science.1114375. URL: <https://www.science.org/doi/abs/10.1126/science.1114375> (cited on pages 31, 33).
- [Sch+20] R. Schwarz et al. “Long term measurement of the ^{87}Sr clock frequency at the limit of primary Cs clocks.” In: *Phys. Rev. Res.* 2 (3 Aug. 2020), p. 033242. DOI: 10.1103/PhysRevResearch.2.033242. URL: <https://link.aps.org/doi/10.1103/PhysRevResearch.2.033242> (cited on pages 8, 10).
- [Sem+18] I. A. Semerikov et al. “Compact Transportable Optical Standard Based on a Single $^{171}\text{Yb}^+$ Ion (“YBIS” Project).” In: *Bulletin of the Lebedev Physics Institute* 45 (11 Nov. 2018), pp. 337–340. DOI: 10.3103/S1068335618110039. URL: <https://doi.org/10.3103/S1068335618110039> (cited on page 26).
- [Sha+18] Ravid Shaniv et al. “Toward Heisenberg-Limited Rabi Spectroscopy.” In: *Phys. Rev. Lett.* 120 (24 June 2018), p. 243603. DOI: 10.1103/PhysRevLett.120.243603. URL: <https://link.aps.org/doi/10.1103/PhysRevLett.120.243603> (cited on page 35).
- [Sha+23] H. Shao et al. “Precision determination of the $5d^2D_{3/2}$ state lifetime of single $^{174}\text{Yb}^+$ ion.” In: *Phys. Rev. Res.* 5 (2 June 2023), p. 023193. DOI: 10.1103/PhysRevResearch.5.023193. URL: <https://link.aps.org/doi/10.1103/PhysRevResearch.5.023193> (cited on pages 27, 29, 83).
- [Sha49] C.E. Shannon. “Communication in the Presence of Noise.” In: *Proceedings of the IRE* 37.1 (1949), pp. 10–21. DOI: 10.1109/JRPROC.1949.232969 (cited on page 28).

- [She+23] Nathaniel Sherrill et al. “Analysis of atomic-clock data to constrain variations of fundamental constants.” In: *New Journal of Physics* 25.9 (Sept. 2023), p. 093012. DOI: 10.1088/1367-2630/aceff6. URL: <https://dx.doi.org/10.1088/1367-2630/aceff6> (cited on page 12).
- [SM00] Anders Sørensen and Klaus Mølmer. “Entanglement and quantum computation with ions in thermal motion.” In: *Phys. Rev. A* 62 (2 July 2000), p. 022311. DOI: 10.1103/PhysRevA.62.022311. URL: <https://link.aps.org/doi/10.1103/PhysRevA.62.022311> (cited on page 31).
- [SPT05] T. Schneider, E. Peik, and Chr. Tamm. “Sub-Hertz Optical Frequency Comparisons between Two Trapped $^{171}\text{Yb}^+$ Ions.” In: *Phys. Rev. Lett.* 94 (23 June 2005), p. 230801. DOI: 10.1103/PhysRevLett.94.230801. URL: <https://link.aps.org/doi/10.1103/PhysRevLett.94.230801> (cited on pages 10, 14, 100, 110–112, 116, 118, 119, 144).
- [SSA16] Sukhjit Singh, B. K. Sahoo, and Bindiya Arora. “Magnetic-sublevel-independent magic wavelengths: Application to Rb and Cs atoms.” In: *Phys. Rev. A* 93 (6 June 2016), p. 063422. DOI: 10.1103/PhysRevA.93.063422. URL: <https://link.aps.org/doi/10.1103/PhysRevA.93.063422> (cited on pages 80, 83, 123).
- [SSC16] M. S. Safronova, U. I. Safronova, and Charles W. Clark. “Magic wavelengths, matrix elements, polarizabilities, and lifetimes of Cs.” In: *Phys. Rev. A* 94 (1 July 2016), p. 012505. DOI: 10.1103/PhysRevA.94.012505. URL: <https://link.aps.org/doi/10.1103/PhysRevA.94.012505> (cited on pages 82, 83).
- [Ste+13] Andreas Steffen et al. “Note: In situ measurement of vacuum window birefringence by atomic spectroscopy.” In: *Review of Scientific Instruments* 84.12 (Dec. 2013), p. 126103. ISSN: 0034-6748. DOI: 10.1063/1.4847075. URL: <https://doi.org/10.1063/1.4847075> (cited on page 90).
- [Ste+23] M. Steinel et al. “Evaluation of a $^{88}\text{Sr}^+$ Optical Clock with a Direct Measurement of the Blackbody Radiation Shift and Determination of the Clock Frequency.” In: *Phys. Rev. Lett.* 131 (8 2023), p. 083002. DOI: 10.1103/PhysRevLett.131.083002. URL: <https://link.aps.org/doi/10.1103/PhysRevLett.131.083002> (cited on pages 10, 15, 121, 139–141, 147).
- [Stu+21] J Stuhler et al. “Opticlock: Transportable and easy-to-operate optical single-ion clock.” In: *Measurement: Sensors* 18 (2021), p. 100264. DOI: 10.1016/j.measen.2021.100264 (cited on pages 10, 11).

- [Szy+16] K Szymaniec et al. “NPL Cs fountain frequency standards and the quest for the ultimate accuracy.” In: *Journal of Physics: Conference Series* 723.1 (June 2016), p. 012003. DOI: 10.1088/1742-6596/723/1/012003. URL: <https://dx.doi.org/10.1088/1742-6596/723/1/012003> (cited on pages 3, 6, 9, 139, 141, 147).
- [Tak+16] Tetsushi Takano et al. “Geopotential measurements with synchronously linked optical lattice clocks.” In: *Nature Photonics* 10.10 (2016), pp. 662–666. DOI: 10.1038/nphoton.2016.159 (cited on page 139).
- [Tak+20] Masao Takamoto et al. “Test of general relativity by a pair of transportable optical lattice clocks.” In: *Nature photonics* 14.7 (2020), pp. 411–415. DOI: 10.1038/s41566-020-0619-8 (cited on page 139).
- [Tam+09] Chr. Tamm et al. “Stray-field-induced quadrupole shift and absolute frequency of the 688-THz $^{171}\text{Yb}^+$ single-ion optical frequency standard.” In: *Phys. Rev. A* 80 (4 Oct. 2009), p. 043403. DOI: 10.1103/PhysRevA.80.043403. URL: <https://link.aps.org/doi/10.1103/PhysRevA.80.043403> (cited on page 10).
- [Tan+23] Zhi-Ming Tang et al. “Suppression of Black-body Radiation Induced Zeeman Shifts in the Optical Clocks due to the Fine-structure Intra-manifold Resonances.” 2023. arXiv: 2309.12548 [physics.atom-ph]. URL: <https://arxiv.org/abs/2309.12548> (cited on page 104).
- [Tay96] Paul Taylor. “Observation of an Ultra-High Q Resonance in a Single Ion of $^{172}\text{Yb}^+$.” PhD thesis. University of Oxford, 1996 (cited on page 39).
- [TK03] Masao Takamoto and Hidetoshi Katori. “Spectroscopy of the $^1S_0-^3P_0$ Clock Transition of ^{87}Sr in an Optical Lattice.” In: *Phys. Rev. Lett.* 91 (22 Nov. 2003), p. 223001. DOI: 10.1103/PhysRevLett.91.223001. URL: <https://link.aps.org/doi/10.1103/PhysRevLett.91.223001> (cited on page 131).
- [TMK17] Tetsushi Takano, Ray Mizushima, and Hidetoshi Katori. “Precise determination of the isotope shift of $^{88}\text{Sr}-^{87}\text{Sr}$ optical lattice clock by sharing perturbations.” In: *Applied Physics Express* 10.7 (June 2017), p. 072801. DOI: 10.7567/APEX.10.072801. URL: <https://dx.doi.org/10.7567/APEX.10.072801> (cited on page 29).
- [Tof+24] A Tofful et al. “ $^{171}\text{Yb}^+$ optical clock with 2.2×10^{-18} systematic uncertainty and absolute frequency measurements.” In: *Metrologia* 61.4 (June 2024), p. 045001. DOI: 10.1088/1681-7575/ad53cd. URL: <https://dx.doi.org/10.1088/1681-7575/ad53cd> (cited on page 11).
- [Vir+20] Pauli Virtanen et al. “SciPy 1.0: Fundamental Algorithms for Scientific Computing in Python.” In: *Nature Methods* 17 (2020), pp. 261–272. DOI: 10.1038/s41592-019-0686-2 (cited on page 21).

- [Vyb+23] Ivan Vybornyi et al. “Sideband Thermometry of Ion Crystals.” In: *PRX Quantum* 4 (4 Dec. 2023), p. 040346. DOI: 10.1103/PRXQuantum.4.040346. URL: <https://link.aps.org/doi/10.1103/PRXQuantum.4.040346> (cited on page 24).
- [Wei+24] Yuan-Fei Wei et al. “Improved Measurement of the Differential Polarizability Using Co-Trapped Ions.” In: *Phys. Rev. Lett.* 133 (3 July 2024), p. 033001. DOI: 10.1103/PhysRevLett.133.033001. URL: <https://link.aps.org/doi/10.1103/PhysRevLett.133.033001> (cited on pages 101, 119, 143).
- [Wey+18] S. Weyers et al. “Advances in the accuracy, stability, and reliability of the PTB primary fountain clocks.” In: *Metrologia* 55 (6 Oct. 2018). ISSN: 16817575. DOI: 10.1088/1681-7575/aae008 (cited on pages 3, 6, 9, 13, 15, 139, 141, 147).
- [Whi+22] Brendan M. White et al. “Isotope-selective laser ablation ion-trap loading of $^{137}\text{Ba}^+$ using a BaCl_2 target.” In: *Phys. Rev. A* 105 (3 Mar. 2022), p. 033102. DOI: 10.1103/PhysRevA.105.033102. URL: <https://link.aps.org/doi/10.1103/PhysRevA.105.033102> (cited on page 63).
- [Wod+21] E Wodey et al. “A robust, high-flux source of laser-cooled ytterbium atoms.” In: *Journal of Physics B: Atomic, Molecular and Optical Physics* 54.3 (Feb. 2021), p. 035301. DOI: 10.1088/1361-6455/abd2d1. URL: <https://dx.doi.org/10.1088/1361-6455/abd2d1> (cited on page 24).
- [YC05] Jun Ye and Steven T Cundiff. *Femtosecond optical frequency comb: principle, operation and applications*. Springer Science & Business Media, 2005 (cited on pages 5, 6).
- [Zee97] Pieter Zeeman. “XXXII. On the influence of magnetism on the nature of the light emitted by a substance.” In: *The London, Edinburgh, and Dublin Philosophical Magazine and Journal of Science* 43.262 (1897), pp. 226–239 (cited on page 37).
- [Zha+16] Helena Zhang et al. “Iterative precision measurement of branching ratios applied to $5P$ states in $^{88}\text{Sr}^+$.” In: *New Journal of Physics* 18.12 (Dec. 2016), p. 123021. DOI: 10.1088/1367-2630/aa511d. URL: <https://dx.doi.org/10.1088/1367-2630/aa511d> (cited on pages 27, 45, 83, 88, 90).

Martin Roland Steinel

Nationality: German

Education

- 06/2020 – today **PhD student**, *Physikalisch-Technische Bundesanstalt*, 4.4 Time and Frequency.
- 04/2017 – 09/2020 **Master Physik**, *Saarland University*.
- 10/2013 – 03/2017 **Bachelor Physik**, *Saarland University*.
- 08/2004 – 06/2013 **Abitur**, *Johannes-Kepler-Gymnasium Lebach*.
- 08/1999 – 07/2004 **Elementary school**, *Lindenschule Riegelsberg*.

Work experience

- 06/2020 – today **PhD student**, *Physikalisch-Technische Bundesanstalt*, 4.4 Time and Frequency.
- 10/2019 – 03/2020 **Leading teaching assistant**, *Saarland University*, AG Eschner.
- 04/2019 – 08/2019 **Tutorial instructor**, *Saarland University*, AG Eschner.
- 04/2016 – 03/2018 **Teaching assistant**, *Saarland University*, AG Eschner.
- 08/2015 **Public education event employee**, *Highlights der Physik 2015*.

Volunteer experience

- 04/2019 – 05/2020 and 04/2016 – 03/2018 **Trainer for medieval fencing (HEMA)**, *Saarland University*, University sports.
- 04/2014 – 03/2018 **Student council member (IT coordinator)**, *Saarland University*, Student council for physics majors.

Experience abroad

- 01/2025, 1 week **Spain**, *Centro Español de Metrologia, Madrid*, Support in planning a new optical clock.
- 09/2023, 2 weeks **Finland**, *VTT MIKES, Espoo*, Laboratory exchange with the group of Thomas Lindvall, setup of a modulation transfer lock.
- 03/2018 – 02/2019 **Japan**, *Tohoku University, Sendai*, COLABS university exchange program.

Awards

- 05/2025 **European Frequency and Time Forum 2025**, *Student Pitch Competition, Honorable Mention Award (2nd place)*.
- 11/2021 **TÜV Saarland Stiftung**, *Best master thesis on the topic of safety and reliability*.
- 07/2021 **European Frequency and Time Forum 2021**, *Winner of the student poster prize in Optical Frequency Standards and Applications*.
- 07/2019 **Photonik-Akademie 2019**, *1st place for Laser induced forward transfer (LIFT) without energy absorbing layers*.

Public relations experience

- 06/2021 – today **Tours PTB**, *Tours about the clocks at PTB for general and expert audiences*.
- 06/2025 **Science Slam**, *Haus der Wissenschaft Braunschweig*, Eine Zelle für geladene Atome.
- 09/2024 **Highlights der Physik 2024**, *Peer-to-Pier: Floßfahrt mit Physik*.
- 06/2024 **Science Slam**, *Haus der Wissenschaft Braunschweig*, Eine Zelle für geladene Atome.
- 06/2023 **Science Slam**, *Haus der Wissenschaft Braunschweig in Kooperation mit dem Exzellenzcluster Quantum Frontiers*, Eine Zelle für geladene Atome.

List of scientific publications

- Elena Jordan, Malte Brinkmann, Alexandre Didier, Erik Jansson, Martin Steinel, Nils Huntemann, Hu Shao, Hendrik Siebeneich, Christof Wunderlich, Michael Johanning and Tanja E Mehlstäubler, *Scalable chip-based 3D ion traps*, Quantum Sci. Technol. 10 045005 (2025), <https://doi.org/10.1088/2058-9565/adf2db>
- Lukas J. Spieß, Shuying Chen, Alexander Wilzewski, Malte Wehrheim, Jan Gilles, Andrey Surzhykov, Erik Benkler, Melina Filzinger, Martin Steinel, Nils Huntemann, Charles Cheung, Sergey G. Porsev, Andrey I. Bondarev, Marianna S. Safronova, José R. Crespo López-Urrutia, and Piet O. Schmidt, *Excited-State Magnetic Properties of Carbon-like Ca^{14+}* , Phys. Rev. Lett. 135, 043002 (2025), <https://doi.org/10.1103/p88p-brnx>
- Thomas Lindvall, Marco Pizzocaro, Rachel M. Godun, Michel Abgrall, Daisuke Akamatsu, Anne Amy-Klein, Erik Benkler, Nishant M. Bhatt, Davide Calonico, Etienne Cantin, Elena Cantoni, Giancarlo Cerretto, Christian Chardonnet, Miguel Angel Cifuentes Marin, Cecilia Clivati, Stefano Conidio, E. Anne Curtis, Heiner Denker, Simone Donadello, Sören Dörscher, Chen-Hao Feng, Melina Filzinger, Thomas Fordell, Irene Goti, Kalle Hanhijärvi, H. Nimrod Hausser, Ian R. Hill, Kazumoto Hosaka, Nils Huntemann, Matthew Y. H. Johnson, Jonas Keller, Joshua Klose, Takumi Kobayashi, Sebastian Koke, Alexander Kuhl, Rodolphe Le Targat, Thomas Legero, Filippo Levi, Burghard Lipphardt, Christian Lisdat, Hongli Liu, Jérôme Lodewyck, Olivier Lopez, Maxime Mazouth-Laurol, Tanja E. Mehlstäubler, Alberto Mura, Akiko Nishiyama, Tabea Nordmann, Adam O. Parsons, Gérard Petit, Benjamin Pointard, Paul-Eric Pottie, Matias Risaro, Billy I. Robertson, Marco Schioppo, Haosen Shang, Kilian Stahl, Martin Steinel, Uwe Sterr, Alexandra Tofful, Mads Tønnes, Dang-Bao-An Tran, Jacob Tunesi, Anders E. Wallin, and Helen S. Margolis, *Coordinated international comparisons between optical clocks connected via fiber and satellite links*, Optica Vol. 12, Issue 6, pp. 843-852 (2025), <https://doi.org/10.1364/OPTICA.561754>
- Alexander Wilzewski, Lukas J. Spieß, Malte Wehrheim, Shuying Chen, Steven A. King, Peter Micke, Melina Filzinger, Martin R. Steinel, Nils Huntemann, Erik Benkler, Piet O. Schmidt, Luca I. Huber, Jeremy Flannery, Roland Matt, Martin Stadler, Robin Oswald, Fabian Schmid, Daniel Kienzler, Jonathan Home, Diana P. L. Aude Craik, Menno Door, Sergey Eliseev, Pavel Filianin, Jost Herkenhoff, Kathrin Kromer, Klaus Blaum, Vladimir A. Yerokhin, Igor

- A. Valuev, Natalia S. Oreshkina, Chunhai Lyu, Sreya Banerjee, Christoph H. Keitel, Zoltán Harman, Julian C. Berengut, Anna Viatkina, Jan Gilles, Andrey Surzhykov, Michael K. Rosner, José R. Crespo López-Urrutia, Jan Richter, Agnese Mariotti, and Elina Fuchs, *Nonlinear Calcium King Plot Constrains New Bosons and Nuclear Properties*, Phys. Rev. Lett. 134, 233002 (2025), <https://doi.org/10.1103/PhysRevLett.134.233002>
- Melina Filzinger, Ashlee R. Caddell, Dhruv Jani, Martin Steinel, Leonardo Giani, Nils Huntemann and Benjamin M. Roberts, *Ultralight Dark Matter Search with Space-Time Separated Atomic Clocks and Cavities*, Phys. Rev. Lett. 134, 031001 (2025), <https://doi.org/10.1103/PhysRevLett.134.031001>
 - Martin Steinel, Hu Shao, Melina Filzinger, Burghard Lipphardt, Malte Brinkmann, Alexandre Didier, Tanja E. Mehlstäubler, Thomas Lindvall, Ekkehard Peik and Nils Huntemann, *Evaluation of a $^{88}\text{Sr}^+$ Optical Clock with a Direct Measurement of the Blackbody Radiation Shift and Determination of the Clock Frequency*, Phys. Rev. Lett. 131, 083002 (2023), <https://doi.org/10.1103/PhysRevLett.131.083002>
 - Melina Filzinger, Sören Dörscher, Richard Lange, Joshua Klose, Martin Steinel, Erik Benkler, Ekkehard Peik, Christian Lisdat and Nils Huntemann, *Improved Limits on the Coupling of Ultralight Bosonic Dark Matter to Photons from Optical Atomic Clock Comparisons*, Phys. Rev. Lett. 130, 253001 (2023), <https://doi.org/10.1103/PhysRevLett.130.253001>
 - Hannes Gothe, Dmitriy Sholokhov, Anna Breunig, Martin Steinel and Jürgen Eschner, *Continuous-wave virtual-state lasing from cold ytterbium atoms*, Phys. Rev. A 99, 013415 (2019), <https://doi.org/10.1103/PhysRevA.99.013415>



Die Physikalisch-Technische Bundesanstalt, das nationale Metrologieinstitut, ist eine wissenschaftlich-technische Bundesoberbehörde im Geschäftsbereich des Bundesministeriums für Wirtschaft und Energie.



Physikalisch-Technische Bundesanstalt
Nationales Metrologieinstitut
ISNI: 0000 0001 2186 1887

Bundesallee 100
38116 Braunschweig

Presse- und Öffentlichkeitsarbeit

Telefon: (0531) 592-93 21
Fax: (0531) 592-30 08
E-Mail: presse@ptb.de
www.ptb.de